Modelling Welding Distortion

Influence of Clamping and Sequencing

Tobias Schenk

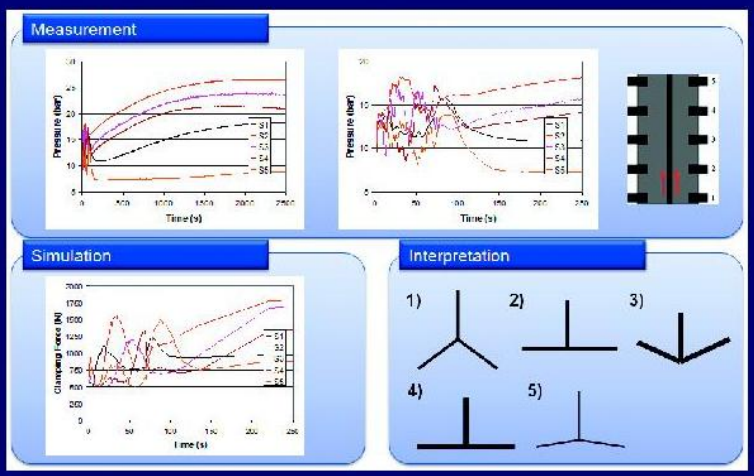

In past decades, mitigation methods have been developed to reduce welding distortion using different approaches such as low-stress no distortion welding with additional cooling, pre-deformation, thermal tensioning, or by using optimized welding sequences. One parameter that affects the distortion, which is not explicitly considered in most studies, is the influence of the clamping system. This is an important aspect since clamps are almost always present during the welding process in order to hold the work-piece components in place. Unlike most of the mitigation techniques, making use of the clamps for in-line distortion control has the potential advantage that no further energy consuming technique has to be introduced into the process.

This thesis deals with techniques to model welding distortion as well as the influence of clamping and sequencing on rthe esidual welding distortion.

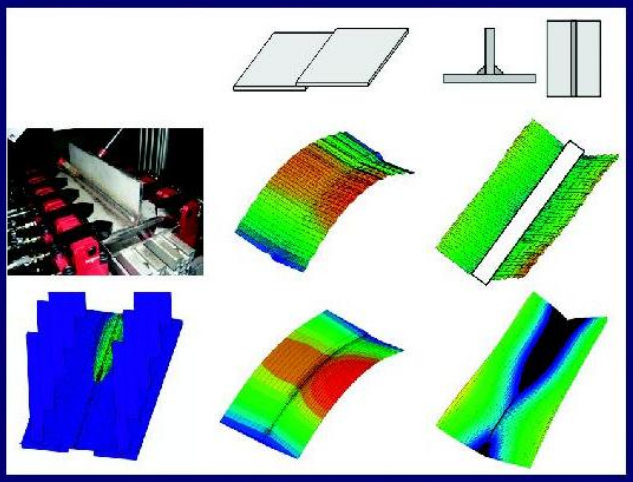

M2i Materials innovation institute

ISBN: 978-90-77172-59-9

Modelling of Welding Distortion

The Influence of Clamping and Sequencing



This research was carried out under project number MC8.06256 in the framework of the Research Program of the Materials innovation institute (M2i) in the Netherlands (www.m2i.nl).

Modelling of Welding Distortion

The Influence of Clamping and Sequencing

PROEFSCHRIFT

ter verkrijging van de graad van doctor
aan de Technische Universiteit Delft,
op gezag van de Rector Magnificus prof. ir. K. Ch. A. M. Luyben
voorzitter van het College voor Promoties,
in het openbaar te verdedigen op 30 Juni 2011 om 12.30 uur

door

Tobias SCHENK

Diplom-Physiker
Albert-Ludwig-Universtität Freiburg, Germany

geboren te Emmendingen, Duitsland

Dit proefschrift is goedgekeurd door de promotor:
Prof. dr. I.M. Richardson

Samenstelling promotiecommissie:

Rector Magnificus, voorzitter
Prof. dr. I.M. Richardson, Technische Universiteit Delft, promotor
Prof. Dr.-Ing. M. Rethmeier, TU Berlin
Prof. dr. ir. J. Huétink, University of Twente
Prof. ir. H.H. Snijder, Technische Universiteit Eindhoven
Prof. dr. ir. A. van Keulen, Technische Universiteit Delft
Prof. dr. ir. J. Sietsma, Technische Universiteit Delft
Dr.-Ing. Martin Kraska, INPRO mbH

ISBN 978-90-77172-59-9

Copyright © 2011 by Tobias Schenk

All rights reserved. No part of the material protected by this copyright notice may be reproduced or utilised in any form or by any means, electronic or mechanical, including photocopying, recording or by any information storage and retrievel system, without written permission from the publisher.

Printed in The Netherlands

Lists of Symbols and Abbreviations xi
1 Introduction 1
1.1 Relevance of this Research 1
1.1.1 Scientific Relevance 1
1.1.2 Industrial Relevance 2
1.2 Research Approach 5
1.2.1 Selected Case Studies 6
1.3 Thesis Structure 7
1.3.1 Coordinate System 7
1.3.2 Thesis Outline 8
2 Background 9
2.1 Gas-Metal-Arc (GMA) Welding 9
2.1.1 Temperature Profile during Welding 10
2.1.2 Heat-Affected Zone 14
2.1.3 Addition of Filler Material 15
2.2 Material Behaviour during Welding 18
2.2.1 Thermomechanical Material Behaviour 18
2.2.2 Phase Transformation 22
2.2.3 Models commonly applied in Literature 25
2.3 Welding & Material Considerations 30
2.3.1 Residual Stresses 31
2.3.2 Welding Distortion 34
2.3.3 Buckling of Plates 35
2.3.4 Distortion of T-Joints 40
2.4 Concluding Remarks 46
3 Distortion Mitigation Techniques 49
3.1 Tensioning & Straightening 49
3.1.1 Mechanical Straightening 49
3.1.2 Thermal Tensioning – LSND-Welding 51
3.1.3 Dynamic LSND-Welding 53
3.1.4 Other Cooling / Heating Techniques 55
3.2 Further Mitigation Techniques 56
3.2.1 Welding Sequence 56
3.2.2 Shrinkage Moment Minimisation 59
3.2.3 Annealing 60
3.2.4 Predeformation / Prestraining 61
3.3 Influence of Clamping & Restraints 62
3.3.1 Thermal Influence 63
3.3.2 Mechanical Reaction 65
3.3.3 Simple Conceptual Models 67
3.4 Concluding Remarks 69
4 Experimental & Numerical Arrangement 71
4.1 Experimental Setup 71
4.1.1 Clamping System 72

4.1.2 Welding Conditions 73
4.1.3 Distortion Measurement 73
4.2 Transient Thermomechanical-Metallurgical Model 76
4.2.1 Flow Chart 76
4.2.2 Finite Element Framework 77
4.2.3 Model Integration 81
4.2.4 Phase Transformation 84
4.2.5 Filler Material Addition 87
4.2.6 Simplified Numerical Clamping Model 88
4.3 Material Properties 89
4.3.1 Thermodynamic Properties 89
4.3.2 Metallurgical Properties 90
4.3.3 Elastic Properties 91
4.3.4 Plastic Properties 92
4.4 Meshing 96
4.4.1 DP600 Overlap Joint 96
4.4.2 S355 T-Joint 96
5 Model Validation & Verification 97
5.1 DP600 Overlap Joint 97
5.1.1 Temperature Field 97
5.1.2 Welding Distortion 100
5.1.3 Phase Transformation 102
5.1.4 Longitudinal Stresses 103
5.1.5 Tensile Tests 107
5.2 S355 T-Joint 108
5.2.1 Temperature Field 108
5.2.2 Welding Distortion 111
5.2.3 Predeformation 112
5.2.4 Variations within Standards 113
5.2.5 Influence of Phase Transformations 115
5.3 Mesh Convergence Analysis & Buckling 116
5.3.1 Convergence Analysis 116
5.3.2 Modal Analysis 118
5.3.3 Error Estimation 120
5.4 Sensitivity Analysis 122
5.4.1 Sensitivity Analysis 122
5.4.2 Summary 126
5.5 Concluding Remarks 127
6 Influence of Clamping & Sequencing 129
6.1 DP600 Overlap Joint 129
6.1.1 Clamping Release Time 129
6.1.2 Delayed Clamping 131
6.1.3 Preheating 132
6.2 S355 T-Joint 133
6.2.1 Clamping Time 133
6.2.2 Transient Clamping Force 136
6.2.3 Clamp Distance 138

6.2.4 Prestraining 141
6.3 Welding Sequencing 141
6.3.1 Selected Sequences & Temperature Profile 141
6.3.2 Welding Distortion & Plastic Deformations 142
6.3.3 Statistical Model 145
6.4 Concluding Remarks 148
7 Simplified Modelling 151
7.1 Simplified Clamping Models 151
7.1.1 0D Friction-Spring Clamp Element 151
7.1.2 Verification 155
7.2 Simplification Studies 159
7.2.1 DP600 Overlap Joint 160
7.2.2 S355 T-Joint 162
7.2.3 Shrinkage Model 164
7.3 Optimisation 167
7.3.1 Parameter Study 168
7.3.2 1D-Scan: Robustness Analysis 169
7.3.3 Automatic Optimisation 171
7.4 Concluding Remarks 173
8 Transverse Control Arm 175
8.1 Numerical and Experimental Configuration 175
8.1.1 Thermomechanical Data 175
8.1.2 Numerical and Experimental Configuration 177
8.1.3 Validation 178
8.2 Predictions 180
8.2.1 Optimisation of Clamping Conditions 180
8.2.2 Geometrical Predeformation 181
8.2.3 Sensitivity Analysis 182
8.3 Concluding Remarks 185
9 General Conclusions 187
10 Future Work 191
Summary 193
References 197
Acknowledgements 213
List of Publications 215
Curriculum Vitae 217

Lists of Symbols and Abbreviations

The lists below include the symbols and abbreviations as they are used in the present thesis. In some cases, the same symbol is used to describe two parameters. However, the explanations in the text and the context in which the symbols are used will make the meaning of all symbols unambiguous. If occasionally other symbols are used in the text, their meaning is explained clearly.

Latin Symbols

Symbol	**Description**	**Units**
A	Area	m^2
A	Strain hardening exponent	-
A_{el}	Eutectoid temperature	K
b	Martensite growth parameter	K^{-1}
b, b_{eff}	Weld seam leg length, effective leg length	m
B	FEM B-Matrix	-
C	Elasticity tensor	Pa
d	Diameter	m
D	Grain size	m
D	Flexural Rigidity	N m^2
E	Young's Modulus	Pa
E	Energy	J
f	Frequency	Hz
f	Multiplication factor	-
f	Internal body force	N m^{-3}
F	Force	N
F_{cr}	Critical buckling load	N
F	Yield criterion	Pa
F_c	Distortion restraint factor	-
F	Deformation gradient	m
g_N	Dirichlet displacement boundary condition	m
g_T	Dirichlet thermal boundary condition	T
h	Heat transfer coefficient	W m^{-2} K^{-1}
h_T	Neumann thermal boundary condition	W m^{-1}
h_N	Neumann displacement boundary condition	N m^{-1}
h	Surface convection film coefficient	W m^{-2} K^{-1}
H, **H**	Hill tensor of plastic anisotropy	-
I	Area moment of inertia, 2nd moment of area	m^4
I	Welding current	A
k	Stiffness, usually in kN / mm	N m^{-1}
k	Volumetric damping factor	kg s^{-1} m^{-3}
k	Damping factor	kg s^{-1}
K	Viscoplastic coefficient	Pa s
K_{oil}	Modulus of compression of oil ≈ 3 GPa	Pa
l, l_{eff}	Length of a sample, effective length	m

M	Bending moment	N m
M_s	Martensite start temperature	K
M	Mass matrix	kg
N_x, N_y, N_z	Neutral bending axes	m
n	Exponent of phase kinetics	-
n_l	Element density in longitudinal direction	-
p	Accumulated plastic strains	-
p, **p**	Hydrostatic stresses / pressure	Pa
P, P^{EQ}	Phase fraction, equilibrium phase fraction	-
q	Heat input per unit volume / density	W m^{-3}
Q	Incremental Load Pattern	N
Q	Net input power	W
Q_l	Heat input per unit length	J m^{-1}
Q_t	Total process power	W
r	Radius, distance	m
R	Isotropic hardening	Pa
R	Rotation tensor	-
R_v	Surface roughness	m
S	Strain rate	s^{-1}
S	Strain hardening saturation	Pa
S, **S**	Deviatoric stresses	Pa
S	Leg length of a weld	m
t	Thickness of a sample	m
t	Time	s
T, T_0	Temperature, initial / room temperature	°C or K
T^*	Homologous temperature	-
$T_{Holding}$	Holding temperature for annealing	°C or K
T_M, $T_{Melting}$	Melting temperature	°C or K
T	External work	J
u, **u**	Nodal displacements	m
w	Deformation shape	m
U	Displacement / compression	m
U	Internal work, deformation energy	J
U	Welding Power	V
U	Deformation tensor	m
v	Welding speed	m s^{-1}
v_w	Wire feeding speed	m s^{-1}
V	Volume	m^3
w	Width of a sample	m

Greek Symbols

Symbol	**Description**	**Units**
α	Thermal diffusivity	m^2 s
α	Rotation angle	°
α, **α**	Kinematic hardening	Pa
α	Thermal expansion coefficient	K^{-1}
Γ	Boundary on volume	m^2

ε	Radiation emissivity coefficient	-
ε, $\boldsymbol{\varepsilon}$	Strains	-
η	Process efficiency	-
θ	Angular Distortion	°
κ	Curvature	m^{-1}
λ	Eigenvalue	-
λ	Heat conductivity	$W\ m^{-1}\ K^{-1}$
μ	Friction coefficient	-
ν	Poisson's ratio	-
ρ	Density	$kg\ m^{-3}$
σ, $\boldsymbol{\sigma}$	Stress, Stress tensor	Pa
σ_{EQ}	equivalent stress	Pa
σ_Y	Yield stress	Pa
σ_B	Stefan-Boltzmann constant = $5{,}6704 \cdot 10^{-8}\ W\ m^{-2}\ K^{-4}$	$W\ m^{-2}\ K^{-4}$
σ_h	Smoothed stress state	Pa
σ_0	Stress in center at the weld seam	Pa
σ_l	Average longitudinal stress	Pa
τ	Relaxation time	s
τ	Phase growth constant	s
τ_{700}	Cooling rate at 700°C	s
υ	Frequency	$Hz = s^{-1}$
υ	Line search parameter	-
Ω	Volume	m^3

Abbreviations

Abbreviation	**Description**
BOP	Bead-on-plate
CBL	Critical buckling load
D	Dirichlet (boundary condition)
FE, FEM	Finite element method
fp	Flange plate of T-joint
GMA, GMAW	Gas metal arc welding
GTA, GTAW	Gas tungsten arc welding
N	Neumann (boundary condition)
wp	Web plate of T-joint

FEM Unit System

In finite element methods (FEM), it is common to use the (mm,t,s) systems. The following table lists the parameters needed for the calculations and their corresponding SI-units and conversion factors.

Parameter	**SI-Units**	**(mm,t,s)-Units**	**Conversion Factor**
Basis Quanitites			
Dimension	m	mm	10^{3}
Mass	kg	t	10^{-3}
Time	s	s	1
Temperature	K	K	1
Derived Quanitites			
Force	N	N	1
Volume	m^3	mm^3	10^{9}
Energy	J = N m	N mm	10^{3}
Power	$W = J\ s^{-1} = N\ ms^{-1}$	$N\ mm\ s^{-1}$	10^{3}
Density	$kg\ m^{-3}$	$t\ mm^{-3}$	10^{-12}
Specific Heat	$J\ kg^{-1}\ K^{-1}$	$N\ mm^{-1}\ t^{-1}K^{-1}$	10^{6}
Heat Conductivity	$W\ m^{-1}\ K^{-1} = N\ s^{-1}\ K^{-1}$	$N\ s^{-1}\ K^{-1}$	1
Strain	$m\ m^{-1} = 1$	$mm\ mm^{-1} = 1$	1
Stress	$Pa = N\ m^{-2}$	$MPa = N\ mm^{-2}$	10^{-6}

1 Introduction

1.1 Relevance of this Research

1.1.1 Scientific Relevance

The distortion of structures due to time-dependent and localized heating imposed during welding is one of the major concerns related to the application of fusion welding as a joining method in industry. In general, distortion is regarded as a critical issue in terms of performance, quality and productivity, and can be problematic because it is not often taken into account in the initial design.

Significant research has been performed in the last four decades on techniques to mitigate residual stresses and distortion after welding. However, most of these techniques introduce new process parameters, increase the production time, and hence the cycle time, or are environmental unfriendly. A review of existing mitigation techniques is given in **chapter 3**. Despite the ongoing attention, the influence of clamping has not been well reported in the literature, although it is generally acknowledged that the influence of clamping is considerable, and clamping fixed arrangements for the reduction of distortion in specific applications have been reported [Newport 1999]. This is an important aspect since clamps are almost always present during welding in order to fix the work-pieces. Unlike most of the mitigation techniques, making use of clamps for in-line distortion control has the potential advantage that no further energy consuming technique need be introduced into the process.

Generally, the clamping conditions are selected either to minimise their influence on weld behaviour, as is the case with the majority of finite element modelling and verification on laboratory based test pieces, or specific clamping arrangements are employed as is the case for simulations of selected industrial applications [Radaj 2002]. However, the influence of clamp placement and activation is rarely considered.

There is some literature available dealing with the influence of the clamping on the thermomechanical behaviour of the workpiece. The mechanical influence of the clamps has been analyzed numerically by Roeren et al. [Roeren 2006] for an overlap joint and the results show that the clamping distance has a crucial influence on the final distortion; the dominating being angular distortion. According to this work, the closer the clamps are situated to the weld, the smaller the final distortion becomes. Also the clamp release time has an influence on the final distortion if the clamps are close to the weld seam; the distortion becomes smaller for increased release times. According to these findings, the release time seems to have no influence if the system is clamped outside the heat-affected-zone. This is in contradiction to the results presented by Schenk et al. [Schenk 2009a, Schenk 2009b] where it is shown that for overlap and T-Joints the release time has a significant influence on the residual welding distortion. Similar results for angular distortions of 6mm GMA bead-on-plate welds have been presented by Liu and Zhang [Liu 2009] and Jung [Jung 2004]. It is shown that the amount of angular distortion after clamp release is reduced by increased clamping forces. Schwenk et al. [Schwenk 2005], report simulations addressing the influence of clamping conditions on the thermal field.

These results show that the cooling rate at the weld seam can be influenced by the clamps and their thermal contact conditions. Similar results have also been presented by Josserand et al. [Josserand 2007].

The aspects of distortion control through clamping design coupled with weld sequence optimisation form the basis of the present work. These aspects appear to be almost neglected in the literature to date, possibly due to the computational difficulties associated with multiple weld passes, large structures and adequate thermal and mechanical descriptions of weld fixtures.

1.1.2 Industrial Relevance

Driven by the need to save fuel and reduce transport and operating costs, there is a growing demand for lightweight structures, for example in the automotive and ship industries. Lighter vehicles can cut both fuel consumption and exhaust emissions. In the automotive industry, for instance, the body-in-white is at the centre of attention in this respect. It accounts for approximately one-fourth of the vehicle weight. The innovative use of high-strength steels is called for, also when it comes to meeting the increasing safety and environmental impact requirements placed on automobiles [Thyssen 1999]. Although many welding techniques are applicable for the joining of these materials, the degree of distortion remains unacceptable and residual stresses often approach component design limits. The residual stresses in the weld and the adjacent heat-affected-zone can decrease the corrosion resistance and increase the cold cracking susceptibility, while welding distortion can cause misfit of welded structures [Radaj 2002]. The increasing reduction in thickness will lead to a growing demand for effective solutions for residual stress and strain control during welding [Aa 2007].

In the following, examples are given for costs incurred for welding distortion correction in the ship, automotive, and railway industries.

Ship Industry

An example of a wave-like buckling welding distortion of a ship hull is shown in **Figure 1-1**. This type of distortion is undesired for luxury ships such as yachts or cruisers, but also for cargo vessels as it increases drag and hence fuel consumption. It is also unacceptable for naval ships that are built with relatively thin plates and require smooth surfaces to maximize hydrodynamic performance and minimize radar signature [Huang 2004]. A conservative estimation for the labour costs accumulating for post-welding distortion correction is approximately 30 % [Andersen 2000]. According to personal communications with Damen Schelde shipyard, the total labour time for the frigate shown in the figure is approximately fifty man year. Assuming an annual gross salary plus non-wage labour costs of 60 k€ in total, and considering that post-welding distortion correction takes up to 5-10 % of the total labour, the saving potential adds up to 200 k€ – 300 k€ per ship. However, this estimation does not include energy consumption required for distortion correction, which might be considerable, for instance in the case of flame straightening.

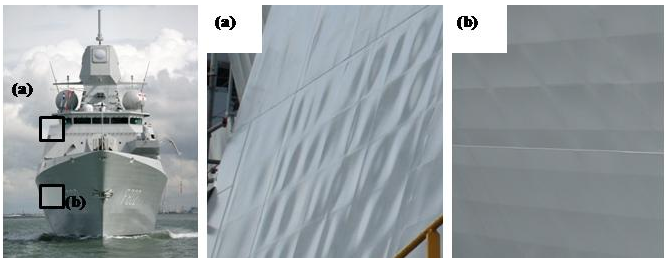

Figure 1-1 Example of remaining welding distortion after distortion mitigation on a ship hull (source: Damen Schelde).

Automotive Industry

Figure 1-2 shows two examples for welding distortion in the automotive industry. Unlike in the previous example, it is preferred to avoid post-welding distortion correction. Here, the intention is to incorporate welding distortion in the prototyping, for instance by pre-deforming components, in order to obtain structures within geometrical tolerances after welding. In order to achieve this, some experimental loops are required.

According to the statement of Volkswagen in [ESI 2008], accurate and fast prediction has the potential to save one to two loops, meaning 10 k€ - 20 k€ per part. In 2008, the German car producers launched approximately thirty new car models. Assuming ten distortion-related parts per car, a number which will increase in particular due to the upcoming application of high-strength steels, the possible savings by accurate and fast welding distortion prediction is in the order of six million euros per year. About six million cars have been built in Germany in 2008, resulting in a saving potential of 1 € per car.

This sum is of course dependent on some assumptions. In particular, the efforts required for in-line welding distortion correction are not considered in this estimation as it is almost impossible to obtain reliable data.

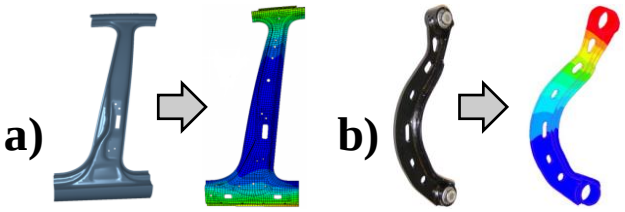

Figure 1-2 Examples of welding distortion in automotive industry. Left: Buckling of a welded B-pillar [Tikhomirov 2007]. Right: Longitudinal shrinkage of a transverse control arm [Tikhomirov 2003].

1.1 Relevance of this Research

Railway Industry

It is common in the railway industry to apply post-welding distortion correction using flame straightening as well as predeformation methods in order to mitigate welding distortion. The effort for distortion correction is in the order of five man-days per railcar body. In the German railway industry in 2008, there were about 150,000 railcars operational (not counting subways and trams), most of them on the Deutsche Bahn. The depreciation period of a rail-car is about thirty years and hence, each year 5,000 new rail-cars are built. Assuming costs of about 250 € per man-day, the total saving potential for the German railway industry adds up to 6.25 M€ per year. It should be mentioned that this estimation does not include efforts required to develop predeformation methods.

Figure 1-3 shows an aluminium railcar body assembled by welding; a final train can be seen in **Figure 1-4**. The surface roughness is due to the welding distortion correction. It should also be mentioned that there is still a high automation potential in the railway industry as most of the welds are performed manually.

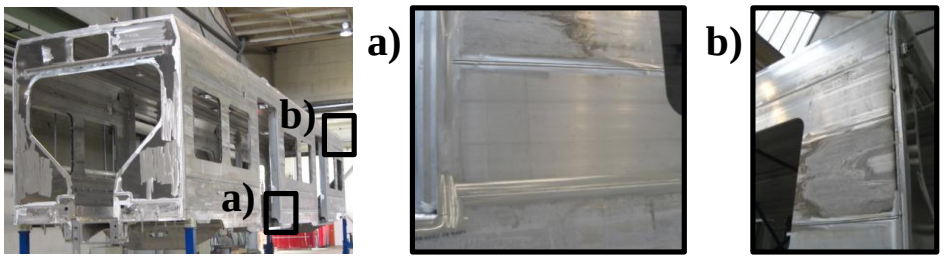

Figure 1-3 Assembly of a railcar body.

The elimination of welding distortion costs money due to labour time and energy consumption. With regard to the number of ships, cars and trains built per year, it is a safe calculation to estimate the costs due to welding distortion to be in the order of a couple of hundred million euros worldwide. Another significant disadvantage of welding distortion correction is that the productivity is decreased due to the need for additional working steps. If these steps could be omitted, it would allow a much higher degree of automation in production.



Figure 1-4 Assembled train and surface roughness due to welding.

1.2 Research Approach

The objective of this research is to investigate the influence of the clamping conditions on the thermomechanical behaviour of welded components. This includes the transient thermal and the mechanical fields during welding; *i.e.*, temperatures, distortions and stresses, until development of the final residual stress and distortion conditions. For these investigations, a combined experimental and modeling approach is performed. **Figure 1-5** shows a flow chart of the research aspects considered in this work.

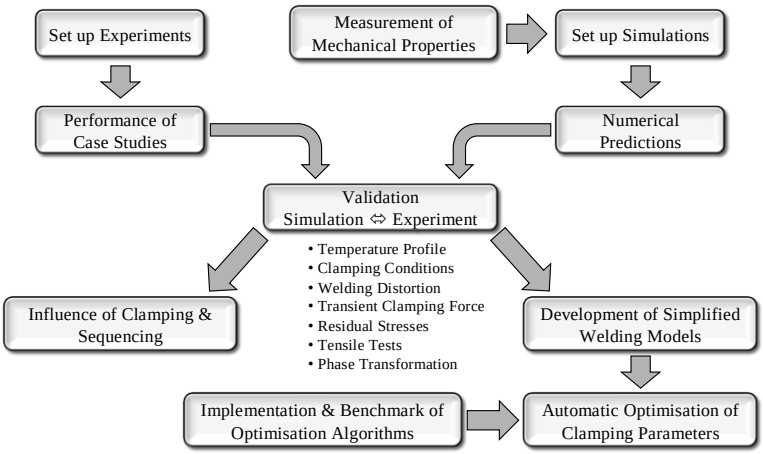

Figure 1-5 Flow chart of the activities reported in the present thesis.

Experimental and the numerical facilities have been set up to study the effect of clamping on the welding process. In order to obtain accurate predictions from the simulations, a thermomechanical-metallurgical model has been developed which includes temperature-dependent viscoplasticity with kinematic-isotropic hardening and phase transformations based on continuous cooling transition (CCT) diagrams. For this model, mechanical properties have been measured and material properties have been gathered from the literature for the case studies applied.

The results obtained from both experiments and simulations have been validated using welding distortion, transient clamping forces and, for the overlap joint, longitudinal residual stresses and phase fractions. Here, the experimentally measured transient temperature field and initial clamping conditions have been applied as input data for the simulations.

Using the validated numerical model, the influence of the clamping conditions and welding sequences has been investigated and simple conceptual models for an understanding of the observed phenomena have been derived. Simplified welding models have been developed based on sensitivity analyses. Using these simplified models, the potential for automatic optimisation of the clamping parameters has been investigated.

This research was carried out under the project number MC8.06256 in the framework of the Research Program of the Materials innovation institute M2i (www.m2i.nl), the former

Netherlands Institute for Metals Research (NIMR). The project started in August 2006 and finished in July 2010.

1.2.1 Selected Case Studies

In the present thesis, two case studies have been chosen to provide experimental data for the model validation and comparisons; a 1 mm thick DP600 overlap joint shown in **Figure 1-6,** and a 6 mm thick S355 T-Joint shown in **Figure 1-7**. The overlap joint consists of two sheets with a width of 80 mm, a length of 300 mm, and a thickness of 1 mm. The overlap between both plates is 10 mm. Hence, the width and the length of the whole workpiece are 150 mm and 300 mm, respectively. The T-Joint consists of a flange plate and a web plate. The flange plate has a width of 140 mm and a length of 300 mm. The web plate has a height of 80 mm and a length of 300 mm. The thickness and the leg length of the weld seam are both 6 mm. Gas metal arc (GMA) welding has been chosen as the welding technique.

For the dual phase steel grade DP600, the yield stress, the ultimate tensile strength and the strain at fracture are 382 MPa, at least 642 MPa and 23.6 %, respectively [Corus 2009]. According to the standardization EN10025, the minimum yield stress, the ultimate tensile strength and the strain at fracture of the fine-grained ferritic structural steel S355 are 355 MPa, 490-630 MPa and at least 22 %, respectively.

Table 1-1 and **Table 1-2** list the chemical compositions of the two steels.

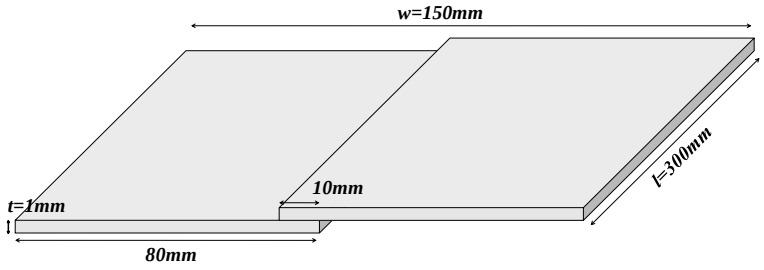

Figure 1-6 Geometry and dimensions of the overlap joint case study.

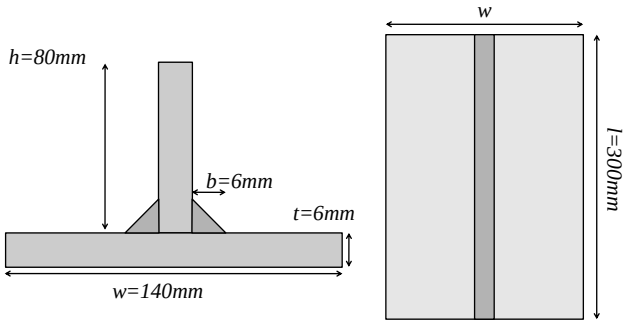

Figure 1-7 Geometry and dimensions of the T-Joint case study.

Table 1-1 Chemical composition of the dual phase steel DP600.

Element	C	Mn	Si	Cr	Mo	V	Ni	Cu	Other	Fe
wt.%	0.102	1.611	0.239	0.564	0.002	0.004	0.024	0.015	0.097	bal

Table 1-2 Chemical composition of the structural steel S355.

Element	C	Mn	Si	Cr	Mo	V	Ni	Cu	Other	Fe
wt.%	0.124	1.420	0.005	0.026	0.002	0.003	0.017	0.018	0.086	bal

The case studies are used to assess the importance of various aspects reported in the literature (**chapters 2 and 3**) as well as to explore the material response due to welding in the present work (**chapters 4-7**).

1.3 Thesis Structure

1.3.1 Coordinate System

Figure 1-8 shows the coordinate system used within the present thesis. The geometry is defined by a length *l*, a width *w*, and a thickness *t*. In all cases, the *y*-direction corresponds to the welding direction while the *x*-direction corresponds to the transverse direction. The out-of-plane direction coincides with the *z*-direction.

In most cases, the centre of the weld seam is situated at half of the width; *i.e.*, *w/2*. However in some case, the centre of the x-axis is shifted to the centre of the weld seam and hence, the plate's dimension extend from $-w/2$ to $+w/2$. For the T-joint case study, the stiffener is positioned at $x=w/2$.

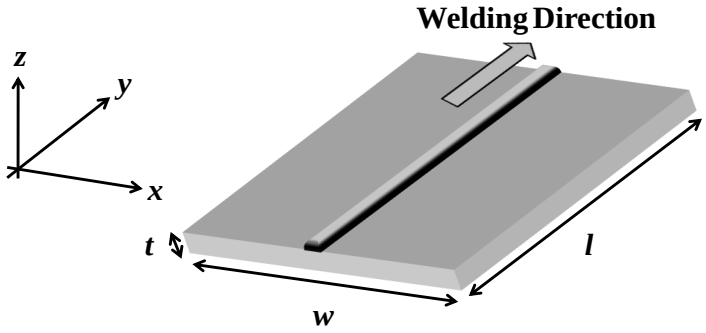

Figure 1-8 Definitions of the plate geometry and coordinate system used for all spatial results in the present thesis.

1.3.2 Thesis Outline

The thesis is subdivided into four main parts. The first part is a review of the state of the art (**chapter 2 and 3**) which includes an exploration of gas metal arc (GMA) welding and its effect on the material behaviour. It also includes the theoretical background of strain and stress development in the workpiece during and after welding and an overview of welding distortion mitigation techniques.

The second component describes the research approach and the validation methodology (**chapter 4 and 5**). The experimental and numerical equipments required to perform the case studies are outlined and data is presented for validation of numerical predictions based on experimental measurements.

Verifications of the case studies are discussed in **chapters 6 and 7** for different clamping conditions and welding sequences. The development of simplified models and the application of optimisation algorithms to these models in order to find optimal clamping parameters are also discussed.

The major findings from this research are presented in the conclusions (**chapter 9**).

2 Background

This chapter presents an overview of gas metal arc (GMA) welding techniques. How the welding process interacts with the workpiece to be welded is described together with the consequences which should be considered due to this treatment. The intention is to draw conclusions on modelling issues relevant to the present work.

In the first section, the GMA welding process is explained, indicating how the heat treatment due to welding affects the workpiece. Here, the focus is on the influence of the energy per unit length, the addition of filler material, and phase transformations occurring in the weld seam and the adjacent heat affected zone. This is followed by an overview of the subsequent material response due to welding. The response is explained by examples taken from thermomechanical-metallurgical material models. These models are compared to a literature survey of models commonly applied for welding simulation. In the last section, the creation of stresses and deformation during and after welding is explained. Some analytical models are presented and compared to simple FE simulations.

2.1 Gas-Metal-Arc (GMA) Welding

In GMA welding [Masubuchi 1980, Norrish 1992, Radaj 1999], a consumable electrode is used as a filler material deposited on the materials to be welded. Both electrodes; *i.e.*, the work piece and the filler material, are heated by an arc burning between them. Due to their small mass, electrons possess a higher velocity than ions and hence, carry the majority of the current. Due to the liberation of the work function energy upon impact at the electrode surface, the anode is heated to a greater extent. Since in GMA welding, it is desired to heat the filler material in order to melt it, the work piece usually has a negative polarity (cathode) whilst the polarity of the filler wire is positive (anode). The way the molten filler material is transferred to the base material can be divided into different transfer modes, which depend on the welding current, see **Figure 2-1**. These include free flight transfer; *i.e.*, spray, globular and pulse mode, and short-circuit or dip transfer.

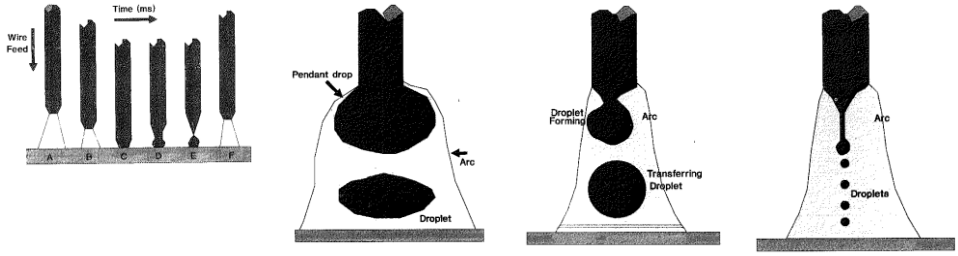

Figure 2-1 Metal transfer mode for increasing current (from left to right) [Norrish 1992].

The droplets of the globular transfer mode are rather large and hence, they are transferred from the wire to the weld pool due to gravity. This mode is only suitable for downhand welds (welding position code 1F and 1G) and is unsuitable for T-joints (position code 2F) and overlap joints. In spray transfer, the electromagnetic forces are large enough to allow welding in all positions. However, the spray mode needs a high heat input which enlarges the molten pool and the associate heat-affected-zone. As a result, it is usually used for plates having a thickness of 6mm and above.

In the present thesis, all welds have been produced using the short-circuit metal transfer mode. Similarly to the other metal transfer modes, an arc is burning between the filler and the workpiece. Molten droplets form on the tip of the electrode, but instead of falling with gravity into the weld pool, they bridge the gap between the electrode and pool. This causes a short circuit and extinguishes the arc, which is quickly reignited after the surface tension of the weld pool and the electromagnetic pinch force act to detach the metal droplet from the electrode tip. The Lorentz force excerts a pinch effect on the globule, aids in neck formation and droplet detachment. This process is repeated about a hundred times per second. This mode requires less heat input but also allows welding in all positions. In addition, fewer spatter droplets are produced compared to the globular transfer mode. However, the problem in this mode is to maintain a stable arc as reported by Hermans [Hermans 1997].

In order to maintain a stable process, gas flows out of the torch and keeps the arc shielded from the atmosphere. Initially, inert gases, like helium and argon, were used. However, it has been found that combinations with other gases improve the welding process, *e.g.* a few percent of O_2 or CO_2 which reduce the surface tension of the liquid metal, see [Dilthey 1994].

2.1.1 Temperature Profile during Welding

The arc burning between the filler wire and the workpiece to be welded generates temperatures up to 20.000 °C. The heat of the arc is transferred to the workpiece leading to an increase of the workpiece temperature above the melting temperature. In order to understand the effect of welding on the behaviour of the workpiece it is important to gain an insight into the temperature distribution during and after welding.

One of the first heat source models is based on Rosenthal's analytical solution [Rosenthal 1941] which gives a fair representation of the temperature distribution while welding. In this model, it is assumed that the net input power Q of the heat source is uniform and moves with a constant velocity and that the material properties are independent of temperature. However, this method is valid only under strong simplifications - for very thin flat sheets and infinitely thick plates, *e.g.* [Grong 1997]:

$$T_{thin} = \left(\frac{Q}{2 \cdot t \cdot \pi \cdot \lambda}\right) \exp\left(\frac{-v \cdot y}{2 \cdot \alpha}\right) \cdot K_0\left(\frac{v \cdot R}{2 \cdot \alpha}\right) + T_0 \qquad \text{for thin plates,} \qquad \textbf{Eq. 2-1}$$

$$T_{thick} = \left(\frac{Q}{2 \cdot \pi \cdot \lambda}\right) \cdot \frac{1}{R} \cdot \exp\left(\frac{-v}{2 \cdot \alpha} \cdot (R + y)\right) + T_0 \qquad \text{for thick plates,} \qquad \textbf{Eq. 2-2}$$

where T_0 is room temperature, v the welding speed, λ the heat conductivity, R the distance to the heat source, t the plate thickness, and $\alpha = \lambda/\rho c$ the thermal diffusivity. K_0 is the second modified (hyperbolic) Bessel function of order zero which can be approximated by:

$$K_0(x) \approx \sqrt{\frac{\pi}{2 \cdot x}} \cdot \exp(-x) \Rightarrow T_{thin} \approx \sqrt{R} \cdot T_{thick}. \qquad \textbf{Eq. 2-3}$$

Figure 2-2 shows the temperature distributions obtained for both thin and thick plate solutions. The thick plate solution exhibits a much faster cooling ($\sim R^{-1}$) than the thin plate solution ($\sim R^{0.5}$). The heat input or energy per unit length Q_l is defined by $Q_l = Q/v$, where Q and v are the total welding power and the welding speed, respectively. It can be shown that the maximum temperatures reached during welding as well as the cooling rates are dependent on the energy per unit length, see [Gery 2005], rather than on the welding power itself. Hence, this value is normally employed as a criterion for assessment of the material response to welding [Radaj 2002, Dilthey 1995].

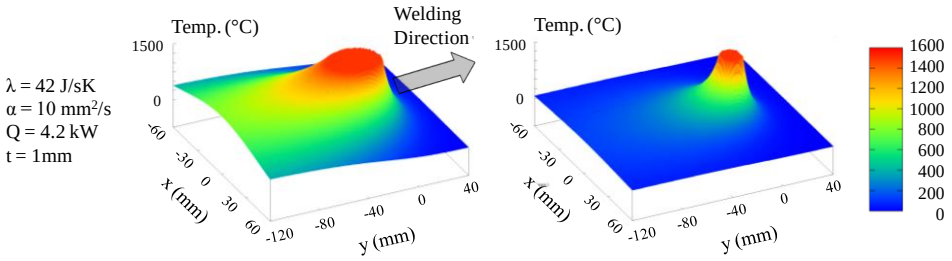

Figure 2-2 Temperature distribution for the thin (left) and thick (right) plate Rosenthal solution at the surface of the plate.

The development of analytical solutions date back to the forties and fifties [Rykalin 1952] of the last century. Although analytical solutions are generally based on many assumptions and are usually only valid under certain circumstances, much research is still being done in order to obtain better descriptions of the temperature field during welding. Firstly, this is due to the significantly faster computation time compared to numerical models. Secondly, analytical models allow a better understanding of the process. For instance, Pittner et al. [Pittner 2004, Pittner 2008] developed more elaborated analytical models than Rosenthal to describe the heat input in hybrid welding. Analytical solutions have been presented for multipass welding by Fassani and Travisan [Fassani 2003]. Poorhaydari et al. [Poorhaydari 2005] applied combined Rosenthal solutions for thin and thick plates with weighting factors in order to reproduce the real temperature distribution in the welded structure.

An early proposition for a distributed heat source model is due to Pavelic [Pavelic 1969]. It describes the heat input by a surface heat source with a Gaussian distribution. However, this model is accurate only for a heating torch which does not melt the material. The first volumetric heat source was presented by Paley and Hibbert [Paley 1975] who used a constant power density function in the fusion zone. This model

accounts for the rapid transportation of heat within the fusion zone. **Figure 2-3** shows the typical heat source used nowadays for simulation of arc welding. This double ellipsoidal heat source was first proposed in the middle eighties by Goldak [Goldak 1984]. This model is motivated by the steep temperature gradient in front of the weld and the slow cooling rate behind the torch due to the convection of heat in the weld pool.

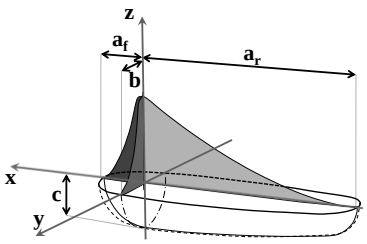

Figure 2-3 Goldak heat source.

In the Goldak model, the heat input per unit volume; *i.e.*, the heat input density, is described by:

$$q_f(x,y,z) = f_f \cdot Q \cdot \frac{6\cdot\sqrt{3}}{a_f \cdot b \cdot c \cdot \pi^{3/2}} \cdot \exp\left(-3\left(\frac{y^2}{b^2}+\frac{z^2}{z^2}+\frac{(x+v\cdot(t-t_0))^2}{{a_f}^2}\right)\right)$$

$$q_r(x,y,z) = f_r \cdot Q \cdot \frac{6\cdot\sqrt{3}}{a_r \cdot b \cdot c \cdot \pi^{3/2}} \cdot \exp\left(-3\left(\frac{y^2}{b^2}+\frac{z^2}{z^2}+\frac{(x+v\cdot(t-t_0))^2}{{a_r}^2}\right)\right) \quad . \qquad \textbf{Eq. 2-4}$$

$$f_f + f_r = 2$$

The model parameters have the meaning as shown in **Figure 2-3**. Q represents the net welding power introduced into the material. In the case of gas metal arc welding, Q is given by ηUI where η, U and I are the welding efficiency, the voltage and the current, respectively. The parameters of the heat source can be determined by measuring the experimentally observed weld pool geometry and performing temperature measurements around the weld seam for comparison with simulations, see [Aa 2007, Huang 2004].

In this equation, Q represents the net power only in the absence of additional filler material. For general weldments, however, the efficiency can be determined using calorimetric measurements [Giedt 1989]. In the present work, the efficiency is determined numerically by means of the Finite Element method. Here the integration of the total heat input over the whole volume is discretized:

$$Q = \int_V q(\vec{x})\,dV = \sum_{n_p} q(\vec{x}_p)\cdot V_p \ , \qquad \textbf{Eq. 2-5}$$

where the summation is performed over all n_p integration points p and multiplied by the volume V_p represented by the integration points. Here, $\vec{x}_p$ is the coordinate of the integration point.

Originally, the Goldak heat source was not developed for GMA welding; however, it has been applied successfully for such [Lindgren 2001, Davis 1994, Wahab 1998] and is also applied within the present thesis. In Goldak's formulation, the distributed heat input is not necessarily continuous. This is of course not supported by the physics of the process. Within the present thesis the following condition has been introduced in order to ensure the continuity of the heat input:

$$\frac{f_f}{a_f} = \frac{f_r}{a_r} \Rightarrow q_f(x=0,y,z) \equiv q_r(x=0,y,z). \qquad \textbf{Eq. 2-6}$$

The temperature distribution in the workpiece is calculated at any coordinate by solving the following differential equation:

$$\rho(\vec{x},T)\cdot c(\vec{x},T)\cdot \dot{T}(\vec{x}) = \lambda(\vec{x},T)\cdot \vec{\nabla} T(\vec{x}) + q(\vec{x},T), \qquad \textbf{Eq. 2-7}$$

where ρ, c, λ and q represent the density, the specific heat, the heat conductivity, and heat sources or losses, respectively. The heat source q can be modeled using the Goldak heat source.

In order to melt a material, an additional energy is required which is referred to as *latent heat*. The latent heat describes the amount of energy in the form of heat required for a material to undergo a phase transition. In general, the fusion zone becomes larger than it should be if this latent heat is disregarded [Radaj 1992]. A value of Q of $2.5\cdot10^5$ J/kg should be adequate for steels, according to Wang et al. [Wang 2001] and Fanous [Fanous 2005]. The findings of Schwenk et al. [Schwenk 2007] indicate that disregarding the latent heat results in seven percent higher distortion. Hence, it should be included in the simulations.

For heat losses, there are three main mechanisms; radiation and heat convection to the environment and heat conduction due to the clamping system. The heat loss due to radiation is represented by:

$$\frac{dQ}{dt} = \varepsilon_r \cdot \sigma_B \cdot A \cdot (T^4 - T_C^4), \qquad \textbf{Eq. 2-8}$$

where ε_r, A, σ_B, T, and T_C are the materials emissivity coefficient, the area of the surface considered for radiation, the Stefan-Boltzmann constant, the current material temperature and the temperature of the surroundings, respectively. The emissivity coefficient is generally temperature-dependent although it is assumed to be constant in many applications, *e.g.* in [Allmeier 2005], because its value is rarely provided in the literature. In the present thesis, the temperature-dependence assumed in [Aa 2007] is applied:

$$\begin{aligned} \varepsilon_r(T) &= 0.7 - 0.02\cdot\exp(900/T) \\ \varepsilon_r(T) &= \min(0.2, \varepsilon_r(T)) \end{aligned} \qquad \textbf{Eq. 2-9}$$

These were obtained for stainless steels and are applied to C-Mn steels in the present thesis. However, it is very difficult to obtain literature values since the emissivity is not only dependent on the material but also on the surface preparation.

Another important heat loss mechanism is heat convection to the environment:

$$\frac{dQ}{dt} = h \cdot A \cdot (T - T_C), \qquad \textbf{Eq. 2-10}$$

where h is the convective heat-transfer coefficient, or film coefficient. Andersen [Andersen 2000] reported that radiation and convection are very small compared to heat conduction and therefore can be neglected. This is probably true for the transient analysis while welding but does not hold if the cooling of the material after welding is of interest. Here, radiation and convection are significant for the cooling and must be included. Tekriwal and Mazumbder [Tekriwal 1988] reported an experimentally determined value of 10 W/m^{2}K. This value has been backed up by van der Aa [Aa 2007], whilst Pilipenko [Pilipenko 2001] assumed a value of 30 W/m^{2}K.

2.1.2 Heat-Affected Zone

Steels undergo solid phase transformations if they are subjected to selected thermal cycles. This can be useful in order to produce steels having advantageous material properties, *e.g.* high formability and high tensile strength. For instance, dual phase (DP) steels have become an important industrial material due to the combination of mechanical properties derived from selected phases [Salzgitter]. These steels, often applied in the automotive industry, possess low yield strengths in combination with high tensile strengths, and hence, exhibit early plasticisation, which is favourable for forming processes, especially for complex components.

When structural members are joined by fusion welding, the material has to be heated to its melting point and then cooled under conditions of restraint imposed by the geometry of the joint. As a result of this severe thermal cycle, the original microstructure of the base material is destroyed completely and returned to the as-cast state which leads to a significant alternation of the material properties. In the fusion zone, the final alloy can be tailored by the addition of filler materials during welding [Thiessen 2006]. The zone next to the weld undergoes phase transformations as well (but cannot be modified from outside during the welding process) and is referred to as the heat-affected zone (HAZ), see **Figure 2-4**. As shown in this figure, the HAZ can be divided into a number of sub-zones. Each sub-zone refers to a different type of microstructure and it is likely to possess different mechanical properties. The zones are:

- Base material – up to a temperature of approximately 500 °C, the base material remains unaffected by the welding process
- Tempered zone – material becomes softer, especially martensite is transformed into bainite or ferrite
- Phase transformations – occur above approximately 700 °C where ferrite transforms to austenite

- Recrystallized zone – nucleation of new undeformed grains in a deformed metal, usually sets in at temperatures higher than half the melting point. Recrystallization occurs until all of the material has been transformed into a new undeformed stress-free microstructure
- Grain growth zone – the grains begin to grow and reduce the yield stress according to $\sigma = \sigma_0 + k \cdot d^{-0.5}$, where d is the average grain size (Hall-Petch equation) [Dahl 1978]. According to *Easterling* [Easterling 1992], the influence of the second term, which describes the influence of the grain size, contributes about 50 % of the total stress.

The phase changes due to welding have been investigated in detail using phase field modelling techniques by Thiessen [Thiessen 2006]. The studies have been performed using a dual-mesh principle; *i.e.*, by a coupling of microscopic and macroscopic behaviour as described in detail in [Thiessen 2006a]. The phase transformation model employed in the present thesis is based on the results of this model.

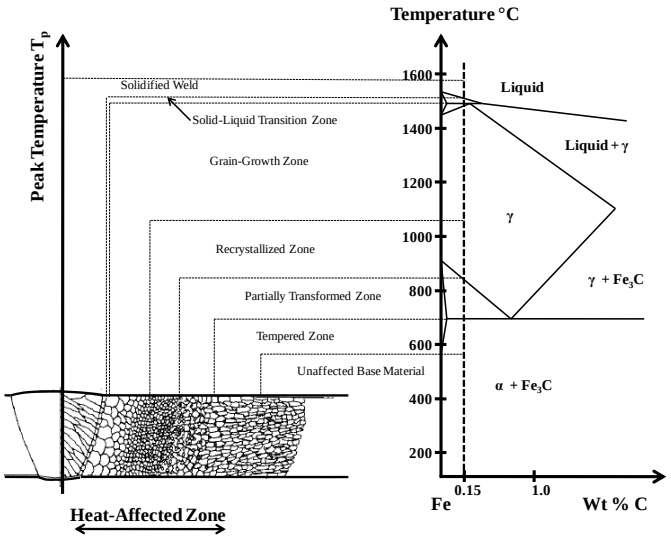

Figure 2-4 The heat-affected-zone (HAZ) [Easterling 1992].

2.1.3 Addition of Filler Material

In GMA welding, a consumable is used as one electrode leading to an addition of filler material at the weld. This filler increases the tensile strength of the weld due to the reinforcement. Filler material can also help to diminish the probability of hot cracking [Cary 2005]. Hence, the use of an appropriate filler material is a major factor in the successful joining of alloys to ensure the quality and integrity of a welded joint. However, the addition of filler material also increases the shrinkage force, which causes residual stresses and welding distortions (see **section 2.3**). **Figure 2-5** shows a bead-on-plate (BOP)

weld on a flat plate. The critical force F above which this plate buckles is given by [Timoshenko 1961]:

$$F_{cr} = \frac{E \cdot w \cdot t^3 \cdot \pi^2}{12 \cdot l^2}, \qquad \textbf{Eq. 2-11}$$

where E, w, t, and l are Young's Modulus, the width, thickness and length of the plate, respectively. Assuming a stiffness E of 200 GPa and a sample width w of 150 mm, a length l of 300 mm, and a thickness t of 1 mm, the critical force F is 275 N. For BOP welding of sheets with a thickness of 1 mm, the energy per unit length Q_l is in the order of 0.5 kJ mm^{-1}, see *e.g.* [Hermans 1997, Schwenk 2007]. Evaluating these results and the findings in [Schneider 2009], the section A of the filler under stable process conditions can be estimated roughly by:

$$A = \frac{\pi}{4} d^2 \cdot \frac{v_w}{v} \approx 5\,mm^2 \left(\frac{kJ}{mm} \right)^{-1} \cdot Q_l \approx 2.5 \cdot mm^2, \qquad \textbf{Eq. 2-12}$$

where d and v_w are the diameter of the filler wire and the wire feeding rate, respectively. Hence, the section of the fillet as well as the wire feeding rate is correlated with the energy per unit length. This factor between fillet section and energy per unit length has also been obtained in the present work.

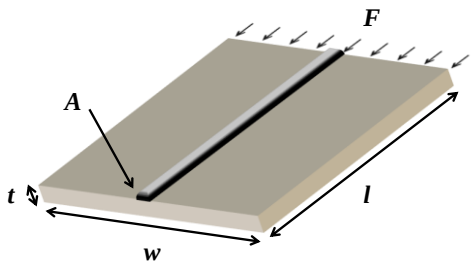

Figure 2-5 Sketch of a bead-on-plate (BOP) weld with an fillet section *A*.

The shrinkage force due to the cooling of the fillet from melting temperature to room temperature can be estimated as shown in the following example: Assuming that above ≈ 500 °C steel is soft and possesses a low yield strength, below this temperature the yield strength σ_Y is approximately 300 MPa for common steels. Assuming a thermal expansion coefficient α of $2 \cdot 10^{-5}$ K^{-1}, the effective shrinkage strain ε is 500°C · α which is in the order of 1 %. This is well within the plastic domain and hence, the stress in the filler material can be assumed to be in the order of the yield stress. The shrinkage force F of the fillet is approximately $\sigma_Y \cdot A$ = 750 N which would be more than enough to cause buckling of the plate.

However, this simple *gedankenexperiment* is not yet complete: On cooling to room temperature, the fillet undergoes phase transformations as well. Metal is added to the weld seam in a liquid state and becomes austenite on solidification. On cooling, the austenite transforms to martensite or ferrite (depending on the cooling rate) which is accompanied by

a volumetric expansion, see **subsection 2.2.2**. This expansion reduces the effective shrinkage force. One topic of current research is to develop new filler materials to take advantage of this effect in order to reduce residual stresses and distortions, as described by Hardesty and Nelson [Hardesty 2007]. Hence, the effective shrinkage force of the added filler material is also dependent on expansion during phase transformation. For phase transformations which occur in temperature ranges where the steel is very soft, for instance the austenite to ferrite transformation, this expansion is compensated easily by plasticisation of the filler.

With regard to the addition of filler material from a numerical point of view, there are some possibilities to model the addition. The modelling problem in this case is that filler material is not present at the beginning of the simulation. Basically, there are two techniques described in the literature to simulate material addition as discussed below.

Philipenko [Pilipenko 2001] applied a method referred to as the *element birth techniques.* Here, elements are not included from the beginning, but become *existent*; *i.e.*, are added, during welding. However, it is mentioned that the element birth technique may introduce serious numerical convergence problems. These problems are caused by large displacements induced by the heating process and due to the modification of the degrees of freedom (DOF) of the equation system during the simulation. This approach has also been applied in [Hackmair 2003, Brown 1992, Wilkening 1993].

Another approach is presented by Lindgren [Lindgren 2001], referred to as the *quiet elements technique*. In the simulations presented by Ma et al. [Ma 1995], the filler material is included in the simulations at the beginning but with material properties chosen to have minimal effect on the adjacent material. The internal material state; *i.e.*, stresses and strains, are set to zero on exceeding the melting temperature. This approach has also been employed in the simulations performed by Teng et al. [Teng 2003] and for multipass welds by Free and Goff [Free 1989]. Unlike the *element birth technique*, the elements are not activated explicitly. This approach is easy to implement in most finite element codes; the whole model can be defined initially and hence, it is also applied in the present work. **Figure 2-6** shows a typical temperature distribution during welding of an overlap joint and the activation of the filler material using this technique.

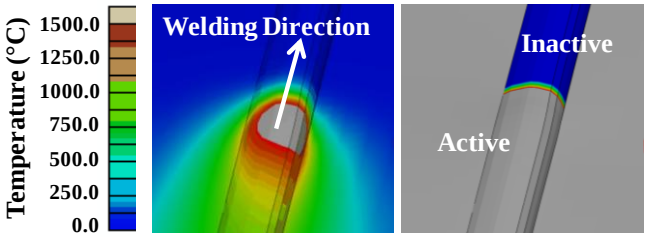

Figure 2-6 Left: Temperature distribution during welding of an overlap joint. Right: Activation of filler material using the quiet element technique.

2.2 Material Behaviour during Welding

In the previous section, the GMA welding process has been presented and its effect on the temperature field has been explained. In the present section, the effect of the thermal treatment on the mechanical and metallurgical behaviour is explained. Additionally, a survey is given of models which are commonly employed in the literature for welding simulations.

2.2.1 Thermomechanical Material Behaviour

Figure 2-7 (left) shows a typical stress-strain curve. After exceeding the yield stress, dislocations start to move in the material which leads to plastic; *i.e.*, permanent, deformation (I). Hardening starts first when the dislocation density increases such that the dislocations cannot move freely anymore or when dislocations impinge on grain boundaries (II). If the dislocation density increases further, dynamic recovery sets in (III); *i.e.*, the dislocation density is so high that dislocations annihilate. This can be seen in the stress-strain curve by a saturating value for the stress. For real metals, dynamic recovery might set in for large deformations. Then, the dislocation density no longer increases; *i.e.*, there is equilibrium between the creation and the annihilation of dislocations. Also static recovery of the stored energy; *i.e.*, a rearranging of dislocations, might occur at elevated temperatures. In order to describe these recovery effects, more sophisticated material models, *e.g.* the model presented by Chaboche [Chaboche 1986], use nonlinear saturating hardening rules, which include a linear hardening for small plastic deformations, as observed experimentally.

In order to increase the yield stress, it is common to introduce obstacles in a crystal to pin dislocations. This could be done either by work hardening, where the dislocation density is increased, by alloying elements which create impurities in the crystal (a precipitation structure), or by optimized grain boundaries for fine grain sizes. As mentioned in **subsection 2.1.2**, grain growth takes place at elevated temperatures.

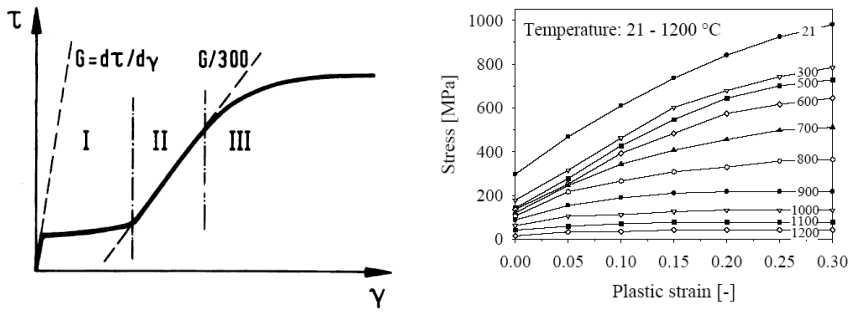

Figure 2-7 Left: Sketch of hardening for tensile tests [Seifert 2003]. Stress τ is shown as function of strain γ. All domains are shown from the elastic domain (G=Young`s Modulus), free movement of dislocations (I) to hardening (II) and dynamic recovery (III). Right: Temperature-dependent stress-strain curves for stainless steel 316L [Aa 2007].

Figure 2-7 (right) shows temperature-dependent stress-strain curves of the austenitic stainless steel 316L [Aa 2007]. For lower homologous temperatures $T^* = T/T_m$, where T_m is the melting temperature, the stress is a function of the strain only. For higher T^*, the material behaviour becomes dependent of the strain-rate which leads to an overstress [Chaboche 1989] [Schenk 2006]. This so-called superplasticity or viscoplasticity is always present. However, its influence is negligible for room temperatures. It becomes significant at about half the melting temperature and increases with increasing temperature. Additionally to the strain rate dependence, typically steel is softer above homologous temperatures of about $T^* \approx 0.3\text{-}0.5$. The yield stress decreases and hence, the material becomes easier to deform. For temperatures >1000 °C, steel is completely viscous.

One process which is responsible for viscoplastic behaviour is the diffusion of vacancies towards dislocations; *i.e.*, towards high stresses which are usually present around dislocations. These vacancies allow dislocations to move around obstacles leading to a relaxation of stress and a plastic deformation. For higher temperatures, the diffusion of these vacancies is higher as well as their number. The second process involved occurs without the contribution of dislocations, but due to the stress-induced diffusion of atoms to grain boundaries. The physical cause is the formation of vacancies in regions of strained material volumes. The corresponding transport of atoms towards the opposite direction yields a macroscopic elongation of the system. Strain-rate dependency can be expected for all steels at elevated homologous temperatures. This has been reported for stainless steels by Hong and Lee [Hong 2004] and high-strength steels by Bleck et al. [Bleck 2004]. Strain rate dependence becomes dominant above the recrystallization temperature $T \approx 0.5 \cdot T^*$, see [Fergueson 1967, Sakin 2003, Gottstein 1998].

Phenomenological Model Formulation

In the following, an outline of the theory of viscoplasticity with mixed isotropic-kinematic hardening is given, see [Backhaus 1983, Simo 1998]. The model presented is also referred to as a *unified plasticity model* [Fossum 1997]. Metals subjected to a multiaxial stress $\boldsymbol{\sigma}$ react by building up a multiaxial total strain $\boldsymbol{\varepsilon}^{tot}$. For linear-elastic conditions, the connection between stresses and strains is given by [Mase 1969]:

$$\boldsymbol{\sigma} = \underline{\mathbf{C}}(T) \cdot \boldsymbol{\varepsilon}^{el} = \underline{\mathbf{C}}(T) \cdot \left(\boldsymbol{\varepsilon}^{tot} - \boldsymbol{\varepsilon}^{ph} - \boldsymbol{\varepsilon}^{th} - \boldsymbol{\varepsilon}^{pl} \right), \qquad \textbf{Eq. 2-13}$$

where $\underline{\mathbf{C}}$, $\boldsymbol{\varepsilon}^{el}$, $\boldsymbol{\varepsilon}^{ph}$, $\boldsymbol{\varepsilon}^{th}$, and $\boldsymbol{\varepsilon}^{pl}$ are the elastic stiffness tensor defined by Young's Modulus E and Poisson's ratio ν, and the elastic, the phase, the thermal and the plastic strain, respectively. The deviatoric stress tensor can be obtained by decomposing the stress tensor $\boldsymbol{\sigma}$ into the deviatoric stress tensor $\mathbf{S}$ and the hydrostatic stress tensor $\mathbf{p}$ with:

$$\begin{aligned} \mathbf{p} &= p \cdot \mathbf{1}\,, \; p = \frac{1}{3} tr(\sigma) \\ \mathbf{S} &= \boldsymbol{\sigma} - \mathbf{p} \end{aligned} \qquad \textbf{Eq. 2-14}$$

This is suitable due to the fact that the hydrostatic stress $\mathbf{p}$, or the average of the normal stresses, is supposed to yield no plastic deformations, or that inelastic deformations are supposed to yield no change of the volume (*i.e.*, υ=0.5). Therefore, models for plasticity are

often defined in terms of deviatoric stresses. However, it is also possible to assume plastic compressibility which makes sense for porous material [Gross 2006], for instance.

The calculation of the phase strains is described in the next subsection. The thermal strains can be determined using the temperature profile during welding (see **subsection 2.1.1**):

$$\dot{\boldsymbol{\varepsilon}}^{th} = \alpha(T) \cdot \dot{T} \cdot \mathbf{1}, \qquad \textbf{Eq. 2-15}$$

where α, T_0 and are the thermal coefficient of expansion and the environmental temperature. The material behaves elastically as long as the yield condition is fulfilled:

$$F = \sigma_{EQ} - \left(\sigma_Y(T) + R(T)\right) \leq 0, \qquad \textbf{Eq. 2-16}$$

where F, σ_Y, σ_{EQ} and R are the yield function, the yield stress, the equivalent stress and the isotropic hardening variable, respectively. The equivalent stress is defined by:

$$\sigma_{EQ}^2 = \frac{3}{2} \cdot (\mathbf{S} - \boldsymbol{\alpha}) \cdot \underline{\mathbf{H}} \cdot (\mathbf{S} - \boldsymbol{\alpha}), \qquad \textbf{Eq. 2-17}$$

where $\underline{\mathbf{H}}$, $\mathbf{S}$ and $\boldsymbol{\alpha}$ are the Hill anisotropic plasticity tensor [Hill 1948], the deviatoric stress tensor and the kinematic hardening tensor. The meaning of the two different hardening effects; *i.e.*, isotropic and kinematic hardening, can be explained as follows (see **Figure 2-8**, left) [Chaboche 1993a, Chaboche 1993b]:

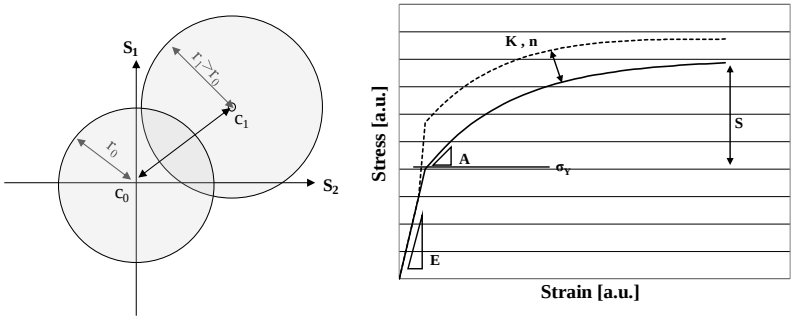

Figure 2-8 Left: 2D **s**ketch of the yield surface in the deviatoric stress space and the effect of the two hardening variables. Right: Sketch of a typical stress-strain curve at room temperature.

Kinematic hardening, also referred to as backstress, involves a translation of the yield surface to a new location $c_0 \rightarrow c_1$. The centre of the yield surface is described by a tensor with components $\boldsymbol{\alpha}$. Kinematic hardening describes the remobilization of the dislocations at a change of the load. Dislocations pile up in front of obstacles during deformation, *e.g.* phase or grain boundaries in polycrystals, leading to mutual rejections and additional residual stresses. If the loading direction is reversed, yielding occurs at lower external loads.

Isotropic hardening implies an increase in the size of the yield surface, $r_0 \rightarrow r_1$ described by a scalar variable R. This describes the increase of the microscopic dislocation density.

As its name implies, it is isotropic in nature. It is also coupled to the number of obstacles for dislocations within the crystal.

If the yield criterion is not fulfilled anymore, plastic flow occurs. It is usually assumed that this flow happens perpendicularly to the original yield surface. It is formulated incrementally:

$$\Delta\boldsymbol{\varepsilon}^{pl} = \frac{\partial F}{\partial \boldsymbol{\sigma}} \cdot \Delta p = \frac{3}{2} \frac{1}{\sigma_{EQ}} \underline{\mathbf{H}} \cdot (\mathbf{S} - \boldsymbol{\alpha}) \cdot \Delta p \,, \qquad \textbf{Eq. 2-18}$$

where Δp is the accumulated plastic strain increment. For elastoplastic behaviour, plastic flow occurs immediately; *i.e.*; $F \equiv 0$ which defines Δp implicitly. In case of viscoplasticity, the yield condition can be violated; *i.e.*, $F > 0$, and the accumulated plastic strain is given explicitly by:

$$\Delta p = \left\langle \frac{F}{K(T)} \right\rangle^{n(T)} \Delta t \,, \quad < x >= \frac{x + |x|}{2} \,, \qquad \textbf{Eq. 2-19}$$

where K, n and Δt are referred to as reference stress or viscosity, Norton's exponent which is one for a Newtonian liquid, and the current time increment, respectively. The value of $F > 0$ is also called overstress and released by stress relaxation as a function of the accumulated plastic strain rate and thus, as a function of the time. The evolution equations for kinematic and isotropic hardening read:

$$\begin{aligned} \Delta\boldsymbol{\alpha}(T) &= A_\alpha \cdot \left[\frac{2}{3} \cdot S_\alpha(T) \cdot \frac{\partial F}{\partial \boldsymbol{\sigma}} - \boldsymbol{\alpha} \right] \cdot \Delta p + \boldsymbol{\alpha} \cdot \frac{1}{S_\alpha(T)} \frac{dS_\alpha(T)}{dT} \Delta T - R_{stat} \cdot \boldsymbol{\alpha} \\ \Delta R &= A_R \cdot \left[S_R(T) - R \right] \cdot \Delta p + R \cdot \frac{1}{S_R(T)} \frac{dS_R(T)}{dT} \Delta T \end{aligned} \,, \qquad \textbf{Eq. 2-20}$$

where S_α, A_α, S_R, A_R and R_{stat} are the saturation value and hardening exponent for kinematic and isotropic hardening and the static recovery parameter, respectively. **Figure 2-8** (right) shows a sketch of a typical stress-strain curve. The initial hardening slope is given by $S_\alpha \cdot A_\alpha$ for kinematic hardening and $A_R \cdot S_R$ for isotropic hardening, respectively. This model is also referred to as Chaboche`s model. Here, the slopes of the hardening cannot be dependent on temperature for thermodynamic consistency as reported by McDowell [McDowell 1992]. In the case of uniaxial isothermal tension, this equation can be integrated to:

$$\begin{aligned} \alpha(p) &= S_\alpha \cdot (1 - \exp(-A_\alpha \cdot p)) \\ R(p) &= S_R \cdot (1 - \exp(-A_R \cdot p)) \end{aligned} \,. \qquad \textbf{Eq. 2-21}$$

For infinitely high saturation values, the evolution equations correspond to the linear-kinematic hardening model proposed by Prager [Prager 1949].

The viscoplastic material models presented with coupled isotropic-kinematic hardening and recovery are state-of-the-art and general insofar as the models are capable of mapping nearly all important effects to be considered in the simulation. It is also possible to perform experiments containing sufficient information to determine all model parameters as

described in [Seifert 2003]. However, performing all experiments needs considerable expertise; also, using these kinds of models for welding simulations is very time-consuming due to the high non-linearity of their evolution equations.

2.2.2 Phase Transformation

Most materials are not only subjected to solid-liquid transitions, but also to solid-solid transitions [Grøng 1997]. This happens if there is a solid state configuration possessing a lower free energy. Since the materials applied within this project are steels, a general knowledge about phase transformations will be explained using the iron-carbon phase diagram. **Figure 2-9** (left) shows the domains of different iron phases as a function of the carbon weight percentage and temperature. The main phases which can occur are:

- Austenite γ (fcc) which is a very ductile phase. Steels transforms to austenite above $T=A_{c1}$. The transformation is completed at $T=A_{c3}$.
- Ferrite α (bcc) with a maximum solubility of carbon of 0.02%. α-Ferrite is very ductile and forms from austenite on cooling below $T=A_{r1}$.
- Cementite (Fe_3C) which is a strong, brittle and hardly deformable phase. Cementite is only meta-stable and decomposes into iron and graphite.

The iron-carbon-diagram displays an equilibrium state and is only valid for very slow heating and cooling rates. The material needs a certain time to transform. The time-dependency of the transformation is usually shown in continuous cooling transformation (CCT) diagrams for a constant carbon content; *i.e.*, for a constant composition. If the material is cooled down very fast; *i.e.*, faster than the time required for the transition, the phases will not form. **Figure 2-9** (right) shows such a CCT-diagram: Dependent on the cooling rate, steel might transform into two or more phases: Martensite (M), which forms below the martensite start temperature, and bainite (B) and perlite (P), which is a combination of ferrite and cementite. The martensite transformation is athermal and occurs without diffusion, but by changing the lattice structure. This phase is only meta-stable, but the decomposition into ferrite and cementite is very slow and not noticeable at room temperature. However, the decomposition can be accelerated by tempering the martensite.

The validity of CCT diagrams depends on the maximum austenitisation temperature and austenitisation time. Higher maximum temperatures shift the transformation towards higher times due to the increased austenite grain size [Dilthey 1995, Berkhout 1968]. The presented CCT from [Seyffarth 1992] has been obtained for a maximum temperature of 1300 °C and hence, it is valid in case of welding and in particular to describe phase transformations of the molten and re-solidified material. However, in the HAZ the maximum temperatures reached are strongly spatially-dependent and it would be correct to employ multiple CCT diagrams [Thiessen 2006].

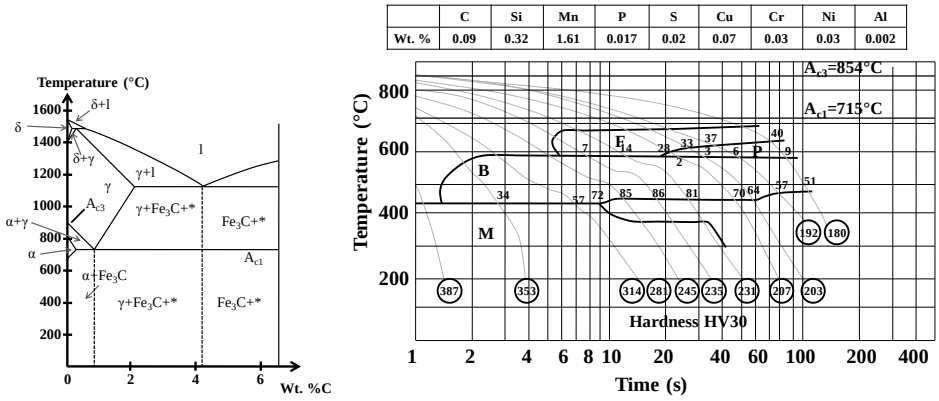

	C	Si	Mn	P	S	Cu	Cr	Ni	Al
Wt. %	0.09	0.32	1.61	0.017	0.02	0.07	0.03	0.03	0.002

Figure 2-9 Left: Iron-Carbon-Diagram. Right: Example of a continuous cooling transition diagram [Seyffarth 1992].

For the diffusion-controlled phase transformation of austenite to ferrite and perlite / bainite, and vice versa, the LeBlond model [LeBlond 1984] can be applied which is based on the Johnson-Mehl-Avrami-Kolmogorov (JMAK) model [Avrami 1939]:

$$\dot{P}_i(T) = n \cdot \left(\frac{P_i^{EQ}(T) - P_i(T)}{\tau(T)} \right) \cdot \left(\ln\left(\frac{P_i^{EQ}(T)}{P_i^{EQ} - P_i(T)} \right) \right)^{\frac{n(T)-1}{n(T)}} . \qquad \textbf{Eq. 2-22}$$

The integrated form of this equation reads

$$P_i(T) = P_i^{EQ}(T) \cdot \left(1 - \exp\left(\frac{-t}{\tau(T)} \right)^{n(T)} \right), \qquad \textbf{Eq. 2-23}$$

where $P_i(T)$, $P_i^{EQ}(T)$, $\tau(T)$, $n(T)$, t and T are the phase fractions of phase i, equilibrium phase fractions, a relaxation time, a dimensionless exponent for the kinetics of the transition, the time and the temperature, respectively. The effect of the cooling rate can be included in the relaxation time.

The diffusion-controlled phase transition from austenite to ferrite occurs over a time scale of about 10^{-3} s [Porter 1992], the diffusionless transition from austenite to martensite happens almost instantaneously. According to Koistinen and Marburger [Koistinen 1959], this transformation can be described by the following time-independent equation, where the transformed martensite phase fraction P_M is defined as a function of the temperature and the growth constant b:

$$P_M(T) = P^{EQ} \cdot \left[1 - \exp\left(-b \cdot \left(M_s - T \right) \right) \right], \; T \le M_s . \qquad \textbf{Eq. 2-24}$$

Here, P^{EQ} corresponds to the austenite phase fraction at the beginning of the transformation. The phase transformation occurs only for temperatures lower than the martensite start temperature M_s. It has been shown by Wilson and Medina [Wilson 2001]

that the Koistinen-Marburger equation can also be employed for high-strength low-alloy (HSLA) steels. According to Pan and Weng [Pan 1992], a value b of 0.011 K^{-1} is reasonable for most plain carbon and HSLA steels. Fitting the values reported by Steven and Haynes [Steven 1956] results in a growth constant b of 0.02 K^{-1}.

Equations have been proposed by Andrews [Andrews 1965] to estimate the transformation temperatures A_{c1}, A_{c3} and M_s in °C from the chemical composition (in wt. %) of the steel:

$$\begin{aligned} A_{c1} &= 723 - 10\cdot Mn - 16.9\cdot Ni + 29.1\cdot Si + 16.9\cdot Cr + 6.38\cdot W + 290\cdot As \\ A_{c3} &= 910 - 203\cdot\sqrt{C} - 30\cdot Mn - 15.2\cdot Ni + 44.7\cdot Si + 104\cdot V + 13.1\cdot W \\ &\quad + 31.5\cdot Mo + 20\cdot Cu - 700\cdot P - 400\cdot Al - 120\cdot As - 400\cdot Ti \\ M_s &= 539 - 423\cdot C - 30.4\cdot Mn - 17.7\cdot Ni - 12.1\cdot Cr - 11\cdot Si - 7\cdot Mo \end{aligned} \qquad \textbf{Eq. 2-25}$$

Effect of Phase Transformations on Material Behaviour

Phase transformations affect the welding process in a number of ways. Firstly, they influence welding distortion and stresses due to their accompanied volumetric expansion which is theoretically 1.3 % for the austenite-ferrite transformation and 4% for the austenite-martensite transformation [Schumann 1991]. If 100 % ferrite is transformed to 100 % martensite due to a heat treatment, this results in a volume difference of 2.7 %.

The volume change $\Delta V_{F\to M}$ from ferrite to martensite is generally dependent on the carbon composition in the material which can be described by [Läpple 2006, Kurdjumov 1975]:

$$\Delta V = \frac{V_M}{V_F} = \frac{(0.28668 + 0.0166\cdot \%C)\cdot(0.28668 - 0.0013\cdot \%C)^2}{0.2866^3}\cdot 10^{-9}\, m\,. \qquad \textbf{Eq. 2-26}$$

This results in a volume change $\Delta V_{F\to M}$ of 4.8 % for 1 wt.% C and 0.5% for 0.1 wt.% carbon. However, it has not yet been proven that this model is valid for carbon concentrations below 0.3 - 0.4 wt.%.

In the literature, the reported volume changes $\Delta V_{\gamma\to\alpha}$ from austenite to ferrite vary strongly. For instance, Velthuis et al. [Velthuis 1998] report an expansion of 1% for Fe-Cu and Fe-Co steels. Measurements by *Chen et al.* [Chen 1985] resulted in an expansion of 2.6 %. Dean and Hidekazu [Dean 2006] reported 0.75 % expansion for an 9Cr-1Mo steel. Moyer and Ansell [Moyer 1975] reported values between 1.3 % and 2.7 % for various tool steels and stainless steels.

Studies performed by Taljat et al. [Taljat 1998] indicate that this volumetric expansion on cooling lowers the residual stresses in the fusion zone of a weld. Mikami et al. [Mikami 2009] reported by means of numerical simulations that angular distortion of T-Joints can be reduced significantly by an increased martensite volume fraction.

The formation of martensite has a significant influence on the yield stress as well. Davies [Davies 1978] reported a value of $d\sigma_Y / df_M \approx 830$ MPa for the dependence of the yield stress on the martensite volume fraction at room temperature for dual-phase steels. Hence, for a 20 % higher martensite volume fraction after welding, the yield stress

increases by 166 MPa. Similar results have been found by Ekrami [Ekrami 2005] and Liedl et al. [Liedl 2002]. Hence, in order to predict the welding stresses and distortions as adequate as possible, it appears to be indispensable to incorporate phase transformations in the model due to the strong spatial dependency of the phase transformations due to different cooling rates (see **subsection 2.1.2**).

Phase transformations also affect the hardness of a material. Formulas have been given by Blondeau [Blondeau 1973] to predict the hardness of the material as function of the chemical composition, the phase fractions and the cooling rate τ_{700} at a temperature of 700 °C. This model neglects the influence of the hardening and the grain size. **Figure 2-10** shows the conversion of Vickers hardness into tensile strength as proposed in the standard *DIN EN ISO 18265:2003*. This conversion can be applied for comparisons of measured hardnesses to welding simulations, since the tensile strength of the material; *i.e.*, the yield stress plus the maximum hardening, can be accommodated in simulations. Therefore, the yield stress and hardening must be available as a function of the phase fractions as well.

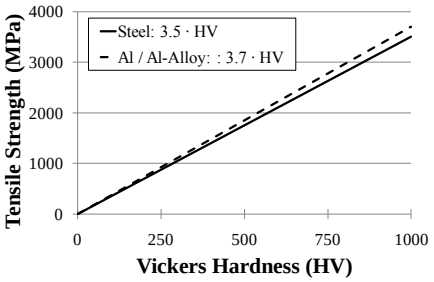

Figure 2-10 Conversion of Vickers hardness into tensile strength according to ISO 18265:2003 [Läpple 2006].

2.2.3 Models commonly applied in Literature

The accurate prediction of welding distortion is an important requirement for industry in order to support production planning. Due to the strong temperature and stress gradients during welding, and the subsequent welding distortion, accurate simulations require a detailed representation of the temperature-dependent material behaviour. Also large numbers of material and process parameters are required as input for the models. Hence, care must be exercised with regard to the choice of the material model and the material properties. In the previous two subsections, an outline of the thermo-mechanical and metallurgical material behaviour of steels has been presented. During welding, the material heats up to the melting temperature. Hence in order to model the welding process adequately, the softening of the material at higher homologous temperatures has to be included in the model as well as the strain-rate dependent hardening. Also, the weld is subjected to phase transformations which can affect the results significantly as explained in the previous subsection and **subsection 2.1.2**. In the present subsection, a critical survey is presented of models commonly employed in the literature for welding simulations.

Phase Transformations

Many models neglect the influence of phase transformations. However, it has been stated by Ferro et al. [Ferro 2006] that the effect of phase transformation is not negligible in case of of bead-on-plate laser welding. **Figure 2-11** shows the results of the calculations. For the longitudinal stresses, the effect of volume change appears to be dominant. However, only the influence of the phase transformations on the yield stress and the thermal strain has been studied. The results have not been compared to experiments. Ideal-plastic behaviour; *i.e.*, no hardening, has been assumed for all phases which appears to be a severe simplification.

Other publications indicate that the influence of phase transformations on distortion and residual stresses is not very significant sufficiently far away from the fusion zone. In the work published by Sorensen [Sorensen 1999], phase transformations have been regarded only implicitly; *i.e.*, by considering temperature dependent material properties. The case study under investigation was a GMA weld of a 12mm thick mild steel T-Joint. An acceptable agreement has been found between simulations and experiments.

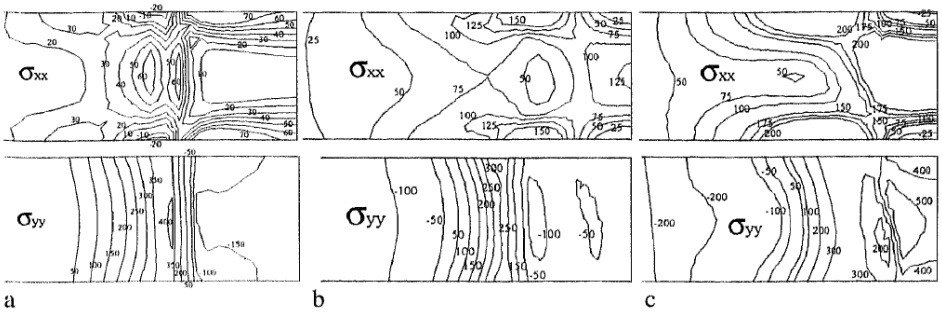

Figure 2-11 Results of the calculations of [Ferro 2001], if no transformation is considered (c), only volume change (b) and also transformation plasticity (a) is considered. The results are shown for the middle cross-section through the welded specimen. σ_{xx} and σ_{yy} correspond to the transversal and longitudinal stresses, respectively.

Especially for case studies; *i.e.*, when tendencies are of interest instead of exact agreement to experiments, phase transformations are often neglected. For instance, in the studies presented by Allmeier [Allmeier 2005], the same tendencies have been found in simulations and experiments. However, the absolute values differed strongly, which might be due to the neglect of phase transformations. Shim et al. [Shim 1992] present the residual stresses determined experimentally for multipass GMA welding of thick section weldments. The measurements have been compared to simulations where phase transformations were disregarded. Also volume changes due to phase transformations were neglected. However, the results obtained in the simulations are a good match to the stresses determined experimentally.

Andersen [Andersen 2000] compared predictions for GMA welding of a structural C-Mn steel T-Joint. It has been found that the agreement of the simulation with experiments is better if phase transformations are incorporated. However, also good agreements have been

obtained between simulations and experiments of butt joint welds by Hibbit and Marcal [Hibbit 1973] although phase transformations were neglected. The reason for this is not given but it must be assumed that the influence of phase transformations is case-dependent.

Thermo-Mechanical Coupling

As already explained, there is a coupling between thermal and mechanical behaviour. This includes heat generation due to plastic deformation and thermal expansion or contraction due to heating or cooling. For physical reasons, these effects should be considered which means that simulations have to be performed employing coupled thermal-mechanical behaviour. However, it is common practice in the literature to omit the coupling and perform uncoupled calculations in order to save computation times [Argyris 1982]. Friedman [Friedman 1975] reported that the thermo-mechanical coupling can be neglected since the thermo-elastic coupling coefficient is very small. Pietzsch [Pietzsch 2000] compared the heat generated by the heat source; *i.e.*, the welding torch, and the heat generation due to the plastic dissipation for GMA welded T-Joints. The contribution of the plastic dissipation to the total heat is four orders of magnitude smaller.

In uncoupled simulations, also the interaction between the thermal expansion and the clamps is omitted. In cases where the clamping system is of relevance it should be guaranteed that the elasticity of the clamps is high enough to keep the workpiece clamped during heating and cooling.

Hardening Model

Hardening models applied in the literature to describe the mechanical behaviour vary strongly. Due to the cyclic heat treatment the material is subjected to cyclic loads: During heating the material attempts to expand and hence, it is subjected to compressive loads due to existing boundaries, while it is subjected to tensile forces on cooling when it attempts to contract. In order to model such cyclic behaviour adequately, mixed isotropic-kinematic hardening must be considered [Chaboche 1986].

However, most numerical welding simulations employ either kinematic or isotropic hardening. For the studies presented by Pietzsch [Pietzsch 2005] about the influence of different post-welding cooling techniques, only isotropic hardening was considered, but no comparisons to experiments are given. Sole isotropic hardening has also been considered by Kadivar [Kadivar 2000] and Lindgren et al. [Lindgren 1997], for instance. Michaleris and Sun [Michaleris 1997] presented a model for the prediction of buckling using kinematic hardening. In order to determine residual stresses, kinematic hardening has also been employed by Andersen [Andersen 2000] and Brickstad and Josefson [Brickstad 1998]. In some publications good agreements have been obtained to experiments, while in some publications the agreement is worse. It appears that it is not clear yet what determines the detail necessary for the hardening model.

In more recent works, ideal-plastic behaviour is assumed, for instance by Zhu and Chao [Zhu 2002] and Hu et al. [Hu 2006]. In the nineties and before, ideal-plastic hardening has been employed very often due to its simple numerical integration and hence, the enormous gain of computation time [Lindgren 2001]. However, it lacks almost any physical

background, especially for lower homologous temperatures. Nowadays it is not problematic to employ more complex hardening rules due to the significant increase of available computation power.

Sensitivity analyses presented by Schwenk [Schwenk 2007a] for laser welding of a dual phase steel grade DP600 indicate that the most important quantities in order to obtain accurate results are the thermal expansion coefficient, the phase transformations and the temperature dependent yield stress. Here, the yield stress appears to be particularly important for homologous temperatures $\leq 0.7\ T_m$. The hardening mechanism plays a less important role.

Strain-rate Dependency

A viscoplastic material model has been used by Argyris [Argyris 1982] to perform numerical simulations of residual stresses after welding of mild steel butt joints. It has been stated that the changes of the material structure on cooling are highly dependent on the cooling rate. Therefore, strain rate dependence should be considered because of material viscosity.

Different material models have been compared by Alberg and Berglund [Alberg 2003] for a martensitic stainless steel component for rate-dependent and rate-independent material models in combination with inclusion or exclusion of phase transformation and transformation induced plasticity. Significant differences have been found between the results employing the different models. However, it is hard to estimate the relevance of this work since no comparison has been made between simulations and experiments. At least it can be stated that the residual stresses obtained can differ strongly for different material models.

Murthy et al. [Murthy 1996] presented a welding model with coupled kinematic-isotropic hardening and strain rate-independent behaviour and its application to single- and multipass butt joint welding. The agreement between simulations and experiments is very good although the strain rate-dependency has been disregarded.

It is stated by Anca et al. [Anca 2004] that rate-dependent plasticity can be neglected even at very high homologous temperatures due to the relatively short time of the weld thermal cycle. However, this argument can be questioned, in particular when the distortion has to be considered after releasing and cooling down to room temperature of the whole component which could take a long time, e.g. as shown by Staubach et al. [Staubach 2006] for a hollow section T-Joint. Additionally due to the relative short cycle, the strain rate might become very high which increases the stiffness of the material.

Temperature-Dependent Material Properties

Another simplification technique, which has been studied widely in the literature involves neglecting the temperature-dependency of the material properties. Just like employing only kinematic or isotropic hardening, there is no physical reason for allowing this simplification. The reason for recommending such a simplification is that temperature-dependent material properties are often not available or are difficult to obtain.

Studies of the effects of temperature-dependent material properties on welding simulation have been performed by Zhu and Chao [Zhu 2002]. It is shown that the temperature field during welding is not affected strongly by the application of room temperature values for the density, the thermal conductivity and the specific heat. However, taking a constant Young's Modulus and yield stress gives incorrect results for the residual stresses. **Figure 2-12** shows the distribution of the longitudinal residual stress and the deflection after welding. Neglecting temperature-dependency has a great influence on the results. It is concluded that the temperature-dependency of the yield stress has a very significant influence and should be included in simulations. The accuracy of the thermal conductivity and Young's Modulus are less important for the results. In this work, it has been found that the residual stresses are zero on applying a constant room-temperature yield stress (case D6 in **Figure 2-12)**. It is mentioned that this is due to the high room temperature yield stress, which prevents yielding. However, the yield strain of 0.2 % is rather small compared to the total thermal strains of about $\alpha \cdot \Delta T = 2 \cdot 10^{-5}\ \mathrm{K}^{-1} \cdot 1500\ \mathrm{K}$; *i.e.*, about 3 %. Hence, this does not appear to be a satisfactory explanation.

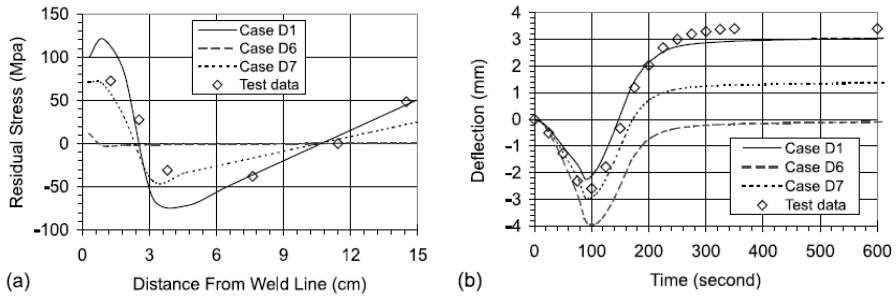

Figure 2-12 Longitudinal residual stress (a) and deflection (b) as function of the distance to the weld after the welding. Results are shown for different approaches for the yield stress: Room temperature values (D6), average values (D7), temperature-dependent values (D1). [Zhu 2002]

Comparing these findings with the results of Little and Kamtekar [Little 1998], the previous results have to be regarded with caution. In this work, it is demonstrated that applying different values for the thermal conductivity λ yields very different temperature distributions. However, the range investigated in this work is from 30-75 $\mathrm{Wm^{-1}K^{-1}}$, whereas the values considered in [Zhu 2002] are in the order of 10-20 $\mathrm{Wm^{-1}K^{-1}}$.

Another very common technique is to define a cut-off temperature whereby all material properties are kept constant above this temperature. For instance, Börjesson and Lindgren [Börjesson 2001] applied 1100 °C as a cut-off temperature. The effect of the temperature-dependency of the thermal material properties on the temperature field has been studied by Beghini et al. [Beghini 2005] for multipass welding, it was seen that the temperature dependence of the parameters has a slight effect on the results and, consequently, one should evaluate carefully the opportunity of employing constant material data, depending on specific application. Acceptable results have been achieved on applying a cut-off temperature of 650 °C which appears to be very low. It is concluded that the material density and the thermal conductivity have only little effect on thermal analysis results.

Temperature-independent values; *i.e.*, room-temperature values, have also been applied by Free and Goff [Free 1989] and Canas et al. [Canas 1996] in order to predict the residual stresses. In the latter work it has been stated that the application of temperature-independent properties, for all properties including the yield stress, yields only a slight increment of the maximum compression stress and a slight decrement of the maximum tensile stress. In this work, considering strain-hardening or assuming ideal-plastic behaviour yields only slightly different results. This is in contradiction to other works in that temperature-independent yield stress and the assumption of no strain-hardening have little influence on the residual stresses.

Conclusion

A large number of different material models / simplifications are applied in the literature to model welding residual stresses and distortion. In some cases, good agreements to experiments have been obtained for models which neglect physical effects such as temperature-dependencies, or accurate hardening models. In some cases, it has been reported that the physics of the welding process has to be modelled as adequately as possible in order to achieve good agreements. With regard to the literature, it appears that it is not possible to make clear definitions for assumptions under which simpler models are sufficiently adequate.

2.3 Welding & Material Considerations

In **section 2.1**, the GMA welding process has been explained and it has been shown how the temperature profile during welding can be calculated. The heating and cooling cycle during welding causes phase transformations in the fusion zone and in the HAZ. The addition of filler material has to be incorporated in the model and can affect the results significantly. The thermomechanical material behaviour has been explained and examples have been given of material models applied in the literature. The intention in this section is to explain the principles of the creation of welding residual stresses and distortions due to the localized heat input by the welding process and the subsequent rapid cooling.

Here, internal stresses are called residual stresses if they are independent of external forces. These stresses are in a self-equilibrium state. The stresses in any cross-section should be balanced by the sum of the forces and the sum of the moments of forces. The stresses can be assigned to strains in the material. In the case of welding, these strains can be subdivided by their origin [Masubuchi 1980]:

(1) Thermal strains caused by non-uniform temperature distribution
(2) Plastic strains caused by plastic deformation of the metal
(3) Phase strains caused by phase transformations

If these residual stresses become too high, they may promote brittle fractures, fatigue, or stress corrosion cracking. Meanwhile, residual stresses in the base plate may reduce the buckling strength of the structure members [Grøng 1997, Teng 2003].

Figure 2-13 sketches how welding residual stresses and strains interact. When the welded work piece is fixed rigidly, the residual distortion will be low, while the residual stresses will be high. The opposite is true for welded parts that are not clamped. In the next subsection, the principles of residual stresses due to welding are shown. In **section 2.3.2**, the creation of welding distortion due to relieved internal stresses is explained. The last subsection focuses on the occurrence of buckling deformation.

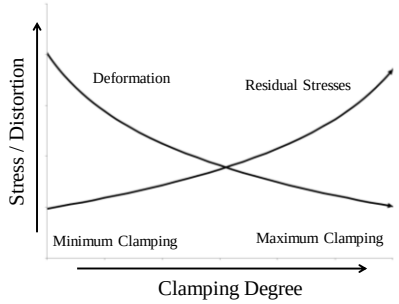

Figure 2-13 Relationship between the degree of clamping and the level of distortion as well as the effect on residual stresses. [Porzner 2005].

2.3.1 Residual Stresses

The welding process causes a highly non-uniform heating of the parts being joined. Areas close to the weld are heated up above the melting temperature, and then cooled down, the heat being conducted to the bulk of the body. This local heating and subsequent cooling induces volumetric changes producing temporary and permanent stresses; *i.e.*, residual stresses.

Figure 2-14 shows schematically how these residual stresses occur due to the transient temperature distribution. Points 1, 2, and 3 are situated along a horizontal line next to the weld seam and hence, they represent the consecutive stress development at a point lying at some distance from the weld line. Firstly, the material is exposed to elastic compression (Point 1), and plastic compression on exceeding the yield stress (Point 2). This is followed by elastic unloading after welding (Point 3). Point 4 represents added filler material. It is only subjected to elastic and plastic tensioning since the material was not present prior to welding.

Due to heating, the material in front of the weld is compressed plastically. The material in the weld pool losses all strength and the stresses are reset to zero upon melting. During subsequent cooling, the material thermally contracts, thus the solidified material in the fusion zone is subject to tension.

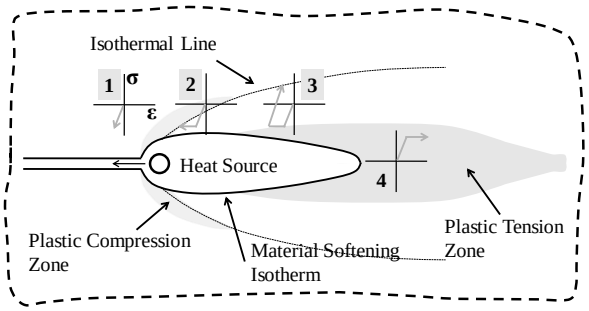

Figure 2-14 Residual stresses as function of the transient temperature distribution [Radaj 1992].

A simple 3-bar model has been proposed by Masubuchi [Masubuchi 1980] in order to explain the creation of longitudinal residual stresses, see **Figure 2-15**. Three bars are linked rigidly together, where the bar in the middle (Bar 1) is assumed to represent the weld. In the beginning (A) the system is assumed to be stress free. If this middle bar is heated; *i.e.*, the weld bead is created; the stress rises first to the yield point (B). Then, the stress declines due to the decreasing yield stress for higher temperatures (B→C). By cooling (C→D), the reaction of the middle bar is elastic again until the yield point (D) is reached. After cooling to room temperature (E), a stress corresponding to the yield stress is obtained. This effect occurs due to the restricted dilatation and contraction due to the presence of the non-heated base material, shown here by the two bars on the left and right. This means that residual stresses can be found in structures welded without any clamping due to the transience of the process. Hence, the only way to avoid residual stresses would be to use an uniform temperature field.

The bar model is a simple and powerful concept to obtain a better understanding of the influence of welding on longitudinal stress development. Since one of the most relevant distortion kinds, the buckling distortion, is governed by these stresses, much research has been performed to develop more sophisticated bar models, see [Pilipenko 2001, Aa 2007].

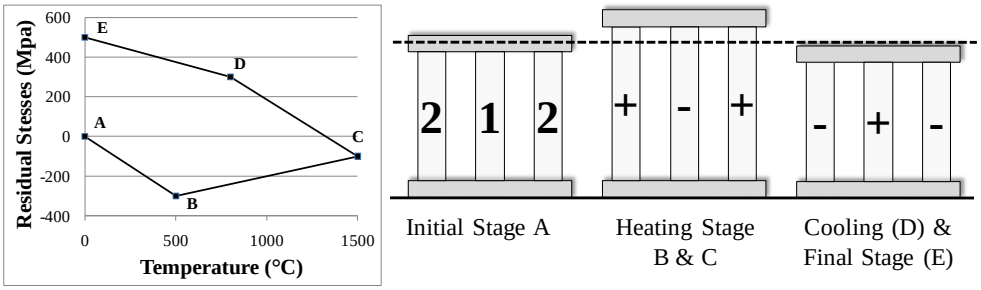

Figure 2-15 Simplified bar model using three bars to explain residual stresses as function of the non-uniform heat treatment in transversal direction [Masubuchi 1980, Pilipenko 2001].

Figure 2-16 shows the transient and final residual stresses if the middle bar is heated up and cooled down. The material has been assumed to be DP600 using the material properties presented in **section 4.3**. The dimensions of the sheet correspond to the overlap joint case

study presented in **subsection 1.2.1**, with a uniform thickness of 1 mm. The width *c* of the tensile zone has been assumed to be 20 mm. The final tensile stress is 500 MPa in the centre and -35 MPa at the outer bars, respectively.

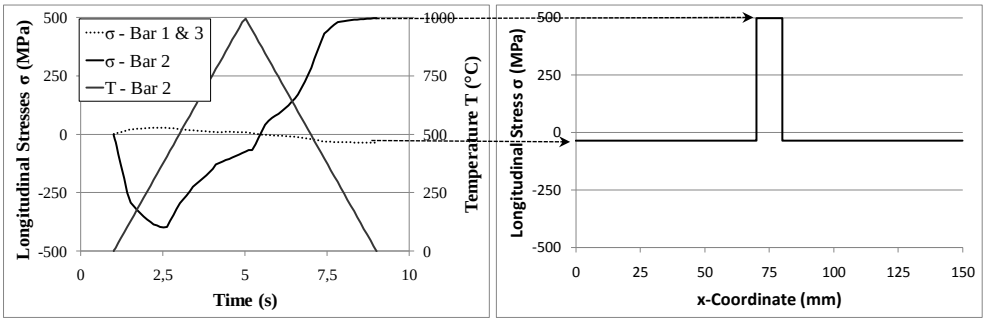

Figure 2-16 Transient and final stresses using the 3-bar model.

Similar principles as for the longitudinal stresses also hold for the development of transverse stresses [Pilipenko 2001, Radaj 2002]. **Figure 2-17** schematically shows the residual stress distribution expected for a butt-welded mild steel plate. The longitudinal stresses are tensile at the weld seam and in compression in the base material. The transverse stresses are tensile at the weld seam and decline towards the edges of the plate. At the beginning and the end of the weld, the transverse stresses are in compression.

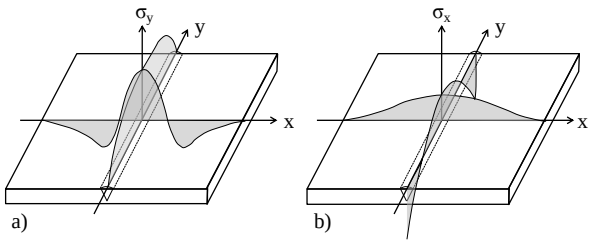

Figure 2-17 Longitudinal (a) and transverse (b) residual stresses in a butt-welded plate (schematically) [Dilthey 1995, Rappe 1974].

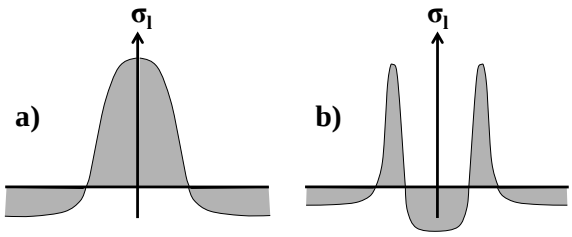

Figure 2-18 Examples of longitudinal residual stresses for mild steel (a) and for high-alloy steel with martensitic filler material (b) [Pilipenko 2001].

As explained in **subsection 2.2.2**, phase transformations can have a significant effect on the shrinkage force and hence, the residual stresses. **Figure 2-18** shows the longitudinal residual stresses for mild steel and for high-alloy steel with a martensitic filler material. If the weld seam transforms to martensite, the gradual thermal contraction changes to a quick volumetric phase expansion which turns the tensile stresses into compression. In the HAZ, the material cools down slower and exhibits no phase transformation to martensite and hence, tensile stresses are still present.

2.3.2 Welding Distortion

As in case of the stresses occurring during and after welding, welding deformation can be transient or residual. **Figure 2-19** gives an overview of various types of welding deformations to be expected when welding plates. All these kinds of distortions are related to the shrinkage of the weld metal during cooling. They can be subdivided into:

(1) Transverse shrinkage – shrinkage perpendicular to the weld seam
(2) Longitudinal shrinkage – shrinkage in direction of the weld seam
(3) Angular distortion – transverse uplift caused by a non-uniform temperature distribution in the through-thickness direction. For instance in case of butt-joints with a V-groove.
(4) Rotational distortion – in-plane angular distortion due to the localized thermal expansion and contractions. Very relevant for overlap joints, for instance.
(5) Bending distortion – longitudinal uplift. The same causes as angular distortion.
(6) Buckling distortion – caused by compressive stresses inducing instabilities in the plates.

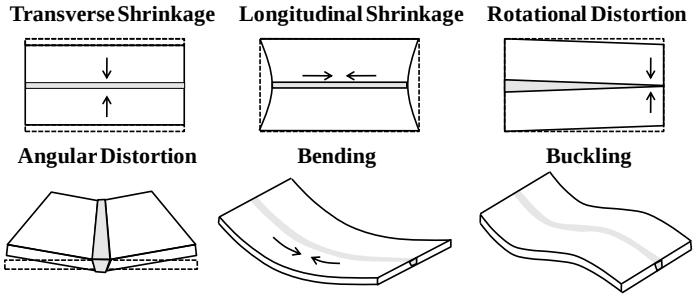

Figure 2-19 Different types of welding distortions. The arrows indicate the shrinkage direction of the weld metal which causes the corresponding distortion [Masubuchi 1980].

While angular and bending distortion is more relevant for thick structures, such as the 6 mm S355 T-Joint case study, structures composed of thin section panels with respect to their dimensions, such as the 1 mm DP600 overlap joint, are usually prone to buckling distortion [Michaleris 2006].

A review of the state-of-the-art of analytical models for the prediction of welding distortion can be found in [Verhaeghe 1999, Hänsch 2006].

2.3.3 Buckling of Plates

Buckling is a failure mode characterized by a sudden failure of a structural member subjected to high compressive stresses, where the actual compressive stress at the point of failure is less than the ultimate compressive stresses that the material is capable of withstanding. This mode of failure is also described as failure due to elastic instability [Timoshenko 1961]. The appearance of the buckling mode is not unique: The plate can buckle up, down, or not buckle, depending on the imperfections present in the plate [Moon 2002, Ho 1972]. The buckling shape is dependent strongly on the boundary conditions applied. Also buckling occurs immediately; *i.e.*, with a very high rate of deformation, as soon as the so-called *critical buckling load* (CBL) is exceeded, which poses strong convergence problems for the numerical simulation of buckling phenomena, as explained in **chapter 4**. The buckling shape *u(x,y)* for a constant applied load boundary N_x can be found from [Timoshenko 1961]:

$$\frac{\partial^4 u}{\partial x^4} + 2 \cdot \frac{\partial^4 u}{\partial x^2 \partial y^2} + \frac{\partial^4 u}{\partial y^4} = \frac{1}{D}\left(N_x \cdot \frac{\partial^2 u}{\partial y^2} \right), \qquad D = \frac{E \cdot w \cdot t^3}{12 \cdot (1 - \upsilon^2)} \qquad \textbf{Eq. 2-27}$$

where D is the so-called flexural rigidity, w the width of the plate, and t its thickness, respectively. The general solution of this differential equation is a superposition of arbitrary combinations of sine and cosine functions. Solutions for various boundary conditions can be found in [Timoshenko61]. Here, the first two buckling modes for a plate subjected to uniform stresses as defined in **Figure 2-21** are investigated in more detail. No outer constraining boundaries have been applied, the plate is simply statically determined; *i.e.*, *u(x=0,y=0)=0*, *u(x=w,y=0)=0*, *u(x=l,y=0)=0*. The deformation shapes for these modes read:

$$(1)\, u_1 = A \cdot \sin\left(\frac{\pi}{l} \cdot y \right)$$
$$(2)\, u_2 = A \cdot \sin\left(\frac{\pi}{2 \cdot w} \cdot x \right) \cdot \sin\left(\frac{\pi}{2 \cdot l} \cdot y \right) \qquad \textbf{Eq. 2-28}$$

Mode (1) and (2) correspond to the bending and torsion mode which are also most likely to occur in welding of thin plates. Assuming an amplitude of A=1 mm and inserting the deformation shapes in **Eq. 2-27** results in the critical buckling loads F_{cr} and stresses σ_{cr} for these modes:

$$(1)\, F_{cr} = -D \cdot \pi^2 \cdot \left(\frac{1}{l}\right)^2 = 300N \;,\; \sigma_{cr} = \frac{F_{cr}}{w \cdot t} = 2\,MPa$$

$$(2)\, F_{cr} = -D \cdot \pi^2 \cdot \frac{1}{2^4} \cdot \left(\frac{1}{l} + \frac{l}{w^2}\right)^2 = 471N \;,\; \sigma_{cr} = \frac{F_{cr}}{w \cdot t} = 3.14\,MPa\,. \qquad \textbf{Eq. 2-29}$$

$$D = 2.748 \cdot 10^6\, Nmm^2$$

Figure 2-20 shows the critical buckling load as a function of the plate length. It can be seen that which buckling mode occurs firstly is dependent on the dimensions of the specimen: For shorter plates, the torsion mode occurs first while for longer plates the bending mode requires a lower load.

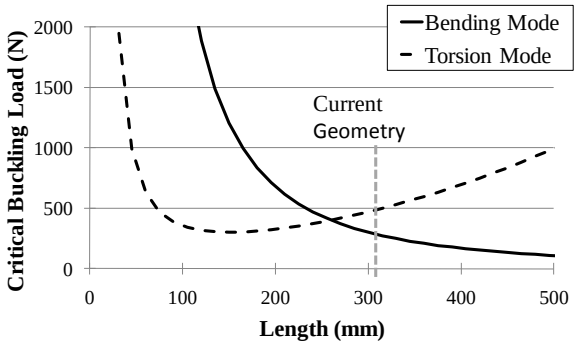

Figure 2-20 Critical buckling load of the first two buckling modes for various lengths and a constant width of *w*=150mm.

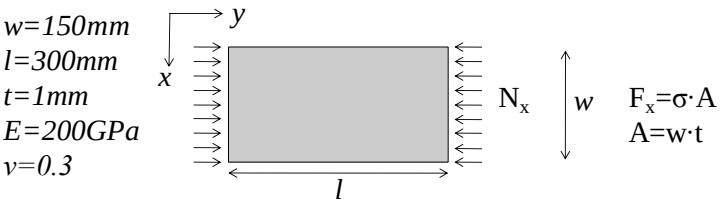

Figure 2-21 Definition for geometry and loads for the considered buckling case under uniform and non-uniform longitudinal stress conditions.

Within the finite element (FE) framework, see **section 4.2.2**, the solution of buckling problems can be written as [Belytschko 2001]:

$$\mathbf{0} = \left(\mathbf{K} + \lambda_i \cdot \mathbf{K}_\sigma\right) \cdot \mathbf{u}_i \,, \qquad \textbf{Eq. 2-30}$$

where $\mathbf{K}$ is the (linear / non-linear) nodal stiffness matrix of the system, $\mathbf{K}_\sigma$ is the load stiffness matrix due to an incremental loading pattern Q , λ_i are the eigenvalues of the

system, and $\mathbf{u}_i$ the nodal displacements of the corresponding buckling shape. The critical buckling load is then given by $F_{cr} = \lambda_i \cdot Q$. **Figure 2-22** shows the result of the first two buckling modes of the plate under consideration as obtained by means of FE buckling analysis using ABAQUS and fully integrated shell elements. The mesh consists of 180.000 elements, 300 elements in the transverse direction and 600 elements in the longitudinal direction. The calculated critical buckling loads F_{cr} are 277 N for the first mode and 471 N for the second mode, respectively. **Figure 2-23** shows the results of the critical buckling load for different mesh densities where the mesh density in the longitudinal and the transversal directions has been coarsened homogeneously. It can be seen that the critical buckling load is mesh-dependent and hence, mesh convergence analyses have to be performed in order to obtain reliable results.

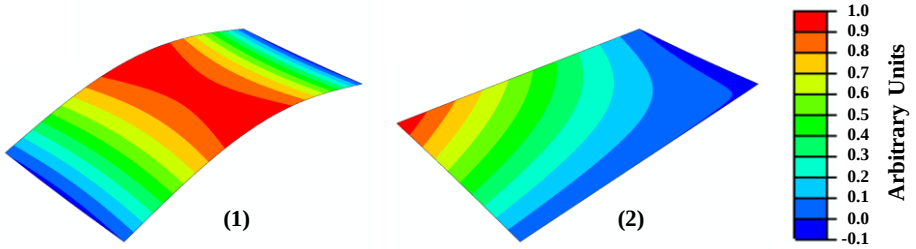

Figure 2-22 First two buckling modes for a plate subjected to loads as shown in **Figure 2-21**: Bending mode (1) and torsion mode (2).

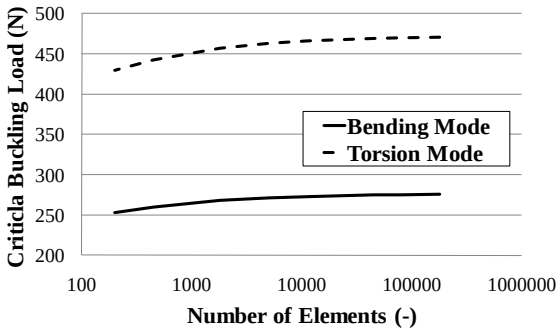

Figure 2-23 Calculated critical buckling load of the first two buckling modes for various mesh densities.

Example with a distributed and a piecewise constant load

Up to now, a constant uniformly distributed compressive load has been considered as the cause for buckling. In the case of welding, however, the longitudinal stresses are rather non-uniform with an appearance as shown in **Figure 2-17** (a). The stress distribution is in self-equilibrium; *i.e.*, the average stress over the width is zero. For such a stress

distribution, the energy approach [Timoshenko 1961] can be applied. A necessary condition for buckling to occur is that the external work T performed on the material corresponds at least to the strain energy U of the buckling shape $u(x,y)$; *i.e.*, if the inequality $T \geq U$ is fulfilled with:

$$T = \int_0^l \int_0^w N_x(x) \cdot \left(\frac{du(x,y)}{dy} \right)^2 dxdy$$
$$U = D \int_0^l \int_0^w \left(\frac{d^2u(x,y)}{dy^2} + \frac{d^2u(x,y)}{dx^2} \right)^2 dxdy \;,\; D = \frac{E \cdot w \cdot t^3}{12 \cdot (1-\upsilon^2)} \quad , \qquad \textbf{Eq. 2-31}$$

Where N_x is the sectional force acting on the workpiece. Employing the deformation shape for the first buckling mode presented in **Eq. 2-28**, the external work T is zero since the average stress in longitudinal direction is zero. This leads to the interpretation that a constant external load in the transverse direction cannot cause this buckling shape; the loads and the shape are incompatible. A numerical approximation of the deformation shape of the second buckling mode which is compatible with a constant load has been proposed by van der Aa [Aa 2007].

$$(1)\, u(x,y) = A \cdot \sin\left(\frac{\pi}{l} \cdot y \right) \cdot \left[p - \sin\left(\frac{\pi}{w} \cdot x \right) \right]$$
$$p = 1 + (1-\nu) \cdot (l/w)^2 = 3.8 \quad . \qquad \textbf{Eq. 2-32}$$
$$(2)\, u(x,y) = A \cdot \sin\left(\frac{\pi}{2 \cdot l} \cdot y \right) \sin\left(\frac{\pi}{2 \cdot w} \cdot x \right)$$

The equation for the deformation shape of the first buckling mode remains unchanged. In general, the longitudinal stresses cannot be given in a closed analytical form, but have to be obtained numerically, for instance by performing finite element simulations. **Eq. 2-31** can be evaluated numerically assuming piecewise constant longitudinal stresses σ_i in $[x_i, x_{i+1}]$. Then, the integrals for T and U become:

$$T = \int_0^l \sum_{i=0}^{n} N_i \int_{x_i}^{x_{i+1}} \left(\frac{du(x,y)}{dy} \right)^2 dxdy$$
$$U = D \int_0^l \sum_{i=0}^{n} \int_{x_i}^{x_{i+1}} \left(\frac{d^2u(x,y)}{dy^2} + \frac{d^2u(x,y)}{dx^2} \right)^2 dxdy \quad , \qquad \textbf{Eq. 2-33}$$

where the stresses σ_i are obtained by integration points in a chosen section of the plate in the transverse direction. The interval $\Delta x_i = x_{i+1} - x_i$ is then given by the volume associated with the integration point. Since the buckling shapes can always be described by superpositions of sine and cosine functions, a helpful identity for the local integration is [Bronstein 1997]:

$$\int \cos^2(a \cdot x)dx = \frac{1}{2} \cdot x + \frac{1}{4 \cdot a} \cdot \sin(2 \cdot a \cdot x)$$
$$\int \sin^2(a \cdot x)dx = \frac{1}{2} \cdot x - \frac{1}{4 \cdot a} \cdot \sin(2 \cdot a \cdot x) \quad . \qquad \textbf{Eq. 2-34}$$

A simple analytical approximation of a longitudinal stress distribution is shown in **Figure 2-24** (left). The equation of this distribution is:

$$N_{Long}(x) = N_0 \cdot \left[\frac{4}{5} \cdot \cos\left(\frac{3}{2} \cdot \pi \cdot \frac{|x|}{w/2} \right) \cdot \left(1 - \frac{|x|}{w/2} \right) + \frac{1}{5} \right],$$
$$\overline{N} = \frac{1}{w} \cdot \int_{-w/2}^{+w/2} N_{Long}(x) \approx 0 \quad , \quad N_{Long}(x = 0) = N_0 \qquad \textbf{Eq. 2-35}$$

where x is the distance to the weld seam. Using this stress distribution and the buckling shapes from **Eq. 2-32**, the peak tensile stresses σ_0 for the first two buckling modes have been evaluated for $T = U$ by numerical integration to be

$$(1)\ \sigma_0 \approx 520MPa$$
$$(2)\ \sigma_0 \approx 770MPa \quad . \qquad \textbf{Eq. 2-36}$$

Another schematic approximation which is often applied for conceptual studies is shown in **Figure 2-24** (right). This simplified stress distribution is deduced from the 3-bar model, see **subsection 2.3.1** and [Masubuchi 1980, Radaj 2002]. A non-uniform stress is applied with a tensile zone in the centre of the plate having a width c, corresponding to the weld seam, and compressive zones towards the plate edges. Assuming that these stresses represent a residual stress state, the average stresses must be zero:

$$\overline{\sigma} = c \cdot \sigma_0 + (w - c) \cdot \sigma_1 = 0 \Rightarrow \sigma_1 = -\frac{c}{(w - c)} \cdot \sigma_o \,. \qquad \textbf{Eq. 2-37}$$

Solving **Eq. 2-31** for the second buckling mode and this stress distribution leads to zero external work T. This can be interpreted in a way that this stress distribution provides no driving force for the torsion mode. This stress distribution introduces neither effective (average) stresses nor shear stresses (zero derivatives in the x-direction) in the plate and hence, will not cause torsion of the plate. This is a similar effect as previously mentioned for a constant load and the bending shape. Hence, this distribution is not suitable to estimate the minimum critical buckling load for narrower plates, see **Figure 2-20**. The solution for the first buckling mode reads:

$$F_{cr} = \frac{D \cdot \frac{\pi^4}{2} \cdot l \cdot \left[\left(\frac{1}{l^2} + \frac{1}{w^2} \right)^2 \cdot \frac{w}{2} + \frac{1}{l^4} \cdot p^2 \cdot w - 4 \cdot \frac{1}{l^2} \cdot p \cdot \frac{w}{\pi} \cdot \left(\frac{1}{l^2} + \frac{1}{w^2} \right) \right]}{\frac{\pi}{l} \cdot w \cdot \left[-\frac{1}{4} \cdot \sin\left(\pi \cdot \frac{c}{w} \right) \cdot \left(1 + \frac{(w-c)}{c} \right) + 2 \cdot p \cdot \sin\left(\frac{\pi}{2} \cdot \frac{c}{w} \right) \left(1 + \frac{(w-c)}{c} \right) - 2 \cdot p \right]} \quad \textbf{Eq. 2-38}$$

.

For the plate under consideration and assuming a width of the tensile zone of c = 10 mm, the critical buckling load F_{cr} and stress σ_1 become 367 N and -2.6 MPa, respectively. The corresponding peak tensile stress σ_0 in the centre is 36.7 MPa.

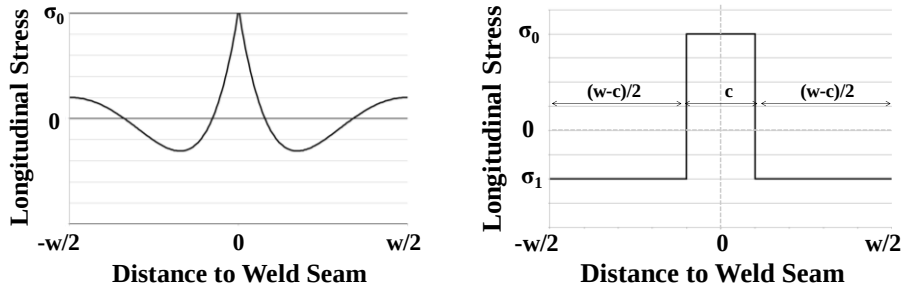

Figure 2-24 Left: Approximated longitudinal stresses function as shown in Eq. 2-35. Right: Schematic longitudinal stresses as obtained from the 3-Bar model (**Figure 2-15**).

Concluding Remarks

The key issue of this section is that for the geometry under investigation, the occurrence of the second buckling mode, the bending mode, is more likely than the occurrence of the first buckling mode, the torsion mode. It has also been found that a constant load is incompatible with the bending shape and a piecewise constant load is incompatible with the torsion shape. Only a distributed load is able to generate both buckling modes depending on the load amplitudes.

2.3.4 Distortion of T-Joints

Unlike thin plates, thick T-Joints are more likely to exhibit angular and bending distortion after welding. Here, examples are given for analytical models for the prediction of angular and bending distortion using the shrinkage volume method. This method is based on the assumption that the linear thermal contraction of a nominal shrinkage volume is the main driving force for distortion.

Angular Distortion

Figure 2-25 shows a simple 2D model based on 1D beam theory to explain angular distortion in which b is the leg length of the fillet. Assuming homogeneous longitudinal shrinkage, the effective shrinkage force of the fillet F and the corresponding bending moment M can be calculated by:

$$\begin{aligned} F &= E \cdot \alpha \cdot \Delta T \cdot A = E \cdot \alpha \cdot \Delta T \cdot \frac{1}{2} b^2 \\ M &= F \cdot \left(t + b_{eff} \right) ,\ b_{eff} = \frac{1}{3} b \end{aligned} \quad , \qquad \textbf{Eq. 2-39}$$

where α is the thermal expansion coefficient and ΔT is the difference between the melting temperature and the room temperature. The curvature κ, the displacement u and the angular distortion θ of the base plate can be calculated using the bending stiffness EI and the effective length b_{eff} of the acting bending moment:

$$\begin{aligned} &\kappa = \frac{M}{EI} ,\ EI = E \cdot \frac{b \cdot t^3}{12}, u = \frac{M \cdot b_{eff}^2}{EI} \\ &\theta \approx \sin(\theta) = u / b_{eff} = \frac{M \cdot b_{eff}}{EI} \sim \frac{b^2}{t^2} + \frac{b^3}{t^3} = s^2 + s^3 \ ,\ s \equiv \frac{b}{t} \end{aligned} \quad . \qquad \textbf{Eq. 2-40}$$

Interestingly, the angular distortion depends only on the leg length – thickness ratio $s=b/t$ and the heat input, modelled here by the temperature difference ΔT. The distortion is independent of the material stiffness E, which is due to the fact that the shrinkage force is a linear function of E. The temperature difference ΔT applied has to be regarded as a tuning factor of the model since the material looses its stiffness above a homologous temperature T^* of approximately 0.5, see **Figure 2-7**. The major disadvantage of this model is that the bending of the fillet is not considered, which leads to an underestimation of the bending stiffness for larger bending amplitudes.

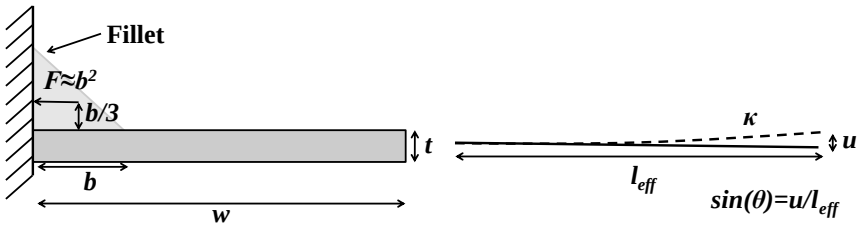

Figure 2-25 Simple analytical spring model to explain angular distortion using the shrinkage volume method.

Figure 2-26 sketches the shrinkage volume approach using elastic springs as proposed firstly by Tsai et al. [Tsai 1995, Tsai 1999] and a simplified 2D plane stress FE model (right) developed in order to study the numerical predictions for angular distortion. The fillet cools down from T_{Max} to room temperature. In order to describe the material response,

an elastic-ideal-plastic material model with Young's Modulus of 200 GPa and yield stress of 350 MPa has been applied in order to describe the reaction of the T-Joint.

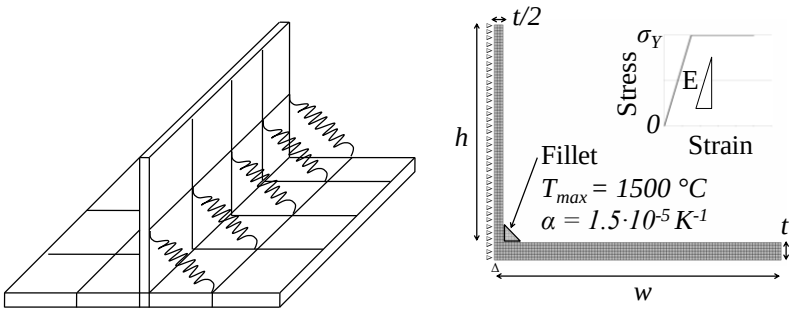

Figure 2-26 Left: Spring model. Right: Simplified 2D FE shrinkage model.

Figure 2-27 (left) shows calculated values for the angular distortion for various plate thicknesses using the 1D beam model and the simplified 2D FE model. Also for the FE shrinkage model, the angular distortion depends only on the ratio *s* between the leg length and the thickness. The increase of angular distortion reduces for higher ratios *s*, which is due to the bending stiffness of the fillet.

However, also the shrinkage model is not complex enough to model angular distortion correctly: **Figure 2-27** (right) shows measurements of the angular distortion for a 6mm steel T-Joint [Malisius 1977]. While the shrinkage model considers the rigidity of the flange and hence, allows a study of the effect of the dimensions for leg lengths up to the plate thickness, it is not appropriate for larger leg lengths; *i.e.*, higher values of *s*, where the heat input becomes more uniform: The flange plate heats up as well, which leads to a reduction of the bending stiffness *EI* as well as to a smaller bending moment *M*. If the heat input is high enough to melt the flange plate, the bending moment even disappears, $M \rightarrow 0$. According to Neumann and Röbenack [Neumann 1978], this effect is reproducible for T-Joints in general. It has also been confirmed for 316L stainless steel butt welds by Kim et al. [Kim 2008]. This effect is not included in the formulation of the simple shrinkage volume model presented here and gives reason for the application of more complex models to predict the distortion due to welding.

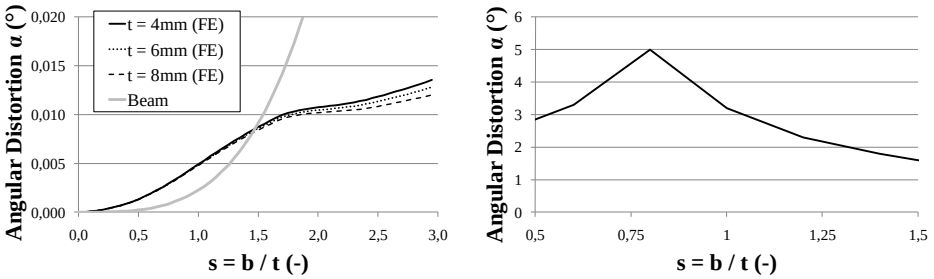

Figure 2-27 Left: Calculated angular distortion using the 1D beam model and the simplified 2D FE model as function of the ratio of leg length and thickness. Right: Measured angular distortion as function of the ratio of leg length and thickness for a St48 GMA welded T-Joint [Malisius 1977].

A fit function incorporating the declining angular distortion has been proposed by Watanabe and Satoh [Watanabe 1961, Lincoln 2000]:

$$\theta \approx C_1 \cdot \left(\frac{I}{t \cdot \sqrt{v \cdot t}} \right)^{m+1} \cdot \exp\left(- C_2 \cdot \frac{I}{t \cdot \sqrt{v \cdot t}} \right), \qquad \textbf{Eq. 2-41}$$

where I is the welding current, v the welding speed, and C_1, C_2, and m are fit parameters. Examples of the application of transient thermo-mechanical models to predict angular distortion of T-Joints are given in references [Teng 2001, Jung 2003, Roeren 2006, Hackmair 2003, Huang 2004].

Bending Distortion

The effect of the plate dimension and the heat input on bending distortion can be considered using 1D beam and 3D FE shrinkage models. Bending distortion is induced by the longitudinal shrinkage forces of the weld which do not coincide with the neutral axis of the workpiece leading to a non-zero bending moment. **Figure 2-28** shows the section of the 1D beam model in order to calculate the bending stiffness and a transverse view on the beam depicting the length and bending shape of the beam.

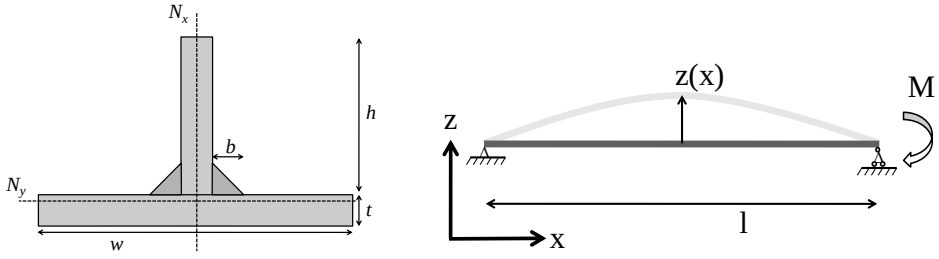

Figure 2-28 Left: Section and dimensions of the T-Joint for the beam model. Right: Transverse view on the beam.

For the three components under investigation; *i.e.*, the flange plate *fp*, the web (stiffener) plate *wp*, and the fillet *f*, the corresponding areas A_i, area moments of inertia I_i, and distances to the centre of mass d_i are given by

$$\begin{aligned} I_{fp} &= \frac{A_{fp}\cdot t^2}{12} + A_{fp}\cdot d_{fp}^2 \qquad A_{fp} = w\cdot t \qquad d_{fp} = N_y \\ I_{wp} &= \frac{A_{wp}\cdot h^2}{12} + A_{wp}\cdot d_{wp}^2 \quad A_{fp} = t\cdot h \qquad d_{wp} = N_y - t\,, \\ I_f &= 2\cdot\frac{A_f\cdot b^2}{36} + A_f\cdot d_f^2 \qquad A_f = 2\cdot\frac{b^2}{2} \quad d_{wp} = N_y - t \end{aligned} \qquad \textbf{Eq. 2-42}$$

where Steiner's theorem and the neutral axis N_y in the height direction have been used. The total bending stiffness of the T-joint is then given by [Mase 1969]

$$EI = E\cdot I_{total} = E\cdot\left(I_{fp} + I_{wp} + I_f\right). \qquad \textbf{Eq. 2-43}$$

The height of the neutral axis N_y corresponds to the centre of mass R_y in height direction:

$$N_y = R_y = \frac{1}{\left(A_{fp} + A_{wp} + A_f\right)}\cdot\left[A_{fp}\cdot\left(\frac{t}{2}\right) + A_{wp}\cdot\left(t + \frac{h}{2}\right) + A_f\cdot\left(t + b_{eff}\right)\right]. \qquad \textbf{Eq. 2-44}$$

For the T-Joint employed in the present thesis, the neutral axis N_y becomes 17.7 mm, and hence, it is situated above the flange plate. The shrinkage force and the bending moment with respect to the neutral axis are given by

$$\begin{aligned} F &= E\cdot\alpha\cdot\Delta T\cdot 2\cdot\frac{1}{2}b^2 \\ M &= F\cdot\left(t + b_{eff} - N_y\right) \end{aligned}. \qquad \textbf{Eq. 2-45}$$

Finally, the bending shape can be obtained by solving $u'' = \kappa$:

$$\begin{aligned} u(x) &= \frac{\kappa}{2}\cdot x\cdot(l - x) \\ u(x = 0) &\equiv u(x = l) \equiv 0 \\ u_{MAX} &= u\left(x = \frac{l}{2}\right) = \kappa\cdot\frac{l^2}{8} \end{aligned}. \qquad \textbf{Eq. 2-46}$$

Neglecting the contribution of the filler material to the bending stiffness, the following dependencies of the curvature κ on the dimensions can be found:

$$\kappa = \frac{M}{EI} \approx \frac{b^2\cdot\left(t + b_{eff} - N_y\right)}{w\cdot t^3 + t\cdot h^3} \underset{t<<w,h}{\approx} \frac{b^2\cdot(t + b)}{t\cdot h^3} = \frac{s^2\cdot t^2}{h^3}. \qquad \textbf{Eq. 2-47}$$

The dependency of the bending shape on the dimensions is much more complex than in the case of angular distortions, see **Eq. 2-40**. According to this 1D beam model, it can be concluded that larger leg lengths *b* and larger lengths *l* increase bending distortion while wider flanges *w*, larger thicknesses *t* and higher webs *h* have a reducing influence. Again, the distortion is not affected by the material stiffness. **Table 2-1** summarizes the dependencies of angular and bending distortion on the dimensions of the T-Joint as obtained from the 1D beam models.

Table 2-1 Dependency of angular and bending distortion of the T-Joint on its dimensions. Results are obtained from the 1D beam models.

Parameter	Angular	Bending
Leg Length *b*	↑↑↑	↑↑↑
Width *w*	O	↓
Height *h*	O	↓↓↓
Length *l*	O	↑
Thickness *t*	↓↓↓	↓↓
Temperature ΔT	↑	↑
Young Modulus *E*	O	O

Figure 2-29 shows the mesh for the 3D model applied for the 3D shrinkage simulation. The symmetry plane has been modelled only in order to save computational time. The same material model has been applied as that used for the study of the angular distortion. In order to force the occurrence of bending distortion instead of angular distortion, thermal shrinkage has only been incorporated in the longitudinal direction. However, even in this case, angular distortion becomes the dominant deformation mode if the bending stiffness becomes too high. The bending amplitude has been evaluated using three points, two at the ends of the plate and one in the centre. The superposed angular distortion has been evaluated at the centre point.

The results of the simulations are shown in **Figure 2-30** for two case studies: For varying *leg length – thickness ratio* and constant dimensions (left), and for constant ratio $s = 1$ ($b = t = 6$ mm) and varying dimensions (right). Also in this case, the amount of angular distortion is mainly dependent on the ratio *s*. However, there is some dependency on the width, which converges towards a constant value for wider plates. As expected from **Eq. 2-47**, the curvature decreases for higher ratios *s* as well as thicker and wider plates.

An overview of empirical models to estimate bending distortion of T-Joints is also given by Suresh et al. [Suresh 1997].

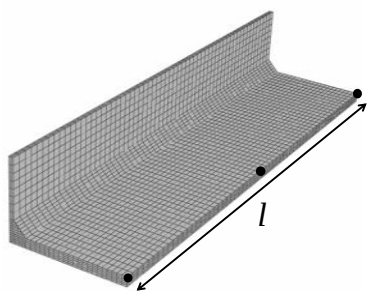

Figure 2-29 FE Mesh of the 3D shrinkage model.

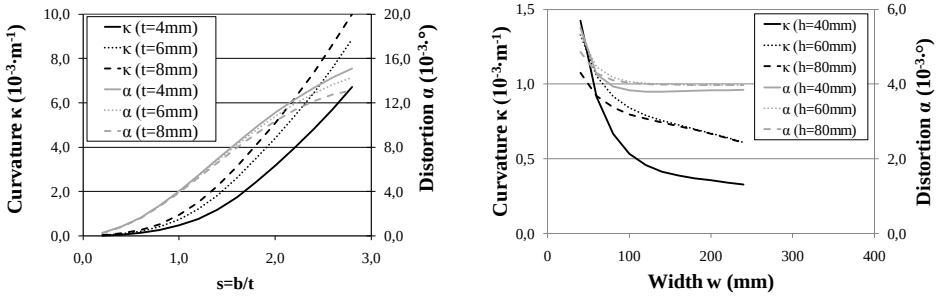

Figure 2-30 Calculated bending and angular distortion using the 3D FE shrinkage model. Left: Results for various *s* and constant dimensions (*w=150mm* , *l=300mm* , *h=80mm*). Right: Results for constant *s=1* (*b=t=6mm*) and various dimensions.

2.4 Concluding Remarks

Welding has a significant effect on the material behaviour. During welding, the material is heated up above the melting temperature and subsequently cooled down to room temperature. This introduces solid-liquid transitions on melting and solidification as well as solid-solid phase transformations due to the mechanical and thermal treatment. Due to this heat treatment, the as-delivered microstructure, which is often set in order to fulfil certain requirements, *e.g.* for deformability, hardenability, or tensile stresses, is destroyed. The combination of thermal strains with temperature- and strain-rate dependent hardening causes inhomogeneous plastic deformations and result in residual stresses and distortions.

In principle, the material shows mixed temperature- and phase-dependent kinematic-isotropic hardening in combination with a strain-rate dependency for higher homologous temperatures. Additionally, if the material undergoes phase transformations, the volume of the material changes and phase strains occur. It has been found that in the literature, however, the effects considered differ significantly and often rely on several assumptions. These are not necessarily correct and their influence has often not been verified by sensitivity analyses. For instance, in some works it is assumed that welding is not cyclic and hence, kinematic hardening can be neglected. In other models, even no hardening is

considered. Sometimes the temperature-dependence of the material properties is neglected and replaced by constant properties. Hence, it is an important task for current research to obtain reliable statements about which model accuracy is required to predict reliable results.

Depending on the geometry, different distortion shapes can be obtained due to welding. Some simplified numerical models and analytical beam models have been presented to predict welding distortion and residual stresses. Some effects can be explained well using these models. However, these models are based on assumptions which cannot be generalized and even if they can predict distortion tendencies, the qualitative and quantitative outcome is not very accurate. As an example, the interaction of the workpiece with clamps cannot be considered. Also, the decline of angular distortion for higher heat inputs could not be predicted using these models. Hence, in order to obtain a better understanding of the welding process, more accurate models are required.

In order to capture a realistic material response to welding, thermomechanical and metallurgical effects have to be considered in order to increase the accuracy of the model. Thus, the approach for welding simulations in the present work is to perform temperature and strain-rate dependent measurements of material properties if no reliable literature data exist. For the thermal model, transient temperature measurements should be performed during welding to adjust numerical heat sources for the modelling of the temperature distribution during and after welding. With the aid of this thermal model, the creation of stresses and distortions can be simulated, and the influence of phase transformations on the results should be taken into account. In order to evaluate the accuracy of the predictions, the results should be validated using residual stress and distortion measurements for different clamping conditions.

2.4 Concluding Remarks

3 Distortion Mitigation Techniques

The easiest possibility to minimize all types of welding distortion is using less heat input since the welding distortion to be expected is correlated to the energy input [Radaj 1992]. This could be done, for instance, by using higher welding speeds, less filler material, or reduced process power. Although the heat input should be controlled in order to reduce distortions as much as possible, the critical heat input to eliminate buckling, for instance, is often below what is practically producible with GMA welding processes [Mandal 2004]. Recently, new welding techniques have been developed which promise to deliver low heat input conditions such as the Cold-Metal-Transfer process developed by Fronius [Fronius] or the coldArc process developed by EWM [EWM].

In this chapter an overview is given of different mitigation techniques devised to reduce either distortion or residual stresses due to welding. Even though all processes presented in this chapter are applicable to reduce the distortion in some way, it is difficult to derive rules concerning how these methods should be applied. Mitigation is achieved either by means of introducing higher amounts of plastic deformation in the weld or by reducing the temperature gradients during welding.

In this chapter, some in-line distortion mitigation approaches are described followed by pre- and post-welding mitigation techniques such as pre-deformation, annealing, and optimized welding methods. The intention of in-line mitigation techniques, which include low-stress no-distortion (LSND) welding, thermal and mechanical tensioning techniques, and welding sequences, is to prevent distortion in-process; *i.e.*, during welding. A general overview is given by Williams et al. [Williams 2008] and Pilipenko [Pilipenko 2001].

In the last section, a survey of the influence of clamping on the thermomechanical material reaction is presented.

3.1 Tensioning & Straightening

3.1.1 Mechanical Straightening

Mechanical straightening, see [Pilipenko 2001, Radaj 1988], can be applied in order to release stresses in a material by means of plastic deformation. In particularly, this method can be employed for materials without phase transformations which exhibit a pronounced tensile region at the weld seam. It can be applied during as well as after welding.

Figure 3-1 shows a sketch of mechanical straightening, demonstrated by the 3-bar system presented in **subsection 2.3.1**. If the sample; *i.e.*, the 3-bar system, is subjected to an external tensile stress σ, the bars are deformed plastically and hence lengthened. Since the middle bar already exhibits tensile stresses after welding, the yield stress is exceeded earlier there, which leads to a higher amount of plastic strain at this bar. As a consequence, the structure possesses lower residual stresses after removal of the external tensile stress.

If the stresses were the same in all three bars in **Figure 3-1** during tension, the residual stresses could be reduced elastically to zero when the external stress is removed. Therefore, the material must be drawn until the hardening has saturated and before the material fails.

This is particularly hard to achieve for high-strength materials which exhibit significant strain hardening potentials.

Figure 3-2 shows the results of post-weld mechanical straightening of the 3-bar system. A tensile straightening stress of 300 MPa has been applied. Using this straightening condition, the peak tensile residual stresses in the weld after straightening is reduced by about 300 MPa as well. However, the tensile force F required to perform the straightening in this example is $w \cdot t \cdot 300$ MPa = 45 kN which corresponds to 4.5 tons.

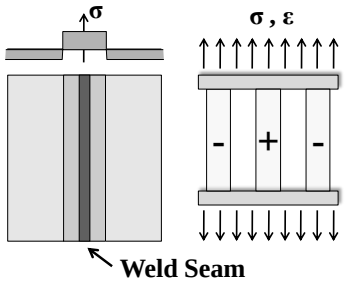

Figure 3-1 Sketch of mechanical straightening. Left: Sketch of the residual stress distribution after welding. Right: 3-Bar system to demonstrate the effect of mechanical straightening [Pilipenko 2001].

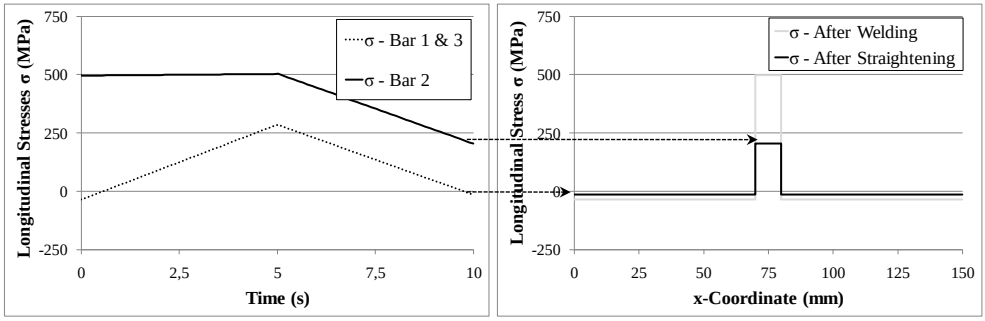

Figure 3-2 Transient and residual stresses in a 3-bar system during post-weld mechanical straightening. The initial residual stress state has been obtained from **Figure 2-16**.

Mechanical straightening can also be applied during welding, in which case a tensile stress is applied to the structure prior to welding and released after welding. **Figure 3-3** shows the stress development when an additional tensile straightening stress of 300 MPa is applied during welding. The tensile stress forces the weld seam; *i.e.*, the middle bar, to deform more plastically during welding than if no stresses were present. Hence, the residual elastic stresses and strains are lowered following release of the stresses after welding.

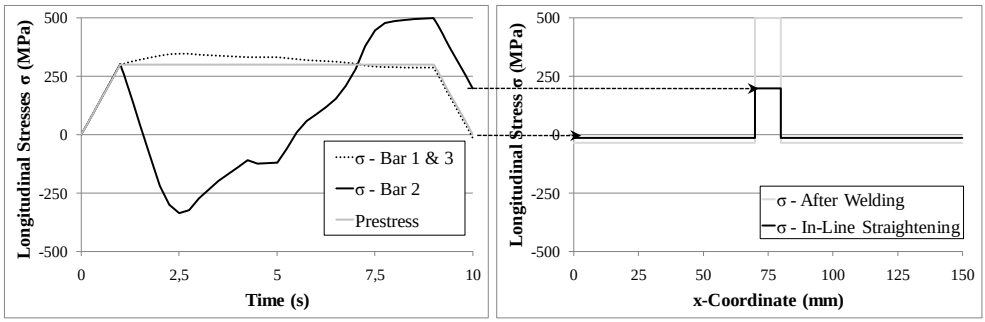

Figure 3-3 Transient and residual stresses in a 3-bar system during welding using in-line mechanical straightening.

In the literature, mechanical straightening is often reported for distortion and stress relief of aluminium welds. A study on the influence of the tensile load for transient mechanical straightening has been presented by Altenkirch et al. [Altenkirch 2008] for friction-stir welded aluminium plates, showing that the residual stresses as well as the distortion could be reduced with increasing tensile loads. Mechanical straightening has successfully been applied for similar cases by Price et al. [Price 2007] and Richards et al. [Richards 2008]. Siddique and Abid [Siddique 2006] employed mechanical tensioning for carbon-manganese steel pipes using axial pulls and internal pressures. It has been reported that both cases are suitable to reduce residual stresses and distortion.

3.1.2 Thermal Tensioning – LSND-Welding

LSND-welding, also referred to as thermal tensioning, makes it possible to avoid buckling completely. The term LSND-welding refers to "low stress no distortion" which describes a method developed by Guan et al. [Guan 1999]. LSND welding can be divided into static and transient applications.

Static LSND welding refers to a stretching effect implemented during welding by means of presetting an adequate temperature profile as shown in **Figure 3-4**. The principles are the same as for mechanical straightening. The preset thermal profile consists of an elevated temperature at some distance from the weld seam, and a low temperature close to the weld. This profile leads to tensile stresses in the weld zone and compressive stresses in the base material. This method is patented by the Chinese patent No. 87100959 [Guan 1987]. It can be shown that distortion-free results can be achieved using such a welding process with optimized process parameters.

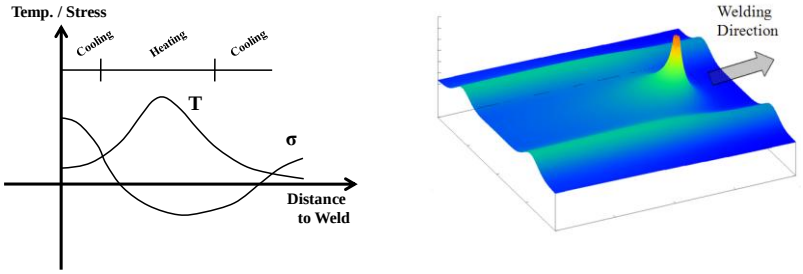

Figure 3-4 Principles of static thermal tensioning. (a) teperature curve for preset heating and cooling, σ orresponds to the stress distribution, (b) 3D temperature profile during welding [Guan 1999].

One problem of this method is that the optimized process parameters are hard to predict and there is some difficulty sustaining the required temperature profile. In fact, the latter is the major drawback because specialised jigs are needed for each weld. Also, the temperature profile of the heaters should avoid phase transformations or tempering of the material. According to Michaleris et al. [Michaleris 1999], further limitations of this method are that it is costly and environmentally unfriendly due to the energy consumption required to sustain the temperature profile.

Figure 3-5 shows the principle of thermal tensioning using the 3-bar system. The outer bars are heated up to 100 °C prior to welding which causes tensile stresses in the centre bar; *i.e.*, at the weld seam. Similarly to in-line mechanical straightening, this leads to an increased plastic deformation at the weld seam during cooling and hence, lowered residual stresses after welding and removal of the external temperature field.

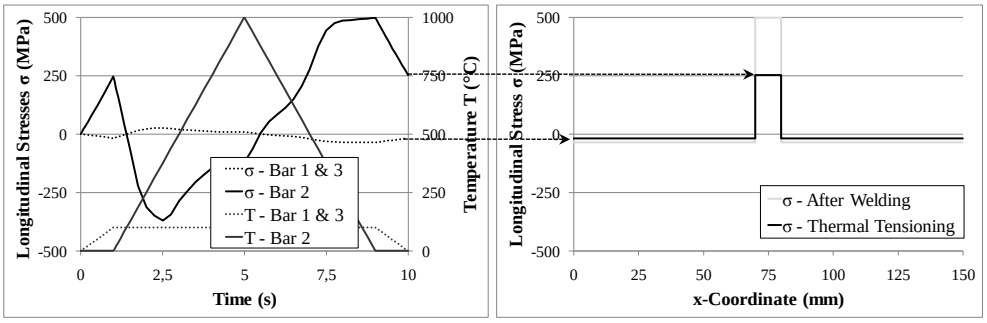

Figure 3-5 Transient and residual stresses in a 3-bar system for thermal tensioning.

Michaleris et al. [Michaleris 1999] also developed a simplified transient thermal tensioning (TTT) technique using moving spot heat sources in front of the weld to obtain the required stretching effect, see **Figure 3-6**. This method employs two heating sources in front of the weld and hence, avoids the need to sustain a constant temperature profile during welding which reduces the complexity of the process enormously. Transient thermal tensioning has been employed effectively by Conrardy et al. [Conrardy 1997,

Conrardy 2006] for thin ship panels (thickness < 10 mm). It has been found that bending and buckling can be reduced using this method while angular distortion is still present. This method has been patented in the US, patent *US 2004/0245231 A1* [Dull 2004]. Transient thermal tensioning has been applied for distortion mitigation of welded ship panels, *e.g.* by Deo et al. [Deo 2002, Deo 2003, Deo 2003a, Deo 2003b], Michaleris et al. [Michaleris 2006, Michaleris 1997], and Nagy et al. [Nagy 2008]. Simulations have been performed by Dong et al. [Dong 1998] to reduce welding distortion for Al-Li repair welds using tensioning by heating and cooling sources. Lin and Chou [Lin 1995] reported a reduction of the residual stresses by 25 % using transient thermal tensioning for bead-on-plate welded 304 stainless steel plates. A numerical parametric study using thermal tensioning was performed by Guo et al. [Guo 2005] for thin aluminium plates. A similar parameter study has been presented by Song et al. [Song 2004] for T-joints. The applicability of transient thermal tensioning to the welding of box beams has also been proven by Xu and Li [Xu 2007, Xu 2007a].

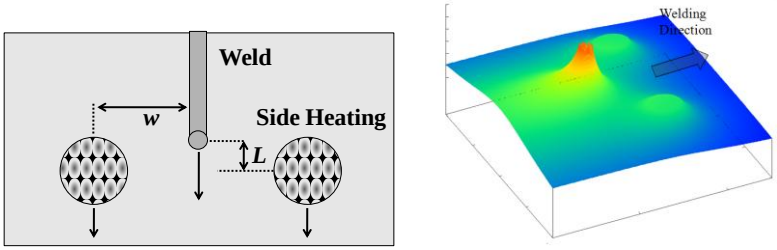

Figure 3-6 Transient thermal tensioning. Left: Schematic drawing of the process. Right: Temperature profile during transient thermal tensioning.

3.1.3 Dynamic LSND-Welding

Dynamic LSND-welding uses no predefined temperature profile but a trailing heat sink close behind the welding torch, as sketched in **Figure 3-7**. The process is also referred to as DC-LSND-welding. The cooling jet following the welding arc creates an abnormal temperature profile field compared to the normal temperature distribution during conventional arc welding which has the appearance of a saddle profile. DC-LSND has been applied successfully to reduce welding distortion for many different materials, *e.g.* for Titanium alloys [Li 2004] or stainless steels [Aa 2006, Guan 1994]. Studies have been performed by van der Aa et al. [Aa 2006] for stainless steels in order to optimise the cooling parameters; *i.e.*, the diameter of the cooling source, the heat sink transfer coefficient and the distance of the heat sink to the welding torch. Engelhard et al. [Engelhard 2000] reported that DC-LSND-welding can be applied to convert tensile into compressive stresses for austenitic steel pipes. Camilleri et al. [Camilleri 2008] presented a numerical investigation on the influence of additional cooling on the out-of-plane distortion of GMA welded T-joints. It has been reported that the amount of out-of-plane distortion can be reduced significantly.

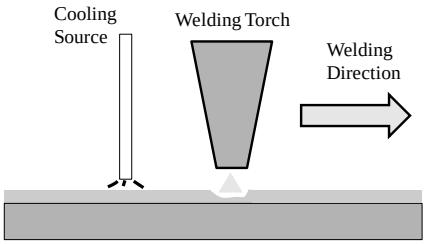

Figure 3-7 Sketch of dynamic LSND-welding. A moving spot heat sink follows the welding torch at a distance L.

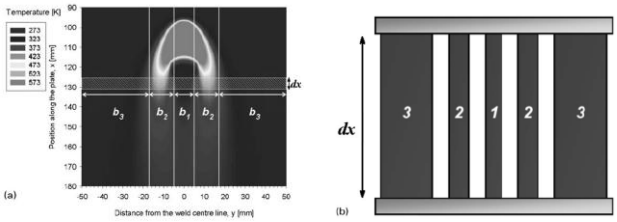

Figure 3-8 (a) Temperature distribution at the topside of the plate and (b) 5-bar model [Aa 2006a].

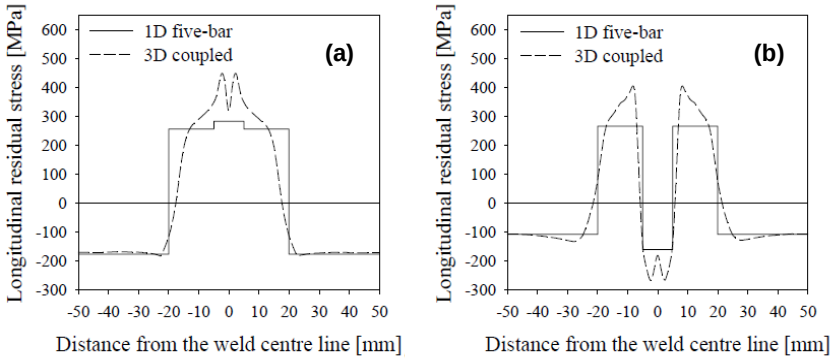

Figure 3-9 Comparison between residual stress distributions calculated with 3D coupled thermal mechanical model, and 1D mechanical 5-bar model for (a) conventional welding and (b) DCLSND welding [Aa 2006a].".

An extension of the 3-bar model shown in **section 2.3** to 5-bars to represent cooling influences has been presented by van der Aa [Aa 2006a]. A temperature profile similar to the simulation of DC-LSND welding is applied for each of the five bars, including the faster cooling of the centre bar. **Figure 3-8** shows a sketch of the 5-bar model. The two additional bars are required to incorporate the faster cooling at the weld seam into the model. **Figure 3-9** shows the results of this 1D model compared to 3D transient FEM

welding simulations. The qualitative tendency for the residual stresses is in good agreement with the transient simulations.

3.1.4 Other Cooling / Heating Techniques

Two processes have been analyzed by Jung and Tsai [Jung 2003, Jung 2004] for GMA welding of T-joints as shown in **Figure 3-10**. A heat sink below the T-joints produces a smaller heat-affected zone while preheating enlarges it. According to these results, the heat sink yields a faster cooling rate, unlike preheating. The heat sink results in a stronger angular distortion since the temperature gradient, which is the important quantity for the determination of distortion, increases when cooling is performed from below the T-joint. This result is interesting since it shows that cooling is not always favourable. However, one advantage of the heat sink is that the heat-affected zone is reduced. Unlike the heat sink, the angular distortion is reduced when preheating is applied. This reduced bend-up distortion is due to more homogeneous deformations and hence, decreased plastic shear strains.

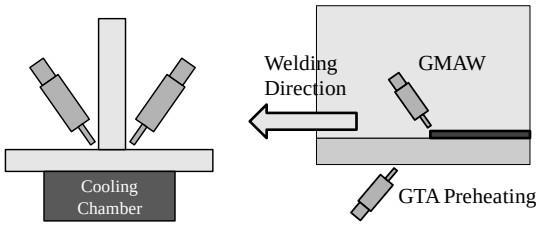

Figure 3-10 Two different mitigation techniques during welding. Left: Heat sink below the T-joint. Right: Pre-heating below the weld using GTAW [Jung 2004].

Pietzsch et al. [Pietzsch 2000, Pietzsch 2005] reported numerical studies on the influence of cooling during welding. **Figure 3-11** shows the four different cooling variations under investigation. It is shown that the angular distortion can be reduced to zero by all different cooling strategies if an optimised heat transfer coefficient h is applied. However, these results are in conflict with the results obtained in [Jung 2004], especially for the third variation, since they suggest a cooling from the underside of the weld is benefical. This is unlikely since such a cooling increases the inhomogeneity of the thermal field which causes plastic shear and hence, angular distortion. Unfortunately, there are no experimental verifications of these results.

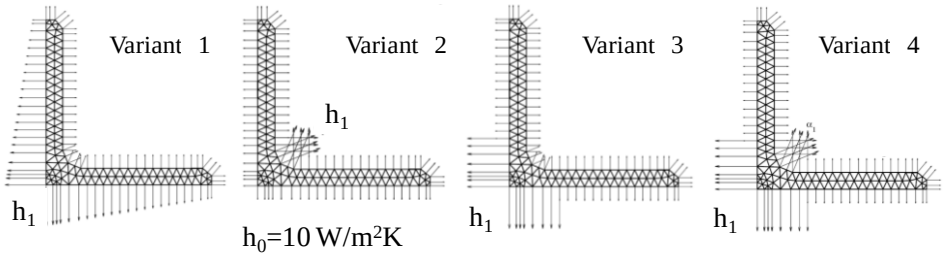

Figure 3-11 Four different variations for cooling during welding of L-profiles. The heat transfer coefficient to air h_0 is fixed. The additional cooling is modelled by h_1 [Pietzsch 2000].

3.2 Further Mitigation Techniques

This section gives an overview of other techniques to mitigate welding distortion including modified welding sequences during welding, post-weld annealing in order to release residual stresses and predeformation prior to welding in order to incorporate the final welding distortion in the design.

3.2.1 Welding Sequence

Research on finding optimum welding sequences dates back to the 1940s [Jonassen 1946] and 1950s [Watanabe 1955] and considerable research has been reported on the reduction of residual stresses due to optimised sequencing. Since residual stresses are coupled directly to bending distortion in case of a T-Joint and buckling distortion in the case of an overlap joint, it is expected that an optimised sequence could lower these kinds of welding distortion.

Distortion reduction has been studied by Tsai et al. [Tsai 1999] who reported welding simulations of ¼ inch thick aluminium sheets. The results are shown in **Figure 3-12** and agree well with experiments performed in order to verify the simulations. Apparently, the distortion can be reduced significantly if the welding sequence is chosen appropriately. The reduction achieved by the optimised welding sequence (A) is approximately a factor of two compared to sequence (B).

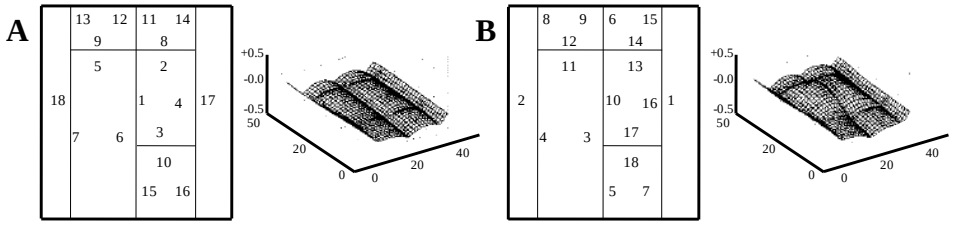

Figure 3-12 Comparison for the resulting distortion for two different welding sequences. The distortion is significantly smaller for sequence A [Tasi 1999].

Not only is the distortion dependent on the welding sequence but also the residual stresses, as shown by Mochizuki et al. [Mochizuki 2000]. Here, the stresses have been calculated elastically and superposed for all welding passes on multi-pass butt-welded pipe joints. The superposed result is in fair agreement for the real distribution of the residual stresses and has been applied to find a welding sequence to minimise the distortion. This optimised sequence has been found by manual comparison of different sequences; *i.e.*, a trial and error approach.

It is also possible to perform numerical analysis in order to find an optimum welding sequence as shown by Kadivar et al. [Kadivar 2000]. Welding simulation has been performed on a circular weld where only the radial distortion is of concern. The welding sequence has been optimised using a genetic algorithm and is a more or less arbitrary combination of eight subwelds. Using this optimal sequence, welding distortion is reduced by 80 %. For continuous welding; *i.e.*, welding in one run without stopping, the radial displacement is significantly higher compared to the optimum welding sequence. However, there is still homogeneous radial shrinkage which cannot be avoided. Unfortunately, no explanation is given concerning why the optimum sequence yields better results.

The influence of welding sequence for GMA welding of butt-welds has been investigated by Teng et al. [Teng 2003]. The dimensions of the plate and the three welding sequences employed are shown in **Figure 3-13**. The thickness of the plate is 5 mm, the material is SAE 1020. **Figure 3-14** shows the resulting longitudinal residual stresses. Symmetric welding caused the lowest residual stresses while backstep and progressive welding show the same results. However, the stresses oscillate in the direction of the weld seam due the welding sequence.

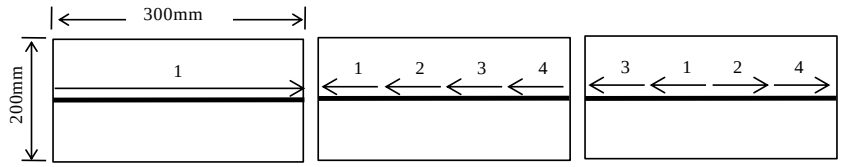

Figure 3-13 Welding sequences for thin-wall butt-welds employed in [Teng 2003]. From left to right: progressive welding, backstep welding, symmetric welding.

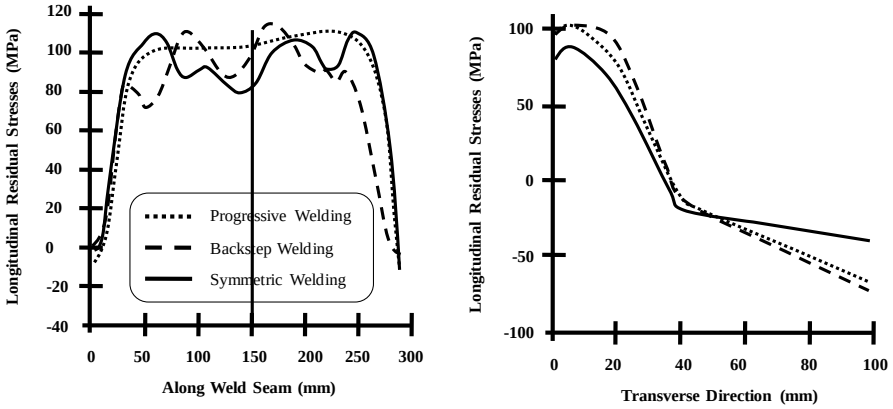

Figure 3-14 Calculated longitudinal stresses for the welding sequences shown in **Figure 3-13**. In seam direction (right) and transverse to the weld seam (right) in the centre of the weld (Y=150mm) [Teng 2003].

Similar studies have been performed by Prasad and Srinivasan [Prasad 1997] for 5 mm thick bead-on-plate welds. However, in this study, two parallel welding torches were used to weld the sample. The dimensions of the plate and the welding sequences employed are shown in **Figure 3-15**. **Figure 3-16** shows the predicted longitudinal and transverse stresses. The welding process from centre to end yields the lowest residual stresses. This result is similar to the results found by Teng et al. Unfortunately, in neither publication are validations given, or a model described to explain the mechanism leading to lower residual stresses.

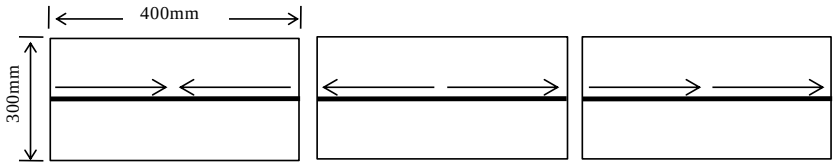

Figure 3-15 Welding sequences for bead-on-plates employed in [Prasad 1997]. From left to right: end-centre, centre-end, end-centre-centre-end.

Zhang et al. [Zhang 2007] reported numerical simulations of GMA welded T-Joints. It has been concluded that the welding sequence can reduce the amount of bending distortion by approximately 25 %. However, neither the material model is explained, nor is it is clear how the welding sequences are employed. Schwenk et al. [Schwenk 2007a] reported a reduction of 37 % of the welding distortion of an electron beam welded (circular) gear wheel using multiple beams in parallel. Lin et al. [Lin 1995] employed different welding sequences for the packaging of butterfly laser diodes. The welding distortion was reduced by a factor of five using the optimum sequence.

Optimised welding sequences are not only applied in order to minimise distortion, but also to minimise the total time required to weld a component. Neural network algorithms, which like genetic algorithms are also a stochastic optimisation method, have been presented by Fukuda and Yoshikawa [Fukuda 1990], Kim et al. [Kim 2002], and Damsbo and Ruhoff [Damsbo 1998] for minimizations of the welding time by optimisation of robot movement. A genetic algorithm has been presented by Xie and Hsieh [Xie 2002] in order to find a distortion and cycle time minimising welding and clamping sequence for resistance spot welding of an automotive vehicle body assembly.

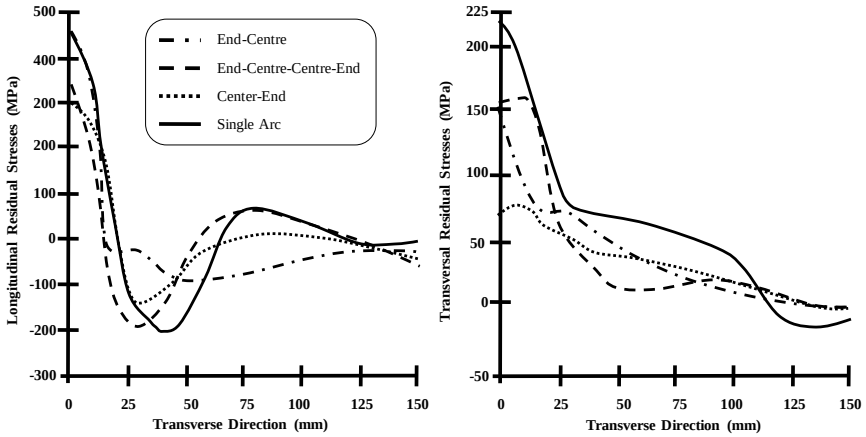

Figure 3-16 Calculated longitudinal (left) and transversal (right) stresses at the weld centre line for the welding sequences shown in **Figure 3-15** [Prasad 1997].

3.2.2 Shrinkage Moment Minimisation

A prerequisite to minimise bending distortion is to minimise the effective shrinkage moment M_{eff}. If the centre of all acting shrinkage moments coincides with the neutral point of the structure N_y, the effective bending moment is zero. As shown in **Figure 3-17**, this could be achieved by welding an additional flange on top of the T-Joint. With reference to **subsection 2.3.4**, in the present example, the bending moment for a leg length b of 6 mm acts at

$$y_{BM} = t + b_{eff} = t + \frac{1}{3} \cdot b \,, \qquad \textbf{Eq. 3-1}$$

with regard to the T-Joint case study, see **subsection 1.2.1**, the bending moment can also be minimized by a reduction of the stiffener height to 41 mm. Then, the neutral axis coincides with the axis of the bending moment. However, this might be unacceptable due to the decrease in strength of the component, and its lower buckling resistance.

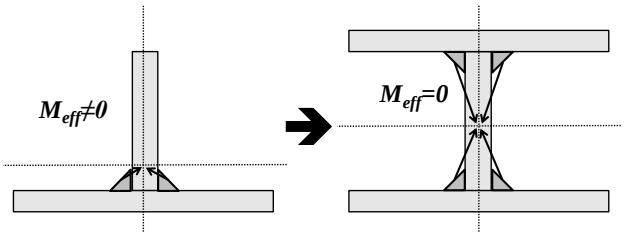

Figure 3-17 Left: Welded T-joint with effective bending moment. Right: T-joint with additional flange at the top and zero shrinkage moment.

3.2.3 Annealing

Heat treatment, *e.g.* annealing, is often used for stress relaxation after welding [Josefson 1983, Provost 1981]. **Figure 3-18** shows a sketch of the temperature history applied for annealing. The process can be divided into a number of sequences. First, the temperature is increased at a certain rate. During the holding level, the temperature is kept constant for a specific time, *e.g.* a couple of hours. At the end, the component is finally cooled down to room temperature. Heating yields a reduction of the temperature-dependent yield limit due to dislocation activation. Then, the stress in the material becomes higher than the yield stress and the material begins to deform plastically which reduces the final stresses. Heating and cooling has to be slow enough in order to yield an almost constant temperature within the material in order to avoid additional stresses due to temperature gradients. According to Radaj [Radaj 1988], it is possible to reduce the residual stresses to about 15 % of the initial stresses. However, it is concluded by Häpple [Häpple 2006] that the residual stresses can only be reduced as low as the yield stress at the heating temperature. Hence, for a significant reduction, the holding temperature $T_{Holding}$ must be higher than 400 °C for the stainless steel grade 316L (compare to **subsection 2.2.1**).

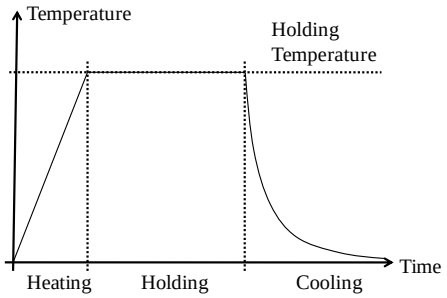

Figure 3-18 Sketch of the temperature history applied to the welded structure in an annealing process.

Post-welding heat treatment (PWHT) has been performed by Berglund et al. [Berglund 2001] for an aerospace component where the welding residual stresses were reduced by 80 %. A successful application of annealing for a reduction of residual stresses

has been presented by Abed et al. [Abed 2008] for laser formed steel plates where it was reported that residual stresses are relieved while the shape does not change. Huang et al. [Huang 1997] reported results for PWHT of electron beam welded SAE 4130 butt-joints. Most of the residual stresses were relieved at a holding temperature of 530 °C and a holding time of approximately two hours. It has also been mentioned that the maximum hardness should be below 450 HV for this steel grade in order to ensure ductile fracture and to avoid brittle fracture. Den Uijl [DenUijl 2007] reported that a hardness reduction can be obtained using tempering of the martensite into soft ferrite.

The effect of annealing has been simulated using the 3-bar model and a maximum temperature T_{Max} of 700 °C, see **Figure 3-19**. The workpiece heats up which leads to a softening of the material and hence, plastic deformation. Here, the longitudinal residual stresses are reduced by about 15%. This is much less than reported in the literature; however, the simple model does not incorporate phase transformation effects.

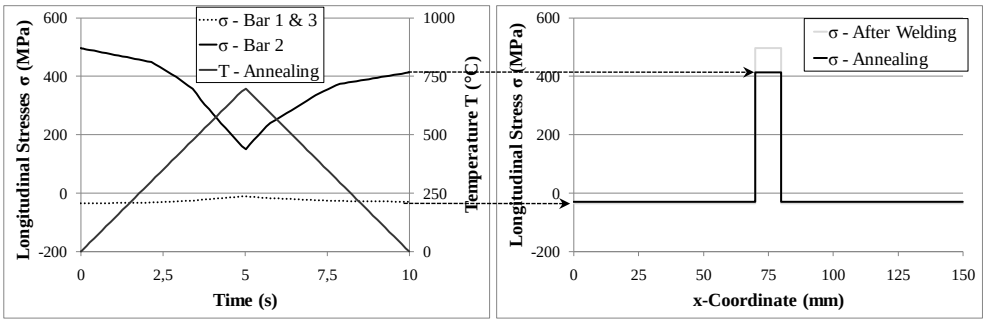

Figure 3-19 Stress development during annealing using the 3-bar model.

3.2.4 Predeformation / Prestraining

Prewelding distortion mitigation is applied widely in industry. **Figure 3-20** shows an example of the predeformation of a railcar body. The predeformation is done using hydraulic cylinders.

The name refers to a predistortion before welding in order to compensate for the distortion occurring during welding. In general, the amount of predistortion required to produce the desired result is evaluated experimentally. These methods can be subdivided into two categories:

- Predeformation – The workpiece is constructed with some pre-deformation; *i.e.*, deviant from the target state, to incorporate welding distortion in a way that the welded workpiece possesses the target geometry.
- Prestraining – The workpiece is clamped with restraints incorporating the expected welding distortion in a way that the welded workpiece possesses the target geometry after release of the clamps.

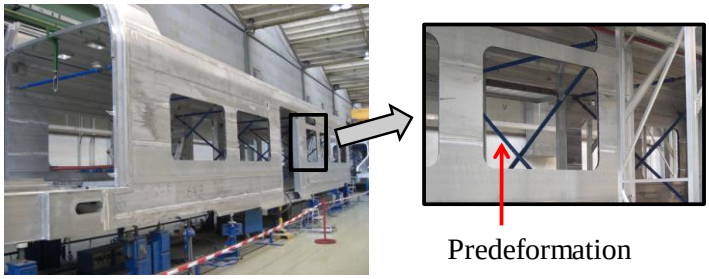

Figure 3-20 Predeformation of a railcar body.

Lists of examples can be found in [Masubuchi 1980]. Some newer examples and estimations for presetting forces are given in [Mandal 2004]. The pre-deformation technique is one which has been adopted widely in industry [Qiao 1996, Sagalevich 1974]. The weld shrinkage is compensated by an adequate amount of deviation to the geometry tolerances in the initial geometry. After welding, the component assumes its correct position and maintains its geometrical integrity.

Two examples for prestraining of a T-Joint are shown in **Figure 3-21**. If a suitable amount of plastic prebending is used, a fillet weld is obtained without any angular distortion. In elastic prestraining (see the right side of the Figure), a restraining jig is required. This could simply be a bar placed under the weld and the plate clamped in a jig. The advantage of the elastic restraining using clamps is that the resulting distortion is always smaller if a clamping system is applied compared to free distortion. Formulas are given for estimations of the prebending required for simple geometries by [Masubuchi 1980]. Prestraining has also been applied by Conrardy et al. [Conrardy 1997, Conrardy 2006] in order to reduce the amount of angular distortion in T-Joints.

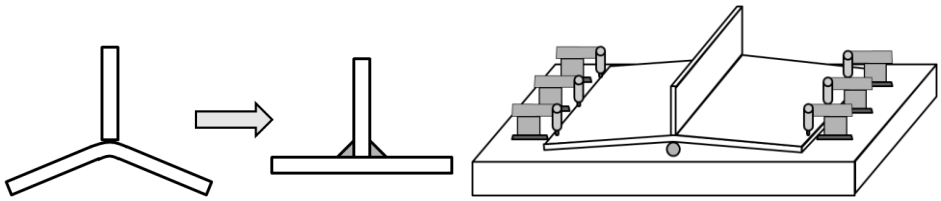

Figure 3-21 Sketch of plastic prebending (left) and elastic presetting (right) [Masubuchi 1980].

3.3 Influence of Clamping & Restraints

This section deals with the influence of clamping and restraints on the residual stresses and deformations of welded structures. Clamps and restraints are present in almost all industrial welding applications and, as will be shown, their influence can be significant.

There is considerable literature available about the influence of restraints on the residual stresses and the cracking susceptibility. Conversely, there is only little literature available dealing with the influence of clamping restraints on distortion in general, and as distortion mitigation technique in particular. The first publications date back to the 1950s

[Watanabe 1955] [Watanabe 1961]. Here, it is mentioned that the two most important factors determining welding distortion are the factors relating to welding power and factors relating to external restraints. Empirical formulas are presented to determine the influence of restraints on welding distortion by a factor F_c:

$$\text{Distortion under external restraint} = \text{Distortion in unrestrained joint} \cdot F_c \qquad \textbf{Eq. 3-2}$$

In order to investigate the potential of minimizing distortion by intelligent clamping, it is interesting to see whether there is enough time to apply such clamping systems. Results reported by Staubach et al. [Staubach 2006] for a stainless steel indicate that the time until final welding distortion is reached can be minutes for two steel beams welded together by four welds, as shown in **Figure 3-22**. The time required to obtain 40% of the final distortion takes about five minutes, for 80 % the time is about ten minutes.

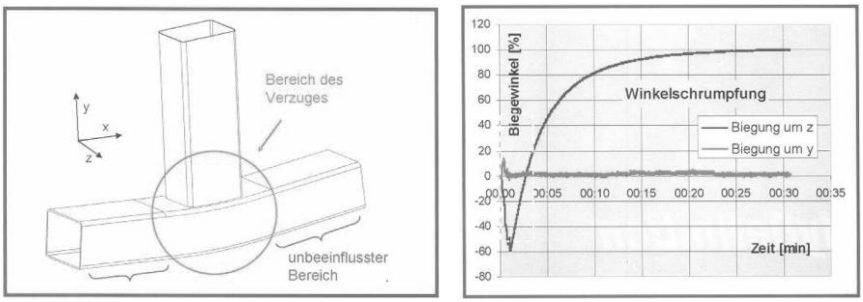

Figure 3-22 Welding of a T-joint by four welds (left) and angular distortion angle for two different directions as function of time for welding of T-joints [Staubach 2006].

3.3.1 Thermal Influence

There is a thermal coupling between the clamps and the workpiece. If the thermal influence of the clamping system is to be considered, the gap conductance between clamp and material has to be included. The equation to be applied reads

$$\frac{dQ_h}{dt} = k \cdot A \cdot (T - T_{Clamp}), \qquad \textbf{Eq. 3-3}$$

where k and T_{Clamp} are the heat transfer coefficient between two solids and the temperature of the clamp, respectively. Numerical predictions performed by Schwenk [Schwenk 2005] presented results for a case study where the cooling rate is increased by a factor of two. Van der Aa [Aa 2007] applied a contact transmission coefficient k of 50 W/m^{2}K. However, the contact conductance is neglected in most works, even in recent publications, *e.g.* [Böllinghaus 2005, Wei 2005, Roehren 2006, Ferro 2006, Pilipenko 2001, Pietzsch 2000]. Jung [Jung 2004], for instance, assumed that the influence of the clamps on the temperature field would be negligible. Song et al. [Song 2004] argued that the residual

stress field should not be affected by the faster cooling due to clamps. However, this assumption has not been backed up by experiments.

Figure 3-23 shows a simple beam model to investigate the effect of the contact conductance. The geometry has been chosen to be similar to the geometry of the T-Joint case study. The specific heat is set to 500 J kg^{-1} K^{-1}, the heat conductivity to 50 W m^{-1} K^{-1}, the convection to 5 W m^{-2} K^{-1}, and the contact conduction to 100 W m^{-2} K^{-1}. These values correspond to the values determined experimentally within the present work (see **chapter 5**). In the beginning; *i.e.*, at time t =0s, the right edge possess a temperature of 1500 °C. The temperature of the clamp remains at room temperature during the whole simulation. The temperature distribution in the beam was calculated using a 2D FE model and the temperatures were evaluated at four points in the centre of the beam, as shown in the figure.

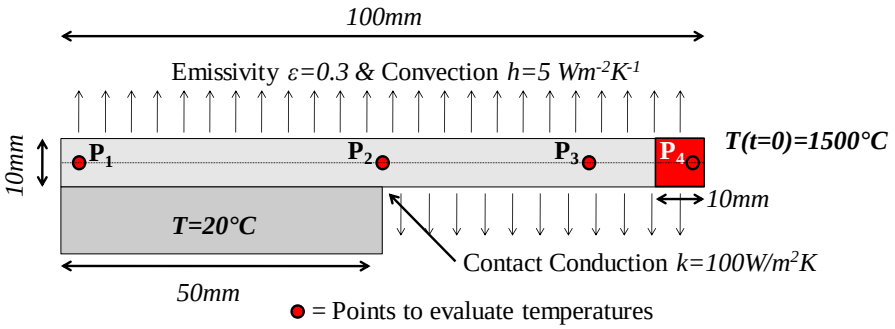

Figure 3-23 Simple model to investigate the effect of contact conductance. The three points indicate the positions where the temperatures are evaluated.

The results of the calculation are shown in **Figure 3-24** for all four points, with and without contact conductance. The cooling rate is much higher if contact conduction is included in the model. The maximum temperature in the workpiece, thousand seconds after welding is about 130 °C in the unclamped and 70 °C in the clamped state, respectively. In particular, the maximum temperature reached in the workpiece close to the clamps is reduced. This might lead to a stiffer behaviour of the base material and affect plastic deformation at the weld seam and the adjacent heat affected zone. It will be shown in **section 5.1** that these results are quite realistic. However, it should be noted that these results are strongly dependent on the dimensions of the workpiece, in particular the distance of the clamp to the weld, and the heat input.

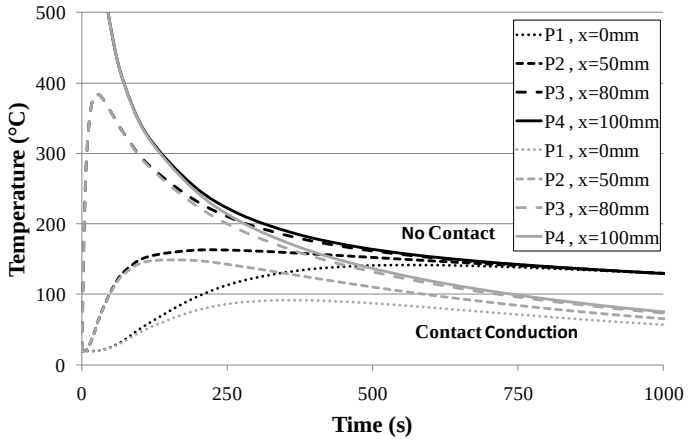

Figure 3-24 Calculated transient temperatures for the four points shown **Figure 3-23** with and without contact conductance. The solid line represents the results without contact and the dashed line with contact conduction, respectively.

3.3.2 Mechanical Reaction

The influence of the distance of the clamps as well as the release time after welding to the weld seam has been investigated by Roeren et al. [Roeren 2006]. **Figure 3-25** shows the results for different clamping distances. The closer the clamps are situated to the weld seam, the smaller the distortion of the structure. The part under investigation is an overlap joint which is often applied in automotive industries. Also the influence of the release time has been analyzed numerically, although no experimental verification was reported. If the system is clamped outside the heat-affected-zone, the release time seems to have no influence. This is in contradiction to the results presented in **chapter 6**, where it is shown that the release time has a significant influence on the residual welding distortion.

Similar results for angular distortions of 6mm GMA bead-on-plate welds have been presented by Liu and Zhang [Liu 2009] and Jung [Jung 2003]. It is shown that the amount of angular distortion after clamp release is reduced by increased clamping forces. However, there is always some distortion remaining; it is not possible to reduce angular distortion to zero.

The influence of the clamping position; *i.e.*, the mechanical constraints, on the welding distortion has been analyzed by Abid and Siddique [Abid 2005] for single "V" GTA butt-welds of 100 mm diameter low carbon steel. The boundary conditions have been modelled by contact pairs instead of applying constraints directly to the structure to be welded. It is concluded that the lateral shrinkage can be reduced significantly with the application of bolting constraints during welding of pipe flange joints. However, the boundary conditions have not been removed after welding. Similar results have been reported by Watanabe and Satoh [Watanabe 1961] for angular distortion in restrained structures.

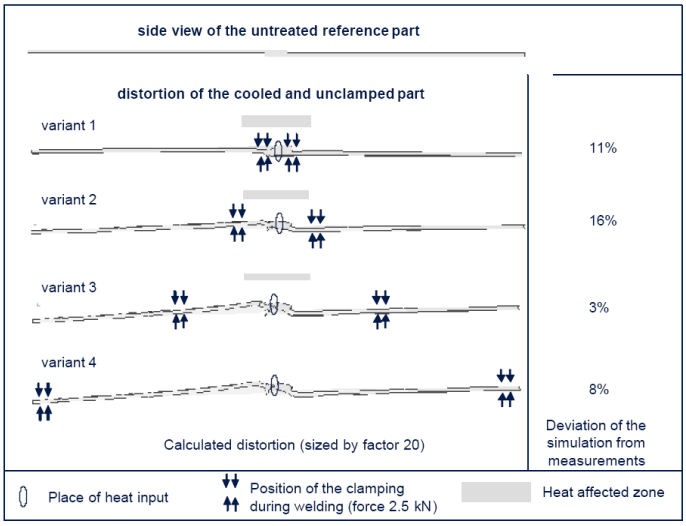

Figure 3-25 Influence of the clamping distance on the distortion after welding [Roeren 2006].

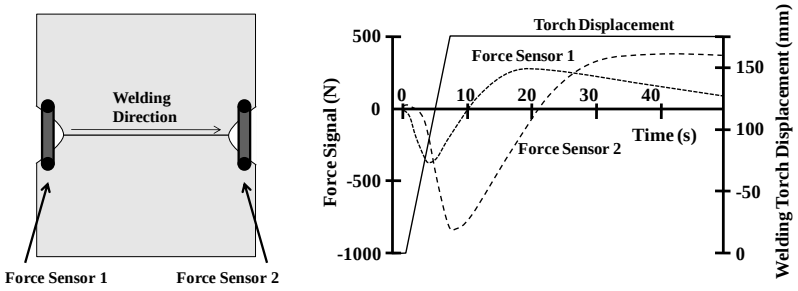

Figure 3-26 Measurement of the transient clamping force in transversal direction [Boldt 2004].

The clamping force has been measured by Boldt [Boldt 2004] for a laser welded St50 overlap joint using a hydraulic system. This allows the adjustment of the initial clamping force as well as an observation of the change of force during welding. **Figure 3-26** shows a sketch of the experimental arrangement as well as the force measured on the force sensors; tensile forces possess a negative sign. The force sensor is subjected firstly to tension when the material is welded, *e.g.* at the start of the welding at sensor 1 and at the end of the welding at sensor 2. After thermal expansion and plastic compression, the material contracts in the longitudinal direction after welding. This can be seen by the asymptotic compressive forces after welding. As can be seen, this process takes much longer than the actual welding procedure due to the inhomogeneous heat distribution and cooling after welding.

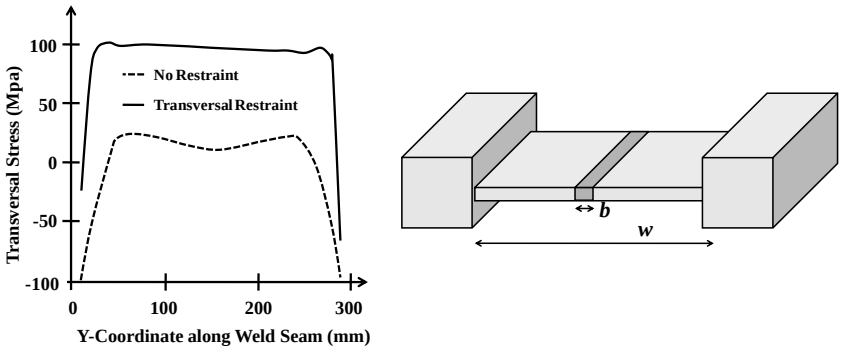

Figure 3-27 Left: Effect of mechanical constraint on transversal stresses at the weld seam. [Teng 1998]. Right: Conceptual model to explain the increase of the stresses in the clamped state [Dilthey 1995].

The maximum reaction force of the clamps has also been determined experimentally by Lenz [Lenz 2001] for various welding speeds and a penetration depth of about fifty percent of the workpiece thickness. For low welding speeds, there is full penetration and no out-of-plane bending distortion (buckling might occur) since the bending moment is zero (see **subsection 2.3.4**), while for very high welding speeds there is no shrinkage. This effect has also been found by Wahab et al. [Wahab 2006].

The effect of the transverse boundaries on the transverse residual stress in the restrained state has been investigated by Teng and Lin [Teng 1998]. The boundary conditions lead to an increase of the stresses, see **Figure 3-27**. Similar results have been found by Legatt [Legatt 1986]. This can be explained using a simple shrinkage volume model [Dilthey 1995]. If the sample width is given by *w* and the width of the weld seam by b, the corresponding increase in transverse residual stresses $\Delta\sigma$ in the clamped state is:

$$\Delta\sigma = E \cdot \Delta b / w \,,\; \Delta b = b \cdot \alpha \cdot T_M \,, \qquad \textbf{Eq. 3-4}$$

where α is the coefficient of thermal expansion and T_M the melting temperature, respectively. The influence of these kinds of boundary conditions on the longitudinal stress distribution has been reported by Prasad and Srinivasan [Prasad 1997]. After release of the restraining conditions, the internal stresses relax into a residual condition, *e.g.* [Zhu 2003].

Roeren [Roeren 2005] also shows that the application of springs as clamp elements leads to more accurate results than simply fixing the displacement of clamped nodes. The application of spring elements as clamps is a common approach employed for welding simulations, *e.g.* [Aa 2007, Lenz 2001].

3.3.3 Simple Conceptual Models

In order to investigate the effect of clamping on welding distortion, the conceptual models for buckling; *i.e.*, the 3-bar model, and the angular distortion model are applied. The modified boundary conditions to incorporate the effect of clamping are shown in

Figure 3-28. In case of the angular distortion model, the out-of-plane deformation is restricted at the outsides while in the case of the 3-bar model, the longitudinal deformation is restricted. The boundary conditions are released after completion of the welding process; *i.e.*, after the sample cooled down to room temperature.

Angular distortion has been reduced by one third using this model. However, no significant reductions of the residual stresses have been observed for the 3-bar model. The 3-bar model assumes that the base material does not heat up at all. In reality, see also **Figure 3-24**, there might be a significant heating of the base material. Hence, the simple 3-bar model overestimates the stiffness of the base material and assumes a more inhomogeneous temperature distribution than occurs in reality. This creates high plastic deformations and lower residual stresses. In order to resolve this oversimplification, the 3-bar model has been modified as shown in **Figure 3-29**. Here, it is assumed that the base material; *i.e.*, the outer bars, heat up as well; the assumed maximum temperature is 200 °C. Using this model, the residual stresses are reduced by one third due to clamping.

Based on the results in the present work, an improved bar model will be presented in **subsection 6.1.3**.

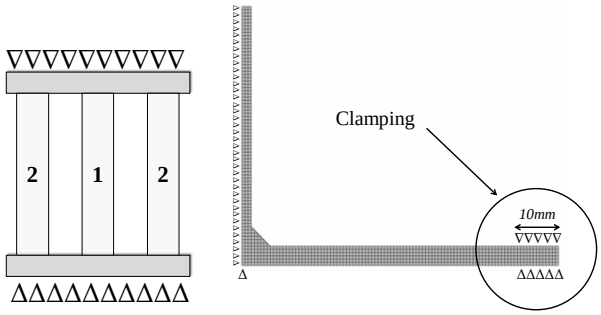

Figure 3-28 Boundaries applied for the 3-Bar model (left) and the angular distortion model (right) in order to simulate the effect of clamping.

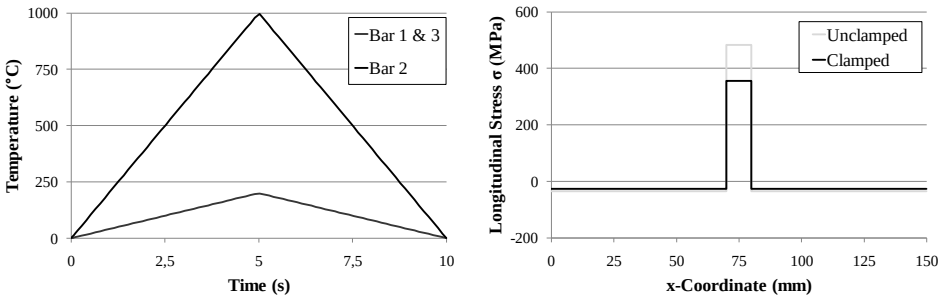

Figure 3-29 Temperature distribution (left) and residual stresses (right) using the modified 3-Bar model.

3.4 Concluding Remarks

In this chapter, an overview has been given of various welding distortion mitigation techniques and their applicability has been demonstrated for simple shrinkage and bar models. Even though most mitigation techniques presented have been proven to be successful in the literature for some case studies, their applications are usually accompanied by increased production time and costs and new process parameters must be optimized. Annealing, for instance, increases the production time significantly. Some methods are also environmentally unfriendly due to an involved heating procedure, *e.g.* for thermal tensioning or LSND-welding. The applicability of some techniques is also dependent on geometrical issues. While for instance straightening and tensioning techniques are suitable in the ship building industry due to the large panel size to be welded, the accessibility to apply these techniques is restricted for automotive applications.

Clamping is almost always present within production and relatively easy to modify. Hence, its optimisation does not necessarily introduce further significant production costs. However, even though there is considerable literature available about the influence of restraints on the residual stresses and the cracking susceptibility, there is only little literature available dealing with the influence of clamping restraints on distortion in general, and as distortion mitigation technique in particular. Several questions still remain to be addressed including:

- To what extent the material is affected by the clamping mechanism; *i.e.*, how the material's response is modified compared to unclamped conditions.
- How the interaction between workpiece and clamping system can be described. Does the workpiece also affects the clamping system and how is that interaction dependent on the clamping parameters?
- To what extent clamping can influence welding distortion. Does clamping worsen the distortion problem, or is it possible to eliminate welding distortion by smart clamping? How should clamping parameters for optimum welding distortion mitigation be determined?
- What accuracy is required for the numerical clamping models. Is it possible to apply simplified models; *i.e.*, springs, or is it required to model detailed contact with friction and thermal contact?

In the present work, the influence of the clamping system on welding distortion is investigated and these issues are explored for the selected case studies.

3.4 Concluding Remarks

4 Experimental & Numerical Arrangement

In this chapter, the experimental and numerical arrangements which are used within the present thesis in order to perform the welding experiments and simulations are described. The first section presents the welding and measurement configuration. In **section 4.2**, the numerical scheme is described; this includes the numerical implementations in the finite element package ABAQUS. In **section 4.3**, the model parameters and the FE mesh employed in the simulations are presented.

4.1 Experimental Setup

Welding of the case studies has been performed using gas metal arc welding (GMAW). **Figure 4-1** shows the clamping table and the experimental configuration, mounted on a linear traverse which moves in the y-direction; *i.e.*, along the weld seam. The welding torches can move in z-direction; *i.e.*, up and down, and in the x-direction, transverse to the weld seam. For the welding experiments, the welding torches are placed in position and fixed. The clamping table moves during welding with a predefined welding speed.

The workpiece is held in place using hydraulic clamps (described in detail in the next section). The welding process, including starting and stopping, clamp activation and releasing, and the measurement of the clamping pressure, was controlled using LabVIEW based software in combination with a data acquisition card (National Instruments NI USB6251). It has been noted that there is a latency of the motion control system of approximately 1.2 s which has been taken into account in the software.

The DP600 was delivered with a zinc coating on both sides with a thickness of approximately 10 µm. This coating was removed in the region of the weld seam using hydrochloric acid (HCl). The S355 was delivered with a primer coating which was removed in the region of the weld by surface grinding. See also **subsection 1.2.1** for more information.

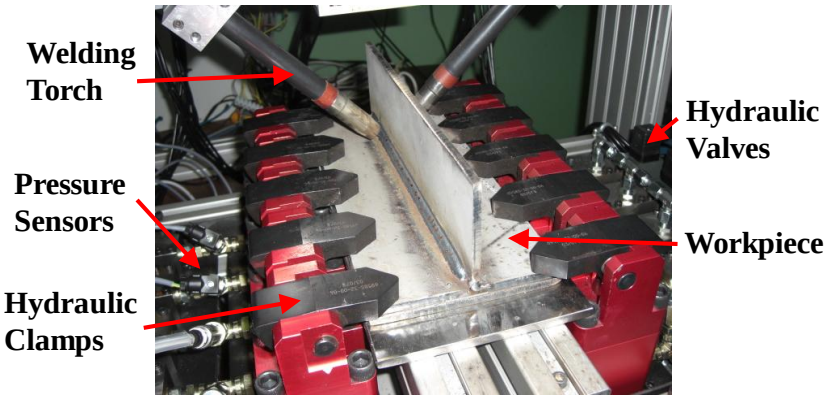

Figure 4-1 Experimental setup after welding of a T-joint.

4.1.1 Clamping System

The workpiece to be welded is placed in the centre of the clamping assembly with five vertical hydraulic clamps (AMF 6958SU-16) at each side of the specimen. **Figure 4-2** shows a flow chart for the hydraulic clamping system. Pressure is supplied by an air operated hydraulic pump (AMF 6904-20) which requires at least five bar air pressure. The maximum oil pressure allowed at the clamp is 150 bar which corresponds to an effective clamping force of 4.8 kN; *i.e.*, 490 kg. The force-pressure ratio F/p is 32 N/bar. In order to control the oil pressure, a pressure valve (AMF 6917-1) is connected between the pump and the clamps. The clamps are controlled by an electrical valve (AMF 6910-06-04) which permits control of clamping and release times for each clamp.

Assuming a stiffness of the oil reservoir of $E = 3 \cdot K_{oil}$, where K_{oil} is about 2GPa, the stiffness of the clamping system is 20 kN/mm. The backing clamp material below the workpiece is a standard structural steel. In the case of the T-joint, the web plate was not clamped but tack welded to the bottom plate.

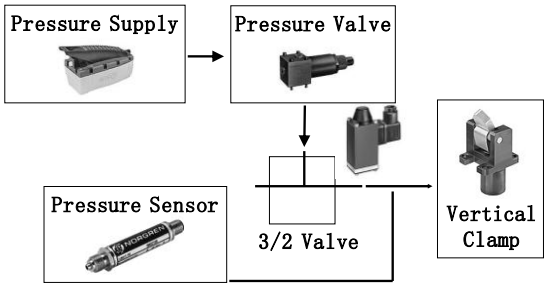

Figure 4-2 Flow chart of the hydraulic clamping system.

In the reference configuration, the oil pressure was set to 12-15 bar, which corresponds to a clamping force of 380-480 N. **Figure 4-3** shows the clamping pressure development prior to welding. At the beginning, the clamping pressure reduces rapidly to an asymptotic value. This decrease is due to heating of the oil on pressurizing and subsequent cooling to room temperature. This cooling leads to some volumetric contraction which reduces the clamping pressure. The final clamping pressure is reached after approximately three hundred seconds. One clamp (Clamp 5) shows some leakage of the oil pressure. The repeatability is ± 1.5 bar.

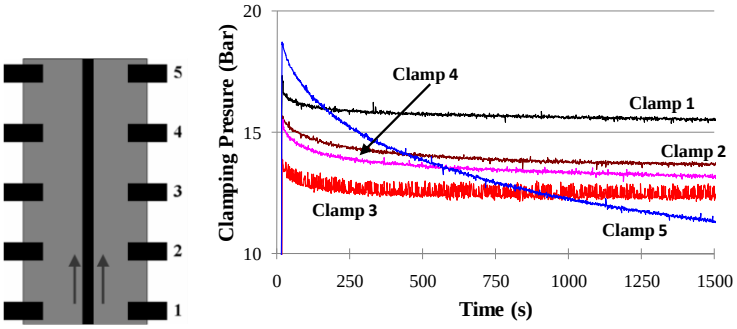

Figure 4-3 Transient clamping pressure prior to welding.

4.1.2 Welding Conditions

Welding was performed using two Cloos Quinto 503 welding machines. The welding conditions applied for the case studies are listed in **Table 4-1**.

Table 4-1 Welding conditions for the case studies.

Material	**DP600**	**S355**
Configuration	Overlap	T-Joint
Metal Transfer	Short Circuit / Dip	
Material Thickness	1 mm	6 mm
Shielding Gas	Ar + 10% CO_2	
Gas Flow	10-15 l $min.^{-1}$	
Welding Speed	8 mm s^{-1}	4 mm s^{-1}
Voltage	17 V	25 V (x2)
Current	90 A	190 A (x2)
Power	1530 W	4750 W (x2)
Energy / Length	190 J mm^{-1}	1190 Jmm^{-1} (x2)
Filler Material	SG2 (DIN)	ER70S-6 (AWS)
Filler Thickness	1 mm	1.2 mm
Feeding Rate	3 m $min.^{-1}$	5 m $min.^{-1}$
Filler Section	4.9 mm^2	23.6 mm^2

4.1.3 Distortion Measurement

Distortion measurements were performed using a linear variable displacement transducer sensor (LVDT Waycon SM series). **Table 4-2** lists the properties of the LVDT, which was mounted at the position of the welding torches. The measurement has been performed using LabView software.

Table 4-2 LVDT properties.

Type	Waycon SM 25-T
Range	0-25 mm
Repeatability	1.5 µm
Linearity	0.3 %

The supplier provided calibration measurements of the linearity for each LVDT which was within the defined range. During the measurement, however, a very strong superposed noise signal with a sinusoidal frequency of $\upsilon \approx 3$ kHz was observed as shown in **Figure 4-4**. Unfortunately, it was found that the origin of this noise is somewhere in the laboratory environment and not due to the power supply or the measurement system. Hence, it was not possible to eliminate it. In order to obtain a clear signal, the signal was measured over a time period of a hundred milliseconds and subsequently, a low-pass filter was applied in the LabView software with a cut-off frequency of $\upsilon_{Cut} \leq 1$ kHz, as shown in the figure. Finally, the last ten percent of the filtered signal have then been averaged and applied as distortion output.

In order to assess the absolute values of the LVDT signal, measurements were performed for various known sheet thicknesses. **Figure 4-5** shows the results. The repeatability was determined to be of the order ± 2 µm. There is a good agreement between the assumed sheet thicknesses and the measurements. However, it should be noted that the real sheet thicknesses also vary from the nominal values.

Calibration measurements were performed in order to assess the accuracy of the measurement system. **Figure 4-6** shows the results for a plate with a width and length of both 100 mm. The roughness R_V of the plate has been estimated to be 10 µm using a dial gauge with an accuracy of ±1 µm.

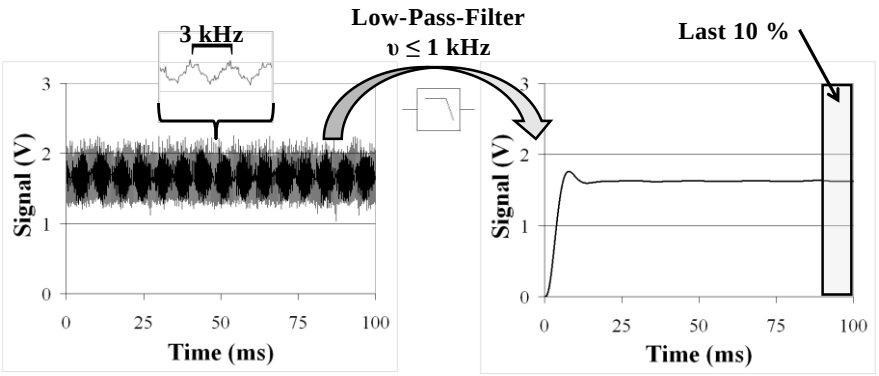

Figure 4-4 LVDT Signal: Low-Pass Filtering.

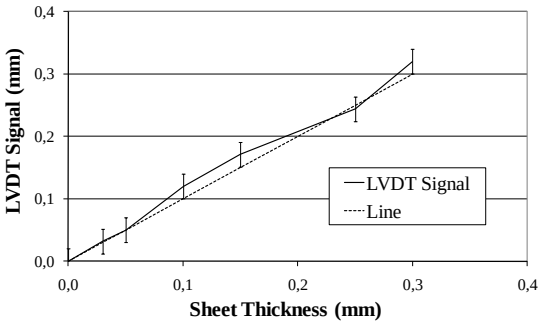

Figure 4-5 LVDT Signal: Measured absolute values.

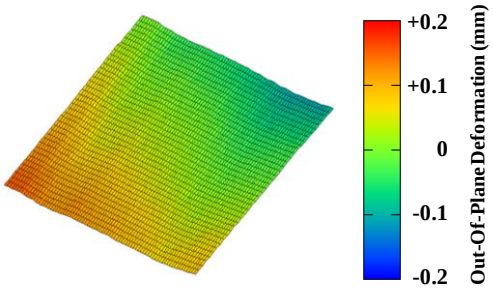

Figure 4-6 LVDT out-of-plane measurement for the calibration plate.

It has been noted that the linear motion system is twisted. The twisting in both x- and y-direction is approximately 10^{-3} degrees. This sounds very small but might cause wrong distortion measurements in the order of 0.4 mm along the plate in the present example. It can be seen later for the S355 T-Joint that this can be in the order of magnitude of the welding distortion.

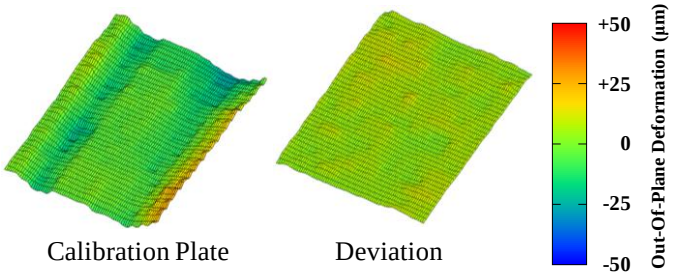

Figure 4-7 Mounted LVDT measurement for the calibration plate.

In order to eliminate the effect of the twisting on the distortion measurements, the measurement data is transformed linearly such that three corners possess zero distortion. This corresponds to a mounting at three edge points which is also performed in the

simulations. **Figure 4-7** shows the results of this mounting and the standard deviation after three repetitions. The maximum deviation is 10 µm and the average deviation is 5 µm.

4.2 Transient Thermomechanical-Metallurgical Model

In this section, the implementation of a thermomechanical-metallurgical model is presented. This model has been applied within the present work to perform the FE simulations. While the evolution equations have been presented in **section 4.1**, this section described the computational framework for the numerical implementation. The model has been implemented in ABAQUS [ABAQUS] using various subroutines:

- UMAT: Thermomechanical-metallurgical model
- DFLUX: Goldak's heat source
- FILM: Heat convection and radiation to the environment
- GAPCON: Contact heat conduction

4.2.1 Flow Chart

Figure 1-5 shows a flow chart of the simulations. Firstly, the transient temperature field is calculated using the heat source and thermal boundaries such as radiation, convection, and contact conduction. The material behaviour is temperature-dependent and hence, affected by the temperature field. Using the temperature changes and heating / cooling rates in the workpiece, the microstructure changes are calculated. The mechanical reaction of the workpiece is determined based on the temperature-dependent material behaviour, thermal strains, phase strains, and outer boundaries, *e.g.* clamping and mounting. Finally, residual stresses and distortions are calculated.

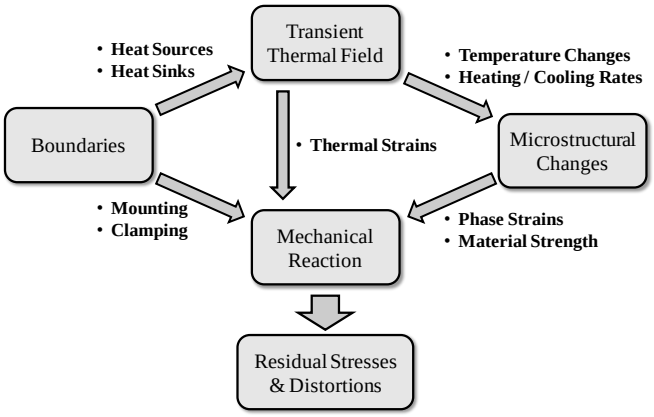

Figure 4-8 Flow chart of the simulation.

4.2.2 Finite Element Framework

In order to perform the welding simulations, the finite element method (FEM) has been employed [Belytschko 2001], which is a numerical technique for finding approximate solutions of partial differential equations (PDE) within a volume $\Omega \subset R^3$, and boundaries $\partial\Omega = \Gamma$ with given Neumann (on Γ_N) or Dirichlet (on Γ_D) conditions and $\Gamma = \Gamma_N \cup \Gamma_D$, $\phi = \Gamma_N \cap \Gamma_D$. In the present case, solutions have to be found for the transient and spatial displacement field $\vec{u}(\vec{x},t)$, temperature distribution $T(\vec{x},t)$, and internal material stress state $\boldsymbol{\sigma}(\vec{x},t)$, here defined by the Cauchy stress tensor. The differential equation considered for the calculation of the temperature field is given by the following parabolic PDE:

$$\rho \cdot c \cdot \dot{T} = \lambda \cdot \Delta T + \dot{q} \text{ on } \Omega, \qquad \textbf{Eq. 4-1}$$

$$T = g_T \text{ on } \Gamma_{D,T}, \qquad \textbf{Eq. 4-2}$$

$$\lambda_\Gamma \cdot \vec{\nabla} T \cdot \vec{n} = h_T \text{ on } \Gamma_{N,T}, \qquad \textbf{Eq. 4-3}$$

where ρ, q, c, λ, $\vec{n}$, g and h represent the density, the internal energy per unit volume, the specific heat, the heat conductivity, the outward normal on Γ, and the external Dirichlet and Neumann boundary conditions, respectively. The subscript T refers to boundary conditions on the thermal field. Boundary conditions in the case of welding simulations are heat dissipation due to clamp contacts, and heat convection $h \sim \Delta T$ and radiation to the environment $\varepsilon \sim \Delta T^4$. As explained in the next chapter, the heat input due to the welding process is modeled using $\dot{q}$.

For the structural analysis, the corresponding differential equation is given by the following hyperbolic equation:

$$\rho \cdot \ddot{\vec{u}} + k \cdot \dot{\vec{u}} = div(\boldsymbol{\sigma}) + \vec{f} \text{ on } \Omega, \qquad \textbf{Eq. 4-4}$$

$$\vec{u} = \vec{g}_u \text{ on } \Gamma_{D,u}, \qquad \textbf{Eq. 4-5}$$

$$\boldsymbol{\sigma} \cdot \vec{n} = \vec{h}_u \text{ on } \Gamma_{N,u}, \qquad \textbf{Eq. 4-6}$$

where $\vec{f}$ and k represent the internal body force and a volumetric damping factor. The damping factor is important to obtain stable simulations in case of buckling, as shown in **section 5.1**. The subscript u refers to boundary conditions of the displacement field. Here, boundary conditions describe fixing of the workpiece due to clamping.

Eq. 4-1 and **Eq. 4-4** represent the so-called strong form of the two equilibrium equations: the linear momentum principle; *i.e.*, the equation of motion, and the conservation of energy [Mase 1969]. The change of the stress distribution is coupled with the change of the temperature distribution:

$$\Delta\boldsymbol{\sigma} = \frac{\partial \underline{\underline{\mathbf{C}}}}{\partial T} \cdot \Delta T \cdot \boldsymbol{\varepsilon}^{el} + \underline{\underline{\mathbf{C}}} \cdot \frac{\partial \Delta\boldsymbol{\varepsilon}^{el}}{\partial T} \cdot \Delta T + \underline{\underline{\mathbf{C}}} \cdot \Delta\boldsymbol{\varepsilon}^{el}$$
$$\boldsymbol{\varepsilon}^{el} = \boldsymbol{\varepsilon}^{tot} - \boldsymbol{\varepsilon}^{p} - \boldsymbol{\varepsilon}^{th}, \qquad \textbf{Eq. 4-7}$$

where $\underline{\underline{\mathbf{C}}}$, $\boldsymbol{\varepsilon}^{el}$, $\boldsymbol{\varepsilon}^{p}$, and $\boldsymbol{\varepsilon}^{th}$ refer to the elastic stiffness tensor and the elastic, plastic, and thermal strains, respectively. Here, $\underline{\underline{\mathbf{X}}}$ and $\mathbf{x}$ denote a tensor of order four and two, respectively. In linear FEM, the total strain is calculated from the displacement field $\vec{u}$ using:

$$\boldsymbol{\varepsilon}^{tot} = \frac{1}{2}\left(\left(\vec{\nabla} \otimes \vec{u}\right) + \left(\vec{\nabla} \otimes \vec{u}\right)^{T} \right). \qquad \textbf{Eq. 4-8}$$

According to *Lindgren* [Lindgren 2001a], the maximum strains reached in the material during welding accumulate up to a few percent. A short estimation gives

$$\alpha \times \Delta T = 2 \cdot 10^{-5} \frac{1}{^{\circ}C} \times 1500^{\circ}C \approx 3\%. \qquad \textbf{Eq. 4-9}$$

Hence, nonlinear; *i.e.*, finite strain, FEM must be employed. The strain tensor is calculated via the deformation gradient **F** given by:

$$\mathbf{F} = \mathbf{1} + \nabla \times \vec{u} = \mathbf{1} + \mathbf{B} \cdot \vec{u}, \qquad \textbf{Eq. 4-10}$$

where the finite element discretisation allows a transformation of the curl operator into a linear equation system using the so-called B-matrix **B**. Using the polar decomposition theorem [Hoger 1984], the deformation gradient **F** can be decomposed into an orthogonal tensor **R** describing the rotation of the material and a positive definite symmetric tensor **U** describing the deformation:

$$\mathbf{F} = \mathbf{R} \cdot \mathbf{U}. \qquad \textbf{Eq. 4-11}$$

Finally, the total strain tensor $\boldsymbol{\varepsilon}^{tot}$ is obtained from **U** using a Padé approximation [Higham 2000] of the logarithm of the displacement tensor [Weber 1988]:

$$\boldsymbol{\varepsilon}^{tot} = \ln(\mathbf{U}) \approx 2 \cdot (\mathbf{U} - \mathbf{1}) \cdot (\mathbf{U} + \mathbf{1})^{-1}. \qquad \textbf{Eq. 4-12}$$

The thermal strains are calculated using the coefficient of thermal expansion α^{T}:

$$\boldsymbol{\varepsilon}^{th} = \left(\alpha^{T} + \frac{\partial \alpha^{T}}{\partial T} \cdot \Delta T \right) \cdot \Delta T \cdot \mathbf{1}. \qquad \textbf{Eq. 4-13}$$

In general, the thermal calculation is also affected by mechanical changes, *e.g.* due to the dissipation energy of plastic deformation. According to Pietzsch [Pietzsch 2000] this influence is about four orders of magnitude lower than the heat input due to welding and commonly neglected in welding simulations, see [Aa 2007, Murthy 1996]. Using the finite element method, the volume is discretized into non-overlapping elements defined by *n*

nodes in order to solve the system of PDEs. For the discretisation, test functions $\vec{v}_u$, v_T, and the displacement functions $\vec{u}$ and temperature functions *T* are introduced:

$$\vec{v}_u(\vec{x}) = \sum_{i=1}^{n} N_i(\vec{x}) \cdot \vec{v}_{ui} \ , \ v_T(\vec{x}) = \sum_{i=1}^{n} N_i(\vec{x}) \cdot \vec{v}_{Ti} \ , \qquad \textbf{Eq. 4-14}$$

$$\vec{u}(\vec{x}) = \sum_{i=1}^{n} N_i(\vec{x}) \cdot \vec{u}_i \ , \ T(\vec{x}) = \sum_{i=1}^{n} N_i(\vec{x}) \cdot T_i \ , \qquad \textbf{Eq. 4-15}$$

where $\vec{v}_u = (\vec{v}_{u1},\ldots,\vec{v}_{un})$, $\vec{v}_T = (v_{T1},\ldots,v_{Tn})$, $\vec{u} = (\vec{u}_1,\ldots,\vec{u}_n)$ and $\vec{T} = (T_1,\ldots,T_n)$ are the corresponding vectors of nodal values and $N_i(\vec{x}_j) = \delta_{ij}$ are shape functions. In FEM, the so-called weak form of the PDEs is solved rather than the strong form. **Eq. 4-1** and **Eq. 4-4** can be rewritten into the weak form according to [Hughes 1987]:

$$(v_T, \rho c\dot{T}) + a(v_T, T) = (v_T, \dot{q}) + (v_T, h_T)_{\Gamma_{N,T}} \ , \qquad \textbf{Eq. 4-16}$$

$$(\vec{v}_u, \rho\ddot{\vec{u}}) + (\vec{v}_u, a\rho\dot{\vec{u}}) + a(\vec{v}_u, \vec{u}) = (\vec{v}_u, \vec{f}) + (\vec{v}_u, \vec{h}_T)_{\Gamma_{N,u}} \ , \qquad \textbf{Eq. 4-17}$$

where

$$(X,Y) = \int_{\Omega} X(\vec{x}) \cdot Y(\vec{x})\, d\Omega \ ,$$
$$a(X,Y) = \int_{\Omega} \vec{\nabla} X(\vec{x}) \cdot \vec{\nabla} Y(\vec{x})\, d\Omega \ . \qquad \textbf{Eq. 4-18}$$

Linearization of these equations yields the following algebraic systems of equations for the iterative calculation of the increments of the displacement field $\Delta\vec{u} = \vec{u}_{n+1} - \vec{u}_n$ and temperature field $\Delta\vec{T} = \vec{T}_{n+1} - \vec{T}_n$:

$$\begin{aligned} \mathbf{M} \cdot \ddot{\vec{u}} + k \cdot \dot{\vec{u}} + \mathbf{K}_u \cdot \Delta\vec{u} - \vec{g}_u &= \vec{R}_u \\ \mathbf{K}_T \cdot \Delta\vec{T} - \vec{g}_T &= \vec{R}_T \end{aligned} \ , \qquad \textbf{Eq. 4-19}$$

where **M**, $\mathbf{K}_u$, $\mathbf{K}_T$, $\vec{R}_u$ and $\vec{R}_T$ are the mass matrix, the mechanical and thermal stiffness matrix and the two residual vectors; the latter one to be minimized using a Newton-Raphson integration scheme, *e.g.* see [Simo 1998]. Here, *k* is the viscous damping factor. The boundaries are dependent on the time increment $\Delta t_{n+1}=t_n$. **Eq. 4-19** can be solved within one step only for linear isothermal elasticity; *i.e.*, $\boldsymbol{\sigma} = \underline{\mathbf{C}} \cdot \boldsymbol{\varepsilon}$ and $\boldsymbol{\varepsilon}^{tot} = \boldsymbol{\varepsilon}^{el}$.

Calculating the thermal stiffness matrix is straight-forward since a linear PDE has been chosen. The determination of the mechanical stiffness is more complicated due to the possible nonlinearity of the mechanical behaviour where the consistent material tangent **D** has to be calculated:

$$\mathbf{K}_u = \int_B \mathbf{B}^T(\vec{x}) \cdot \mathbf{D}(\vec{x}) \cdot \mathbf{B}(\vec{x})\, dB \ , \ \mathbf{D} = \partial\boldsymbol{\sigma} / \partial\boldsymbol{\varepsilon} \ . \qquad \textbf{Eq. 4-20}$$

The quality of the result is determined mainly by the shape function employed. In the present work, trilinear elements are applied with incompatible modes [Simo 1990]. This element type has been introduced to improve the bending behaviour of linear elements and to reduce shear locking, see also [Koschnick 2004]. The term incompatible is derived from the fact that additional shape functions are added internally to the elements. The values of these shape functions are not compatible at the border of adjacent elements. For these modes, Gauss integration has to be performed at the element centre in order to pass the Patch-test [Taylor 1976]. **Figure 4-9** shows the shape functions for a 2D bilinear element with unit area, including the two incompatible modes.

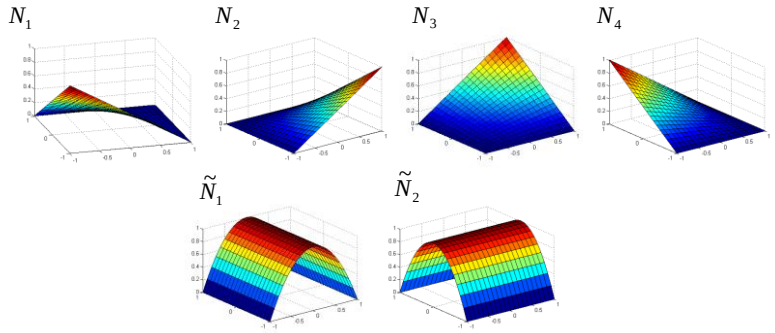

Figure 4-9 Shape functions for 2D elements with four compatible and two incompatible modes and unit area.

The element contains four nodes and the following shape functions:

$$\begin{aligned}
N_1(x,y) &= 0.25 \cdot (1-x)(1-y) \\
N_2(x,y) &= 0.25 \cdot (1+x)(1-y) \\
N_3(x,y) &= 0.25 \cdot (1+x)(1+y) \\
N_4(x,y) &= 0.25 \cdot (1-x)(1+y) \\
\tilde{N}_1(x,y) &= (1-x^2) \\
\tilde{N}_2(x,y) &= (1-y^2)
\end{aligned} \qquad \textbf{Eq. 4-21}$$

The primary effect of the incompatible modes is to eliminate the so-called parasitic shear stresses that are observed in regular displacement elements if they are loaded in bending; *i.e.*, reducing the geometrical stiffness. The total number of integration points per element is thirteen compared to eight for the standard trilinear brick and hence, the computation time is increased by about 50 %. It has been reported that incompatible mode elements perform almost as well as second-order elements in many situations if the elements have an approximately rectangular shape [ABAQUS]. This is often the case in

welding simulations, especially in the present work. Hence, whether it is necessary to employ second order elements should be verified, for instance, since the computation time increases by a factor of seven (21 c.f. 8 DOF) compared to the standard linear brick.

In FEM, for a given displacement field and boundary conditions, the strains in the material are calculated. The material response; *i.e.*, the stress $\boldsymbol{\sigma} = \boldsymbol{\sigma}(\boldsymbol{\varepsilon})$ and the material stiffness **D**, are dependent on the thermomechanical material model applied. The integration of the material model to obtain the stress and stiffness is explained in the following subsection. As mentioned in **subsection 1.3.1**, there are basically two unit systems which are commonly applied. The formulation of the FE method does not demand a specific unit systems, the only importance is that the units are consistent.

4.2.3 Model Integration

For the integration of the constitutive equations, the algorithm presented by Seifert and Schenk [Seifert 2007, Schenk 2006] is extended for the case of non-isothermal plasticity. For computational efficiency, Voigt's notation has been employed; *i.e.*, second order tensors are represented by vectors, and forth order tensors by second order tensors:

$$\begin{aligned} &\boldsymbol{\varepsilon} \rightarrow \vec{\varepsilon}^{\,T} = \left(\varepsilon_{11} \quad \varepsilon_{22} \quad \varepsilon_{33} \quad 2\varepsilon_{23} \quad 2\varepsilon_{12} \quad 2\varepsilon_{13}\right) \\ &\boldsymbol{\sigma} \rightarrow \vec{\sigma}^{\,T} = \left(\sigma_{11} \quad \sigma_{22} \quad \sigma_{33} \quad \sigma_{23} \quad \sigma_{12} \quad \sigma_{13}\right) . \\ &\underline{\mathbf{C}} \rightarrow \mathbf{C} \end{aligned} \qquad \textbf{Eq. 4-22}$$

Using this notation, the calculation of the equivalent stress, the flow direction, and the plastic strain increment can be rewritten in a vectorial form:

$$\sigma_{EQ} = \sqrt{3/2 \cdot \vec{S} \cdot \mathbf{H} \cdot \mathbf{M} \cdot \vec{S}} \,, \qquad \textbf{Eq. 4-23}$$

$$\vec{n} = \frac{\partial \phi}{\partial \vec{\sigma}} = \frac{3}{2} \cdot \frac{1}{\sigma_{EQ}} \cdot \mathbf{H} \cdot \mathbf{M} \cdot \vec{S} \,, \qquad \textbf{Eq. 4-24}$$

$$\Delta \vec{\varepsilon}^{\,pl} = \frac{\partial \phi}{\partial \vec{\sigma}} \cdot \Delta p = \vec{n} \cdot \Delta p \,, \qquad \textbf{Eq. 4-25}$$

where

$$\left(\mathbf{M}\right)_{ij} = \begin{cases} 1 \cdot \delta_{ij} \,, \{i, j \le 3\} \\ 2 \cdot \delta_{ij} \,, \textit{else} \end{cases} \qquad \textbf{Eq. 4-26}$$

is the metric transformation tensor from the stress system into the strain system in Voigt notation. It is useful to know that the transformation tensor **M** and the anisotropy tensor **H** permute; *i.e.*, $[\mathbf{H},\mathbf{M}]=\mathbf{H}\cdot\mathbf{M}-\mathbf{M}\cdot\mathbf{H}=\mathbf{0}$. The constitutive equations are rewritten by collecting constant terms and terms depending on the plastic strain and temperature, respectively:

$$\vec{Y}_{n+1} = \vec{Y}_n + \vec{N} + \vec{M} \cdot \Delta p + \vec{K} \cdot \Delta T \,. \qquad \textbf{Eq. 4-27}$$

Here, the states at the start (known) and the end (unknown) of the increment

$$\vec{Y}_{n+1} = \begin{pmatrix} \vec{\sigma}_{n+1} = \vec{\sigma}_n + \Delta\vec{\sigma} \\ \vec{\alpha}_{n+1} = \vec{\alpha}_n + \Delta\vec{\alpha} \\ R_{n+1} = R_n + \Delta R \end{pmatrix}, \; \vec{Y}_n = \begin{pmatrix} \vec{\sigma}_n \\ \vec{\alpha}_n \\ R_n \end{pmatrix} \qquad \textbf{Eq. 4-28}$$

and the abbreviations

$$\vec{N} = \begin{pmatrix} \mathbf{C} \cdot (\vec{\varepsilon}^{tot} + \Delta\vec{\varepsilon}^{tot}) \\ 0 \\ 0 \end{pmatrix}, \; \vec{M} = \begin{pmatrix} -\mathbf{C} \cdot \vec{n} \\ A_\alpha \cdot (2/3 \cdot S_\alpha \cdot \vec{n} - \vec{\alpha}) \\ A_R \cdot (S_R - R) \end{pmatrix}, \; \vec{K} = \begin{pmatrix} \dfrac{\partial \mathbf{C}}{\partial T} \cdot \vec{\varepsilon}^{el} \\ \dfrac{\vec{\alpha}}{S_\alpha} \cdot \dfrac{dS_\alpha}{dT} \\ \dfrac{R}{S_R} \cdot \dfrac{dS_R}{dT} \end{pmatrix} \qquad \textbf{Eq. 4-29}$$

have been used. The vectors $\vec{N}$, $\vec{K}$ and $\vec{M}$ are also referred to as the elastic and thermal predictor and the plastic corrector, respectively. The thermal strains depend only on the temperature increment which is assumed to be dependent on time only. Hence, they have already been subtracted from $\vec{\varepsilon}^{tot}$ for simplicity. Using this formulation, a residual can be defined as

$$\vec{G}_{n+1} = -\vec{Y}_{n+1} + \vec{Y}_n + \vec{N} + \vec{M} \cdot \Delta p + \vec{K} \cdot \Delta T = \vec{0}. \qquad \textbf{Eq. 4-30}$$

The solution of this equation can be found iteratively by applying a Newtonian scheme using a linearization of the previous equation:

$$\vec{Y}_{n+1}^{m+1} = \vec{Y}_{n+1}^{m} - \upsilon \cdot \mathbf{J}_{n+1} \cdot \vec{G}_{n+1}^{m}, \; \mathbf{J}_{n+1} = \left(\frac{\partial \vec{G}_{n+1}^{m}}{\partial \vec{Y}_{n+1}^{m}} \right), \qquad \textbf{Eq. 4-31}$$

where υ is a line-search parameter determined on the basis of the Armijo and Goldstein conditions, see [Dennis 1987]. However, experience indicates that the line-search parameter is usually not necessary for Chaboche-type models and is simply set to $\upsilon=1$.

As initial guess, the elastic predictor is applied:

$$\vec{Y}_{n+1} = \vec{Y}_n + \vec{N}. \qquad \textbf{Eq. 4-32}$$

This update rule is applied until convergence occurs. The Jacobian matrix can be calculated analytically by

$$\mathbf{J} = \left(\frac{\partial \vec{G}}{\partial \vec{Y}} \right) = -\mathbf{1} - \frac{\partial \vec{M}}{\partial \vec{Y}} + \frac{\partial \vec{N}}{\partial \vec{Y}} \cdot \Delta p + \vec{N}^T \otimes \frac{\Delta p}{\partial \vec{Y}} + \frac{\partial \vec{K}}{\partial \vec{Y}} \cdot \Delta T. \qquad \textbf{Eq. 4-33}$$

In order to calculate the Jacobian analytically, the derivative of the flow direction with respect to the stresses is required in Voigt notation:

$$\frac{\partial \vec{n}}{\partial \vec{\sigma}} = \frac{\partial}{\partial \vec{\sigma}}\left(\frac{3}{2}\cdot\frac{1}{\sigma_{EQ}}\cdot\mathbf{M}\cdot\mathbf{H}\cdot\vec{S}\right) = \frac{1}{\sigma_{EQ}}\left(\frac{3}{2}\cdot\mathbf{M}\cdot\mathbf{H}-\vec{n}^{T}\cdot\vec{n}\right). \qquad \textbf{Eq. 4-34}$$

In order to construct the global iteration matrix in FE simulations, see **Eq. 4-20**, the consistent material tangent $\mathbf{D} = \partial\boldsymbol{\sigma} / \partial\boldsymbol{\varepsilon}$ has to be calculated. This can be done easily using the Jacobian matrix at the converged state and the following identity:

$$\frac{\partial \vec{G}}{\partial \vec{\varepsilon}} = \frac{d\vec{G}}{d\vec{\varepsilon}} + \frac{d\vec{G}}{d\vec{Y}}\cdot\frac{d\vec{Y}}{d\vec{\varepsilon}} = \vec{0} \;\Rightarrow\; \frac{d\vec{Y}}{d\vec{\varepsilon}} = -\left(\frac{d\vec{G}}{d\vec{Y}}\right)^{-1}\cdot\frac{d\vec{G}}{d\vec{\varepsilon}}. \qquad \textbf{Eq. 4-35}$$

The anisotropic Hill tensor is defined by:

$$\mathbf{H} = \begin{pmatrix} G+H & -H & -G & 0 & 0 & 0 \\ -H & F+H & -F & 0 & 0 & 0 \\ -G & -F & F+G & 0 & 0 & 0 \\ 0 & 0 & 0 & 3/2L & 0 & 0 \\ 0 & 0 & 0 & 0 & 3/2M & 0 \\ 0 & 0 & 0 & 0 & 0 & 3/2N \end{pmatrix}, \qquad \textbf{Eq. 4-36}$$

where *L*, *M*, and *N* describe anisotropic plasticity due to shearing of the material. F, G, and H are correlated by

$$\begin{aligned} 2F &= \frac{1}{Y^2}+\frac{1}{Z^2}-\frac{1}{X^2} \\ 2G &= \frac{1}{Z^2}+\frac{1}{X^2}-\frac{1}{Y^2} \\ 2H &= \frac{1}{X^2}+\frac{1}{Y^2}-\frac{1}{Z^2} \end{aligned} \qquad \textbf{Eq. 4-37}$$

and *X*, *Y*, and *Z* define the dimensionless scaling factors of the yield stress in the x, y, and z direction with respect to the average yield stress, respectively. For plastic isotropy; *i.e.*, *X=Y=Z=1*, the Hill tensor simplifies to the deviatoric projection tensor:

$$\mathbf{P} = \begin{pmatrix} +2/3 & -1/3 & -1/3 & 0 & 0 & 0 \\ -1/3 & +2/3 & -1/3 & 0 & 0 & 0 \\ -1/3 & -1/3 & +2/3 & 0 & 0 & 0 \\ 0 & 0 & 0 & 1 & 0 & 0 \\ 0 & 0 & 0 & 0 & 1 & 0 \\ 0 & 0 & 0 & 0 & 0 & 1 \end{pmatrix}, \qquad \textbf{Eq. 4-38}$$

with

$$\mathbf{P} \cdot \vec{\sigma} = \mathbf{P} \cdot \vec{S} = \vec{S} \quad , \quad \mathbf{P}^2 = \mathbf{P} . \qquad \textbf{Eq. 4-39}$$

The meaning of the material parameters has been explained in **section 4.2** and is summarized in **Table 4-3**.

Table 4-3 Summary of the material parameters of the thermomechanical model and their dimensions.

Property	Dimension	Meaning
α	K^{-1}	Coefficient of thermal expansion
E	MPa	Young Modulus
ν	1	Poisson Ratio
σ_Y	MPa	Yield Stress
K	MPa·s	Viscosity Coefficient
n	1	Norton Exponent of Viscosity
A_R	1	Isotropic Hardening Exponent
S_R	MPa	Isotropic Hardening Saturation
A_α	1	Kinematic Hardening Exponent
S_α	MPa	Kinematic Hardening Saturation

4.2.4 Phase Transformation

The physical background of phase transformations has been described previously in **subsection 2.2.2**. In the present thesis, solid-solid phase transformations are modelled using CCT diagrams. In order to model phase transformations during cooling, the CCT diagram has to be parameterized.

In principle, there is a lower limit M_S below which martensite growth starts and all remaining austenite will transform to martensite (or eventually remain as retained austenite as is the case for TRIP steels), and a higher limit A_{c1} above which austenitization occurs. Formulas for the calculation of the austenite start temperature as a function of the steel composition can be taken from [Andrews 1965]. The martensite start temperature can be estimated according to [Steven 1956]. In-between these two limits, phase transformation from austenite to ferrite or bainite can occur.

The boundaries of the domains where these phases grow as functions of the temperature T and the time t can be modelled with polygons. There are algorithms to determine whether a point (T,t) is within the domain or not. In the present work, a simplified method has been implemented using an inverse parabolic approach for each phase domain:

$$\begin{aligned} T(t) &= \pm a \cdot \sqrt{t - t_0} + T_0 \ , \ t > t_0 \\ T(t) &= \min(T, T_{Up}) \quad , \\ T(t) &= \max(T, T_{Low}) \end{aligned} \qquad \textbf{Eq. 4-40}$$

where a, t_0, T_0, T_{Low}, T_{Up} are a scaling factor, the start time for the transition, an offset temperature, the lower temperature limit and the upper temperature limit for the phase, respectively. If the current state (T,t) is within the domain of any phase, this phase grows. **Figure 4-10** shows an example of such a parameterized CCT diagram. In order to

determine t_0 in simulations, it is important to track at each material point; *i.e.*, integration point in the FE grid, when the CCT diagram becomes valid.

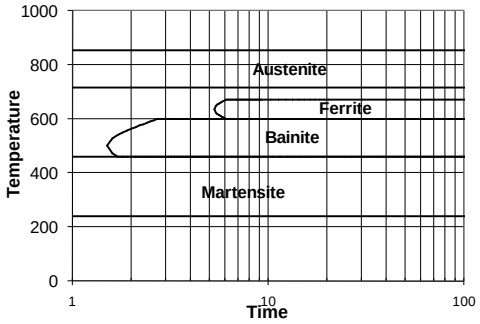

Figure 4-10 Parameterized CCT diagram.

For the diffusion-controlled solid-solid phase transformations on cooling; *i.e.*, austenite→ferrite or austenite→perlite/bainite, the equation of LeBlond is applied with $n \equiv 1$. For a constant temperature change rate, this equation can be integrated analytically to

$$P_i(T,t) = P_i^{EQ}(T)\left(1-\exp\left(\frac{-t}{\tau}\right)\right). \qquad \textbf{Eq. 4-41}$$

For any phase except austenite, the equilibrium fraction of phase *i* is set to the current fraction of phase *i* plus the austenite phase fraction: $P_i^{EQ}=P_i+P_{austenite}$. For austenite above the A_{c3} temperature, the equilibrium phase fraction is set to $P_{austenite}^{EQ}=1$. The reduced LeBlond equation can be rewritten in a differential form:

$$\dot{P}_i(T,t) = \left(\frac{\overline{P}(T)-P_i(T)}{\tau}\right), \qquad \textbf{Eq. 4-42}$$

which can be solved within each time increment using an implicit integration scheme:

$$P_i(T+\Delta T, t+\Delta t) = \frac{P_i(T,t)+P_i(T+\Delta T, t+\Delta t)\cdot \Delta t/\tau}{1+\Delta t/\tau}. \qquad \textbf{Eq. 4-43}$$

If the temperature change within one increment is above 50 K, the integration is performed with sub-increments in order to increase the accuracy of the prediction. The growth parameter τ has been set to a constant value although it is generally temperature-dependent [Murugaiyan 2006]. Its value has been determined using the small numbers in the CCT which mention the phase fraction after a certain time in the related domain.

The diffusionless transition from austenite to martensite is described by the time-independent Koistinen-Marburger equation:

$$P_M(T) = P^{EQ}\cdot\left[1-\exp\left(-b\cdot\left(M_s-T\right)\right)\right],\ T \le M_s. \qquad \textbf{Eq. 4-44}$$

Here, P^{EQ} is the initial austenite fraction on start of the martensite growth. The total phase volume V, the phase volume change ΔV and the incremental phase strain $\Delta\varepsilon^{ph}$ is determined using a linear mixing rule involving the fraction P_i of each phase i:

$$V = \sum_{i=1}^{nPhases} V_i \cdot P_i$$

$$\Delta V = \sum_{i=1}^{nPhases} V_i \cdot \Delta P_i \quad . \qquad \textbf{Eq. 4-45}$$

$$\Delta\varepsilon^{ph} = \frac{1}{3}\frac{\Delta V}{V_{Start}}$$

The initial phase volume V_{Start} is determined by the initial phase fractions. Modelling austenite growth from any other phase is more complex than the opposite case, and is in general not fully understood. There is some research ongoing to obtain a better understanding, *e.g.* [Savran 2009, Thiessen 2006, Mukherjee 2009]. Here, a temperature-dependent austenite growth has been assumed using the martensite growth parameter b. This is superposed by a time-dependent growth from ferrite and bainite using the LeBlond model.

The solid-liquid phase transformation has been modelled using a constant melting temperature $T_{Melting}$ = 1450 °C. Above this temperature, the material behaves in a purely viscous manner: The initial stress and hardening state at the start of the time increment is reset to zero and hence, the material possesses a stiffness which is dependent on the strain increment only.

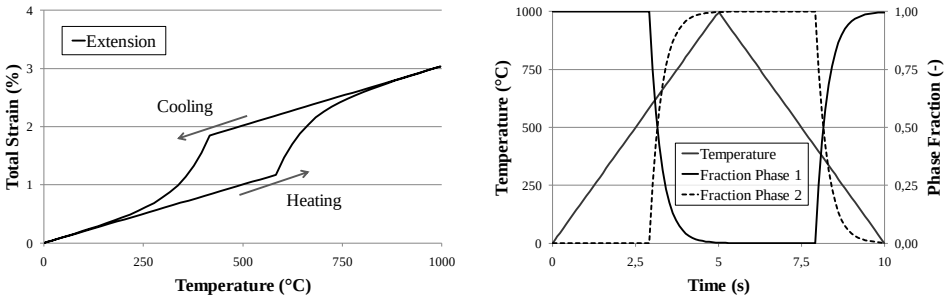

Figure 4-11 Simulated dilatometer curves using two phases (left), and diffusion controlled phase growth (right).

Figure 4-11 shows an example of a computed dilatometer curve for an arbitrary two-phase material. The material is heated up to 1000 °C with subsequent cooling to room temperature. Phase 1 grows below 400 °C, phase 2 above 600 °C. It is assumed that both phases show diffusion-controlled growth with a common growth constant of 0.3 s. The coefficient of thermal expansion is set to $2 \cdot 10^{-5}\,K^{-1}$. The volume change from phase 1 to phase 2 is set to 9 % leading to a maximum phase strain of 3 % (which is one third of the volume change).

4.2.5 Filler Material Addition

Filler material is added to the workpiece during welding using the quiet element technique. The geometry of the fillet to be laid is included in the FE mesh from the very beginning. However, until activation the elements are practically deactivated but possess material properties such that they do not affect the rest of the model, *e.g.* very low values for Young's Modulus, the yield stress, the plastic hardening, and heat conductivity. Hence, the complexity is reduced from a topological change to a time-dependent change in material properties.

In order to avoid large stresses in the quiet elements, especially uniform pressures, the stresses, thermal strains and hardenings are released at the start of each increment. Hence, the material behaves similar to a viscous material and the stress is only in the order of the actual strain increment multiplied by the reduced stiffness. This strain can be assumed to be very small compared to the total strain for the quiet elements. The argument for such an incremental viscosity is that an ill-conditioned system matrix can be avoided, but the global solution is still not affected by the quiet elements. However, here a compromise has also to be found for the residual stiffness of the quiet elements.

Soft Activation / Modified quiet element technique

In the deactivated state, the Young's Modulus, yield stress and hardening parameters have been set to the values assigned to the material at the melting temperature multiplied by an activation factor of $f = 10\ \%$. In the first approach the elements were activated instantaneously; *i.e.*, the mechanical properties were set to realistic values when the welding torch; *i.e.*, the heat source, was situated directly over the element.

This approach can lead to unstable simulations and increased the calculation time significantly. In particular, this approach leads to discontinuities in the material parameters in time due to the abrupt activation. In FEM, however the continuity of derivatives is required to solve the system of differential equations; *i.e.*, to minimize the numerical residual forces. Unsteady derivatives might cause an oscillating bevhaviour of the Newton-Raphson iteration, which can only be resolved by reduced time increments and hence, increased total computation time.

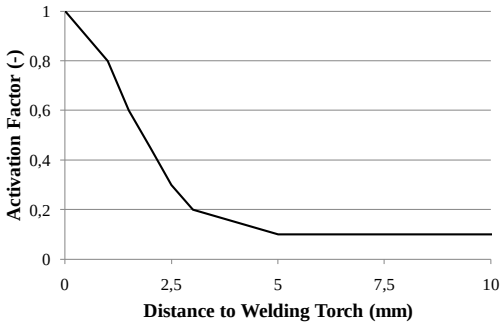

Figure 4-12 Activation factor.

In order to resolve this problem, the material parameters of the elements to be activated are set to real values continuously. **Figure 4-12** shows the activation factor *f* as a function of the distance to the heat source before the torch reaches the position of the element. The material state is still released at the start of each increment until the element becomes finally active. However, the incremental material response converges smoothly towards a realistic behaviour. Using this modified quiet element technique; it was possible to activate the elements without numerical problems.

4.2.6 Simplified Numerical Clamping Model

In order to represent the clamping stiffness, it is not required to model all kinematics of the vertical clamps. In particular, modelling them is quite a complicated task. An equivalent model of the clamping system has been developed as shown in **Figure 4-13**. The requirement for this model is that the workpiece "sees" no difference between the real clamp and the equivalent model; *i.e.*, the transient displacement *U(t)*, the transient clamping force *F(t)* and the clamping surface A_1 have to be the same. The pressures *p* and the strains ε within the clamps may be different. In order to simplify the calculation, it has been presumed that the volumes *V* of both clamps are the same.

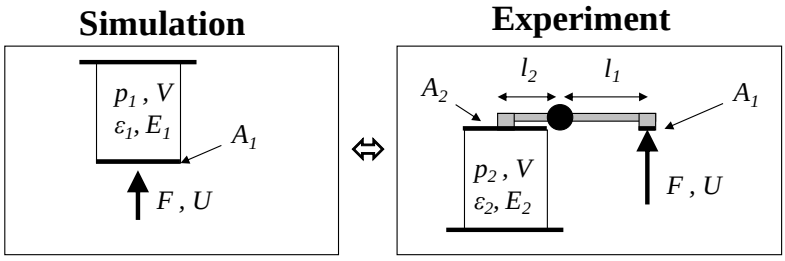

Figure 4-13 Derivation of the equivalent clamping model from experiments.

The strains built up upon a compression / displacement *U* in both the simple clamp (1) and the vertical clamp (2) are given by

$$\varepsilon_1 = \frac{U \cdot A_1}{V} \quad , \quad \varepsilon_2 = \frac{U \cdot A_2}{f \cdot V} \quad , \quad f = l_1 / l_2 \,, \qquad \textbf{Eq. 4-46}$$

where *f* is the lever arm relation. These strains induce pressures in the clamps:

$$\begin{aligned} p_1 &= \frac{F}{A_1} = E_1 \cdot \varepsilon_1 = E_1 \cdot \frac{U \cdot A_1}{V} \\ p_2 &= \frac{f \cdot F}{A_1} = E_2 \cdot \varepsilon_2 = E_2 \cdot \frac{U \cdot A_1}{f \cdot V} \end{aligned} \,. \qquad \textbf{Eq. 4-47}$$

Since the displacement *U* and the clamp volume *V* have to be the same for both clamps, resolving of this equation for *U/V* leads to;

$$\frac{U}{V} = \frac{F}{A_1^2 \cdot E_1} = \frac{f^2 \cdot F}{A_2^2 \cdot E_2} \Rightarrow E_1 = \frac{E_2}{f^2} \cdot \frac{A_2^2}{A_1^2}. \qquad \textbf{Eq. 4-48}$$

Due to the fact that the stiffness of oil is about a factor of one hundred smaller than the stiffness of steel, the total volume of the hydraulic clamp can be assumed to be its oil reservoir of 18 ml = $18 \cdot 10^3$ mm^3. Using the vertical clamp geometries $A_1 = 120$ mm^2, $A_2 = 800$ mm^2, the lever arm relation of $f = 3.3$ and $E_2 = 3 \cdot K_{oil} \approx 6$GPa, where K_{oil} is the modulus of compression of oil, the stiffness of the simplified clamping system is determined to be 25 GPa. The height of the clamp is $h = V/A_1 = 150$ mm. Hence, the stiffness of the clamp is given by

$$k_1 = \frac{E_1 \cdot A_1}{h} = 20 kN mm^{-1}. \qquad \textbf{Eq. 4-49}$$

The contact condition between the clamps and the workpiece has been modelled assuming a linear overclosure-pressure relationship which allows some penetration, *e.g.* [Kloosterman 2002]. A hard (rigid) contact formulation has not been employed since it yields strong numerical problems and often causes numerical divergence due to the discontinuous force-displacement relationship. However, finding a suitable slope for the overclosure-pressure relationship is also a complicated task: It has been found that very low values, say $k = 0.1$ GPa mm^{-1} let the workpiece slip and make the clamps useless. If the slope is too high, say $k = 1000$ GPa mm^{-1}, the formulation approaches the hard contact formulation and the simulation becomes less stable. For the simulations, the slope has been set to $k = 10$ GPa mm^{-1} which is fifty times stiffer than the underlying clamp stiffness, corresponding to a penetration error of two percent. Simulations show that the out-of-plane distortion u of the workpiece below the clamp is about 10^{-4} mm (in a clamped state) and hence, the penetration error Δu due to the assumed slope is $2 \cdot 10^{-6}$ mm which is considered to be acceptable.

Linear Coulomb friction has been assumed between the clamps and the workpiece. The friction coefficient μ has been set to 0.3, which is in accordance with values found in literature [Kang 1996, Matuszak 2000]. The influence of the parameters employed for friction and numerical contact conditions are verified in **section 5.4** as part of a sensitivity analysis performed for the model parameters.

4.3 Material Properties

4.3.1 Thermodynamic Properties

Figure 4-14 shows the thermodynamic material properties; *i.e.*, the specific heat, the density, and the thermal conductivity, for DP600 and S355, respectively. The data has been obtained from Richter [Richter 1971] for a steel grade with a similar chemical composition.

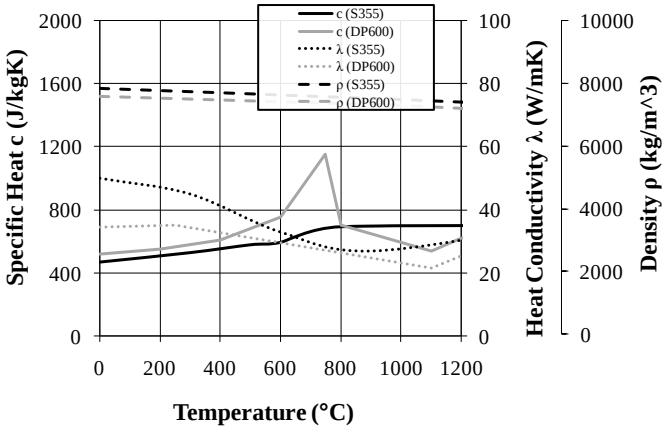

Figure 4-14 Thermodynamic material properties of DP600 and S355.

4.3.2 Metallurgical Properties

For the modelling of phase transformations, the CCT diagrams of [Seyffarth 1992] have been parameterized and employed for DP600 and S355, respectively. **Table 4-4** lists all required parameters as extracted from the CCT diagrams for the two intermediate phases. The parameterized CCT diagrams of DP600 and S355 are shown in **Figure 4-15**. The growth parameter τ from ferrite / pearlite / bainite to austenite has been set to 0.05 s in order to obtain a good agreement to the results of the phase field predictions for welding of DP600 reported by Thiessen [Thiessen 2006]. This is a rough approximation and should be validated and / or refined by experiments in the future. The martensite start and finish temperatures have been set to 460 °C and 240 °C for DP600 and 420 °C and 240 °C for S355, respectively.

It is generally reasonable to model volume expansion and contraction due to phase transformations as well as the influence of martensite on the yield stress. The martensite volume fraction has a strong influence on the yield stress. Here, a value of $d\sigma_Y / df_M \approx 830$ MPa has been employed as reported by *Davies* [Davies 1978] for the dependence of the yield stress on the martensite volume fraction at room temperature. The volume change from austenite to ferrite is assumed to be 1.4 % and from austenite to martensite 1 % which is in accordance to values reported in the literature [Dean 2006, Moyer 1975, Velthuis 1998].

Table 4-4 Phase transformation parameters.

Parameter	DP600		S355	
	Ferrite	Bainite	Ferrite	Bainite
a (K $s^{-1/2}$)	40	90	40	70
t_0 (s)	5.3	1.5	13.0	7.0
T_0 (°C)	635	500	665	470
T_{Low} (°C)	600	460	630	420
T_{Up} (°C)	670	600	700	630
τ (s)	29	4	45	12

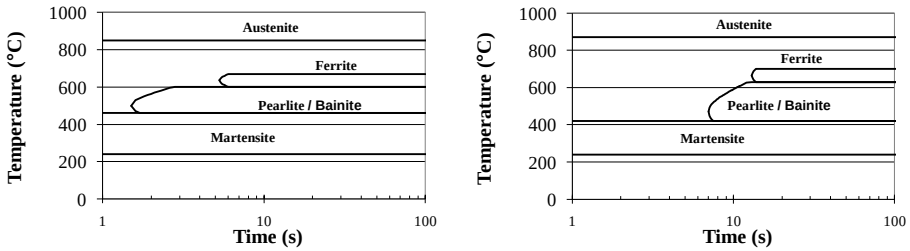

Figure 4-15 Parameterized CCT for DP600 (left) and S355 (right).

4.3.3 Elastic Properties

Figure 4-16 shows the temperature-dependent elastic material properties. Similarly to the thermodynamic material properties, these properties have been taken from [Richter 1971].

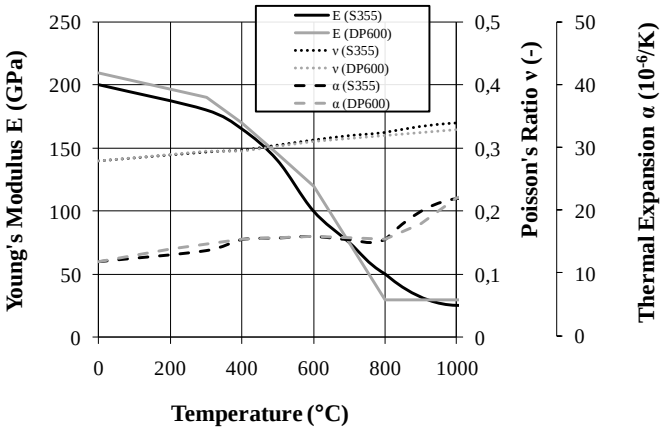

Figure 4-16 Elastic material properties for DP600 and S355 as obtained from [Richter 1971].

4.3.4 Plastic Properties

Plasticity - DP600

Temperature-dependent tensile tests were performed at seven temperatures between room temperature and 1000 °C using a Gleeble® thermomechanical simulator. The strains have been measured using extensometers. Each test has been repeated three times in order to obtain an error indication. The tests have been performed in rolling direction (R) and transversal (T) to the rolling direction. For temperatures above 500 °C, tests were performed for two different strain rates: $d\varepsilon/dt_1 = 2.5 \cdot 10^{-3}\,s^{-1}$ and $d\varepsilon/dt_2 = 6 \cdot 10^{-4}\,s^{-1}$. These strain rates were kept constant during the whole tensile test. **Figure 4-17** shows the true stress-strain curves obtained. Above 400 °C, softening sets in and the material shows an increased dependency on the strain rate applied.

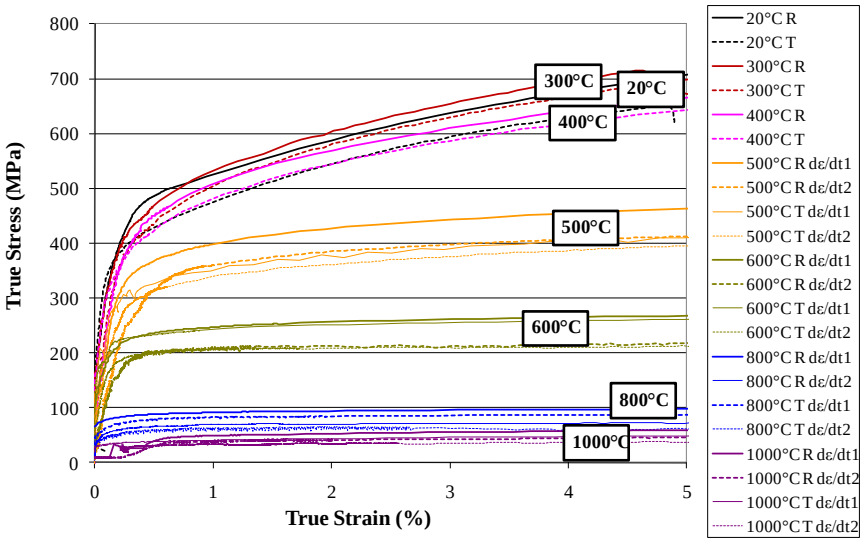

Figure 4-17 True stress-strain curves obtained from tensile tests for DP600 in rolling (R) and transversal (T) direction for both strain rates.

Using the results of the tensile tests, the viscoplastic material properties have been identified using the uniaxial analytical solution of the viscoplastic Chaboche model (see **subsections 2.2.1 and 4.2.3**) for plastic yielding:

$$\sigma(\varepsilon,\dot{\varepsilon}) = \sigma_Y + K \cdot \dot{\varepsilon}^{1/n} + \sum_{i=1}^{2} S_i \cdot \left(1 - \exp\left(-A_i \cdot p\right)\right),\ p \approx \varepsilon - \sigma_Y / E, \qquad \textbf{Eq. 4-50}$$

where, A_i is the hardening exponent, S_i is the hardening saturation value, E is the Young's Modulus, K is the plastic viscosity, n the viscoplastic Norton exponent, and p the plastic

strain. The material behaves elastically below the yield stress $\sigma \leq \sigma_Y$, $\sigma(\varepsilon) = E \cdot \varepsilon$. In general, all these material parameters are temperature-dependent.

The curves have been fitted using two hardening components as shown in **Figure 4-18** (left) for room temperature: One component having a very steep slope; *i.e.*, the hardening exponent is high, and one component increasing slowly; *i.e.*, the hardening exponent is low. It can be seen that the work hardening in the rolling direction is larger than in the transverse direction; hence, an anisotropy factor *f* has been applied:

$$\begin{aligned} \sigma_{Y,Rolling} &= \sigma_{Y,0}(1+f) \\ \sigma_{Y,Transversd} &= \sigma_{Y,0}(1-f)\,. \\ \sigma_{Y,Thickness} &= \sigma_{Y,0} \end{aligned} \qquad \textbf{Eq. 4-51}$$

This anisotropy factor decreases for increasing temperatures. It has been implemented in a way that this factor decreases monotonically in time; *i.e.*, it will not increase again on cooling and is only dependent on the maximum temperature reached $f(t)=f(T_{Max}(t))$. **Figure 4-18** (right) shows the temperature-dependent anisotropy factor for DP600 as obtained from experiments. The calculated r-values of the sample are $r_{00} = 1.35$ and $r_{90} = 0.82$ which are in the range of values found in the literature [Zang 2007]. The temperature-dependent material properties are shown in **Figure 4-19**.

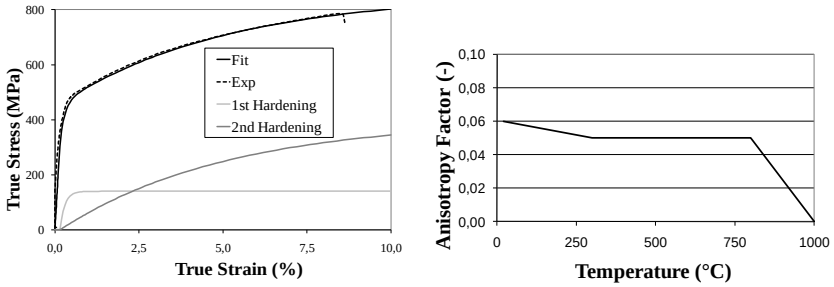

Figure 4-18 Left: Fit for room temperature and rolling direction using two hardening components. Right: Anisotropy factor *f* for DP600.

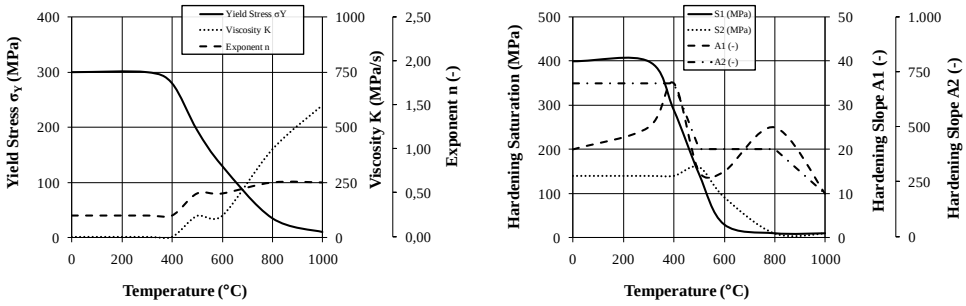

Figure 4-19 Plastic material properties obtained for DP600.

Up to now, the plastic hardening has not been split into isotropic and kinematic hardening. In particular, tensile tests do not allow such a separation. Also it is possible to perform cyclic tests; *i.e.*, tension-compression, for thin sheets which, however, might buckle on changing the load direction to compression. In order to determine the fraction of kinematic and isotropic hardening for both hardening components, bend tests have been performed [Kraska 2004, Doig 2009]. A bending machine has been developed to allow a fast and simple identification of the material properties of thin sheets, including the fractions of isotropic and kinematic hardening. **Figure 4-20** (left) shows a sketch of the bending configuration. A strip of the DP600 steel is clamped between two jaws and bent up and down. The first set of jaws is free to move in the horizontal direction. The force required for the bending and the displacement at the second set of jaws are measured.

Using FE simulations of the bending process and inverse optimization [Mahnken 1994], the isotropic and kinematic fractions of the saturation values of the two hardening components have been determined, as shown in **Figure 4-20** (right). The best agreement with experiments has been obtained for an isotropic hardening fraction of 50% for the first hardening component and 20% for the second hardening component, respectively. It has been assumed that these fractions are temperature-independent which is probably not the case in general. Hence, temperature-dependent tests should be performed. This has not been possible using the present experimental configuration.

Regarding the simulation, some deviation between experiment and simulation can be observed on bending the strip back. This effect occurs often if initial parameters are taken from tensile tests, and its explanation is a matter of current research to improve understanding and interpretation [Wyrwich 2009].

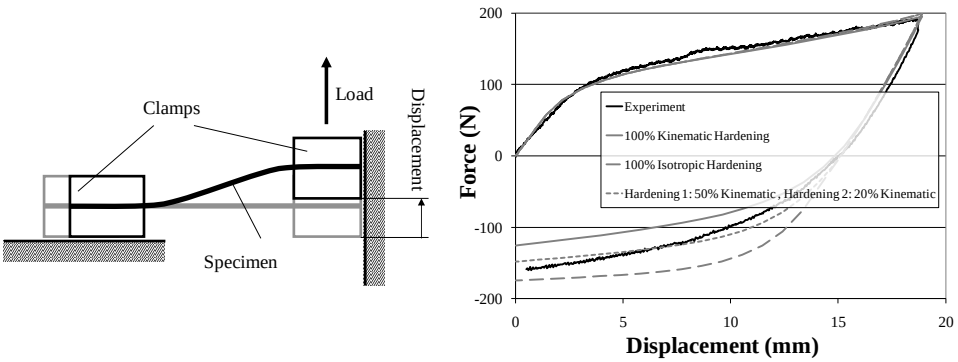

Figure 4-20 Left: Sketch of the bending machine [Kraska 2004]. Right: Comparison of experiment and simulation for different isotropic and kinematic hardening fractions.

Plasticity – S355

The experimental data for S355 has been obtained from Peil [Peil 2004] who performed tensile tests for various temperatures and strain rates. Anisotropy has been neglected since there is no data available for modelling. The strain rates are $d\varepsilon/dt_1 = 3.3 \cdot 10^{-3}\,s^{-1}$ and $d\varepsilon/dt_2 = 3.3 \cdot 10^{-4}\,s^{-1}$, respectively. **Figure 4-21** shows the fits obtained, the elasto- and viscoplastic material properties are shown in **Figure 4-22**.

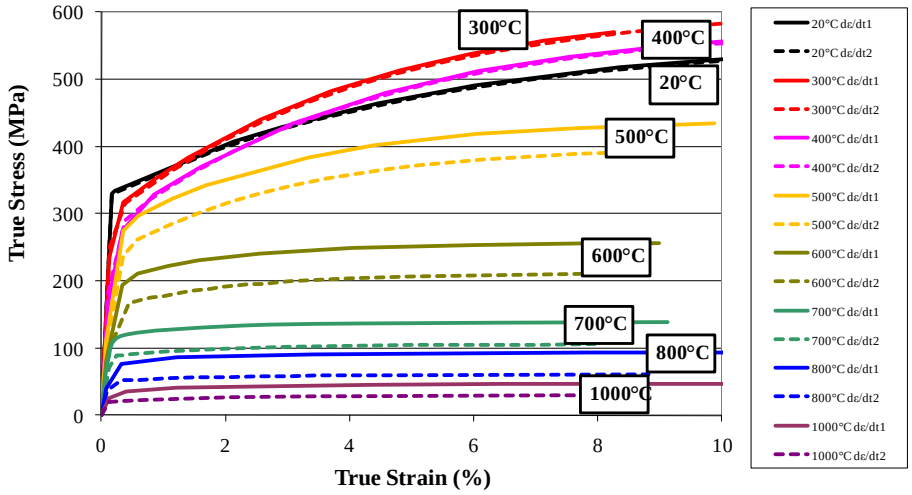

Figure 4-21 Fitted true stress-strain curves obtained from tensile tests for two strain rates S1 and S2.

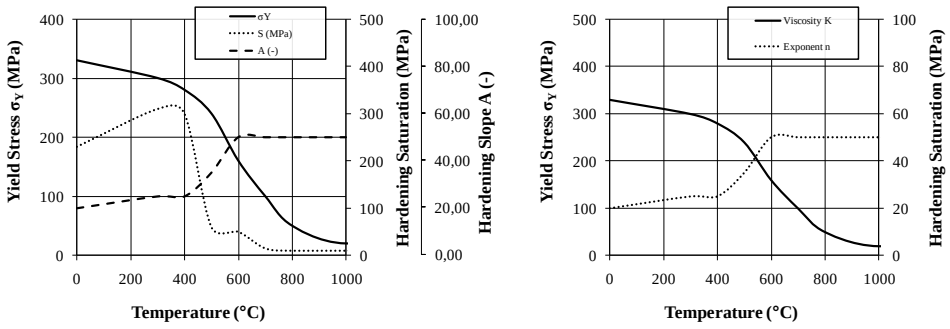

Figure 4-22 Elastoplastic (left) and viscoplastic (right) material properties obtained for S355.

4.4 Meshing

4.4.1 DP600 Overlap Joint

The FE mesh employed for the welding simulations of the DP600 overlap joint is shown in **Figure 4-23**. The dimensions of the joint have been presented in **subsection 1.2.1**. Also in this case, no coarsening has been applied towards the edges of the mesh. The height of the clamps is set to 150 mm. In total, the mesh consists of 22983 elements. The number of elements in longitudinal direction n_l is 207. The same element types have been employed as for the T-Joint.

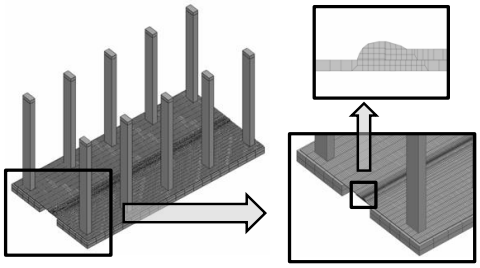

Figure 4-23 Mesh employed for welding simulations of the DP600 overlap joint.

4.4.2 S355 T-Joint

The FE mesh employed for the welding simulations of the S355 T-Joint is shown in **Figure 4-24**. The dimensions of the joint have been presented in **subsection 1.2.1**. No coarsening has been applied towards the edges of the mesh, as explained in **section 5.3**. The height of the clamps is set to 150 mm as derived in **subsection 4.2.6**. In total, the mesh consists of 26772 elements. The number of elements in the longitudinal direction n_l is 108. The element types for the mechanical calculation are either eight nodes bricks with incompatible modes (ABAQUS: C3D8I) or six node triangular prisms (ABAQUS: C3D6). For the calculation of the transient temperature distribution, the corresponding thermal elements have been employed (ABAQUS: DC3D8, DC3D6).

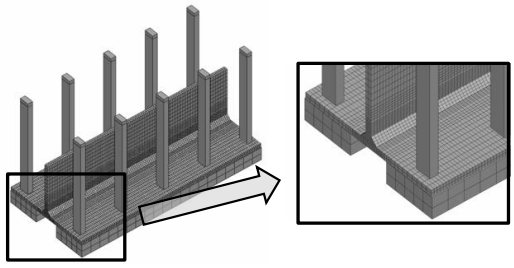

Figure 4-24 Mesh employed for welding simulations of the S355 T-Joint.

5 Model Validation & Verification

In the previous chapter, a transient thermomechanical-metallurgical model for simulations of GMA welding of 1mm thick DP600 overlap joints and 6mm thick S355 T-Joints has been presented. A facility has been built in order to perform experiments for validation purposes.

In the present chapter, model validations are presented for both case studies. The validations have been performed for two clamping cases; a hot release, where the clamps are opened immediately after welding and the workpiece cools down freely, and a cold release, where the workpiece is restrained and remains in intimate contact with the clamping assembly during cooling. For the validations, temperature, phase fraction, distortion, and residual stress measurements have been performed and compared to the simulations.

5.1 DP600 Overlap Joint

5.1.1 Temperature Field

Temperature measurements were performed using K-type thermocouples with a diameter of 0.25 mm connected to an oscilloscope (Yokogawa DL series). The thermocouples were spot welded on a line transverse to the weld, 120 mm from the starting edge of the plate in-between the second and the third clamp, the latter being on the centre of the plate. The temperature measurement error is estimated to be of the order five percent, errors in positioning of the thermocouple being the main contributory factor. **Figure 5-1** shows the coordinate systems for the temperature measurements. The letter determines the top (T) and bottom (B) side. The number determines the distance in millimeters to the defined reference coordinate.

Figure 5-2 shows the temperature measurements and the corresponding fit using Goldak heat sources to model the heat input. The characteristics of the heat sources are described in the next section.

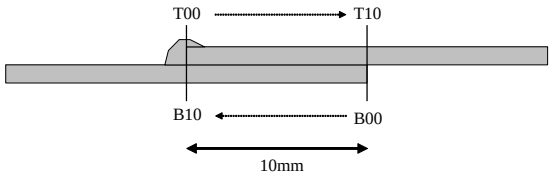

Figure 5-1 Positioning of the thermocouples for the 1mm thick DP600 overlap joint (Units in mm).

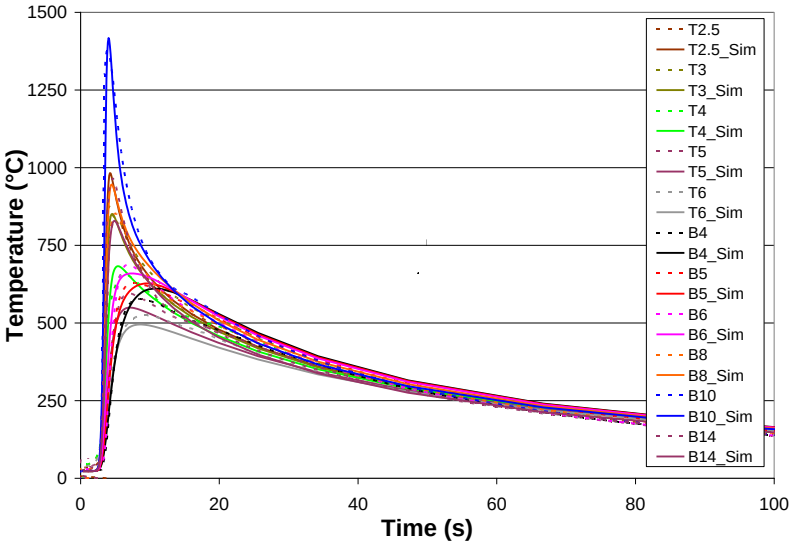

Figure 5-2 Temperature measurements and fit for the DP600 overlap joint. For positions T and B see **Figure 5-1**.

Fit of the Goldak Heat Source

The fit of the temperature measurements has been performed using trial-and-error modifications; *i.e.*, by hand. The heat source parameters are given in **Table 5-1**. **Figure 5-3** shows the maximum temperature profile at the weld seam as well as the positions of the heat source and the thermocouples. The molten zone agrees well with the results expected from experiments in general, but is slightly too small. The reason could be due to the physical material properties, but also due to the heat source: Firstly, the temperature-dependent material data for the heat conductance and specific heat capacity might not be suitable for higher temperatures; which is a very complicated task to verify. Secondly, the Goldak heat source was not developed to model the heat input of GMA welding. Also, the FEM model cannot simulate the liquid material flow which will occur due to the geometry.

It can be expected that the mechanical calculation; *i.e.*, the determination of stresses and deformations, is not affected significantly by this error. There is a good agreement up to about one thousand degrees for the heating rate as well as the cooling rate of the workpiece. Above this temperature, the material looses its stiffness completely and is also transformed to austenite. Hence, what is happening above this temperature should not affect the mechanical calculation.

Table 5-1 Goldak heat source parameters for the 1mm DP600 overlap joint.

Parameter	Value	Dimension
a_f	4.0	mm
a_r	8.0	mm
b	4.5	mm
c	1.8	mm
Q	1700	W mm^{-3}
Y_0	69.0	mm
Z_0	1.95	mm

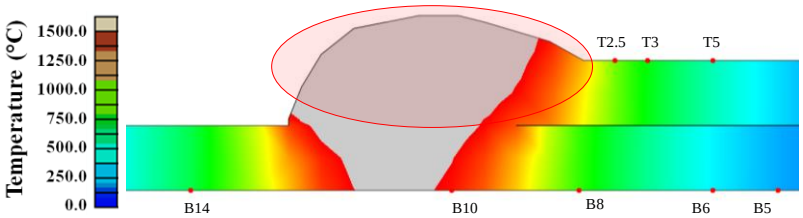

Figure 5-3 Maximum temperature profile at the weld seam for the DP600 overlap joint. The ellipsoid sketches the position of the Goldak heat source. The dots represent thermocouple positions.

Hot Release ↔ Cold Release

The temperature measurements and fits were repeated for the cold release condition. **Figure 5-4** shows a comparison of the maximum temperatures reached for both conditions. It can be seen that the maximum temperature reached in the workpiece are lower for the cold release case due to the heat removal of the clamping system. Close to the clamp, for instance, the maximum temperature reached is about 40 °C for the cold release condition compared to 100 °C for the hot release condition. However, this is not always consistent due to positioning errors. In addition to the lower maximum temperatures, the workpiece also generally cools down faster, see **Figure 5-5**. Two hundred fifty seconds after welding, the average temperature in the workpiece is about 100 °C for the hot release condition and 40 °C for the cold release condition.

Using these measurements, the contact heat transfer coefficient h_c between the DP600 workpiece and the steel backing was found to be 50 Wm^{-2}K^{-1}.

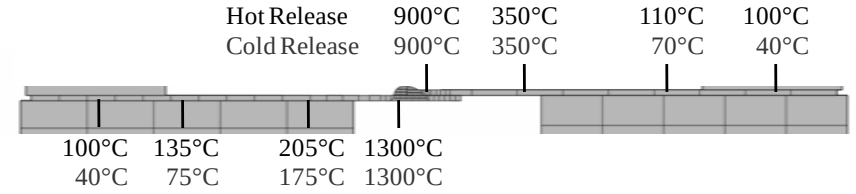

Figure 5-4 Maximum temperatures in transversal direction for the hot and cold release condition.

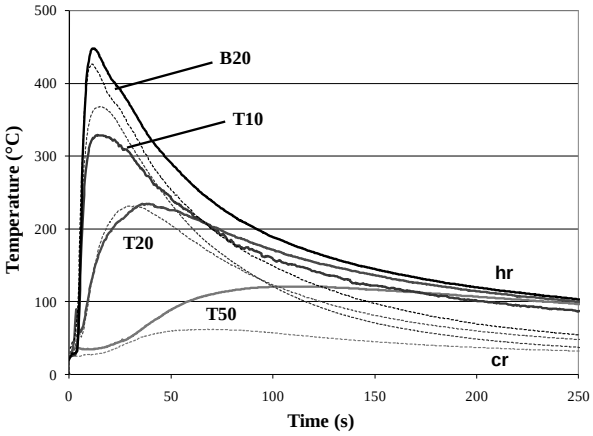

Figure 5-5 Comparison of temperature measurements for the hot release (thick, solid) and cold release (thin, dotted) condition.

Efficiency

The efficiency of the process has been determined. While for plane bead-on-plate (BOP) joints, for instance, the total heat input can be obtained directly from the Goldak heat source parameters, this is not possible in the case of asymmetric welds. Here, the total heat input can be calculated by an integration of the volumetric heat input q over the whole volume V:

$$Q = \int_V q(\vec{x})\, dV \,. \qquad \textbf{Eq. 5-1}$$

In the finite element method (FEM), this calculation is replaced by a summation of the heat input for all n_p integration points multiplied by their volume V_p:

$$Q = \sum_{n_p} q(\vec{x}_p) \cdot V_p \,. \qquad \textbf{Eq. 5-2}$$

The total heat input can be compared to the experimentally measured process power $Q = UI$ in order to calculate the efficiency. This results in an efficiency η of 64 % which is in the range expected for GMA welding, see DIN EN 1011-1.

5.1.2 Welding Distortion

Figure 5-6 shows comparisons of simulations and experiments as obtained from the reference model for the hot and cold release conditions. In both cases, the second buckling mode has been obtained as the final distortion shape. There is good agreement between model and experiments regarding the buckling mode as well as the buckling direction. The

experimental measurement deviation is about 15 %. The simulations overmatch the experimental buckling amplitudes by 15 %, but are still within the experimental deviation.

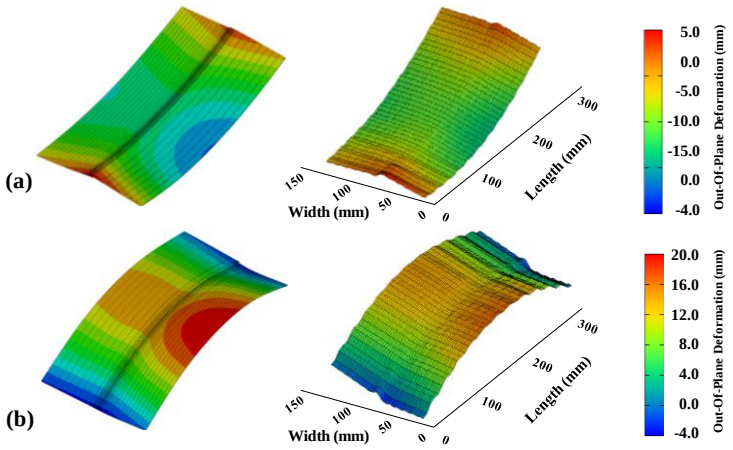

Figure 5-6 Comparison of the buckling distortion obtained from simulations (left) and experiments (right) for the cold release condition (a) and the hot release condition (b) for a welding speed of 8 mm/s.

Buckling Stabilization

As explained in **subsection 2.3.3**, buckling is an unstable effect; it occurs virtually instantaneously as soon as the critical buckling load is reached. This instantaneous occurrence is instable from a numerical point of view. As soon as the simulation reaches this point, it will be impossible to find a new equilibrium and hence, the integration algorithm reduces the time step. The incremental speed v at which buckling occurs can be defined by the buckling amplitude U divided by the time increment Δt and hence, it increases with reduced time increments. This leads to numerical divergence and eventually to the abortion of the simulation.

However, it is possible to apply a counteracting damping force with a damping factor k, see **subsection 4.2.2**. For decreasing time increments, the damping force increases, the forming of buckling is slowed down and the algorithms eventually find a solution. This effect can be imagined by putting the workpiece into a viscous liquid. Here, the damping coefficient has to be chosen small enough to affect the solution as little as possible but large enough to avoid an abortion of the simulation. In particular, the damping force should not introduce any new plastic deformation. For the present simulations, studies have been performed on the damping coefficient and its value has been set to 10^{-9} Ns mm^{-2} which corresponds approximately to the viscosity of water.

5.1.3 Phase Transformation

In order to determine the phase transformation behaviour and to validate the metallurgical model, the phase fractions have been evaluated at two points, see **Figure 5-7**: Point (a) in the fusion zone and point (b) in the heat-affected zone. Apparently, the cooling rate below 800 °C is the same at both points. However, the heating condition is different: While point (a) is heated above the melting temperature, point (b) is heated up to a maximum temperature of approximately 1200 °C. This difference in heat treatment affects the austenitisation.

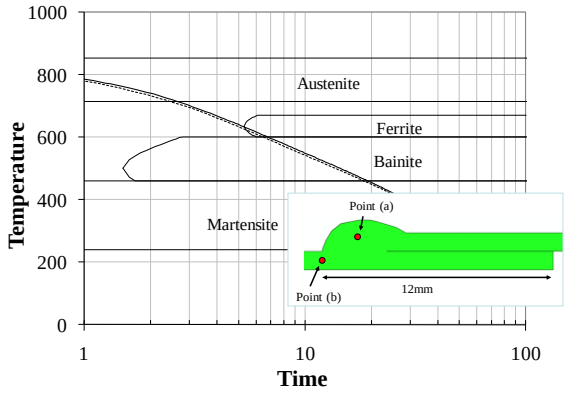

Figure 5-7 Parameterized CCT and temperature development for two points: Point (a) in this fusion zone (solid), and point (b) in the heat-affected zone (dotted).

Figure 5-8 shows the development of the phase fractions during welding and subsequent cooling. While the model predicts 100 % austenite in the fusion zone, the austenite volume fraction at point (b) is about 50 %. In both cases, however, martensite is transformed completely to austenite. After welding, the phase distribution is completely different from the original state of 15 % martensite and 85 % ferrite. In particular, the martensite volume fraction is reduced and a large fraction of bainite appears.

In order to validate these results, experiments have been performed and the resultant welds sectioned and etched for sixty seconds with LePera's reagent, see **Figure 5-9**. The martensite content at point (a) is found to be 5±2 vol.% in the experiments compared to 4.3 vol.% in the simulations. At point (b) 8±4 vol.% have been found compared to 2 vol.% in the simulations. Hence, the martensite volume fraction is underestimated by the model. The rest is an almost equal mixture of ferrite and bainite.

The simulations with the current model show deviations from the experiments. However, there is a good agreement in the fusion zone. The deviations in the heat affected zone are most likely due to the austenitisation model on heating. Here, it might be reasonable to develop more profound models based on phase field modelling. As mentioned in **subsection 4.2.4**, this phenomenon is yet not completely understood and there is still research ongoing [Savran 2009].

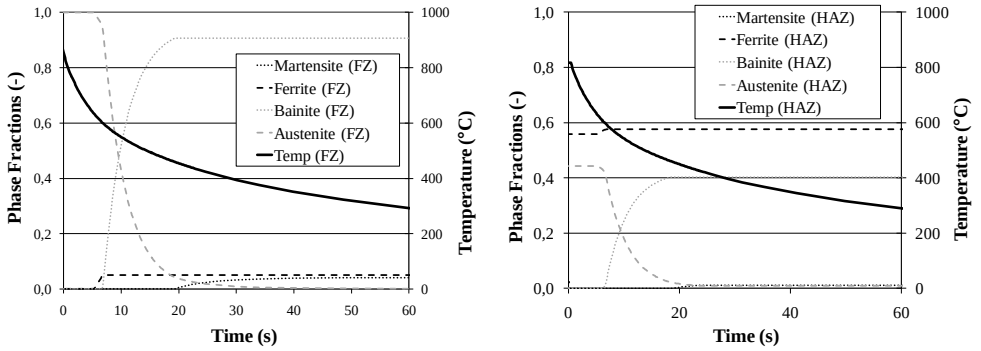

Figure 5-8 Development of the phase fractions predicted for Point (a) in the fusion zone (left) and point (b) in the heat-affected zone (right).

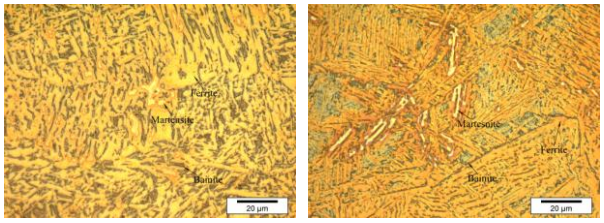

Point (a) FZ Point (b) HAZ

Figure 5-9 Measured phase fractions after welding at point (a) and (b).

5.1.4 Longitudinal Stresses

The longitudinal residual stresses after welding have been measured at the surface of the workpiece transverse to the weld at the centre line in the longitudinal direction. The measurements have been performed for three samples for both the hot and cold release condition using a mobile StressTech X3000 X-ray diffractometer. The measurement error of the stresses at each point has been determined by the half-width of the reflection peaks. Due to the equipment; *i.e.*, the applied aperture, the average stresses are obtained in a spatial resolution of ±2 mm in order to resolve large gradients accurately.

The results are shown in **Figure 5-10** and compared to simulations. Even though it can be seen that there is a good agreement in principle, there are some deviations visible. However, it has also been found that there is a strong experimental scatter. Deviations can arise for many reasons; one of the most likely is that no stress relaxation annealing has been done prior to welding. It has to be considered that the residual stresses are not in equilibrium; *i.e.*, the integral over the width at the surface is not zero. This can be expected because the measurements have been performed at the top side of the joint. It can be seen that the peak residual stresses are somewhat lower for the cold release condition than for the hot release condition, which is expected due to the higher restraints during cooling.

In general, the amplitudes of the predicted residual stress are higher than the values found in experiments. This is in accordance with the welding distortion where the predicted

buckling amplitudes are higher than the experimental measured amplitudes as well. In order to investigate the sensitivity of the simulations, the simulations have been repeated for three variations.

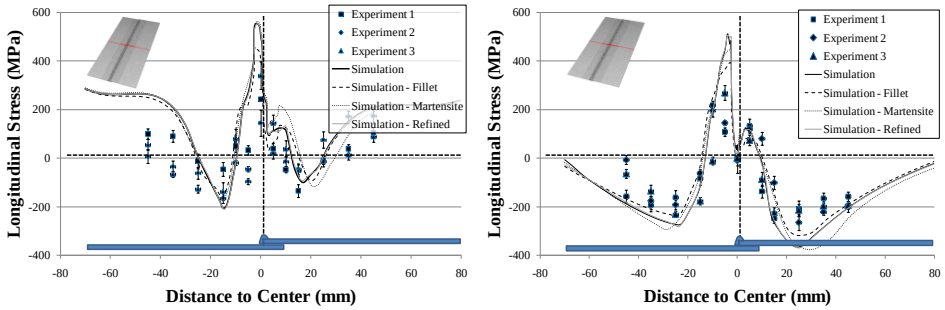

Figure 5-10 Comparison of longitudinal residual stresses obtained from simulations and experiments for the hot release (left) and the cold release (right) condition.

Firstly, the material behaviour of the consumable is assumed to be DP600 in the present model. According to EN440, the yield stress σ_Y of the consumable SG2 lies in the range of 400-500 MPa and hence, in the order of the DP600 values. The ultimate tensile strength, however, is around 550 MPa compared to about 700 MPa for DP600. If this is considered in the simulations, the fillet becomes softer and as a result, the residual stresses are closer to the experimentally expected values. Additionally, the welding distortion is reduced by 5% and 10 % for the hot and cold release condition, respectively.

In the second test, the assumed volume expansion ΔV upon transformation from austenite to martensite has been varied. In the present model, this value is set to 1 % which is in good agreement with experimental measurements [Moyer 1975, Velthuis 1998]. This value has been modified up to the maximum theoretical volume expansion of 4.4 %. During welding, however, the martensite volume fraction is reduced from 15 % in the base material to 4 % in the heat-affected zone and in the fusion zone. This leads to higher residual stresses due to the fact that the material effectively shrinks compared to the base material.

It has been found by this sensitivity study that the general residual stress distribution is not affected significantly. In particular, the compressive stress amplitudes at the top plate compared to the bottom plate are always higher for the cold release and lower for the hot release condition. Additionally, a steep drop of the residual stresses has been found at the weld centre where the reinforcement of the joint is the highest.

300 Bar Model

The longitudinal stresses can be studied using simple bar models, as proposed by Masubuchi [Masubuchi 1980], for instance. In the present paper, a 300 bar model has been applied as shown in **Figure 5-11**. The length *l* of the bars is 300 mm, the thickness *t* is 1 mm, and the width w is 0.5 mm. The mechanical parameters of DP600 at room temperature have been applied for the stress calculations. The bars are heated up within five seconds and cooled down to room temperature within another five seconds. The maximum

temperatures for each bar in the transverse direction to the weld seam correspond to the values obtained in experiments.

The bars are linked using spring elements instead of a rigid linkage. For the spring stiffness K_i between the ith and the (i+1)th bar, van der Aa [Aa 2006] proposed the following value:

$$K_i = \frac{E \cdot A}{(w_i + w_{i+1})/2} \ , \ A = t \cdot l \ , \qquad \textbf{Eq. 5-3}$$

where E is the Young's Modulus. It has been found by trial-and-error that this approach is too stiff in this case and hence, the stiffness has been downscaled by a factor of twenty in order to obtain a more realistic longitudinal residual stress distribution.

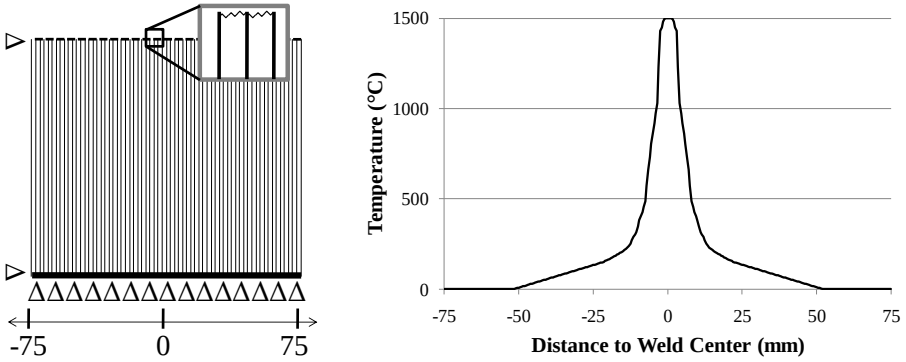

Figure 5-11 Left: 300 bar model with fixed nodes at the bottom and spring linkage at the top. Right: Maximum temperatures applied to the bars in transversal direction.

Figure 5-12 shows the predicted longitudinal residual stresses using the 300 bar model for a flat plate. If it is assumed that the same heat input Q is applied to the overlap joint as to the flat plate, the longitudinal shrinkage forces F remain the same for both cases. The longitudinal stresses, however, are determined by $\sigma=F/t$, where t is the thickness of the joint. Hence, the drop of the stresses at the centre can be understood by purely geometrical issues; the reinforcement reduces the stress level.

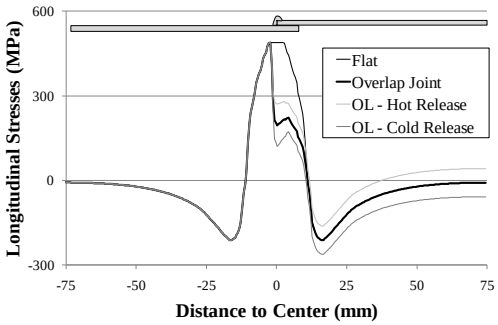

Figure 5-12 Results of the 300 bar model and influence of the thickness variations and the bending on the longitudinal residual stresses predicted by the bar model.

Additionally, there is a superposition of the stresses at the top side with bending stresses due to the buckling distortion. A sketch of the neutral axis for a longitudinal bending and the expected bending stress distribution is shown in **Figure 5-13**.The maximum bending stresses can be estimated by beam theory: If it is assumed, that the bending in the longitudinal direction *x* can be described by

$$y(x) = A \cdot \sin\left(\frac{\pi}{l} \cdot x\right), \qquad \textbf{Eq. 5-4}$$

where A_{cr} is -13mm and A_{hr} is +18mm for the cold release (cr) and hot release (hr) condition, respectively, the maximum bending stresses at $x = l/2$ become

$$\sigma_{MAX}(t) = \left(\frac{\pi}{l}\right)^2 \cdot E \cdot \frac{1}{2} \cdot t \cdot A, \qquad \textbf{Eq. 5-5}$$

where *t* is the distance of the top side to the neutral axis. These superposed bending stresses shift the maximum compressive stress amplitudes at the top plate compared to the bottom plate by -120 MPa and +160 MPa for the cold and hot release condition respectively.

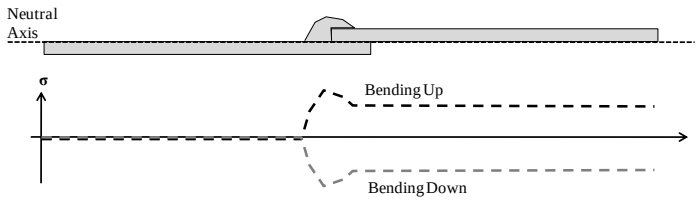

Figure 5-13 Bending stresses due to the buckling distortion.

5.1.5 Tensile Tests

Experimental and numerical (see **Figure 5-15)** tensile tests have been performed for both clamping conditions. The resulting force-extension curves are shown in **Figure 5-14**. It has been observed that the sample fails in the heat-affected zone of the bottom plate in more than 90 % of the experiments. As found for the welding distortion and the residual stresses, also in this case the material response is overestimated by about 15 % in the simulations compared to the experiments.

The difference in the elastic stiffness at the beginning is likely to be a measurement inaccuracy. The extension measurement is derived from the machine displacement, which includes any elasticity in the system. In order to measure the true elastic stiffness of the specimen, it is required to measure the extension locally; e.g. using an extensometer.

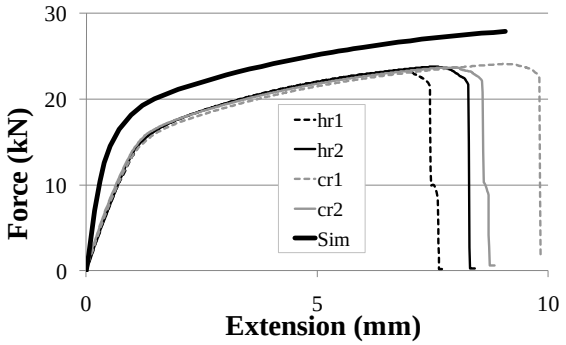

Figure 5-14 Force-extension curves for the cold (cr) release condition, the hot (hr) release condition, and simulations (Sim).

Figure 5-15 shows the transverse stress distribution during tensioning as obtained from the simulations. There is no failure criterion implemented in the model. However, it has been found that the ultimate elongation ε_{MAX} of about 25 % is reached firstly in the heat-affected zone of the lower plate which is in good agreement with the experimental observations. The simulations have been performed with the material properties after welding corresponding to those for the hot and cold release conditions and for a virgin DP600. It has been found that the simulations differ only a few percent, even for the virgin material state. Hence, the failure of the sample at the lower plate close to the weld seam appears to be a geometrical issue of the overlap joint.

The fracture stress of the sample is approximately given by

$$\sigma_{MAX} = 24\ kN / 40\ mm^2 = 600\ MPa\ , \qquad \textbf{Eq. 5-6}$$

which corresponds to around 80 % of the fracture stress of the base material. The measured forces and extensions at fracture are 24.1 ± 0.4 kN and 8.5 ± 0.3 mm for the cold release condition and 23.5 ± 0.4 kN and 7.8 ± 0.8 mm for the hot release condition respectively; hence, the samples obtained from the cold release conditions are slightly stronger. This can

be explained by the cold release condition: Firstly, it can be assumed that there is a higher strain hardening due to the restraining during cooling, and secondly, the faster cooling leads to a higher martensite volume fraction.

The increase of the strength is usually accompanied by a loss of deformability. Here, however, an increase of the maximum extension has been found. The increase of the strength of the HAZ in case of the cold release compared to the hot release leads to a redistribution of the elastic strains into the base material and hence, to a higher maximum extension of the total sample: The strain in the base material at fracture of the joint is 1.73 % for the cold release condition and 1.70 % for the hot release condition.

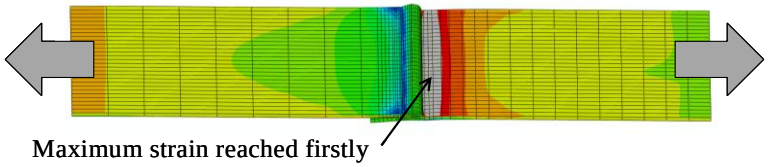

Figure 5-15 Transversal stresses during tension.

5.2 S355 T-Joint

5.2.1 Temperature Field

For the S355 T-joint, temperature measurements have been performed over the whole section of the workpiece, see **Figure 5-1**. The results are shown in **Figure 5-2**. Also here, a significant influence of the clamping on the temperatures and cooling rates was found.

Figure 5-18 shows the maximum peak temperature measured during welding as well as the temperature at a time of 500 seconds after welding for both clamping conditions. For the clamped cold release condition, the workpiece cools down much faster than for the unclamped hot release condition. The maximum temperature reached in the workpiece close to the clamps; *i.e.*, at the outside of the base plate, is about one third less for the cold release condition. At a time of 500 seconds after the start of welding, the temperature of the workpiece is 160 °C for the hot release. At this time, the temperatures and cooling rates are the same for the whole workpiece. In the case of the cold release, however, the joint has already cooled down to 90 °C.

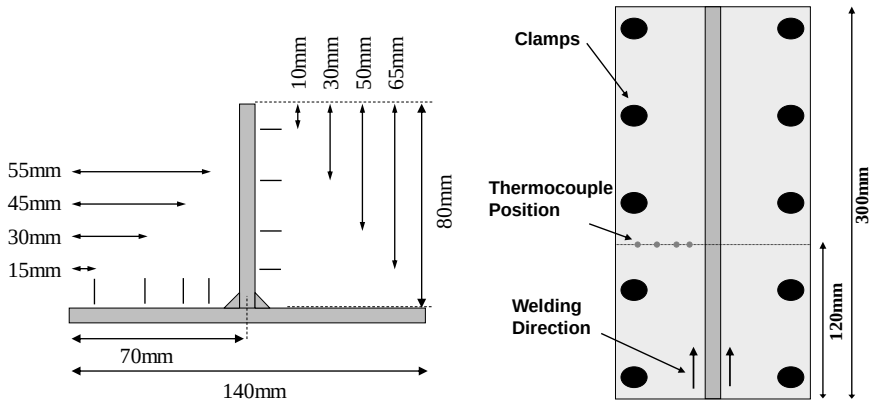

Figure 5-16 Positioning of the thermocouples for the 6 mm thick S355 T-joint.

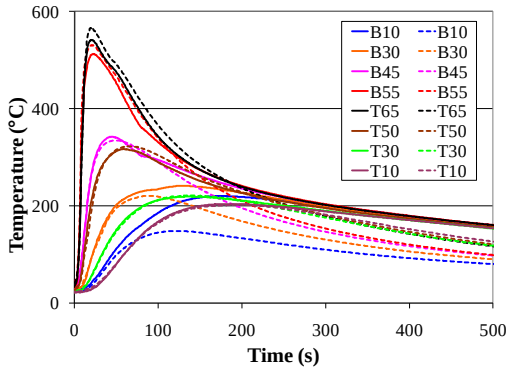

Figure 5-17 Comparison of temperature measurements for the hot release (thick, solid) and cold release (thin, dotted) condition at the positions defined in **Figure 5-17**.

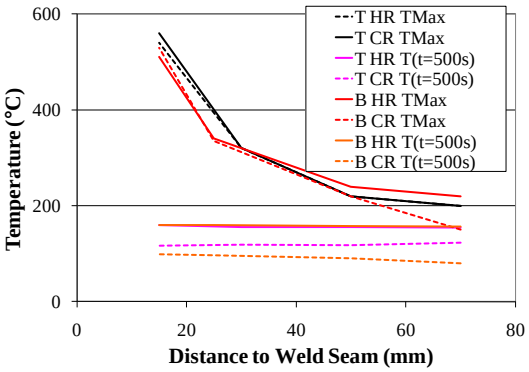

Figure 5-18 Measured peak temperatures T_{Max} and temperatures at t=500 s after welding for the hot release (solid) and the cold release (dotted).

Temperature measurements have also been performed within the heat affected zone in order to calibrate the thermal input for the welding model. Here, the heat source in the thermal model was rotated by an angle α of ±45 ° in order to account for the position of the welding torch. In a similar manner to the overlap joint, the fit of the temperature measurements has been performed using trial-and-error modifications. The heat source parameters are given in **Table 5-2**. **Figure 5-3** shows the maximum temperature profile at the weld seam as well as the positions of the heat source and the thermocouples. For a detailed discussion, see **subsection 5.1.1**.

Using the calibrated heat source and the total heat input of 2·4.75 kW measured in the experiments, the efficiency has been calculated to be 52 % which is a little lower than expected for GMA welding processes.

Table 5-2 Goldak heat source parameters for the 6mm S355 T-joint.

Parameter	Left Side	Right Side	Dimension
a_f	7.0	7.0	mm
a_r	10.0	10.0	mm
b	8.0	8.0	mm
c	3.5	3.5	mm
Q	6100	6100	W mm^{-3}
Y_0	67.0	73.0	mm
Z_0	10.7	10.7	Mm
α	+45	-45	°

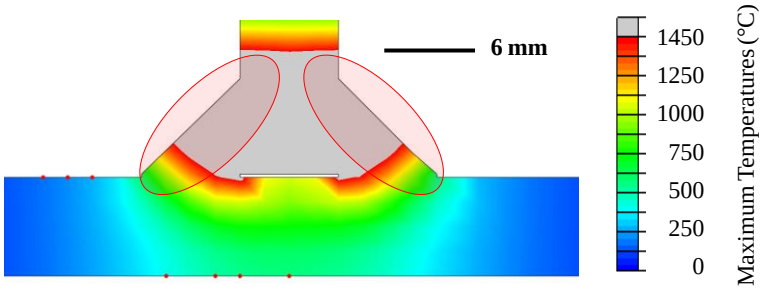

Figure 5-19 Maximum temperature profile at the weld seam for the S355 T-joint. The ellipsoid shows the position of the Goldak heat source. The dots represent thermocouple positions for the calibration measurements.

Up to now, the temperatures have only been measured at one position in the longitudinal direction. In order to determine a possible difference in heat conductance at the clamps and in-between the clamps, temperature measurements have also been performed using a pyrometer. However, no measurable temperature difference could be found. In general, the contact conduction is also dependent on the surface topology which might change due to the clamping. However, surface analyses using interferometry showed that

there is no significant change of the surface topology due to the clamping. This gives reason to assume a constant; *i.e.*, pressure-independent heat transfer coefficient.

5.2.2 Welding Distortion

For the S355 T-joint, the welding distortion has been measured for welding completely without clamping and for the hot and cold release condition. For every welding condition, the measurements have been repeated three times and averaged in order to give an estimation of the standard deviation. The deformation of the base plate has been measured prior to and after welding. Measurements in both the experiments as well as the simulations are made with the plate mounted at three edge points. This has been done to cover any initial predeformation which might exist due to rolling, surface grinding, tack welding, or other handling effects. The difference between both measurements is the *effective welding distortion*.

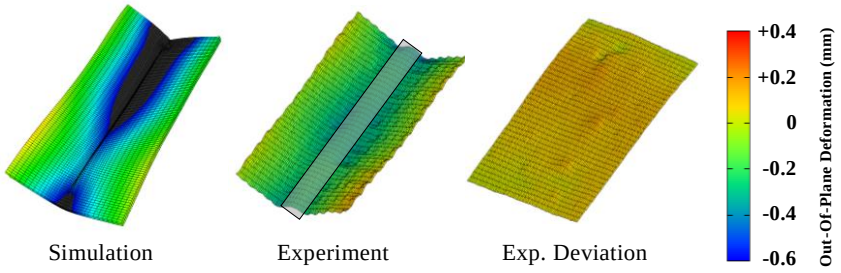

Figure 5-20 Effective welding distortion of the base plate without any clamping for simulations, experiments, and the corresponding standard deviation. The shaded area is situated below the stiffener and the fillet and can not be measured in experiments.

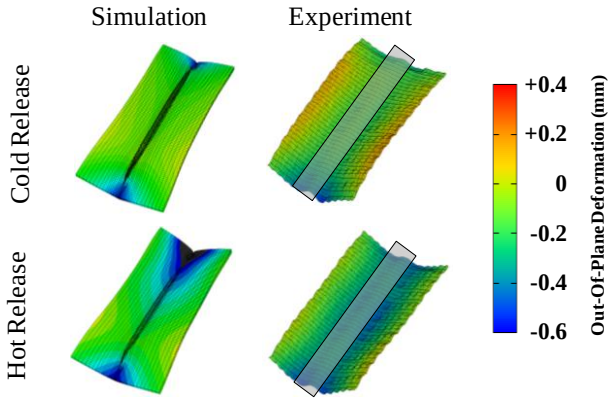

Figure 5-21 Predicted and measured welding distortion. The shaded area is situated below the stiffener and the fillet and cannot be measured in experiments.

Figure 5-20 shows the predicted and measured welding distortion of the base plate after welding without clamping. The magnification factor for the deformations in all simulations presented in this paper is set to fifty. The simulations show a reasonable good agreement with the experiments. For all experiments presented, the experimental standard deviation is about 0.15 mm, which is quite high compared to the total deformation amplitudes (about 30%). Since the measured welding distortion is much larger than the repeatability of the measurements; *i.e.*, the measurement error, it is assumed that this deviation is likely to be related to the initial material condition.

Figure 5-21 shows the predicted and measured welding distortion for the cold and hot release condition. It can be seen that in both cases the dominant distortion mode is angular distortion for the hot release condition and bending distortion for the cold release condition. Hence, the tendencies in the experiments and simulations are the same for both clamping conditions. However, there are some deviations notable. In case of the cold release, the bending amplitude is more pronounced in the experiments. In particular, the bending at the edges is significantly stronger than at the centre. In the simulations, however, the bending shape is more homogeneous and the amplitude is lower. For the hot release condition, the experiments show mainly angular distortion. In the simulations, the angular distortion is superposed with some bending. In the following sections, possible sources for the deviations are investigated.

5.2.3 Predeformation

The most likely reason for the large standard deviation in experimental measurements is predeformation of the base plate prior to welding. **Figure 5-22** shows experimentally measured predeformations for three cases. In the first case, the predeformation is torsion, in the second case there is some angular distortion present, and in the third case there is some bending. Usually it is assumed in simulations that the predeformation has no significant influence on the residual welding distortion. However, the amplitudes of the predeformation in these cases are in the order of some tenths of a millimetre and hence, about 30-50 % of the final distortion amplitude.

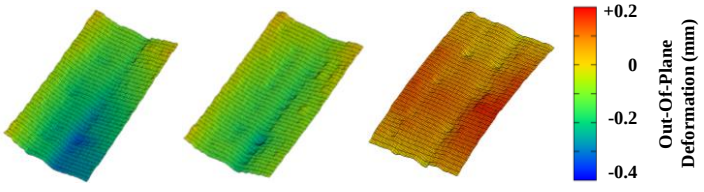

Figure 5-22 Experimentally determined predeformation of the base plate prior to welding for three cases.

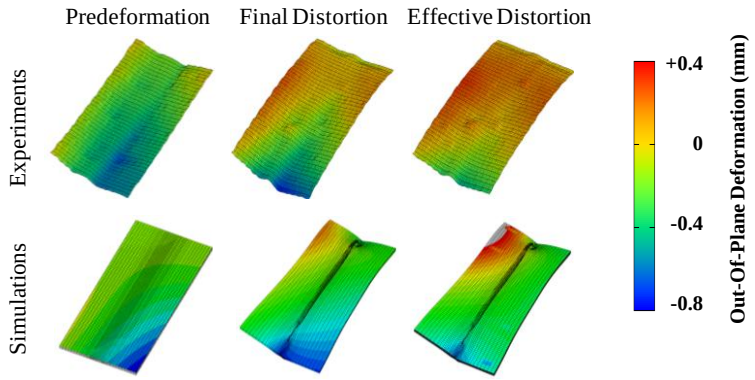

Figure 5-23 Comparison of experiments and simulations for the predeformation, the final distortion, and the effective distortion for case 1 from **Figure 5-22**.

Since this predeformation is present in the as-delivered condition of the plates, it has not been possible to remove it. However, it is possible to incorporate the predeformation in the simulations even though this is a complicated and time-consuming task. **Figure 5-23** shows the predeformation, the final distortion, and the effective distortion (predeformation subtracted from final distortion) of the first case shown in **Figure 5-22** for the cold release condition. The appearance of the experimentally determined torsion is similar to the first eigenmode of the workpiece. Hence, this eigenmode has been applied as predeformation in the simulations with an amplitude of 0.4 mm.

In both the simulations and experiments the predeformation is visible in the final distortion after welding, and it is still visible in the effective welding distortion. Assuming that the initial torsion imperfection and the bending welding distortion can be superposed linearly, this means that the initial predeformation is amplified by the welding process. Hence, in order to obtain accurate results in both simulations and experiments, the predeformation has to be implemented.

5.2.4 Variations within Standards

Comparing the experiments and simulations for the cold release condition, it can be seen that the maximum bending is at the edges in the experiments while it is most pronounced underneath the stiffener in the simulations. This is a very important aspect if the workpiece is considered to be part of a large assembly; the reaction force might differ significantly for both cases. The two most likely reasons for this behaviour have been found to be the material hardening parameters and the assumed phase volume change.

Figure 5-24 shows the results for measured tensile tests for the 6mm thick S355 at room temperature in longitudinal and transversal direction. No anisotropy has been found between both directions. The tests have been performed for tension and compression. It has been found that the sample buckles on compression in the early plastic region. However, the kinematic hardening fraction could be estimated to be approximately 50 %.

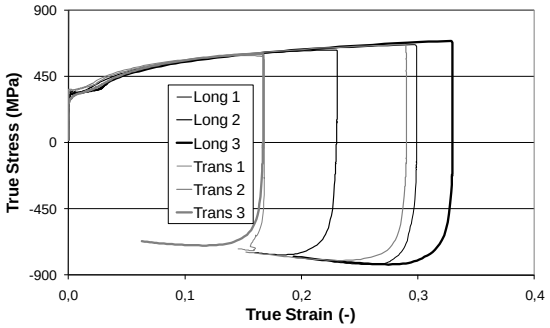

Figure 5-24 Tensile tests for the 6mm thick S355 at room temperature in longitudinal and transversal direction.

Figure 5-25 shows the bandwidth of the mechanical behaviour as defined in EN10025. Additionally, three technical stress-strain curves are shown. Data (1) denotes the literature values applied for the reference model as obtained by Peil and Wichers [Peil 2004], data (2) shows the measured curve, and data (3) a rescaling of data (1) with a 25 % higher yield stress. While all three stress-strain curves are within the allowed bandwidth for S355, the material stiffness increases from data set (1) to (2) to (3).

Figure 5-26 shows the effect of the material parameters on the predicted bending distortion for the cold release condition and a clamping support distance of 50 mm. For data (1), which is the reference data, bending is most pronounced at the centre underneath the stiffener. For higher material strength, the bending shifts towards the edges of the workpiece. For the measured data (2), which is only slightly stronger than the reference data (1), the highest bending amplitude is already present at the edges.

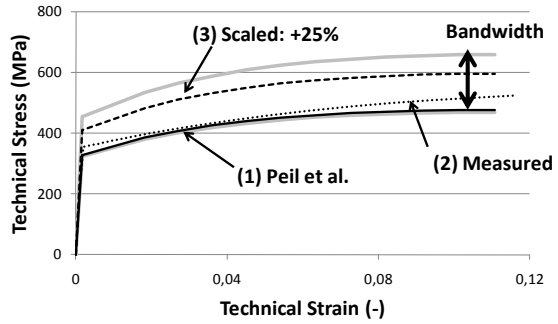

Figure 5-25 Material norm EN10025 for S355 and technical stress-strain curves of the data applied in this sensitivity analysis.

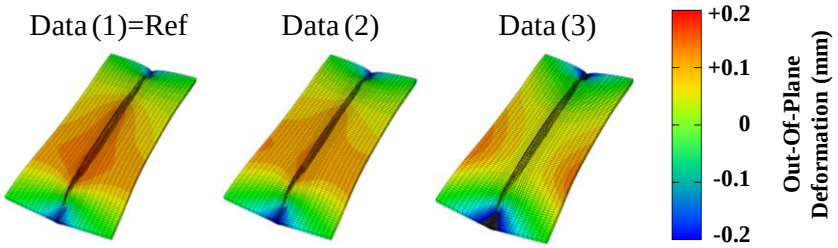

Figure 5-26 Predicted bending distortion for the cold release condition with the three material data sets shown in **Figure 5-25**.

The best agreement to experiments has been obtained for data set (3) which is significantly stronger than the real hardening behaviour. Hence, it can be concluded that the hardening cannot solely account for all differences between the simulations and the experiments.

5.2.5 Influence of Phase Transformations

It has been found that another important set of parameters is the volume change from austenite to ferrite ΔV_{aust} and from austenite to martensite ΔV_{mart}. In the reference model, these values have been set to 1.3 % from austenite to ferrite and 1 % from austenite to martensite, respectively. However, these values vary strongly in the literature, see [Schumann 1991, Dean 2006, Chen 1985, Taljat 1998]. **Table 5-3** shows three parameter variations applied. Set (1) correspond to the reference model, set (2) to the maximum theoretical values, and set (3) assumes volume changes less than or equal to the reference model. The bending distortions obtained for all three sets are shown in **Figure 5-27**. It can be seen that the higher the volume change, the more pronounced the bending becomes at the centre.

The assumed phase volume change has a significant influence on the predicted distortion shape. In order to obtain reliable results it is therefore recommended to perform dilatometer tests.

Table 5-3 Different sets for the volume change from austenite to ferrite and martensite. Set (1) correspond to the reference model.

Volume Change	Set (1)	Set (2)	Set (3)
Austenite → Ferrite	1.3%	1.3%	0.8%
Austenite → Martensite	1.0%	4.4%	1.0%
Reference	Reference Model	[Schumann91]	[Dean06]

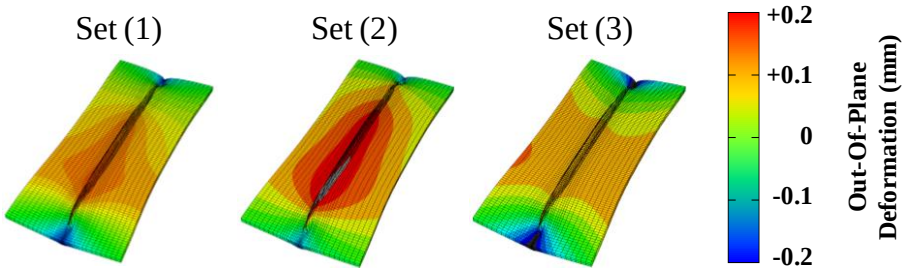

Figure 5-27 Predicted bending distortion for the cold release condition and the three sets of parameters for the phase change volume.

5.3 Mesh Convergence Analysis & Buckling

5.3.1 Convergence Analysis

The mesh employed for the reference model of the DP600 overlap joint presented in the previous chapter has been obtained using a mesh convergence analysis. The welding simulations were repeated for six FE meshes as listed in **Table 5-4**. Three of those possess 207 elements in the longitudinal direction at the weld seam, but are coarsened to 23 elements towards the outside, also referred to as T-meshes, see **Figure 5-28**. Three posses no coarsening towards the outside but have different numbers of elements in the longitudinal directions (126, 225, 342), also referred to as L-meshes, see **Figure 5-29**.

The simulations have been performed for the hot release condition using three different finite element types: standard trilinear volume elements (S), elements with incompatible modes (I) and elements with reduced integration (R), see **subsection 4.2.2**. It has been noted that the total computation time for the (I) elements is about one third higher than for the (S) elements, while it is reduced by about one third when the (R) elements are applied.

Table 5-4 Overview of the meshes applied for the study including the number of elements and the normalized computation time.

Mesh	Refined	# Elements	Norm. Calc. Time
Ref	207 - No	31315	1.00
T1	207 - 23	21333	0.46
T2	207 - 23	25567	0.67
T3	207 - 23	29529	0.89
L1	126 - No	19114	0.37
L2	225 - No	36815	1.38
L3	342 - No	51002	2.65

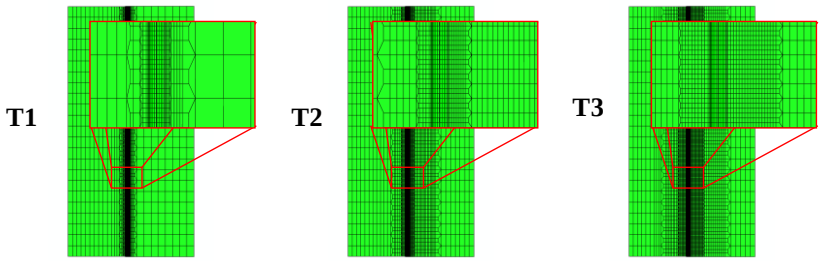

Figure 5-28 FE Meshes with element density coarsening towards the outside (T-Mesh).

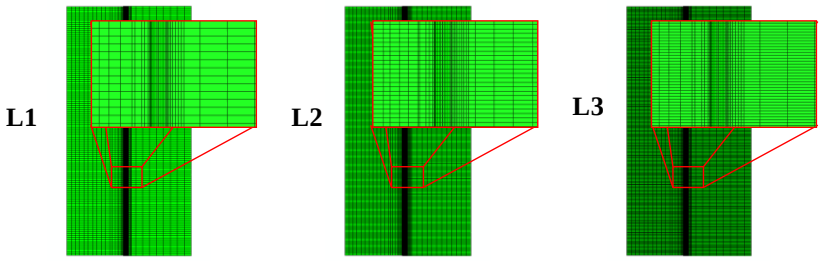

Figure 5-29 FE Meshes with element density coarsening in the longitudinal direction (L-Mesh).

Figure 5-30 shows the out-of-plane distortions obtained after the welding simulation for the meshes T1(S) and L3(S). For mesh T1(S), the first buckling mode has been obtained, whilst for mesh L2(S), with the same number of elements in the longitudinal direction, the second buckling mode has been obtained. This effect did not occur with reduced integration, or when using elements with incompatible modes. A comparison of the longitudinal stresses revealed that these are comparable for both meshes. In fact, the compressive stresses are slightly larger for the coarsened T-mesh which means that the same or even a higher order buckling mode could be expected. Hence, it can be assumed that the critical buckling load (CBL) must be mesh-dependent as well.

Figure 5-31 shows the calculated buckling amplitudes for all meshes. For some simulations the buckling direction is positive and for some negative. The buckling direction is dependent on the initial disturbance from equilibrium; both directions are almost equally possible but are not controllable in the simulations. Unfortunately, this restricts the possibility to compare the meshes since the amplitudes are not exactly the same in both directions due to lack of symmetry arising from the presence of filler material on the top side. However, a convergence tendency can be readily seen. For the L(I) meshes which are applied for the reference mesh, extrapolation shows a convergence level of ε=0.006 meaning that the distortion changes by 0.6 % if the number of elements is doubled. This convergence level is considered to be acceptable.

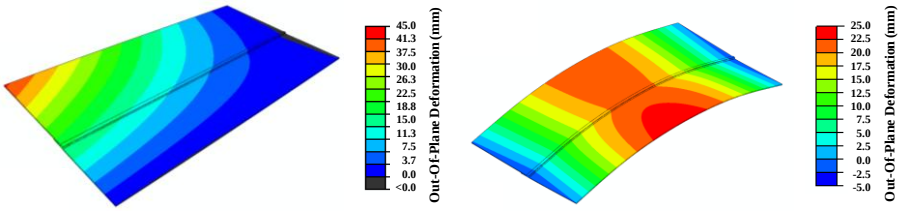

Figure 5-30 Out-of-plane distortions for mesh T1(S) (left) and mesh L3(S) (right).

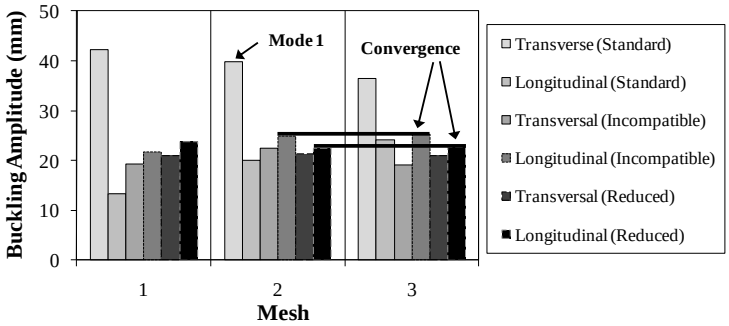

Figure 5-31 Calculated buckling amplitudes for all meshes and elements.

It can be concluded that if higher order buckling or bending modes are to be expected, either more elements must be incorporated within the model, or elements having a lower geometrical stiffness must be employed, for instance the (R) or (I) elements. The results also show that for a validation of the distortion model, not only do the material properties have to be considered, but discretisation properties as well. In particular, coarsening towards the outside is not suitable if bending or buckling is to be expected.

These results are interesting since it is common to apply many elements close to the weld seam for an adequate description of the steep temperature and stress gradients. However, many workers use coarsening towards the specimen edges [Pilipenko 2001, Aa 2007, Camilleri 2005, Friedman 1975]. Additionally, in most cases, linear elements are applied for the simulations [Aa 2007, Friedman 1975], although some works [Canas 1996] indicate that quadratic interpolation functions give more accurate results close to the weld seam.

5.3.2 Modal Analysis

In order to explain the mesh-dependence of the critical buckling load (CBL), modal analyses have been performed. Buckling in the present case occurs due to internal stresses without any external constraints. Considering a free flat sheet subjected to uniaxial loads, for instance, the CBL can be estimated from an eigenfrequency analysis. The CBL and the corresponding eigenfrequencies f are correlated quadratically:

$$CBL \approx const. \cdot f^2 . \qquad \textbf{Eq. 5-7}$$

In FE simulations, the eigenfrequencies and eigenmodes of the system can be calculated by [Belytschko 2001]

$$(-f^2\mathbf{M} + \mathbf{K}) \cdot \vec{\phi} = \vec{0}, \qquad \textbf{Eq. 5-8}$$

where $\vec{\phi}$ is the normalized eigenvector (eigenmode) of the system corresponding to an eigenfrequency. The calculation of the eigenvectors and eigenfrequencies can be performed using a Jacobian transformation [Press 2001], for instance. **Figure 5-32** shows the calculated second eigenmode of the T(S)-meshes and mesh L3(S). Most remarkably, the appearance of the buckling modes is dependent on the mesh density: For the L(S)-meshes, without coarsening towards the edges of the sample, the plate bends uniformly, while for the coarsened T(S)-meshes the bending is more pronounced at the centre line.

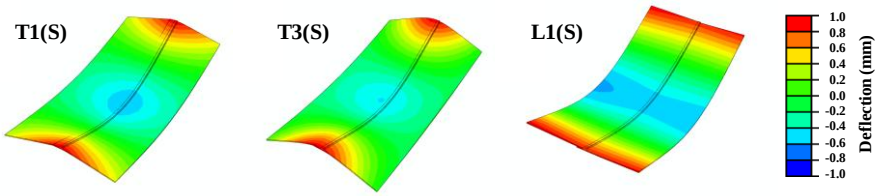

Figure 5-32 Appearance of the second eigenmode for the meshes T1(S), T3(S) and L1(S).

This can be explained by the shear locking of the finite element. Here, the shear locking in the coarsened outside region is larger since the element length in bending direction is increased. These results indicate that if higher buckling modes are to be expected, either more elements must be incorporated within the model, or elements having a lower geometrical stiffness must be employed. The results also show that for a validation of the distortion model, not only do the material properties have to be considered, but geometrical properties as well.

Figure 5-33 shows the convergence behaviour of the eigenfrequencies of the second eigenmode. The fastest convergence rate has been found for the (I)- and (R)-elements. If the (S)-elements are employed, the L-meshes converge much faster than the T-meshes. Comparing the results to **Figure 5-31**, a correlation between the eigenfrequency and the buckling amplitude can be seen. This supports the assumption that the eigenfrequency, the critical buckling load and hence, the buckling amplitude are correlated. Simulations with (R)-elements converge towards lower eigenfrequencies which might be due to the under-integration of the element. Unfortunately, it is not possible to predict such behaviour and element dependency must be investigated by trial and error.

Comparing the results obtained for mesh L1(R) with the converged results for L3(I), the deviation is about ten percent, whilst the computational time is reduced by a factor of thirty: a factor of ten due to the mesh and a factor of one third due to the element choice. In some cases, for instance for parameter studies, this gain of speed might outweigh the loss of accuracy.

For mesh convergence analyses for the simulation of buckling distortion, it seems to be favourable to apply either an eigenmode analysis or a calculation of the error value of the expected buckling shape. This is possible in a fraction of the computation time required for the completion of the whole welding simulation; *i.e.*, some minutes instead of days.

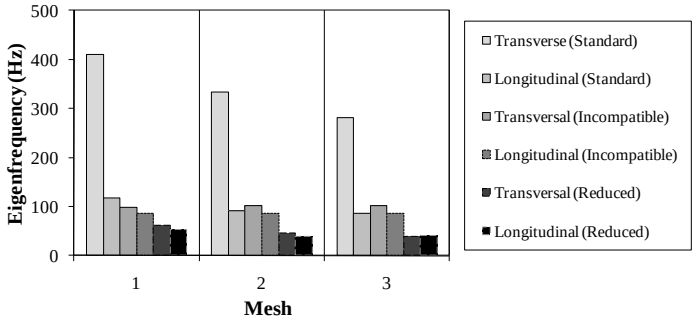

Figure 5-33 Eigenfrequencies of the second eigenmode.

5.3.3 Error Estimation

Starting from the Galerkin-method [Belytschko 2001], see **subsection 4.2.2**, and applying the finite element method, there is always a difference between the stresses at the borders of adjacent elements. For instance for 1D linear elements, bending is constant within the element and hence, the shear strain and stress as well. These constants are in general not the same for adjacent elements. The deviation of the stresses between two adjacent elements can therefore be employed in order to give an error indication [Ohnimus 1996]. The total deformation energy E of the model is calculated via:

$$E = \sum_{nE} \sqrt{\int_V \sigma \cdot C^{-1} \cdot \sigma \, dV} \,, \qquad \textbf{Eq. 5-9}$$

where σ, C and V refer to the space dependent stress and stiffness and the volume of an element. The summation is performed over all nE elements. The energy error indicator is calculated for each element using the Zienkiewicz-Zhu criterion [Zienkiewicz 1987]:

$$\Delta E = \sum_{nE} \sqrt{\int_V (\sigma - \sigma_h) C^{-1} (\sigma - \sigma_h) dV} \,/\, E \,, \qquad \textbf{Eq. 5-10}$$

were, σ_h is the so-called "smoothed" stress state obtained within the element by an interpolation of the average stresses at each node for all adjacent elements. The total error of the element is obtained by integrating over the whole element volume. The summation of all element errors yields the total error of the simulation.

Table 5-5 shows the calculated energies and error indicators for all meshes. No of the energy indicator with the meshes could be observed. The value ranges for most meshes five to seven percent which is generally considered to be acceptable. For reduced integration,

the error is somewhat higher throughout all meshes, which might be due to the under-integration of the element. However, it is unclear how the error of 94% of the T1(S)-mesh can be explained.

In order to understand the failure of the Zienkiewicz-Zhu error indicator as convergence criterion, **Eq. 5-10** has to be considered: The error indicator determines the quality of the stress calculation and might therefore be appropriate for a stress convergence analysis. The influence of displacements and deformations are ignored in this definition. Since it has been found that the geometrical stiffness has no significant influence on the residual stress distribution, this error indicator can unfortunately not be employed.

Table 5-5 Calculated normalized energy and error indicator for all meshes under consideration and three element types**.**

		T1	**T2**	**T3**	**L1**	**L2**	**L3**
(S)-Element	E	1.62	1.89	1.69	1.13	0.97	0.71
	ΔE (%)	94.0	4.5	5.1	6.2	7.0	5.6
(I)-Element	E	0.89	1.11	1.18	0.91	0.91	0.91
	ΔE (%)	7.0	7.4	7.5	7.2	7.2	7.1
(R)-Element	E	0.76	0.75	0.81	0.63	0.63	0.64
	ΔE (%)	23.0	23.5	26.1	23.8	25.6	25.9

However, a correlation can be found between the total deformation energy *E*, the eigenfrequencies and the buckling amplitude by comparing **Table 5-5** to **Figure 5-31** and **Figure 5-33**. The eigenfrequencies, and hence the critical buckling load, are higher for coarse meshes due to the geometrical stiffness, and converge towards the real value for finer mesh densities. It can also be seen that there is a correlation between the eigenfrequency and the energy of the mode. For a minimum geometrical stiffness the energy required in order to obtain a certain deformation state converges to a constant value and hence, it is also possible to apply the deformation energy as a quantity for a convergence analysis. For the full-integrated (S) and (I) elements, which possess asymptotical correctness, the energy even converges towards the lowest value.

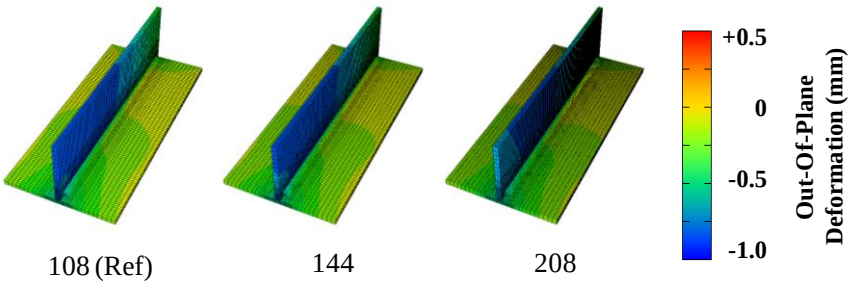

Figure 5-34 Out-of-plane deformation for the S355 T-joint for different numbers of elements in longitudinal direction.

Based on the results presented above, the reference mesh for the 6mm S355 T-joint was created. Elements with incompatible modes; *i.e.*, the (I) elements, have been applied

without any transverse coarsening. The number of elements in the longitudinal direction is 108. **Figure 5-34** shows the out-of-plane deformations for variations of the longitudinal mesh density. Obviously, there is no significant dependency on the mesh in this case.

5.4 Sensitivity Analysis

In order to determine the robustness of the welding model, it is generally proposed to perform sensitivity analyses [Lindgren 2002] (see also **subsection 2.2.3**). Here, model parameters, *e.g.* material properties, are changed and their influence on output variables, here the residual welding distortion, is assessed.

5.4.1 Sensitivity Analysis

In order to perform accurate simulations of the welding process, large numbers of material and process parameters are required to fit the models. Care must be exercised regarding the choice of the material model and the material properties. It is common to neglect certain effects to simplify the physics, see **subsection 2.2.3**. However, it is not always clear if these simplifications are reasonable. Hence, it is required to perform sensitivity studies in order to evaluate the dependency of the final welding distortion on different variables. In the present section, the results obtained for both case studies are presented for the cold release condition. For the 1 mm DP600 overlap joint, the buckling amplitude has been evaluated and in case of the 6 mm S355 T-joint, the maximum out-of-plane distortion amplitude. The analyses have been performed for variations of

- The assumed volume change at phase transformations,
- The mechanical behaviour,
- The clamping model and behaviour and
- The temperature-dependency of the thermomechanical model parameters.

Phase Transformation

Table 5-6 shows variations of the phase volume change from austenite to ferrite or martensite as obtained from literature, see **subsection 2.2.2** and **5.2.5**. In case (7), the dependency of the yield stress on the martensite volume fraction has been neglected. The resulting distortion amplitudes are shown in **Figure 5-35**. Additionally, the total phase volume changes after welding are shown for the DP600 overlap joint.

In general, the variations of the phase volume change resulted in changes of the predicted distortion amplitude of maximum 25 %. In case of the T-Joint, it has been found that the maximum bending amplitude is at the specimens edges in some cases (1,5,6,7) and at the centre below the stiffener in others (2,3,4), see also **subsection 5.2.5**. This makes comparisons much more complicated.

Table 5-6 Assumed phase volume changes.

Case	Austenite → Ferrite	Austenite → Martensite
(1)	0.00 %	0.00 %
(2) – Reference	1.30 %	1.00 %
(3)	1.30 %	4.40 %
(4)	0.77 %	4.40 %
(5)	0.77 %	1.00 %
(6)	0.77 %	0.80 %
(7) – No Yield Stress Change	1.30 %	1.00 %

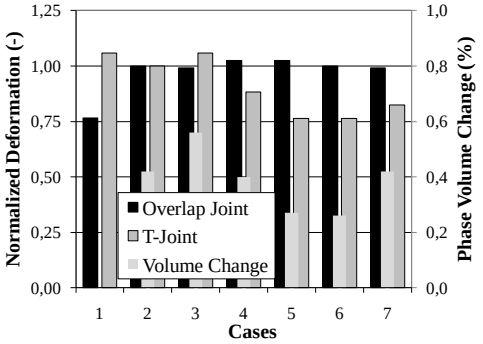

Figure 5-35 Distortion amplitude for the variations of the phase volume change as shown in **Table 5-6** and phase volume changes after welding of the DP600 overlap joint.

Based on these findings, it seems to be difficult to deduce general rules. In particular, for the GMA welding process employed, the martensite volume fraction is reduced, while for laser welding with its faster cooling rates, for instance, the opposite case might occur. However, it appears to be very important to characterise the phase volume change by dilatometer tests, for instance, instead of relying only on literature values.

Mechanical Behaviour

In order to investigate the effect of the strain hardening model, tests have been performed for the reference model and with 100 % kinematic or isotropic hardening, see **Figure 5-36**. It has been found that isotropic hardening overmatches the welding distortion, while it is undermatched with kinematic hardening. Hence, the reality is somewhere in-between. This effect can be understood because a higher deformation energy is required for plastic deformation of the workpiece in the case of isotropic hardening. This reduces plastic deformations and leads to higher stresses and distortions.

It is notable that the kinematic hardening model for the prediction of welding distortion in the case of the overlap joint presents a numerical result closer to experimental observation than the physically more realistic combined isotropic and kinematic approach. This illustrates that the choice of model should not necessarily be based on calibration; *i.e.*,

choosing the hardening approach which fits the model better, if the correct material behaviour is of interest.

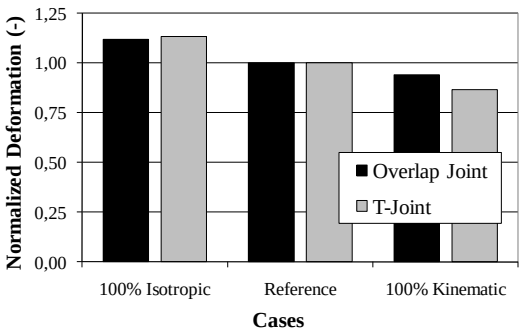

Figure 5-36 Distortion amplitude for the variations of strain hardening model.

Also the activation of the filler material affects the solution: Neglecting the volume of the fillet; *i.e.*, connecting the sheets directly, reduces the shrinkage force and lowers the distortion significantly. If the filler material is active from the beginning, welding distortion increases compared to the application of the quiet element technique. However, this affects the distortion less than neglecting the fillet.

Wyrwich [Wyrwich 2009] reported that Young's Modulus *E* decreases to 180 GPa for thin-rolled steel sheets due to the forming process. Since it is very complicated to determine Young's Modulus in tensile tests, its sensitivity has been assessed; however, it has been found that a change from 210 GPa to 180 GPa has no significant effect on the residual distortion. Also it has been found that neglecting the strain-rate dependency and Hill-Anisotropy has no significant influence.

Contact Model & Behaviour

Studies have been performed to investigate the influence of the clamping stiffness and the initial clamping pressure on the residual welding distortionTwelding distortion is only slightly dependent on these parameters for the present case study. The stiffness of the clamping system appears to be already within a converged range; *i.e.*, much stiffer than a threshold above which the distortion remains the same. This effect has also been noticed recently for a similar configuration in [Liu 2008]. However, it has been found that the maximum clamp reaction force *RF* at the end of the welding process of the T-joint is dependent on the clamp stiffness *E*, see **Figure 5-37**:

$$RF \approx A \cdot \left(1 - \exp\left(-b \cdot k\right)\right) \text{ , } A \approx 3kN \text{ , } b \approx 3 \cdot 10^{-5} MPa^{-1} . \qquad \textbf{Eq. 5-11}$$

Hence, there is an upper limit for the effective clamping stiffness and there might be no use in designing much stiffer clamps.

Figure 5-38 shows the influence of the contact stiffness on the residual welding distortion. In particular, it can be assumed that the contact stiffness does not affect the

results significantly as long as its value is much higher than the stiffness of the clamping system. The error due to the contact stiffness is approximately:

$$Err = Contact\ Stiffness\ /\ Clamp\ Stiffness. \qquad \textbf{Eq. 5-12}$$

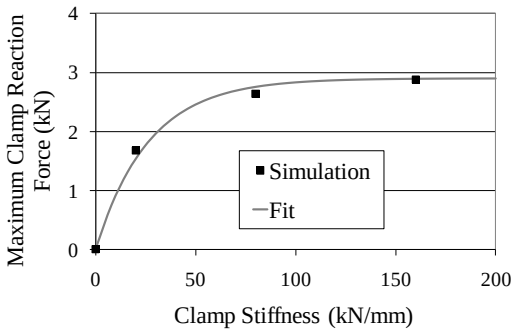

Figure 5-37 Maximum clamp reaction force at the end of the welding process of the T-joint as function of the clamp stiffness.

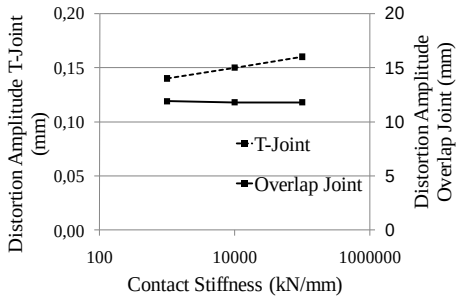

Figure 5-38 Influence of the contact stiffness on the residual welding distortion.

In order to determine the influence of the friction coefficient μ, its value has been varied between 0.1 and 0.5. It was found that the influence of the friction coefficient on the final welding distortion is approximately 3 %, which is rather small compared to other effects.

Temperature Dependency

In order to evaluate the influence of the temperature-dependency of the yield stress and the strain hardening, three simplified dependencies have been modelled, see **Figure 5-39** (left):

Case 1) Temperature-dependency ignored, only room temperature values applied
Case 2) Temperature-dependency simplified: Room temperature values up to 400 °C, and then linearly ramped down to zero at 1000 °C.
Case 3) Temperature-dependency simplified, room temperature values up to 350 °C, and then linearly ramped down to zero at 700 °C.

The different simplified temperature dependencies are derivated from the temperature-dependent yield stress shown in **Figure 4-19**. The results are shown in **Figure 5-39** (right). For the simplified temperature-dependencies, strong deviations have been found: The predicted welding distortion is overestimated significantly by the simulations. This effect is probably due to the strong material stiffness modelled in these cases compared to the reference model. The neglect of the strain-rate dependency as well as reduced Young's Modulus has no significant effect on the predictions.

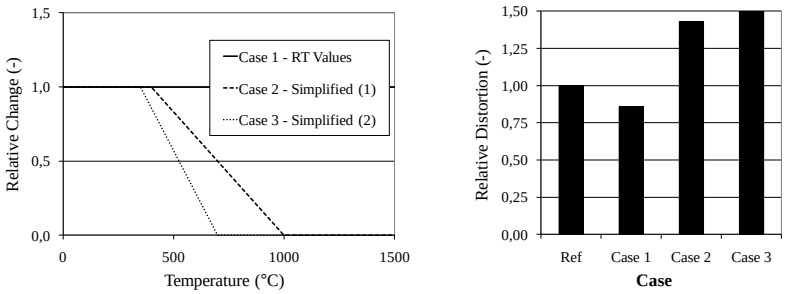

Figure 5-39 Left: Simplified temperature-dependencies. Right: Relative changes of the welding distortions for the DP600 overlap joint compared to the reference model.

5.4.2 Summary

Table 5-7 summarises the findings of the performed sensitivity analyses; there is a very strong influence of the mesh density on the predicted welding distortion if the mesh is not within a converged domain. Within the converged domain, there should not be any significant change for small mesh modifications.

Table 5-7 Results for the sensitivity analysis.

Variations	Result
Mesh Density	⇔
100% isotropic hardening instead of mixed	
100% kinematic hardening instead of mixed	
Fillet: Volume of filler material neglected	
Fillet: Activated from the beginning	
Volumetric phase change	
Influence of martensite on yield stress neglected	
Young's Modulus reduced	
Strain-Rate Dependency neglected	
Hill-Anisotropy neglected	
Friction Coefficient to μ=0.5 / μ=0.1	
emperature-Dependency	

0-5%, 5-10%, 10-20%, >20% Deviation

5.5 Concluding Remarks

In the present chapter, the thermomechanical-metallurgical welding model presented in **chapter 4** has been applied to the simulation of gas metal arc welding of a 1 mm thick DP600 overlap joint and a 6 mm thick S355 T-joint. The experimental validation measurements have been performed for a hot release condition, where the clamps are opened immediately after welding and the workpiece cools down freely, and a cold release, where the workpiece is restrained and remains in intimate contact with the clamping assembly during cooling. For the validations, temperature, phase fraction, distortion, and residual stress measurements have been performed and compared to the simulations. Additionally, the results of tensile tests have been validated for the DP600 overlap joint.

In case of the DP600 overlap joint, the second buckling mode has been obtained as the dominant distortion mode. The agreement between simulations and experiments is good. In particular, a general overmatching of about 15 % of the simulations has been found. Here, the material response appears to be too stiff. The reason for this behaviour is not clear, although it has been found that the results are improved if the mechanical behaviour of the filler material is softened. Another error source is the phase transformation behaviour. It has been found that the martensite volume fraction is underestimated in the model. This causes higher contractions compared to the experiments and hence, increases residual stresses and distortions.

It has been found that the residual longitudinal stresses as well as the failure in tensile tests are determined by the geometry rather than the modified material behaviour in the fusion zone and the heat-affected zone due to welding. In particular, the qualitative

distribution of the longitudinal stresses after welding could be modelled using a simple 300 bar model.

In the case of the S355 T-joint, the dominant distortion mode is angular distortion in case of no clamping and also for the hot release condition. The predictions are well within the experimental standard deviation in these cases. However, it has been found that the experimental standard deviation is very high (about 30 %). The most likely reason for this is the influence of the predeformation. Here, the amplitude of the predeformation is about one third of the final distortion amplitude. If the initial predeformation shape is taken into account in the model, a good agreement with experiments can be achieved.

The distortion mode switches to bending distortion for the cold release condition. Here, a good agreement has been obtained for the bending amplitude. However, in experiments the bending is most pronounced at the edges of the workpiece while in simulations, bending is most pronounced underneath the stiffeners. This is a very important aspect if the workpiece is considered to be part of a large assembly; the reaction force might differ significantly for the two conditions. The two most likely reasons for this behaviour have been found to be the material hardening parameters and the assumed phase volume change: If the material is stiffer, as assumed in the model or if the phase volume strains are reduced, bending shifts to the edges.

For both case studies, mesh convergence analyses have been performed. It has been found that for standard linear elements, the geometrical stiffness is high and affects bending as well as the critical buckling load. It is recommended to apply elements with integrated incompatible modes in order to overcome this problem. Additionally, the geometrical stiffness is reduced significantly if no coarsening of the mesh towards the workpiece's edges is applied. In order to perform mesh convergence analyses, it has been found that the application of modal analyses is effective and much faster than welding simulations; *i.e.*, the calculation time for one test is in the order of minutes instead of days.

The models have been subjected to sensitivity analyses in order to evaluate their robustness. Such analyses are important in order to find and exclude possible error sources for inaccuracies in the model. It has been found that the most influential parameters here are the hardening model, the filler material and the volume change due to phase transformations.

6 Influence of Clamping & Sequencing

In the previous chapter, a model for welding simulations has been presented and validated experimentally for two case studies. The present chapter deals with the influence of the clamping conditions and the welding sequences on the distortion behaviour.

6.1 DP600 Overlap Joint

6.1.1 Clamping Release Time

In the previous chapter, it has been found that the buckling direction changes and the distortion amplitude is reduced for the cold release condition. The simulations and experiments have been repeated for intermediate release times between the hot and cold release condition, see **Figure 6-1**. The buckling amplitude and direction are shown as a function of the clamp release time after completion of welding. The results for t = 0 s and t = 500 s correspond to the hot and cold release condition, respectively. There is a good agreement between experiments and the numerical predictions for the switch of the buckling direction as well as the buckling amplitude. On average, the deviation between simulations and experiments is about fifteen percent.

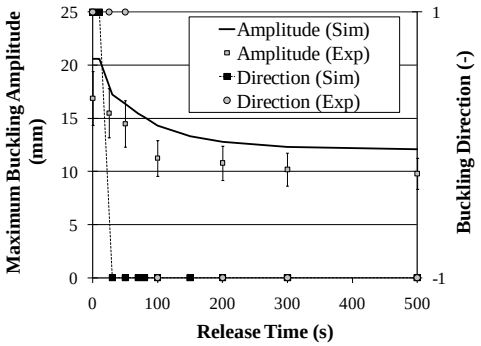

Figure 6-1 Influence of the clamp release time on the buckling amplitude and buckling direction. +1 and -1 correspond to the buckling direction up and down, respectively.

The weld zone is subject to tension, which can be explained by the thermal shrinkage of the hot material which tries to contract but is restrained by the adjacent base material. In an equilibrium state, compressive stresses arise in the base material due to the tensile stresses in the weld seam. These compressive stresses cause the buckling distortion. In the cold release condition, there is a larger restraint at the outside due to the clamps, compared to the hot release condition, which hinders weld seam contraction. This leads to higher plastic strains and hence, to lower elastic strains and stresses remaining after release of the clamps.

This effect of longer clamping times can be studied using the 300 bar model presented in **subsection 5.1.4**. **Figure 6-2** shows the longitudinal residual stresses obtained from the bar model. In order to simulate the hot release condition, the nodes at the top side remain unrestrained. In the case of the cold release, the nodes at the top side have been fixed during welding and released afterwards. It can be seen that for the cold release condition, the longitudinal residual stresses are increased after welding and prior to release. The restraints cause higher hardening and plastic deformations. Hence, after release of the clamps, the remaining elastic strains as well as the residual stresses are lower. Since the buckling distortion amplitude is correlated to the compressive longitudinal residual stresses, it is also lowered as a result.

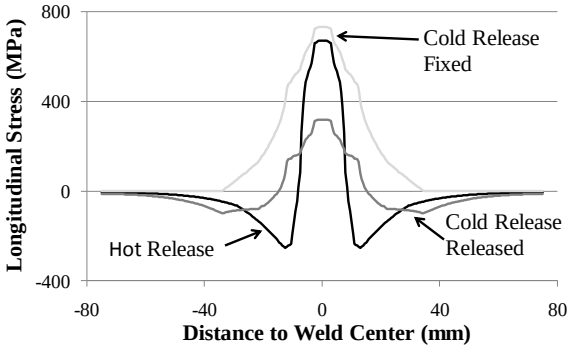

Figure 6-2 Longitudinal residual stress distribution as obtained for the 300 bar model with free and released nodes at the top side.

Here, the clamping system plays the role of an additional stiffener. This effect can also be explained with reference to **Figure 6-3**. Due to this higher stiffness, the material in the weld zone deforms more plastically which yields a larger relief of the elastic strains and hence the resulting residual stresses become smaller. It has been found from the simulations that the longitudinal tensile stresses in the HAZ are reduced by about 100 MPa if the clamps are released after cooling. This is accompanied by an increased plastic deformation Δp of 2.29 % to 2.39 % (taken form the centre of the fillet). Hence, the elastic strains are reduced by a tenth of a percent, which yields a theoretical reduction of

$$\Delta\sigma = E \cdot \Delta\varepsilon \approx E \cdot \Delta p = 200 MPa \; . \qquad \textbf{Eq. 6-1}$$

This estimation is already close to the relieved stress found in the simulations. It can be assumed that the higher value results from neglecting the temperature-dependent stiffness.

Unlike the process of mechanical tensioning, which is able to reduce the residual stresses to zero, it should be mentioned that this is not possible with the clamping system employed here. In order to reduce the residual stresses to zero, the weld zone has to be deformed more which can only be obtained by another superposed tension.

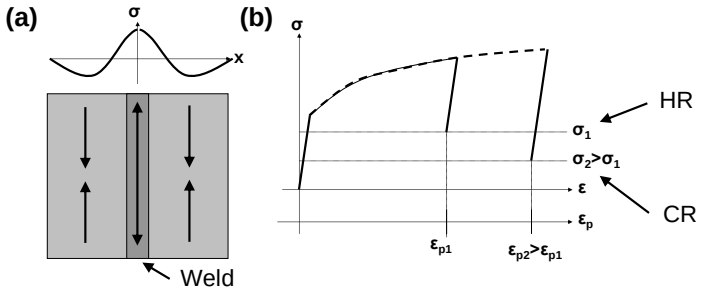

Figure 6-3 (a) Longitudinal stress distribution. (b) Influence of the clamping time on the plastic deformation.

6.1.2 Delayed Clamping

Additionally to longer clamping release times, the clamping time has been modified using delayed clamping, as shown in **Figure 6-4**. The remaining sets of clamps become active as soon as the welding torch reaches their position.

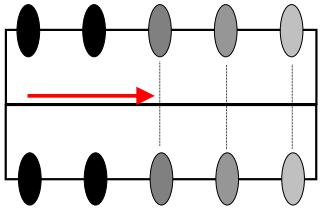

Figure 6-4 Transient clamping: The first two clamps are active from the beginning.

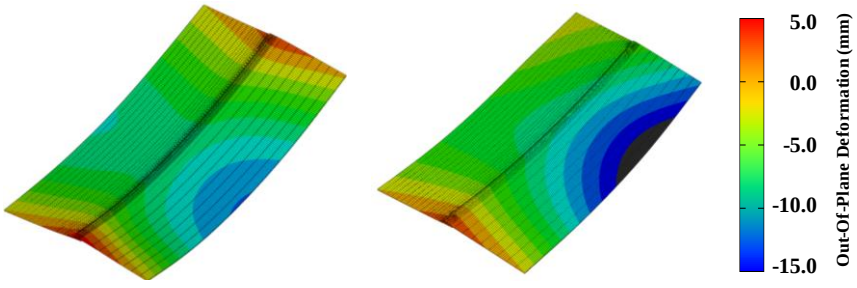

Figure 6-5 Deformation shape and deformation magnitude for the cold release with all clamps active from the beginning (left) and with delayed clamping (right), respectively.

Due to numerical reasons, the first two sets of clamps were both active from the beginning. Using only the first set of clamps does not restrain the workpiece strongly enough leading to iteratively opening and closing of the contact conditions between the workpiece and the backing which yields numerically unstable contact conditions.

In **Figure 6-5**, the final distortion of the cold release condition is compared for an activation of the clamps at the beginning and the late clamping. Here, the lower plate does not buckle anymore. The increase of the buckling amplitude at the top plate might be due to the fact that the stresses cannot be redistributed in a homogeneous distortion shape as for the standard cold release condition. Unfortunately, it has not been possible to perform experiments with late clamping using the present equipment.

In order to explain the effects during delayed clamping, the 300 bar model is applied. Here, for delayed clamping, the bars are allowed to expand freely upon heating and are restrained only during cooling. The resulting longitudinal stress distributions using this model are shown in **Figure 6-6**. For the late clamping condition, the distribution of the longitudinal stresses is more homogeneous than for the standard clamping condition. The reason for this behaviour is that the material extends due to heating and is then clamped in the extended state. Hence, the weld seam is forced to undergo additional plastic deformation while cooling due to the effective thermal pre-strain. This reduces the final longitudinal stresses at the weld seam after release of the clamps and hence, the resulting buckling amplitude. It should be noted that this effect is only significant for the cold release state and is understandably negligible for a hot release.

Delayed clamping condition is considered again in **subsection 0** which discusses the automatic optimisation of the clamping conditions using simplified models.

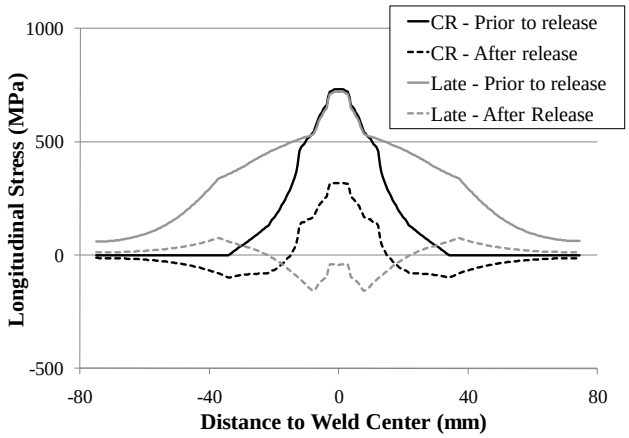

Figure 6-6 Longitudinal residual stress distribution obtained for the 300 bar model for the cold release condition with and without delayed clamping prior and after clamp release.

6.1.3 Preheating

The effect of preheating of the clamps has been investigated for preheating temperatures of 200 °C and 300 °C. Here, in a steady state taking account of the heat loss to the surrounding environment, the temperature at the weld seam prior to welding reaches about 60 ° less than the preheating temperature of the clamps, see, **Figure 6-7**. Using such a preheating, the model predicts a reduction of the distortion amplitude. This is the result of

two effects: Firstly, the temperature gradient in the material is reduced, which allows for a more homogeneous contraction of the workpiece in the longitudinal direction on cooling, and hence lower longitudinal residual stresses. Secondly, the preheating also reduces the cooling rate and hence, the martensite fraction is reduced and the bainite fraction is increased which reduces the strength of the weld.

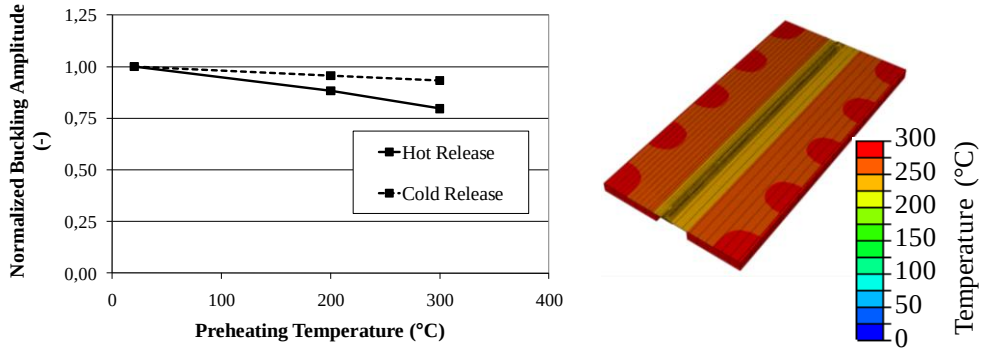

Figure 6-7 Left: Normalized buckling amplitude for various preheating temperatures. Right: Preheated sample for a preheating to 300 °C.

6.2 S355 T-Joint

6.2.1 Clamping Time

In the case of the 6 mm thick S355 T-Joint, it has been found that angular distortion is dominant for the hot release condition while bending is dominant for the cold release condition. **Figure 6-8** shows the out-of-plane distortion for various intermediate release times between the hot release condition at t = 0 s and the cold release condition at t = 3000 s. The distortions at the center are evaluated at two points parallel to the weld seam.

In order to understand the diagram, the deformations at the outside and the inside have to be compared: Angular distortion is present if the distortion at the outside (point 2) is larger than at the inside (point 1), otherwise there is bending distortion. In any case, there is some angular distortion present at the start and the end of the weld seam. As mentioned before, the deformation is dominated by angular distortion in the case of the hot release. However, already for a release time of 25 seconds, bending distortion becomes the dominant deformation mode. Additionally it has been found that the total deformation amplitude; *i.e.*, the bending amplitude, is reduced by approximately one third for longer release times.

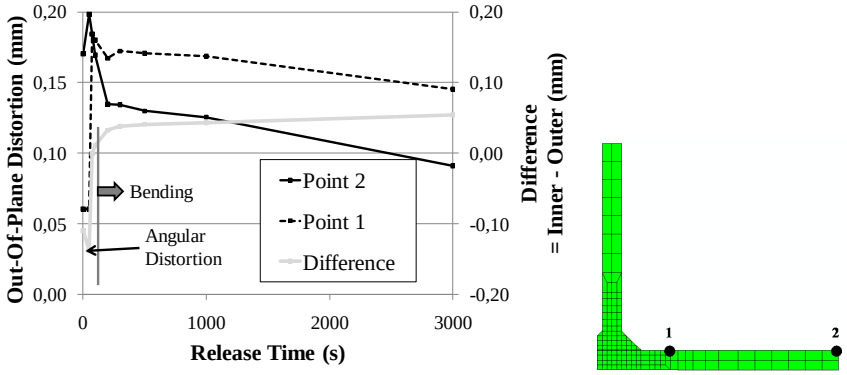

Figure 6-8 Predicted out-of-plane deformation at the cewnter of the flange for several release times at the outside (point 2) and close to the weld (point 1).

In GMA welding, there is a through-thickness gradient of the thermal shrinkage due to the varying extension of the molten zone and peak temperatures. This causes elastic shear strains at the weld seam. If the material is not restrained, these strains are relieved and angular distortion occurs. For increased release times, the elastic shear strains are reduced while the plastic shear strains p_{13}, where 1 and 3 are the transverse and the out-of-plane directions, increase due to the clamping conditions (see **Figure 6-9**), which leads to the observed reduction of the angular distortion. If angular distortion is suppressed, bending distortion appears due to the difference in longitudinal residual stresses in the through-thickness direction as a results of the one-sided deposition of filler material.

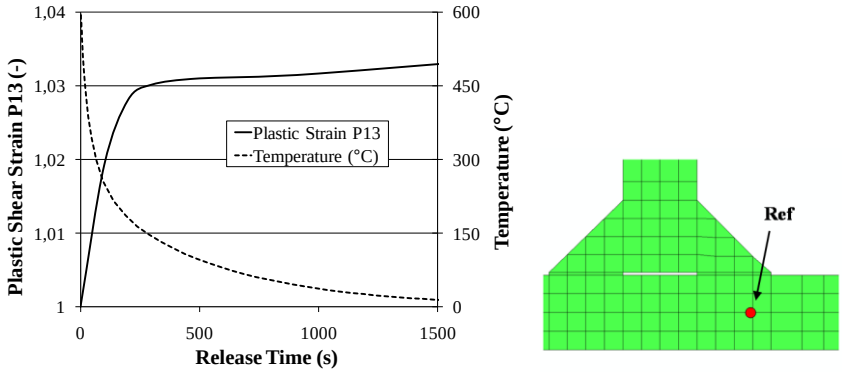

Figure 6-9 Normalized plastic shear strain (at release time t=0s) and total temperature at point Ref in the weld seam.

The reduction of the bending amplitude for higher release times can be explained with reference to **Figure 6-10**. The accumulated plastic strains in the seam at the top side and the bottom side of the flange are compared after welding has been completed. The initial difference is due to the viscous flow at the top side due to the melting process. This occurs

without the creation of residual stresses. The development of the difference between both determines the amount of bending: Smaller differences mean more homogeneous deformation, and hence less bending.

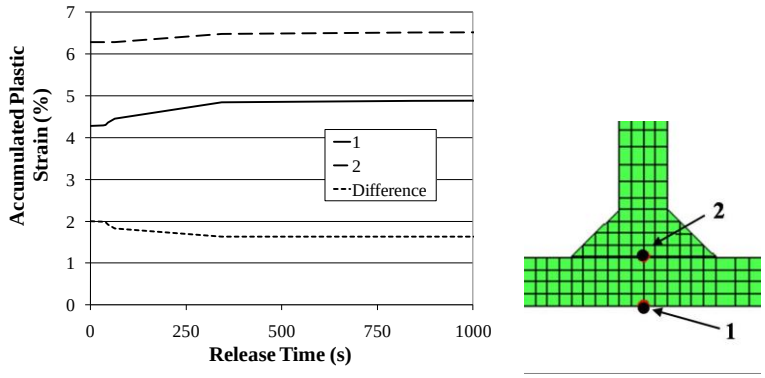

Figure 6-10 Accumulated plastic strains in the seam at the top side (2) and the bottom side (1) of the flange.

Workpiece Size Effects

For the present configuration, angular distortion is suppressed already for short clamping times. In order to investigate this effect, the simulations have been repeated with a sample length of 900 millimetres, see **Figure 6-11**. Hence, the sample is about three times longer and fifteen clamps have been used. As expected, the whole plate exhibits bending in this case for both hot and cold release due to the longer clamping time resulting from the longer welding time. Also in this case, the distortion amplitude is reduced for longer clamping times. At the end of the weld seam, some small angular distortion can be seen again.

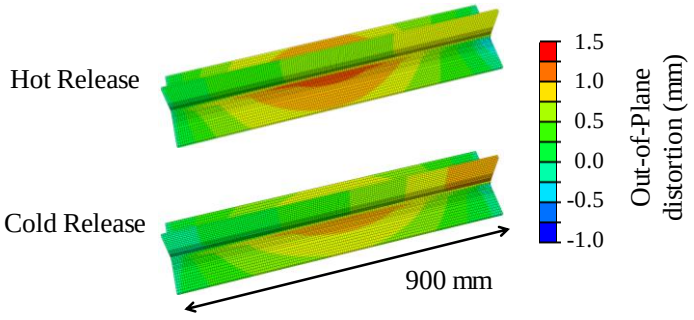

Figure 6-11 Predicted out-of-plane deformation for hot and cold release, respectively, for a sample length of 900 millimetre.

6.2.2 Transient Clamping Force

It is possible to measure the workpiece interaction with the clamps by recording the transient clamping pressure. **Figure 6-12** shows the numbering of the clamps and the pressure sensors.

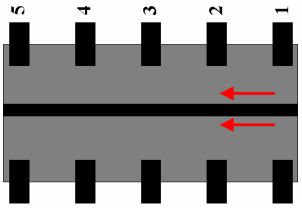

Figure 6-12 Numbering of the clamps and pressure sensors. The arrows indicate the welding direction.

In order to investigate which effects can be expected, a simple 2D finite element (FE) model has been created as shown in **Figure 6-13**. The model consists of 940 plane stress elements (ABAQUS CPS3 and CPS4). The heat input has been modelled using a 2D simplification of the Goldak heat source. **Figure 6-13** shows the simulated transient clamping pressure obtained from the 2D model. It can be subdivided into four phases:

1. Liquid filler material is added, the workpiece at the weld seam heats up and expands.
2. The weld cools down and contracts, angular distortion occurs.
3. The weld contracts further, the material below the clamps heats up and expands due to heat conduction from the weld.
4. The material below the clamps cools down to room temperature and contracts. Angular distortion becomes suppressed by the mechanical restraints.

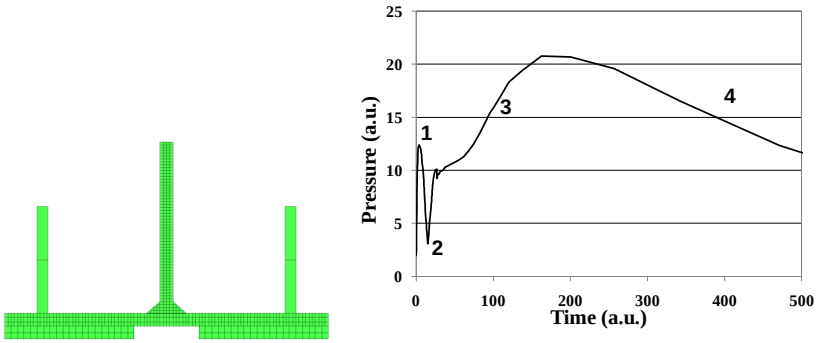

Figure 6-13 2D model and simulated transient clamping pressure.

After the final cooling to room temperature, a steady state condition is reached where no further changes of the distortion and the clamping pressure occur. If angular distortion is suppressed completely by plastic deformations, the pressure reduces asymptotically to zero during cooling. 3D bending cannot be identified with this model.

Figure 6-14 shows the measured clamping pressure of the hydraulic oil in the vertical clamp during and after welding. For longer clamping times, the pressures at the sensors show strong deviations from each other. This is the effect of the three dimensional bending distortion shown in the previous subsection and **subsection 5.2.2**. The pressure increase is the strongest at the clamps in the centre; *i.e.*, for sensors two to four. For the outer clamps, the increase is smaller and it is even possible that the pressure decreases.

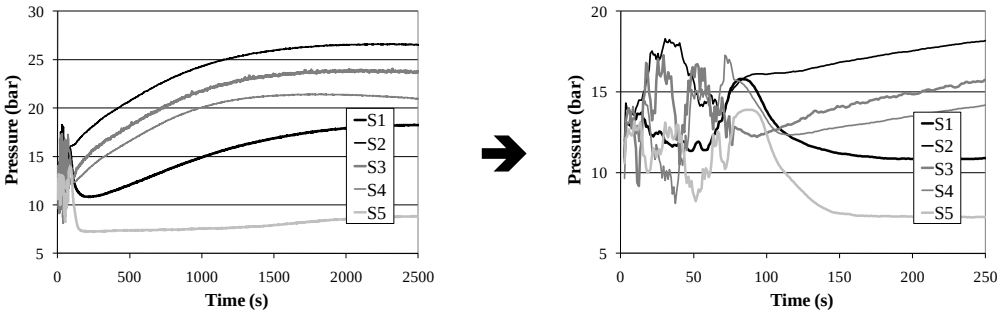

Figure 6-14 Measured transient clamping pressure for the S355 T-joint (left) and zoom in the initial development of the pressure (right).

In principle, it can be assumed that the pressure eventually reaches a constant level after cooling of the workpiece. The pressure decrease at longer clamping times, however, is the effect of a small leakage of the hydraulic clamping system, which unfortunately restricts the accuracy of the measurements. The measurements reveal some disadvantages of a hydraulic clamping system; the peaks obtained for higher release times can differ from measurement to measurement by up to five bar. Fortunately, the tendency for the transient clamping pressure development; *i.e.*, which sensors show the highest and lowest peaks, is always the same.

Regarding the peaks occurring during the welding process, within the first 250 seconds, two peaks can be identified instead of one as suggested by the 2D model. In order to investigate the difference between the 2D model, the predicted transient clamping pressure of the 3D welding simulation is shown in **Figure 6-15**. There is a good qualitative agreement between simulations and experiments. In particularly the same peaks appear at the same times for each clamp. The difference of the amplitude between the simulations and experiments is about 3-4 bars.

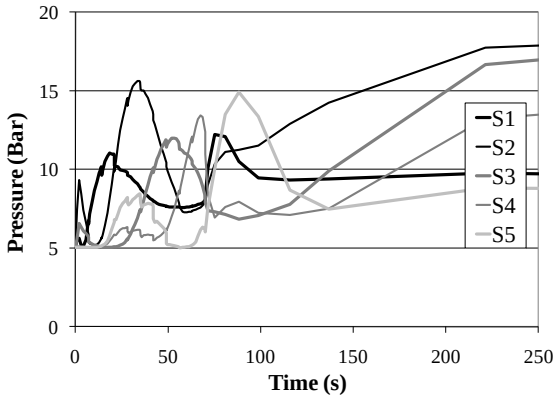

Figure 6-15 Predicted transient clamping force for the S355 T-joint for the first 250 seconds.

These findings lead to the conclusion that the occurrence of multiple peaks is due to 3D coupling between the clamps and cannot be explained using the 2D model. Unlike in two dimensions, a new phase is present in three dimensions as sketched in **Figure 6-16**: Angular distortion is suppressed (phase 4) and bending distortion appears (phase 5). This becomes obvious by comparing the measured clamping pressure to the welding distortions for the cold release condition shown in **Figure 5-21**.

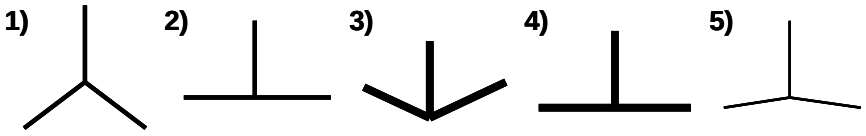

Figure 6-16 Phases during welding and subsequent cooling in 3D. Phase 5 is not pronounced in 2D and occurs due to the 3D bending shape.

6.2.3 Clamp Distance

In order to assess the influence of the clamping support distance from the workpiece edge on the welding distortions, simulations and experiments have been performed for three distances *d*: 40 mm, 50 mm, and 60 mm. The parameter *d* is defined in **Figure 6-17**. The clamps at the top are situated at a distance of 10 mm from the edges of the workpiece.

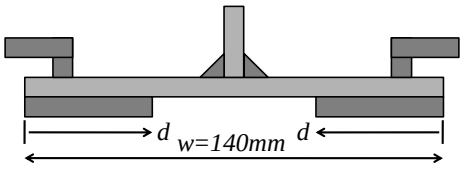

Figure 6-17 Definition of the clamping distance d.

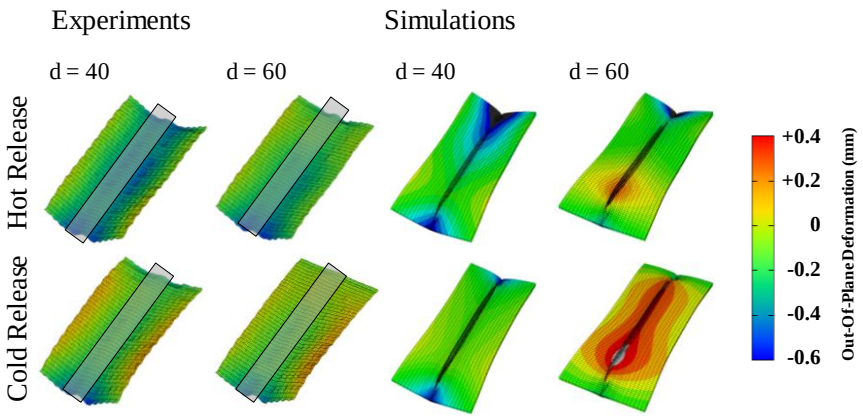

Figure 6-18 Measured and predicted effective welding distortion for different clamping support distances and the hot and cold release conditions, respectively.

Figure 6-18 shows the results for the final welding distortions obtained from the experiments and simulations, respectively. The results have been obtained for both the hot and cold release conditions. Two tendencies can be seen for all cases: Firstly, the amount of angular distortion is reduced for closer clamping support to the weld seam; *i.e.*, higher values of *d*. Secondly, angular distortion is suppressed for longer clamping times; *i.e.*, for the cold release condition. Here, bending distortion becomes the dominant distortion mode if angular distortion is suppressed. The amplitude of the bending distortion, however, is reduced for longer clamping and closer support as well.

Obviously, the qualitative tendencies are the same for both simulations and experiments. For details of the occurring deviations between experiments and simulations see **section 5.2**.

Simplified Models

In order to investigate the influence of the clamping distance on the angular distortion, two simplified models have been applied, see **Figure 6-19**; the first is a simplified shrinkage model using FEM. Temperature-independent isotropic ideal plastic hardening is assumed using a yield stress of 350 MPa. The initial temperature of the fillet is set to 1500 °C in order to simulate the addition of liquid filler material. The temperature of the fillet is ramped down to room temperature within ten seconds. The nodes at the clamping positions are fixed during and released after welding.

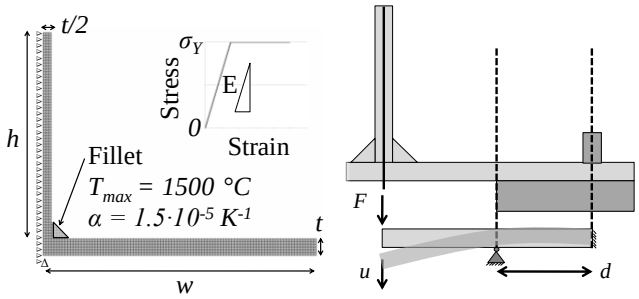

Figure 6-19 Simplified shrinkage model (left) and analytical planar beam model (right).

The second model applied is an analytical planar beam. The constant force F acting at one edge is assumed to correspond to the maximum elastic stresses the material can sustain on shrinkage. The angular distortion is then correlated to the displacement u due to the acting force F in the clamped configuration and a displacement $u_0=F/k$ depending on the stiffness of the material. Using beam theory, the displacement u can be calculated from

$$EI \cdot (u - u_0) = \frac{d}{6} \cdot \frac{F}{2} \cdot \left[4 \cdot w \cdot (w-d) + 5 \cdot (w-d)^2\right] + \frac{F}{3} \cdot (w-d)^3 \approx F \cdot (w-d)^3 , \qquad \textbf{Eq. 6-2}$$

where $EI = E \cdot b \cdot t^3$ is the bending stiffness of the beam and E is the Young's Modulus.

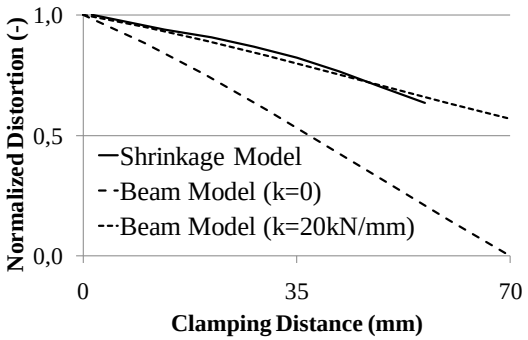

Figure 6-20 Normalized angular distortions for the shrinkage model and the planar beam model as a function of the clamping distance.

The angular distortions for both simplified models are shown in **Figure 6-20.** The calculated normalized angular distortions agree very well for an assumed materials stiffness of 20 kN mm^{-1}, which is within the order of magnitude expected for steels. The tendencies obtained for both the transient thermomechanical simulations and the experiments are supported by these models; a closer clamping support d results in less angular distortion. According to these results, it appears to be sufficient to study the effect of the clamping support distance on angular distortion using simplified models. However, these models are incapable of predicting the switch from angular to bending distortion.

6.2.4 Prestraining

For a compensation of angular distortion it is assumed that an adequate prestraining of the initial geometry is useful, see **subsection 3.2.4**. In order to investigate this effect, the welding distortion for the hot release condition with a clamping support distance of 50 mm has been examined using an elastic prestraining with an amplitude of 0.8 mm. **Figure 6-21 (left)** shows the prestraining applied for the T-joint which is applied during clamping below the stiffener and kept until the clamps or released.

The results from simulations and experiments are shown in **Figure 6-21 (right)**. The angular distortion has been suppressed completely and again bending distortion occurs as the dominant distortion mode. This is due to the geometry which allows 3D bending of the workpiece.

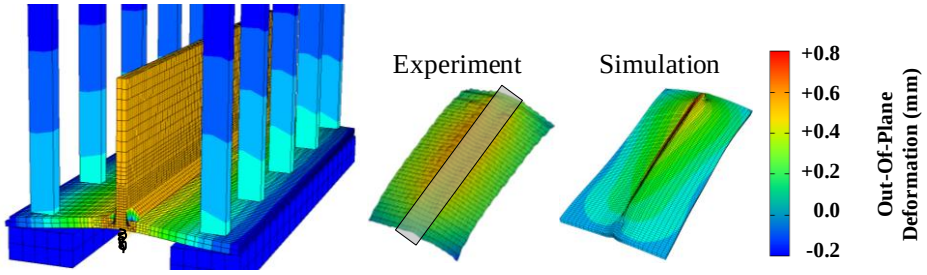

Figure 6-21 Prestraining of the T-Joint during clamping.

6.3 Welding Sequencing

In **subsection 3.2.1**, a literature survey has been presented on the influence of welding sequences on residual stresses and distortions. In order to investigate this effect, the influence of welding sequences on the residual welding distortion has been examined for gas metal arc welding of 6 mm thick S355 T-joints and 1 mm thick DP600 overlap joints for various sequences and the results are reported in this section.

6.3.1 Selected Sequences & Temperature Profile

Figure 6-22 shows the welding sequences under investigation. The reference sequence refers to welding in one step. Various sequences have been investigated using four and eight steps and combinations of forward and backward welding. The sequences one and two correspond to the sequences shown in **Figure 3-15**. The sequences one and three are commonly referred to as backstep or pilgrim welding. **Figure 6-23** shows the temperature profile during welding as function of the time along the weld seam for the 1 mm thick DP600 overlap joint. In the case of the 6 mm thick S355 T-joint, the temperature profile has the same appearance with time scaled by a factor two as these were welded at half the welding speed.

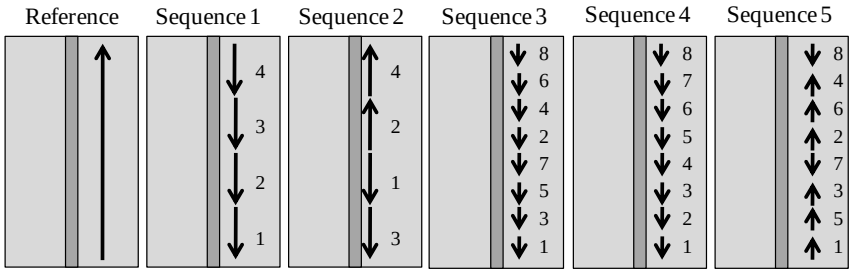

Figure 6-22 Applied welding sequences.

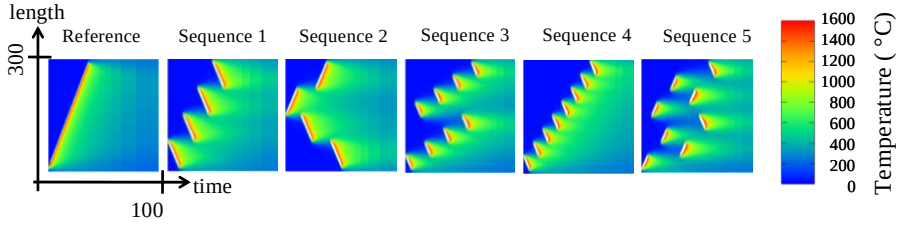

Figure 6-23 Temperature profile during welding as a function of the time along the weld seam for the 1mm thick DP600 overlap joint.

Regarding the temperature profile, in particular for the last three sequences, two possibilities have been identified in order to explain the effect of sequencing on the distortion behaviour: Firstly, weld sequencing leads to a *preheating* of the material. It is known that preheating reduces the temperature inhomogeneity and hence, leads to lower distortion, see **subsection 6.1.3**. In particular, for sequence five, the whole sample is preheated when the last sequence is welded. Secondly, the workpiece is subjected to *reheating* at the edges. This effect is similar to annealing, which is sometimes applied for stress relaxation after welding [Josefson 1983, Provost 1981]. For example, annealing was performed by Berglund et al. [Beglund 2001] for an aerospace component where the welding residual stresses were reduced by 80 %.

6.3.2 Welding Distortion & Plastic Deformations

Figure 6-24 and **Figure 6-25** show the predicted and measured out-of-plane distortion for both case studies and all sequences under consideration. In the case of the DP600 overlap joint, the second buckling (bending) mode has been obtained for all sequences. There is a good agreement between simulations and experiments. The deviation is about 20 %; see **section 5.1** for more details regarding the accuracy.

In the case of the S355 T-joint, the deviation between experiments and simulations is about 30 % while the tendencies agree well in general. In particular, bending is most pronounced at the edges of the plate in experiments while in the simulations, the maximum amplitudes are below the stiffener. In **section 5.2**, a sensitivity study is presented which indicates that this deviation is due to the assumed material stiffness; *i.e.*, the application of

literature values for the thermomechanical behaviour of the steel instead of values obtained from measurements for this particular plate. Additionally, it has been found that the experimental standard deviation is about 0.15 mm which is relatively high compared to the total deformation amplitudes (about 30 %), see **Figure 5-20**.

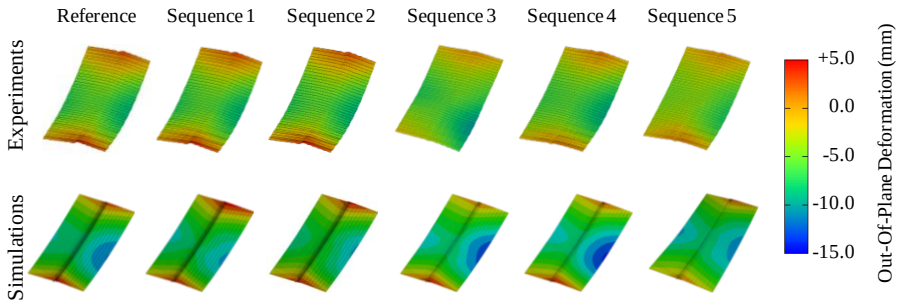

Figure 6-24 Predicted and measured buckling distortion for the 1mm thick DP600 overlap joint and all sequences under consideration.

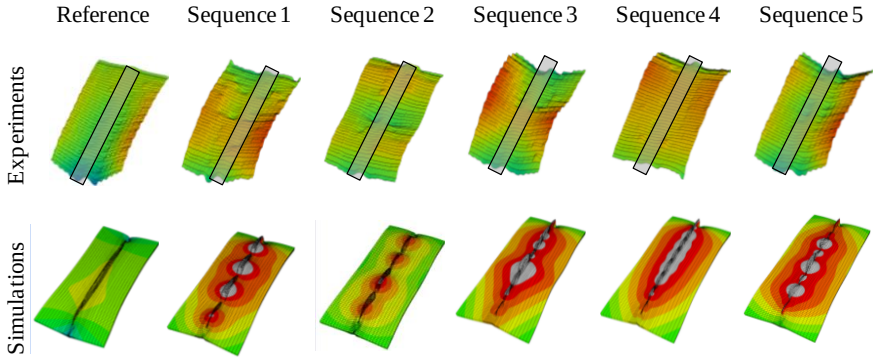

Figure 6-25 Predicted and measured out-of-plane distortion for the 6mm thick S355 T-joint and all sequences under consideration.

Table 6-1 lists the welding distortion for all sequences and both case studies. In the case of the S355 T-joint, the distortion has been obtained by averaging the distortions at each node in the simulation. Additionally, the averaged accumulated plastic strains along the weld seam are shown for the case of the DP600 overlap joint. Apparently, the second sequence; *i.e.*, symmetric welding, is the most effective sequence. This sequence leads to the lowest distortion amplitudes as well as the highest plastic deformations at the weld seam. Here, these two effects are coupled since the state with the lowest residual stresses in the clamped state also leads to the lowest distortions after unclamping.

Table 6-1 Welding distortion amplitudes and averaged accumulated plastic strains for all sequences.

	Seq 1	**Seq 2**	**Seq 3**	**Seq 4**
Overlap Joint (Exp.) (mm)	10.1	8.6	8.2	11.3
Overlap Joint (Sim.) (mm)	11.8	10.5	10.3	12.7
Overlap Joint – Average Plastic Deformation (%)	6.71	6.79	6.49	6.74
T-joint (Sim., Averaged) (mm)	0.313	0.212	0.328	0.336

Figure 6-26 shows the predicted accumulated plastic strains along the weld seam for the 1mm thick DP600 overlap joint and all sequences. The oscillations along the seam length are due to the discretisation of the finite element method. For a sequence where the seam is divided into n steps, there are n-1 intermediate points where exactly two times a step starts or ends. For the sequences under investigation, this results in three or seven points. At these points, it can be seen that the plastic deformations are increased by a factor two. This is due to the second reheating, and possibly melting, of the material at these points.

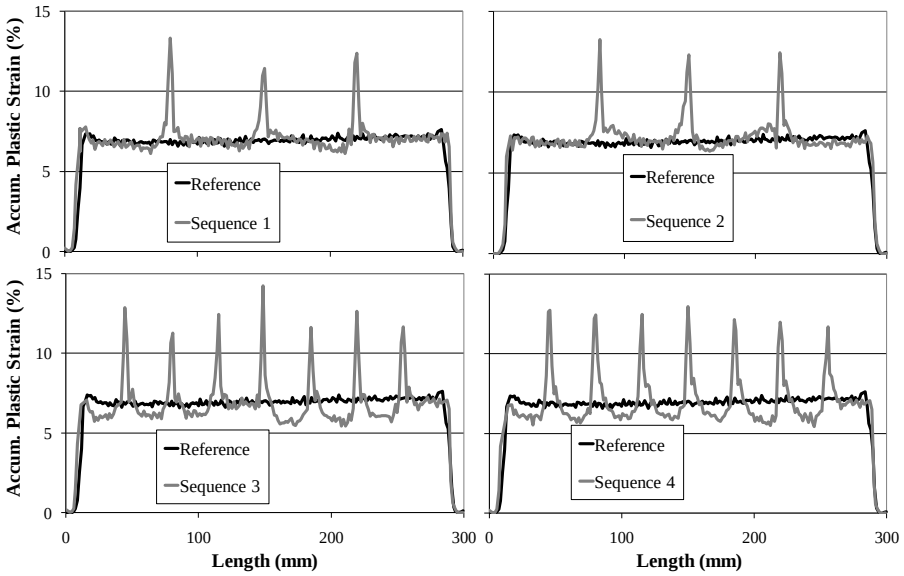

Figure 6-26 Predicted accumulated plastic strains along the weld seam for the 1mm thick overlap joint and the first four sequences under consideration.

It is interesting to note that the base level of the accumulated plastic strains is in most cases lower than for the reference case. In particular, the base level is the lowest for the last three sequences with eight steps. It appears that the shrinkage forces of each step are too small to build up a sufficient stress level to force plastic deformations. Regarding the second sequence, the plastic strains are always at least as high as the reference level without

sequencing. This is also the reason for the lower distortions. From these findings it appears to be reasonable to apply a limited number of steps in order to obtain lower distortions, here four steps yield better results than eight.

Up to now, it is not clear whether the effect of welding sequences on the distortion behaviour is determined by *reheating* or *preheating* of the material. In order to investigate this, simulations have been performed where cooling to room temperature occurs in between the steps. If the effect of sequencing is increased by this interposed cooling, this indicates that *reheating* is the dominant effect; otherwise *preheating* dominates.

Figure 6-27 shows the results for both case studies and the second sequence applied with and without cooling. It can be seen that the residual welding distortion is even lower with an interposed cooling. In case of the S355 T-joint, the distortion is much lower and almost concentrated at the weld seam. For the DP600 overlap joint, the workpiece does not buckle anymore and the distortion amplitude is reduced to less than five millimetres. Hence, these findings indicate that the influence of sequencing is dominated by *reheating* rather than *preheating*.

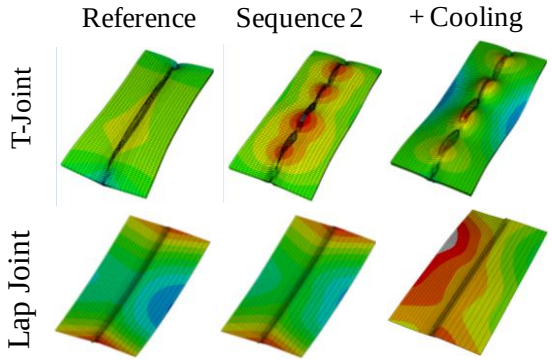

Figure 6-27 Welding distortion for the second sequence and both case studies with a cooling to room temperature in-between the steps.

6.3.3 Statistical Model

Assuming that the influence of the welding sequence on the residual distortion is determined by an optimal *reheating* of the weld seam; *i.e.*, a stress relaxation, a simple statistical model has been developed in order to determine the optimal sequence. In this model, for all *n-1* intermediate points the difference of the *step time* is counted in number of steps between the first *step time* t_1 and the second *step time* t_2 the welding torches reaches the same position:

$$m = \frac{1}{n}\sum_{i=1}^{n-1}\left(t_2^i - t_1^i\right). \qquad \textbf{Eq. 6-3}$$

The scaling factor *1/n* is introduced to account for the fact that the welding speed is assumed to be the same in all cases, and hence represents the total welding time after all

steps. If a step reaches an intermediate point the first time after the end of step three, for instance, the *step time* t_1 is four (3+1 due to ending). If step six starts from this point, the *step time* t_2 is six. The objective values for the four sequences under investigation are shown in **Table 6-2**.

Table 6-2 Objective values for the four sequences under investigation.

	Seq 1	**Seq 2**	**Seq 3**	**Seq 4**
m	1.50	1.50	2.75	1.75

This model relies on the assumption that the longer the material has to cool down after the torch reaches an intermediate point the first time, the higher the residual stresses that can be built up at that location. These stresses are relieved when the torch reaches the same point for the second time. The higher stresses are relieved and lower residual stresses remain after cooling prior to unclamping. It should be mentioned that this model does not consider the fact that there is a maximum time after which no additional effect occurs; *i.e.*, the time after which the material cooled down to room temperature. This might be important, for example, in case of laser welding due to the high cooling rates involved. In the present case for gas metal arc welding however, the time until the workpiece cools down to room temperatures is reasonably high enough to be neglected in the model; *i.e.*, between five minutes for the case of the DP600 overlap joint and about half an hour for the S355 T-joint, see **subsection 4.4.2**.

For n steps, the total number of combinations is given by $n!$ possible sequences multiplied by 2^n possible variations of the directions (forward or backward). It has also been found that there are multiple sequences having the same maximum objective value m. **Figure 6-28** shows the maximum objective function m as a function of the number of steps in a sequence compared to a linear fit. Apparently, the maximum value increases almost linearly with the number of steps. However, this is in contradiction with the observations made here; *i.e.*, that sequences with four steps yield better results than sequences with eight steps.

The reason for this behaviour is not entirely clear, but is thought to be due to a minimum seam length required to build up sufficient stresses to be relieved by the reheating. Also the model considers only longitudinal stresses at the weld seam and neglects the development of the stresses in transverse direction.

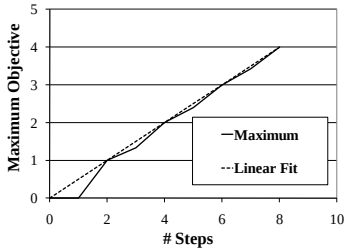

Figure 6-28 Maximum objective function m as function of the number of steps in a sequence compared to a linear fit.

Figure 6-29 shows the best sequences obtained by this model with four and eight steps assuming only forward welding. The objective values for these sequences are the maximum possible values: four for sequence six with eight steps and two for sequence seven with four steps. Some symmetry can be readily seen between the sequences: Sequence six with eight steps corresponds to two times sequence seven with four steps.

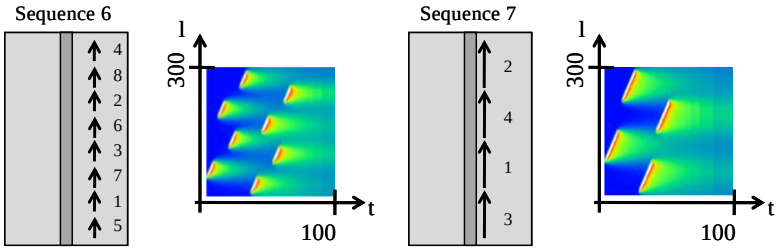

Figure 6-29 Best sequences for forward welding with four and eight steps and the corresponding temperature-time profile along the weld seam.

For the S355 T-joint, sequence seven shows the lowest amount of welding distortion in practice. In the simulations, the correct distortion shape is predicted but the amplitudes are significantly higher.

Figure 6-30 and **Figure 6-31** show the predicted and measured out-of-plane distortion for both case studies, the second sequence and the two *optimized* sequences six and seven. Regarding the results obtained for the DP600 overlap joint, the distortion predicted by sequence six (with eight steps) is lower than the distortion for the sequences three and four, but higher than the distortion of sequence five. Hence, compared to all sequences with eight steps, sequence six yields good results, but not the best.

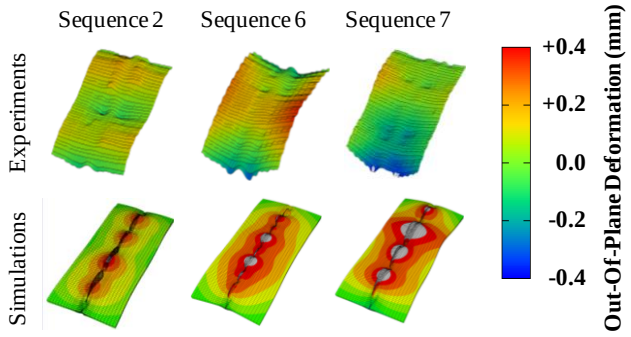

Figure 6-30 Predicted and measured out-of-plane distortion for the 6mm thick S355 T-joint for the sequences two, six and seven.

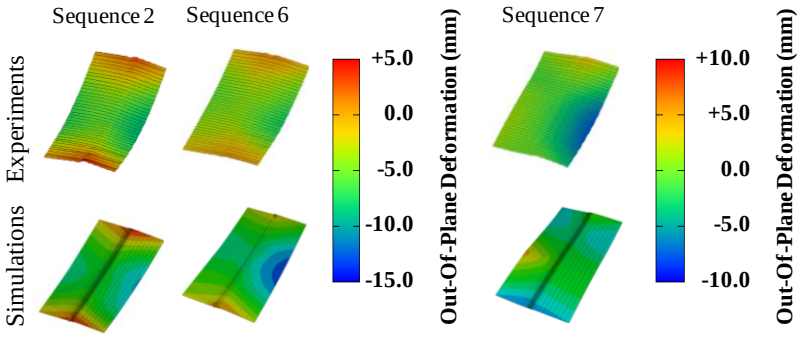

Figure 6-31 Predicted and measured out-of-plane distortion for the 1mm thick DP600 overlap joint for the sequences two, six and seven.

The distortion for sequence seven (with four steps) is much lower; the distortion amplitude is about six millimetres. Here, the buckling distortion is also much less pronounced than for the other sequences. This is also predicted in the simulations where the distortion shape shows some deviations from results obtained by the experiment. However, compared to the other sequences, the accumulated plastic strains are also increased in the model.

6.4 Concluding Remarks

The influence of clamping conditions and sequencing on welding distortion has been studied. The basic principle is a modification of the forces and stresses in the workpiece and thus the distribution of the plastic deformations.

In case of the 1mm thick DP600 overlap joint, optimized clamping conditions lead to reduced compressive stresses on unclamping and hence, lower buckling distortion. For the 6 mm thick S355 T-Joint, angular distortion can be suppressed by increased plastic shear strains at the weld seam. However, if angular distortion is suppressed, bending appears as the dominant distortion mode. The inhomogeneity of the through-thickness stress distribution can be reduced by optimized conditions in order to minimize bending distortion. In general, the following conditions have been found to be suitable to mitigate welding distortion:

- Longer clamping times leading to higher restraints on cooling
- Later clamping; *i.e.*, when the workpiece reaches its maximum thermal expansion
- Closer clamping leading to higher restrains at the weld seam
- Preheating reduces the inhomogeneity of the temperature distribution

Additionally, the transient clamping force has been measured and compared to simulations. A good qualitative and quantitative agreement has been obtained for the simplified linear-elastic clamping system with contact modelling. For the 6 mm thick 355

T-Joint, a clear workpiece-clamp interaction has been identified. In particular, the development of the distortion can be estimated by the transient clamping forces.

Several welding sequences have been investigated for both case studies. Sequencing leads to two effects on the workpiece, which are both able to reduce welding distortion. Preheating of the material leads to more homogeneous temperature distributions and reheating leads to stress relaxation. It has been found that the dominant effect in this case is reheating for both case studies. A statistical model has been developed in order to identify welding sequences which maximize the effect of reheating. Using this model, two sequences have been chosen where one exhibits an encouraging potential to reduce welding distortion.

7 Simplified Modelling

In the present chapter, simplified models have been developed for both case studies in order to reduce the complexity of the simulations and to reduce the computation time significantly. Simulations have been performed in order to explore the consequences and limitations of simplifying assumptions as well as to verify the predictability of these models and to optimize the clamping conditions.

7.1 Simplified Clamping Models

7.1.1 0D Friction-Spring Clamp Element

In order to simplify the clamping model and to avoid the need to adjust contact parameters, a general clamping element has been developed. Here, its implementation as a 0D finite element; *i.e.*, as a node, is described in detail.

Figure 7-1 shows the FricSpring element model and **Table 7-1** lists the associated variables and their meaning. The degrees of freedom (DOF) of the element are the displacements of node **A**. Node **B** denotes a virtual node defined by the direction in which the clamp acts and the initial clamp length L. In the present formulation, this direction remains fixed.

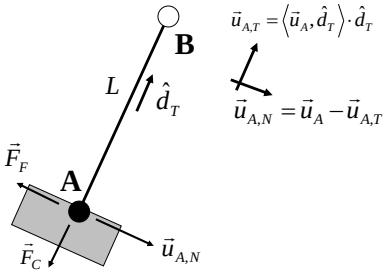

Figure 7-1 Model of the FricSpring clamping element.

The initial coordinates of node **B** are given by:

$$\vec{x}_B = \vec{x}_A + L \cdot \hat{d}_T \,. \qquad \textbf{Eq. 7-1}$$

The length L can change to $L+\Delta L$ due either to a displacement of node **A** or node **B**. The position of node **A** might change due to material reaction, *e.g.* thermal expansion, during welding. The displacement of node **B** in the clamp direction is set by

$$\vec{u}_{B,T} = \mathbf{u_{B,T}}(t) \cdot \hat{d}_T \,, \qquad \textbf{Eq. 7-2}$$

where $\mathbf{u_{B,T}}(t)$ is an arbitrary time-dependent function. The length change ΔL is then given by

$$\begin{aligned}\Delta\vec{u}_T &= \vec{u}_{B,T} - \vec{u}_{A,T} \\ \Delta L &= \left\|\Delta\vec{u}_T\right\| = \mathrm{u}_{\mathrm{B,T}} - \left\|\vec{u}_{A,T}\right\|\end{aligned}. \qquad \textbf{Eq. 7-3}$$

Due to the length change in the clamping direction, a clamping force is applied on the material beneath node **A**. This clamping force can generally be written as:

$$\vec{F}_C = F_C(\Delta L)\cdot\hat{d}_T\,, \qquad \textbf{Eq. 7-4}$$

where $F_C(\Delta L)$ is a function describing the force-displacement relationship. In this formulation, it is defined that the workpiece is clamped for negative $\mathbf{u}_{\mathbf{B,T}}(t)$. In principle, the clamping force should be zero for positive ΔL and increase linearly for negative values. This approach is often applied if linear spring elements are employed as clamps.

Table 7-1 Meaning of the variables in **Figure 7-1**.

Variable	Meaning
L	Initial Clamp Length
$\hat{d}_T$	Unity Vector in *Tangential* Clamping Direction
N	Direction of Friction (Normal to Clamping Direction)
$\vec{F}_C$	Clamping Force
$\vec{F}_F$	Friction Force
$\vec{x}_A = (x_A, y_A, z_A)$	Initial Coordinates of Node **A**
$\vec{u}_A = (u_A, v_A, w_A)$	Displacement of Node **A**
$\vec{u}_{A,T}$	Displacement of Node **A** in Clamp Direction
$\vec{u}_{A,N}$	Displacement of Node **A** normal to the Clamp Direction

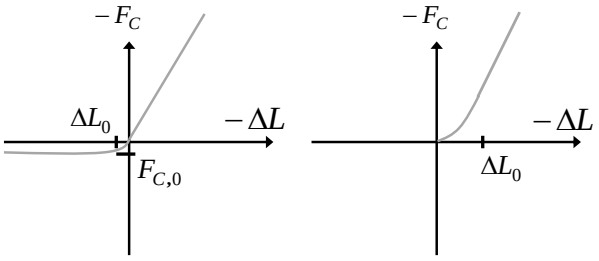

Figure 7-2 Linear force-displacement relation with **arctan** stabilisation (left) and parabolic function (right).

However, the force derivative is unsteady at the origin,

$$\begin{matrix} \lim_{\Delta L \to +0} \dfrac{d}{d\Delta L} F_C(\Delta L) = k \\ \lim_{\Delta L \to -0} \dfrac{d}{d\Delta L} F_C(\Delta L) = 0 \end{matrix} \quad . \qquad \textbf{Eq. 7-5}$$

where k is the clamp stiffness with dimension [k] = N/mm. This leads to oscillations in the initial clamping phase and causes convergence problems and possible divergence of the simulation. In an attempt to overcome this problem, two further approaches have been assessed, see **Figure 7-2**. The first approach is a linear-force displacement relationship with an **arctan** stabilisation term for positive length changes:

$$F_C = \begin{cases} +k \cdot \Delta L \ , \ \Delta L \le 0 \\ A_0 \cdot \arctan(k / A_0 \cdot \Delta L) \ , \ \Delta L > 0 \end{cases} . \qquad \textbf{Eq. 7-6}$$

This stabilisation has been chosen because it possesses an asymptotic convergence towards a finite value and it leads to steady derivatives at the origin. This stabilisation has to be small enough to avoid large residual forces. For a displacement ΔL_0, the residual stiffness of the clamp must be:

$$\begin{aligned} & \frac{d}{d\Delta L} F_C(\Delta L_0) \le \varepsilon \cdot k \\ & \Rightarrow k / F_{C,0}(\Delta L_0) = 1 + {\Delta L_0}^2 (k / A_0) \le \varepsilon \quad , \quad \left(\frac{\pi}{2}\right) \cdot A_0 = F_{C,0} \ . \\ & \Leftrightarrow F_{C,0}(\Delta L_0, \varepsilon) = \frac{1}{\sqrt{\varepsilon - 1}} \cdot k \cdot \Delta L_0 \cdot \frac{\pi}{2} \end{aligned} \qquad \textbf{Eq. 7-7}$$

For the parameters applied here; *i.e.*, k = 20 kN mm^{-1}, ΔL_0 = 10^{-7} mm and ε = 0.1, the maximum residual force $F_{C,0}$ is 10^{-4} N, which can be considered to be small compared to the clamping force F_C of 300-400 N. Numerical evaluations indicate that an oscillation of the system can be avoided successfully using this stabilisation. The second approach uses a parabolic function to obtain steady force derivatives with respect to the displacement:

$$F_C = \begin{cases} 0 \ , \ \Delta L \ge 0 \\ -a \cdot \Delta L^2 \ , \ \Delta L \in [\Delta L_0, 0] \\ +k \cdot (\Delta L - \Delta L_0) = +k \cdot \Delta \vec{u}_T \ , \ \Delta L \le \Delta L_0 \end{cases} . \qquad \textbf{Eq. 7-8}$$

The parameter a results from the definition of ΔL_0. Here, the force derivatives are identically to zero for an extension of the clamp, but positive for any compression. It has been found that this zero stiffness compared to small positive values suffice to provoke an oscillation of the system. The first approach appears to be much more stable and has therefore been adopted.

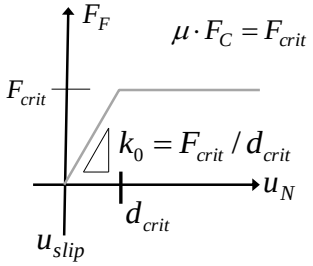

Figure 7-3 Friction-displacement relation normal to the clamp.

If the clamp is under pressure; *i.e.*, if $F_C<0$, and the workpiece attempts to move below the clamp, the workpiece is subjected to friction. **Figure 7-3** shows the friction-displacement relationship. The maximum friction force depends on the clamping force applied and the friction coefficient μ. As long as the displacement of the workpiece below the clamps is smaller than a critical displacement d_{crit}, the workpiece adheres to the clamp. On exceeding this displacement, the workpiece moves underneath the clamp leading to a movement of the origin u_{slip}, similar to ideal-plastic material behaviour; hence:

$$\vec{F}_F = \begin{cases} \vec{F}_F = -\mu \cdot k_F \cdot \vec{u}_D \ , \ k_F = \dfrac{F_C(\Delta L)}{d_{crit}} \ , \ \varphi \geq 0 \\ F_{crit}(\Delta L) \cdot \vec{u}_N = -\mu \cdot F_C(\Delta L) \cdot \hat{u}_D \ , \ \varphi < 0 \end{cases} , \qquad \textbf{Eq. 7-9}$$

where $\varphi=u-d_{crit}$ is the friction potential, and the distance to the centre *slip* point is

$$\vec{u}_D = \vec{u}_{A,N} - \vec{u}_{slip} \ , \ u = \left\| \vec{u}_D \right\| \ , \ \hat{u}_D = \vec{u}_D / \left\| \vec{u}_D \right\| . \qquad \textbf{Eq. 7-10}$$

If the material is slipping, the slip point moves to

$$\vec{u}_{slip} \to \vec{u}_{slip} + \varphi \cdot \hat{u}_D . \qquad \textbf{Eq. 7-11}$$

The critical distance d_{crit} is set to 10^{-3} mm. For $\varphi\geq 0$ friction is also referred to as *elastic friction*, and for $\varphi<0$ as *plastic friction*.

Including the effect of friction, the total force acting on the workpiece is given by

$$\vec{F} = \vec{F}_C + \vec{F}_F . \qquad \textbf{Eq. 7-12}$$

Using the projection tensors in tangential and normal direction,

$$\begin{aligned} \frac{\partial \vec{u}_{A,T}}{\partial \vec{u}_A} &= \frac{\partial \left\langle \vec{u}_A, \hat{d}_T \right\rangle}{\partial \vec{u}_A} \cdot \hat{d}_T = \hat{d}_T{}^T \cdot \hat{d}_T = \mathrm{Pr}_T \\ \frac{\partial \vec{u}_{A,N}}{\partial \vec{u}_A} &= \frac{\partial \vec{u}_A}{\partial \vec{u}_A} - \frac{\partial \vec{u}_{A,T}}{\partial \vec{u}_A} = \mathbf{1} - \hat{d}_T{}^T \cdot \hat{d}_T = \mathbf{1} - \mathrm{Pr}_T = \mathrm{Pr}_N \end{aligned} , \qquad \textbf{Eq. 7-13}$$

the contribution of the clamping force to the stiffness matrix is

$$\frac{\partial \vec{F}_C(\Delta L)}{\partial \vec{u}_A} = -\frac{dF_C(\Delta L)}{d\Delta L} \cdot \mathrm{Pr}_T \,. \qquad \textbf{Eq. 7-14}$$

Similarly, the contribution to the stiffness matrix for elastic friction is

$$\frac{\partial \vec{F}_F}{\partial \vec{u}_A} = -k_F \cdot \frac{\partial \vec{u}_D}{\partial \vec{u}_{A,N}} \cdot \frac{\partial \vec{u}_{A,N}}{\partial \vec{u}_A} = -k_F \cdot \mathrm{Pr}_N \,. \qquad \textbf{Eq. 7-15}$$

In case of plastic friction, the contribution is a little bit more complex:

$$\frac{\partial \vec{F}_F}{\partial \vec{u}_A} = -\mu \cdot \frac{\vec{u}_D}{\|\vec{u}_D\|} \cdot \frac{\partial \|\vec{F}_C\|}{\partial \vec{u}_A} - \mu \cdot \|\vec{F}_C\| \cdot \frac{\partial}{\partial \vec{u}_A} \frac{\vec{u}_D}{\|\vec{u}_D\|} \,. \qquad \textbf{Eq. 7-16}$$

Unclamping can be represented using the displacement boundary $\mathbf{u_{B,T}}(t)$ at node **B**, *e.g.* by lifting the node up. However, it has been found that convergence is much better by ramping the clamping force linearly down within a time period Δt:

$$\vec{F}_C(t) = \vec{F}_C(t_0) \cdot \max\left(\frac{t - t_0}{\Delta t}, 0\right), \qquad \textbf{Eq. 7-17}$$

then, the contribution of the clamping force to the stiffness matrix is zero during unclamping.

7.1.2 Verification

Element Performance

In order to validate the FricSpring clamping element, tests have been performed for a linear 8-node brick with unity dimensions (w,b,h) = (1,1,1). Hence, the area A of all faces is 1 mm^2. The stiffness E of the material is 200 GPa, the friction coefficient μ is set to 0.3. **Figure 7-4** shows the testing scheme for one element in order to verify the friction response to deformation. The clamp stiffness k is 20 kN mm^{-1}.

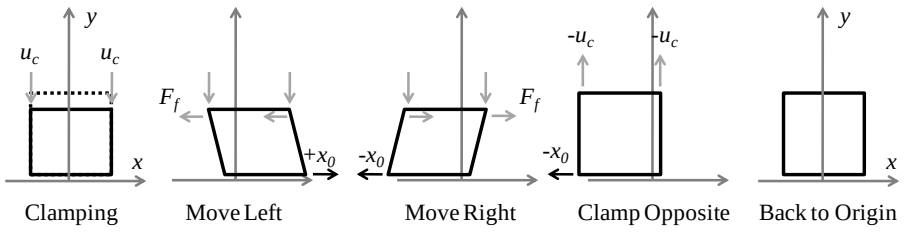

Figure 7-4 Testing scheme for one element.

Firstly, the element is clamped in the *x-direction* by a displacement to $\mathbf{u_{B,T}} = -u_c = -0.01$ mm, leading to a compression of the element. Integrating the clamping force over all four clamp nodes, the total clamping pressure σ_C and the compression Δy of the element are given by

$$\sigma_C = 4 \cdot k \cdot \mathrm{u}_{\mathrm{B,T}} / A = 800\,MPa\,,$$
$$\Delta y = \varepsilon \cdot t = 800\,MPa / 200GPa \cdot t = 4 \cdot 10^{-3}\,mm\,. \qquad \textbf{Eq. 7-18}$$

These values have been obtained in the simulations. Secondly, the element is moved to the right leading to a shearing of the element due to the friction. This shearing is built up to a maximum value when *plastic friction* is reached. The shear stress in the element is

$$\sigma_{xy} = \mu \cdot \sigma_C = 0.3 \cdot 800MPa = 240MPa\,. \qquad \textbf{Eq. 7-19}$$

Subsequently, the element is moved to the left and hence, the friction-force direction as well as the shearing amplitude changes. In order to evaluate the influence of the **arctan** stabilisation term, the displacement of the clamp node B is reversed; *i.e.*, $\mathbf{u_{B,T}} = +u_c$. For the residual stress $\sigma_{C,R}$ due to the stabilisation, the following value has been found:

$$\sigma_{C,R} = 4 \cdot F_{C,R} / A = 4 \cdot 1.1 \cdot 10^{-4}\ N / 1mm^2 = 4.4 \cdot 10^{-4}\ MPa\,. \qquad \textbf{Eq. 7-20}$$

As a second example, the clamping process prior to welding has been simulated using the FricSpring elements. The displacement $\mathbf{u_{B,T}}$ for the FricSpring elements can either be determined using the clamping pressure σ_C, or using the area of the contact A_C and the clamping force F_C:

$$\mathrm{u}_{\mathrm{B,T}} = \frac{F_C}{k_C} = \frac{\sigma_C}{k_C \cdot A_C}\,, \qquad \textbf{Eq. 7-21}$$

where $k_C = 20$ kN mm^{-1} is the stiffness of the clamps. The stiffness k of each FricSpring element has to be modified to obtain the correct total clamp stiffness. This can be determined from the number of FricSprings n_C representing the clamp:

$$k = k_C / n_C\,. \qquad \textbf{Eq. 7-22}$$

Figure 7-5 shows the clamping pressure (in the out-of-plane direction) obtained with contact elements and FricSpring elements with $\Delta L_0 = 10^{-9}$ mm and $\Delta L_0 = 10^{-6}$ mm. The stress distribution with $\Delta L_0 = 10^{-9}$ mm agrees well with the results obtained using contacts. For $\Delta L_0 = 10^{-6}$ mm, the stress distribution is much more irregular. This is due to the FricSpring elements underneath the workpiece; below the clamps they are compressed, while between clamps they are in tension. Here, a value of $\Delta L_0 = 10^{-6}$ mm is not sufficient to suppress residual forces.

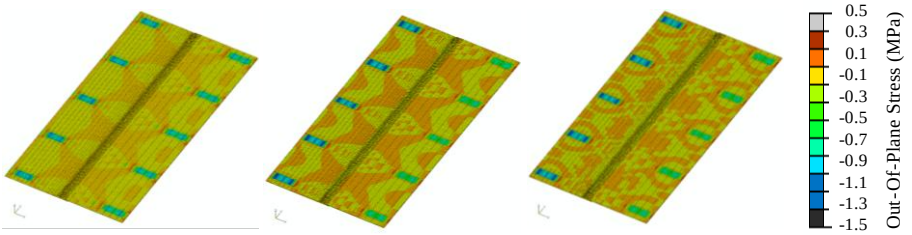

Figure 7-5 Clamping Pressure (in the out-of-plane direction) in the workpiece for clamping with contact elements (left) and FricSpring elements with $\Delta L_0 = 10^{-9}\,mm$ (centre) and $\Delta L_0 = 10^{-6}\,mm$ (right).

With regard to these results, it is recommended that the value applied for ΔL_0 is also dependent on the number of FricSpring elements employed to represent the clamp. As a rule-of-thumb, the following value is proposed:

$$\Delta L_0 = 10^{-6}\,mm / n_C\,. \qquad \textbf{Eq. 7-23}$$

Comparative Study

In order to assess the quality of the predictions using the FricSpring element, the predicted buckling amplitudes and the required computation time for the HR and CR condition have been compared for contact elements, the FricSpring element, and linear spring elements with a stiffness k of 20 kN mm^{-1}. In order to obtain a CPU-independent computation time, the following formula has been employed:

$$Time = \#nodes^2 \times total\ \#iterations\,. \qquad \textbf{Eq. 7-24}$$

The computation time is shown for the mechanical calculation of the CR condition. The following cases have been compared:

(1) Contact elements with contact stiffness $k_c = 10\,\text{GPa mm}^{-1}$ (Reference model)

(2) FricSpring elements

(3) Linear springs, free to move in the tangential direction

Figure 7-6 shows a comparison of the models employed using contacts, spring elements, and FricSpring elements for a modelling of the clamping system. It is clear that the complexity of the model is reduced using FricSpring elements.

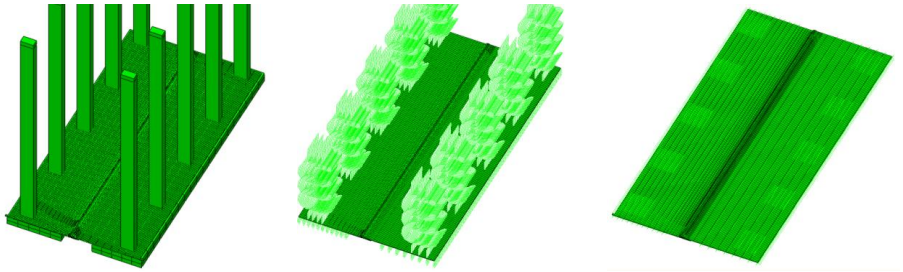

Figure 7-6 Comparison of the models using contacts (left), spring elements (middle), and FricSpring elements (right).

The results are shown in **Figure 7-7**. The predicted welding distortion does not vary significantly between the various cases. Hence in this case, it does not matter whether clamping is modelled using contacts, FricSprings, or linear spring elements. However, this picture changes if the computation time is considered. While FricSprings are slightly faster than contacts, the simulation needs much more computation time in the case of linear spring elements.

The reason for the slow convergence of linear spring elements can be explained with reference to transverse shearing, see **Figure 7-8**. In this case there is no friction present to hinder the transverse movement of the workpiece. The maximum shearing amplitude is about 1.8 mm and hence, a factor ten larger then in case of contacts or FricSprings. This leads to oscillations as well as excessive element distortions in the weld seam where the average element size is about 0.25-0.5 mm.

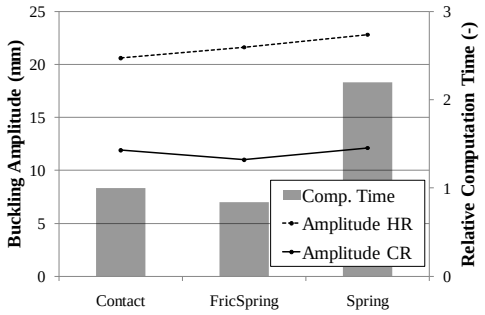

Figure 7-7 Predicted welding distortion for the HR and CR condition and required computation time for all cases considered.

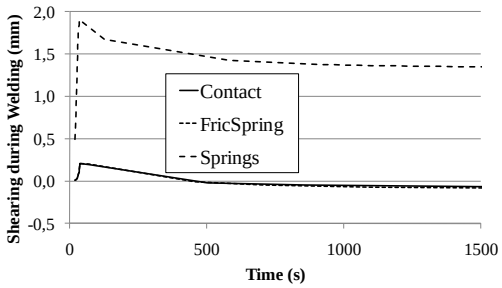

Figure 7-8 Shearing of the top plate for contacts (case 1), FricSprings (case 3), and linear springs (case 4).

7.2 Simplification Studies

In order to reduce the complexity of the model as well as the computation time, simplification studies have been performed. The studies are based on the results of the sensitivity analyses presented in **subsection 5.4.1**. In the following, two simplification approaches are presented which are employed in the subsequent studies.

Shell Meshes

The simplest way to improve the computation time is to reduce the size of the mesh; the overall computation time required to complete a simulation is correlated quadratically to the number of elements. Also the element choice plays an important role. The determination of the mechanical response within a standard linear 8-node brick with incompatible modes takes about thirty percent more computation time than standard bricks, while a reduced integration reduces the computation time by about thirty percent. As shown in **section 5.3**, care must be taken in order to simplify the mesh. Every simplification tends to increase the geometrical stiffness of the mesh and hence, reduce the predicted welding distortion or even suppresses buckling or bending.

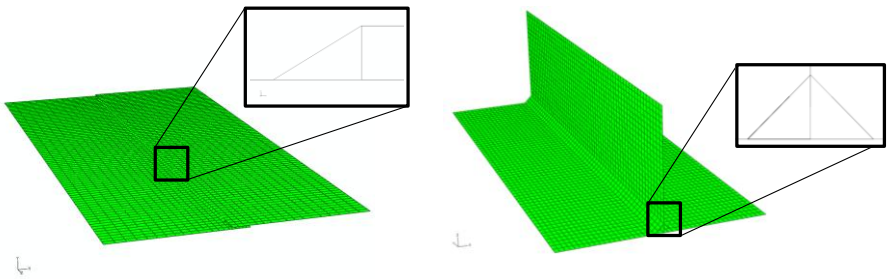

Figure 7-9 Shell mesh for both case studies.

Additionally to the reduced volume meshes, shell meshes have been employed, see **Figure 7-9**. The filler material is included by elements connecting the single parts. The thicknesses of these connection elements have been adjusted in order to correspond to the fillet section. Here, the longitudinal mesh density has been set to $n_l = 60$. The total number of elements is 8369 for the overlap joint and 4321 for the T-joint.

Simplified Temperature-Dependency

In general, it is a very complicated and time-consuming task to obtain temperature-dependent material properties for steels at elevated temperatures. However, for both steels under investigation, similar tendencies have been found, see **section 4.3**: The material behaviour is approximately constant up to 400 °C followed by a softening until 1000 °C where the material looses all strength. Here, a simplified interpolation rule has been investigated: The yield stress and hardening remain at room temperature values up to 400 °C and are then linearly ramped down to zero at 1000 °C..

7.2.1 DP600 Overlap Joint

In order to study the influence of simplified models on the results and the computation time, simulations have been performed for all cases listed in **Table 7-2**. The studies have been performed for three clamping approaches; contact elements, spring elements, and the FricSpring elements presented previously. The longitudinal mesh density has been varied as well as the integration type; *i.e.*, full integrated, reduced integrated and with incompatible modes, see **section 5.3**. *#El* represents the number of elements in the longitudinal direction.

Table 7-2 Cases applied for the simplification studies for the DP600 overlap joint.

Case	# El	Clamp	Integration	Type	Temp.-dep.	Phase	Hardening	Aniso	Heat
Ref	207	Contact	Incompatible	Volume	full	Yes	Mixed	Yes	Goldak
1	207	FricSprings	Incompatible	Volume	full	Yes	Mixed	Yes	Goldak
2	207	Contact	Incompatible	Volume	Simplified	Yes	Mixed	Yes	Goldak
3	207	Contact	Incompatible	Volume	Simplified	Yes	Mixed	Yes	Simplified
4	126	Springs	Incompatible	Volume	Simplified	No	Isotropic	No	Goldak
5	126	Springs	Reduced	Volume	Simplified	No	Isotropic	No	Goldak
6	90	Springs	Reduced	Volume	Simplified	No	Isotropic	No	Goldak
7	90	Springs	Reduced	Volume	Simplified	Yes	Mixed	Yes	Goldak
8	90	FricSprings	Reduced	Volume	Simplified	Yes	Mixed	Yes	Goldak
9	60	FricSprings	Reduced	Volume	Simplified	Yes	Mixed	Yes	Goldak
10	60	FricSprings	Reduced	Shell	Simplified	Yes	Mixed	Yes	Goldak
11	60	FricSprings	Reduced	Shell	Simplified	No	Isotropic	No	Goldak
12	60	FricSprings	Reduced	Shell	full	Yes	Mixed	Yes	Goldak
13	100	FricSprings	Reduced	Shell	full	Yes	Mixed	Yes	Goldak

The resulting computation times as well as the buckling amplitudes for the hot and cold release are shown in **Figure 7-10**. The calculation time has been evaluated for the cold release condition are shown in **Figure 7-10**. Here, the calculation time for the reference model is approximately two days. Regarding these studies, the following conclusions can be drawn:

- Using the FricSpring elements instead of contacts results in similar results to the reference model. However, the computation time is reduced and the handling is much easier.
- Simplified temperature-dependencies of the mechanical material properties lead to a significant over-estimation of the welding distortion. Here, the saving of complexity is large while the effect on the computation time is small.
- The application of isotropic hardening reduces the internal degrees of freedom and reduces the computation time by approximately 30 %. However, the distortion amplitude is significantly increased.
- The applied reduction strategy of the mesh density and the application of reduced integrated elements reduce the computation time significantly, but did not change the results much in the case of the overlap joint.
- Case 9 results in the smallest computation time for volume elements (about 3-4 hours). The deviation to the reference model is small.
- The application of shell elements reduces the computation time significantly. The welding simulation can be performed within 30-40 minutes. However, the welding distortion is overestimated for shell elements.

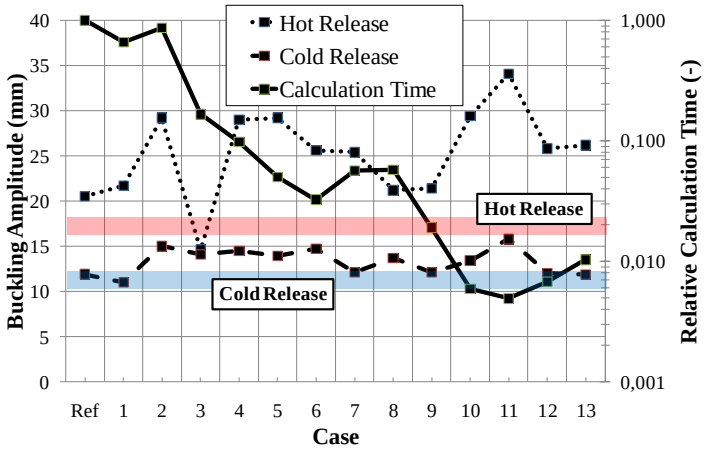

Figure 7-10 Results of the predicted welding distortions and the total computation time for all cases under investigation. The bands represent the experimental values. The calculation time has been evaluated for the cold release condition.

In particular the last point required some more detailed explanation. In order to assess the overestimation, the simulations were repeated with a higher mesh density (case 12 and 13). It has been found that the mesh is already within a converged range. The most likely reason here might be due to the missing asymptotic correctness of reduced integrated shell elements. Additionally with the shell mesh, the model always predicted a bending buckling

upwards, also for the cold release. Hence, for qualitative results and for an optimisation of the clamping conditions; *i.e.*, if only tendencies are of interest, such a model might be applicable, but for quantitative results, a volume mesh is required.

Influence of the Filler Material

In **subsection 2.1.3**, it has been found that the amount of filler material added to the weld increases the welding distortion. Using shell meshes, the influence of the filler material on the welding distortion can be studied. Here, the section of the filler material in the reference case is about 5 mm^2.

Figure 7-11 shows the results using case 12 where the thickness of the elements has been varied. It can be seen that there is an almost linear increase of the distortion with an increase of the filler material. This is in good agreement with the shrinkage force which is also linearly dependent on the section of the fillet.

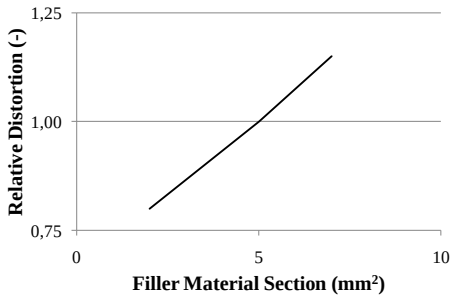

Figure 7-11 Influence of the filler material section on the final welding distortion.

7.2.2 S355 T-Joint

In common with the DP600 overlap joint, a simplification study has been performed for the S355 T-joint. The investigated cases are listed in **Table 7-3**. Here, for the cold release condition, bending distortion is expected. In some simplified cases, however, it has been found that the material behaviour is overmatched and angular distortion appears. Hence, the results of the model have only been evaluated for the hot release condition.

The resulting computation times as well as the angular distortion for the hot release condition are shown in **Figure 7-12**. The band indicates the approximate range of the experimental values. However, for this case study, there are some deviations as explained earlier. The results of the case studies can be concluded as follows:

- Using FricSpring elements or springs instead of contacts gives similar results to the reference model. However, the computation time is reduced and the handling is much easier.
- Simplified temperature-dependencies of the mechanical material properties lead to a significant over-estimation of the welding distortion. This effect is the

same as for the overlap joint. Additionally, the convergence is worse and hence, the computation time is significantly increased.

- Assuming pure isotropic hardening instead of 50% kinematic hardening overestimates the welding distortion significantly.
- A reduction of the mesh density and the application of reduced integrated elements reduce the computation time significantly, but do not change the results much.
- Angular distortion appears to be less susceptible to the mesh density than bending distortion for the present T-joint. This might be because no shear locking can occur for angular distortion..

Table 7-3 Cases applied for the simplification studies for the S355 T-Joint.

Case	# El	Clamp	Integration	Type	Temp.-dep.	Phase	Heat	Hardening
Ref	108	Contact	Incomp	Volume	full	Yes	Goldak	Mixed
1	108	Springs	Incomp	Volume	full	Yes	Goldak	Mixed
2	108	FricSprings	Incomp	Volume	full	Yes	Goldak	Mixed
3	108	FricSprings	Incomp	Volume	Simplified	Yes	Goldak	Mixed
4	108	FricSprings	Incomp	Volume	Simplified	No	Goldak	Isotropic
5	108	FricSprings	Reduced	Volume	full	Yes	Goldak	Mixed
6	108	FricSprings	Reduced	Volume	full	Yes	Simplified	Mixed
7	90	FricSprings	Incomp	Volume	Simplified	Yes	Goldak	Mixed
8	90	FricSprings	Reduced	Volume	Simplified	Yes	Goldak	Mixed
9	70	FricSprings	Incomp	Volume	Simplified	Yes	Goldak	Mixed
10	70	FricSprings	Reduced	Volume	Simplified	Yes	Goldak	Mixed
11	50	FricSprings	Incomp	Volume	Simplified	Yes	Goldak	Mixed
12	50	FricSprings	Reduced	Volume	Simplified	Yes	Goldak	Mixed
13	60	FricSprings	Reduced	Shell	full	Yes	Goldak	Mixed
14	60	FricSprings	Reduced	Shell	Simplified	No	Simplified	Isotropic

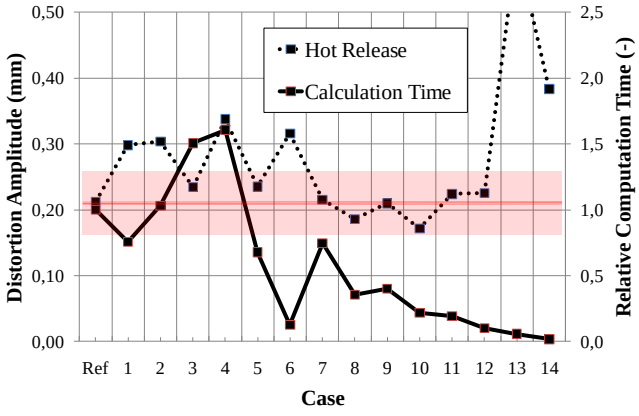

Figure 7-12 Results of the predicted welding distortions and the total computation time for all cases under investigation. The band sketches approximately the experimental values.

For the fastest volume model (Case 12), the computation time has been reduced by an order of magnitude compared to the reference model while the predicted welding distortion is approximately the same. Hence, also in case of the 6 mm S355 T-Joint, the most promising factor to reduce the computation time is to reduce the mesh density and use reduced integration elements.

Shell Mesh

For the shell mesh applied here, no angular distortion has been obtained for the hot release condition. Bending distortion is always present as the dominant distortion mode, see **Figure 7-13**. The most likely reason for this behaviour is that angular distortion is caused by through-thickness variations of the temperatures and hence, the resulting strains and stresses. These through-thickness variations cannot be mapped with the emplyoed shell elements S4R in ABAQUS.
Although the model is not able to predict angular distortion, the expected tendency can be seen for bending distortion: Longer clamping times reduce the bending amplitude due to an increased plastic deformation.

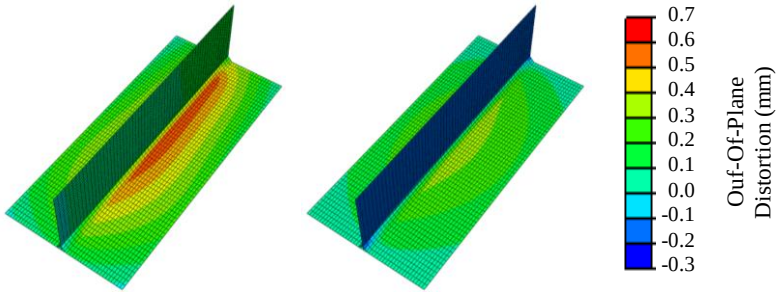

Figure 7-13 Predicted distortion for the shell mesh and the hot release (left) and cold release (right) condition.

7.2.3 Shrinkage Model

Simultaneous Heating

An attempt has also been made to reduce the computation time by simplifying the heat source in combination with the shell mesh. As a first step, a *simultaneous Goldak source* has been employed, see **Figure 7-14**. Here, the heat source corresponds to the transient source apart from the fact that it ignores the transient heat input over the weld seam. The Goldak heat source is applied, but over the whole weld seam at once; the dependency in the length-direction is ignored. This is done by removing the ellipsoidal spatial distribution of the Goldak source in the weld seam direction. The temperature gradients in the transverse direction are not modified. The heating time has been adjusted in order to obtain an

equivalent total heat input into the material; *i.e.*, the maximum temperatures in the weld should correspond to the maximum temperatures obtained for the transient heat source. This equivalent time t has been determined to be 1.9 seconds instead of 35 seconds as required for the whole transient welding process. The cooling process as well as the clamp release are not modified. A major disadvantage of this approach is that it has still to be calibrated, similarly to the Goldak heat source; only the two parameters in the welding direction can be omitted.

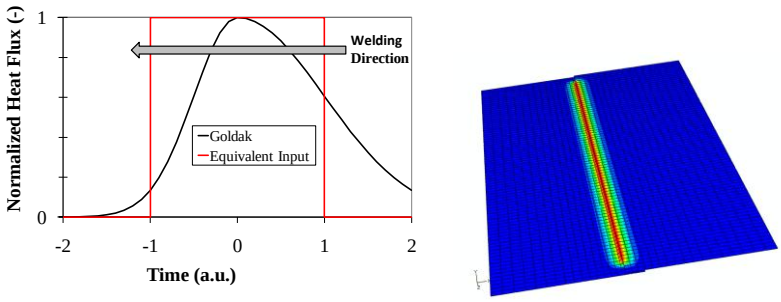

Figure 7-14 Left: Equivalent heat input. Right: Calculated temperature distribution.

Thermal Shrinkage Model

As another simplification technique, *thermal shrinkage* can be employed. The initial temperature is set to the melting temperature within a radius $r = \alpha \cdot r_{TM}$ around the weld centre, and ramped down linearly. Here, r_{TM} represents the radius of the melting zone and α is a calibration factor which has to be determined manually for each welding condition. This model is applied widely in industry and it has been reported that it can be employed successfully for qualitative welding distortion predictions [Tikhomirov 2005]. However, it has also been reported, *e.g.* by Schneider [Schneider 2009], that the calibration factor does not necessarily have to possess any physical meaning.

Initial tests performed here show that the strong temperature, deformation and stress gradients implied by this model, in combination with the occurrence of (unstable) buckling deformation, lead to very strong numerical convergence problems: The computation time is many times higher than for the transient 60(S) model. Hence, this approach has not been followed further here.

In order to devise a physically more realistic shrinkage model, the maximum temperatures reached in the transverse direction to the weld have been investigated, since these correspond to the maximum shrinkage strains in the material. In order to model these maximum temperatures, two different approaches have been employed: *Rosenthal's analytical solution for thin plates* [Grøng 1997] and a simple *exponential* approach. The equation for the exponential approach reads:

$$T(d) = T_0 \cdot \exp(-b \cdot d), \qquad \textbf{Eq. 7-25}$$

where T_0 is the initial plate temperature, b a calibration parameter and d the transverse distance to the weld centre. The parameters have been calibrated in such a way that the function reproduces the correct diameter of the molten area r_{TM} and the HAZ r_{HAZ}.

The transient equation for Rosenthal's solution for thin plates reads:

$$T_{thin} = \left(\frac{Q}{2 \cdot t \cdot \pi \cdot \lambda} \right) \exp\left(\frac{-v \cdot y}{2 \cdot \alpha} \right) \cdot K_0 \left(\frac{v \cdot R}{2 \cdot a} \right) + T_0 , \qquad \textbf{Eq. 7-26}$$

where T_0 is room temperature, Q the heat input, v the welding speed, λ the heat conductivity, R the distance to the heat source, t the plate thickness, y the distance to the weld seam in weld direction, and $\alpha = \lambda/\rho c$ the thermal diffusivity. K_0 is the second modified (hyperbolic) Bessel function of order zero which can be approximated by:

$$K_0(x) \approx \sqrt{\frac{\pi}{2 \cdot x}} \cdot \exp(-x) \Rightarrow T_{thin} \approx \sqrt{R} \cdot T_{thick} . \qquad \textbf{Eq. 7-27}$$

Here, the heat input Q has been calibrated in order to reproduce the correct diameter of the molten area r_{TM}. The maximum temperatures in the transverse direction $d = x$ can be obtained via

$$\left. \frac{dT_{thin}(x,y)}{dy} \right|_{x=d} \equiv 0 \Rightarrow T_{Max}(d) . \qquad \textbf{Eq. 7-28}$$

The Rosenthal solution generates maximum temperatures T_{Max} up to 6500 °C in the weld centre. These values have been cut to 1500 °C.

Since both r_{TM} and r_{HAZ} are easily accessible in experiments, *e.g.* by cutting and etching of the sample, it should be justified to apply them as calibration factors. However, while the Rosenthal solution introduces only one parameter to be calibrated, the exponential fit function requires two. In particular, the width of the HAZ r_{HAZ} is often not known in the development phase, while the throat thickness, which corresponds to r_{TM}, is often preconditioned by standardizations, *e.g.* DIN or EN.

Figure 7-15 shows the computed maximum temperatures. In the case of the simultaneous Goldak source, the same results are obtained as for the reference case. Regarding the Rosenthal solution, the maximum temperatures in the transverse direction; *i.e.*, as function of the distance d to the weld seam, show a good agreement with the reference model, especially for higher values of d. In particular, the predicted width of the HAZ r_{HAZ} agrees well with the reference case although only the width of the fusion zone r_{TM} has been used for calibration. The exponential fit function cools down too fast although the width of the fusion zone and the width of the HAZ have been applied for calibration. In this case, Rosenthal's solution does not only require less parameters, it also yields a better agreement to the real temperature distribution.

While much research has been performed in order to derive analytical expressions to calculate the temperature field for simple and moderate complex geometries [Pittner 2008], it is much more complex to derive analytical expressions for real welding situations. Some expressions are available for simple unconstrained geometries [Verhaeghe 1999]. In general, however, analytical expressions cannot be derived due to the strongly nonlinear

temperature, phase, and deformation dependent material behaviour coupled with transient boundary conditions, *e.g.* by elastic clamps. Hence, the residual stresses and distortions have been calculated using FEM.

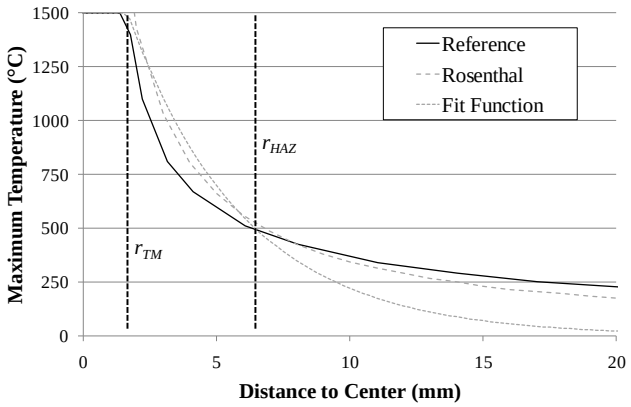

Figure 7-15 Maximum temperatures transverse to the weld direction as obtained from the transient simulations, Rosenthal's thin plate solution and the fit function.

Results

Figure 7-16 shows the predicted buckling amplitude and the relative computation time to complete the simulations for all heat sources under investigation. For all simplified heat sources, the computation time of the whole simulation, including clamping and unclamping, has been reduced by approximately two thirds compared to the reference case.

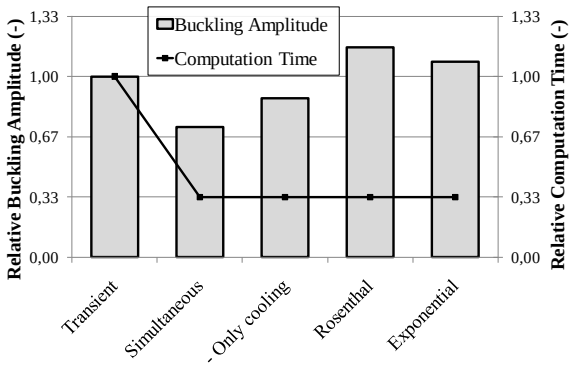

Figure 7-16 Predicted buckling amplitude for the HR condition and the required computation time to complete the simulation or all heat sources under investigation.

In the case of the simultaneous heat source, the predicted residual stresses and welding distortions are about forty percent lower than for the transient simulation. However, if

heating is ignored and only cooling is considered, the result provides a better match. Homogeneous simultaneous heating reduces the amount of plastic deformation at the weld and hence, reduces residual stresses and distortions. For both the Rosenthal and the exponential approaches, reasonable quantitative results have been achieved. In particular, the Rosenthal solution appears to be a good approximation for industrial purposes.

7.3 Optimisation

7.3.1 Parameter Study

Using the FricSpring elements allows a high flexibility in the modification of the clamping parameters. The clamping position, the clamping time and the clamp release time, can be easily specified. In order to assess the prediction of the simulations using FricSpring elements, simulations have been performed for various clamping times and clamp offsets, see **Figure 7-17**. The first case corresponds to clamping the workpiece prior to welding, the third case to a full transient clamping accompanying the welding process (see **subsection 6.1.2**), the forth case to clamping after welding. The clamps are released after the workpiece has cooled down to room temperature; *i.e.*, for the cold release condition.

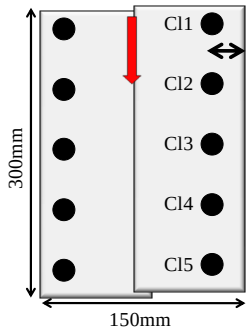

Offset: 10 mm, 30 mm, 50 mm

Clamping Time

Clamp	C0	C1	C2	C3
1	0	0	0	0
2	0	7	9	20
3	0	14	18	30
4	0	21	27	40
5	0	28	36	40

Figure 7-17 Definition of the clamp offset and the clamping times.

The results of this study for the 1mm thick DP600 overlap joint are shown in **Figure 7-18**. The simulations have been performed using the simplified model 12 with shell mesh (**Table 7-2**). The buckling amplitude is reduced for closer clamping to the weld seam and for late or transient clamping. For Case 4 and an offset of 10 mm, the distortion amplitude is much lower as in the other cases. This is because the buckling direction changes from down to up, while the amplitudes of the buckling directions are not equal, even for the same conditions, due to the asymmetry of the joint.

The results for the 6mm thick S355 T-joint are shown in **Figure 7-19**. The simulations have been performed using the simplified model 13 with shell mesh (**Table 7-3**). Here, the clamping times have been multiplied by a factor of two in order to account for the half welding speed for this case study. Similarly to the findings of the overlap joint, the bending distortion amplitude is reduced by closer and later clamping.

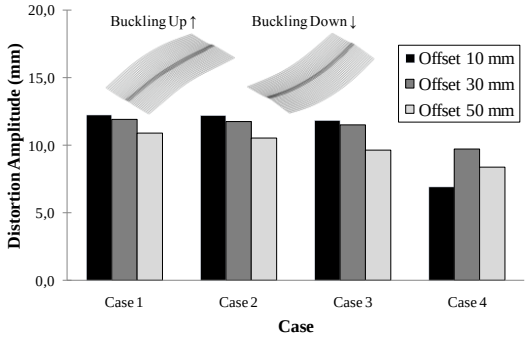

Figure 7-18 Results for the 1mm thick DP600 overlap joint and the clamping cases shown in **Figure 7-17**. For Case 4 and 10mm offset, the workpiece buckles up. In all other cases, it buckles downwards.

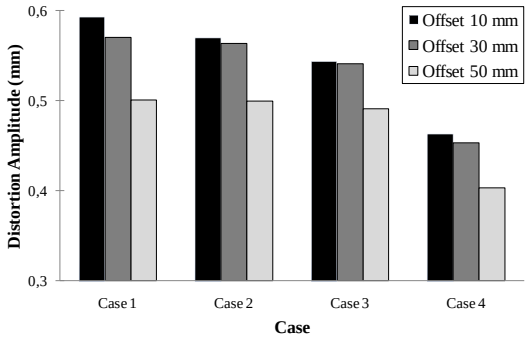

Figure 7-19 Results for the 6mm thick S355 T-joint and the clamping cases shown in **Figure 7-17** multiplied by a factor of two.

7.3.2 1D-Scan: Robustness Analysis

During automatic optimisation it is required that the simulations remain robust; *i.e.*, that small changes of model parameters lead to small changes in the results. In order to assess the robustness of the welding model, a linear 1D scan has been performed. Here, the reference clamping times shown in **Table 7-4** (case 3) are multiplied by a dimensionless scaling factor *f* between [0,2].

Table 7-4 Reference clamping times.

	Clamp 1	**Clamp 2**	**Clamp 3**	**Clamp 4**	**Clamp 5**
Overlap Joint	0	9	18	27	36
T-Joint	0	18	36	54	72

The scan for the overlap joint using the simplified model 12 is shown in **Figure 7-20** (left). Firstly, it can be seen that the simulation appears not to be robust. There are very large discontinuities; *i.e.*, oscillations, in the results as function of the scaling factor. Secondly, a tendency can be seen towards lower distortion amplitudes for higher scaling factors. For optimisation purposes, however, the robustness of the model is not sufficient.

The scan has been repeated using the simplified model 13; *i.e.*, the same model as the simplified model 12 but with an increased mesh density; *i.e.*, +66 % more elements, see **Figure 7-20** (right). Here, the minimum is clearly visible for a scaling factor of ≈ 1.2. Also the distortion as function of the scaling factor is smooth. This is in particular interesting since both models show a good agreement for the hot and cold release condition, see **Figure 7-10**,

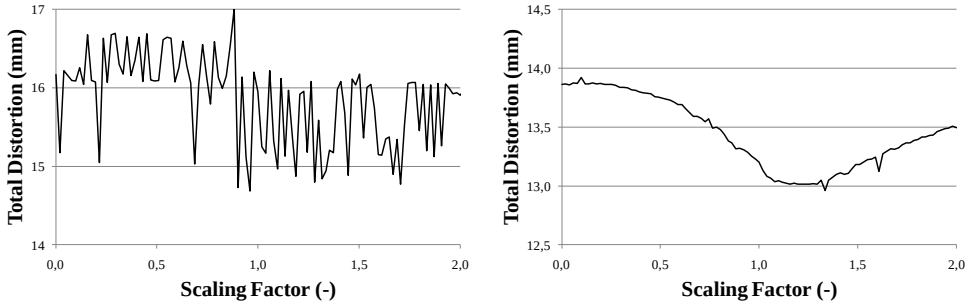

Figure 7-20 1D-Scan for the DP600 overlap joint using the simplified models 12 (left) and 13 (right).

The scan for the T- joint using the simplified model 13 is shown in **Figure 7-21**. Also in this case, a clear minimum has been found for a scaling factor of 1.2. Here, small numerical perturbations have been observed, but no significant discontinuities. Hence, the most likely reason in order to explain the results found for the overlap joint appears to be a more severe influence of the mesh density in case of buckling than for bending.

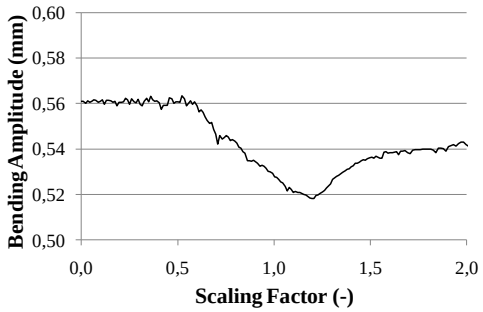

Figure 7-21 1D-Scan for the S355 overlap joint using model 13.

7.3.3 Automatic Optimisation

Using the previous studies it has been found to be the most favourable approach in order to mitigate welding distortion to use a late clamping combined with a cold release condition. In order to investigate whether this is indeed the most effective condition, an automatic optimisation of the clamping times has been performed using the optimisation library presented in [Schenk 2006]. The clamp offset; *i.e.*, the distance of the clamps from the edge of the plate, was set to the reference value of ten millimetres.

Algorithms

Since numerical perturbations of the results are present, the optimisations have been performed using two global optimisation algorithms for non-linear problems. The first algorithm is referred to as Covariance Matrix Adaptation Evolution Strategy (CMA-ES) [Auger 2005, Igel 2006]. Evolution strategies use natural problem-dependent representations, and primarily mutation and selection as search operators. It is common with evolutionary algorithms that the operators are applied in a loop. An iteration of the loop is called a generation. The sequence of generations is continued until a termination criterion is met.

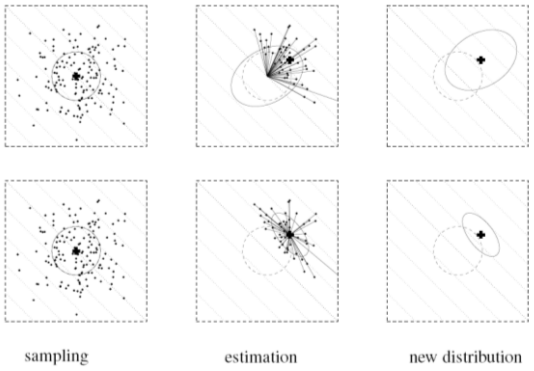

Figure 7-22 Sampling of a distribution (left), estimation of the best results (middle) and new distribution based on the covariance matrix adaptation (right) for two examples [Hansen 2010].

Here, two principles for the adaptation of parameters of the search distribution are exploited. First, a maximum likelihood principle, based on the idea to increase the probability of a successful search step. The covariance matrix of the distribution is updated such that the likelihood of previously realized successful steps to appear again is increased. Second, two paths of the time evolution of the distribution mean of the strategy are recorded, called evolution paths. Such a path contains significant information of the correlation between consecutive steps. **Figure 7-22** sketches the new distribution obtained for the CMA-ES for two examples.

The second algorithm is the downhill simplex method developed by Nelder and Mead [Nelder 1965]. The method uses the concept of a simplex, which is a special polytope of N

+ 1 vertices in N dimensions. The objective function is measured at each test point. The algorithm as implemented here generates a new test position by replacing the worst point with a point reflected through the centroid of the remaining N points. If this point is better than the best current point, it is also attempted to stretch the reflection by a factor of 1.5 along this line. If this new point is not better than the previous value, the reflection is reduced by a factor of 0.5.

Automatic Optimisation

Figure 7-23 shows the results for both algorithms applied to the S355 T-joint (simplified model 13). The objective value corresponds to the bending distortion amplitude. One function call represents one simulation. For the CMA-ES, each generation consists of ten units; *i.e.*, simulations. The starting point corresponds to a full transient clamping. It has been found that the simplex method converges very fast while the CMA-ES is able to find a significantly better optimum.

For the CMA-ES algorithm, the objective value and the clamping times for all five clamps are shown as function of the generation in **Figure 7-24**. The first clamp is activated at the beginning and not varied. The algorithm is able to improve the results further until generation twenty when convergence is reached. The results are almost converged after the fifth generation, corresponding to fifty simulations.

Also it is found that the algorithm principally increases the clamping time which corresponds to the results shown in **Figure 7-18**. However, the results found in the parameter study are better than the results found using the automatic optimisation. Additionally, for all twenty generations, two hundred simulations are performed. Considering a calculation time of approximately four hours per simulation and a parallelization of three simulations at the same time, the total time required for the present optimization run is about ten days.

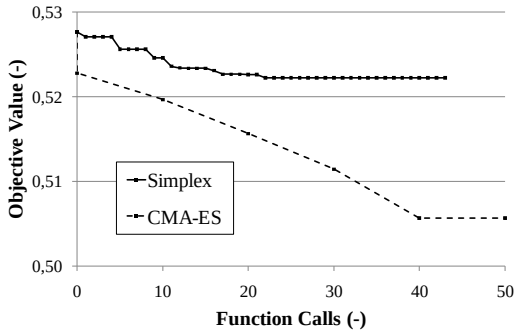

Figure 7-23 Objective value as function of the first fifty function calls; *i.e.*, simulations.

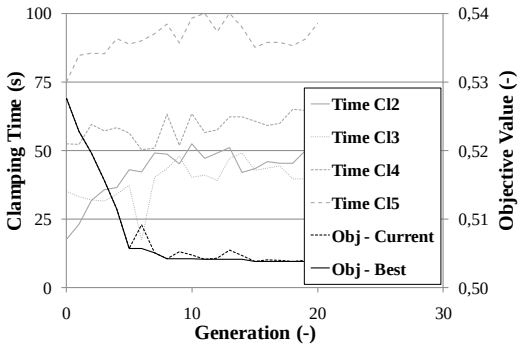

Figure 7-24 Objective value and clamping times as function of the generation. One generation corresponds to ten function calls.

7.4 Concluding Remarks

In order to simplify the clamping model, a FricSpring element has been developed, implemented as a user element in the finite element package ABAQUS and validated for a simple clamping case. In principally, the FricSpring element is a 0D finite element describing a linear-elastic clamp with tangential friction. Using this element, similar accuracies have been obtained as for an explicit modelling of the clamps with contact conditions. Additionally, the computation is reduced since the model possesses less desgrees of freedoms and the complexity of the model is reduced. In case of the overlap joint, due to the incooporated friction in tangential direction, the shearing is predicted correctly while for spring elements without friction, the workpiece is free to move below the clamp. This leads to an overestimation of the shearing during welding and to excessive element distortion which worsens the convergence rate and hence, increases the computation time.

Simplification studies have been performed for both case studies. The simplifications considered simplified temperature-dependencies, clamping models, mesh densities, shell meshes, and heat sources. Compared to the reference model, with a calculation time in the order to two days, the computation time could be reduced to approximately 4-5 hours for both case studies and volume meshes without significant loss of accuracy.

The computation time could be reduced significantly on employing shell meshes. Here, to approximately thirty minutes for the overlap joint for a full transient simulation with phase transformations and mixed isotropic-kinematic hardening. However, for shell elements the asymptotic correctness of the results is not guaranteed. Hence, the resulting distortion amplitudes might differ from the volume model.

Studies have been performed using the shell meshes to optimise the clamping conditions. The results found in the previous chapter, indicating that delayed clamping leads to lower distortion amplitudes than initial clamping prior to welding, were supported by a parameter study. In particular, the study showed that clamping can even be favourable after welding.

7.4 Concluding Remarks

A 1D scan revealed problems regarding the robustness of the shell model for the overlap joint. While the results are relatively stable for the simulations of the T-joint, large discontinuities have been found. This problem has been solved using a higher mesh density. However, this has been achieved to the price of a significantly increased computation time.

For the shell model of the T-joint, an optimisation run has been performed using two global optimisation algorithms, a covariance adaptation of the evolutionary strategy (CMA-ES) and the downhill simplex method. The results of the optimisation supported the parameter study in that the welding distortion is reduced for a later clamping.

The total optimisation potential found here is high; *i.e.*, about one third less distortion, compared to the case where the clamps are activated initially prior to welding. The reduction of the distortion amplitude due to the late clamping together with a cold release, is approximately another ten percent.

8 Transverse Control Arm

In order to apply the models and results presented in the previous chapters, simulations and experiments were performed for an industrial component. Here, a 6 mm thick S500MC transverse control arm has been provided by Volkswagen Braunschweig. The numerical results presented in this chapter have been obtained to a great extent within the M2i valorisation project MA08.078 [Gorzkulla 2010].

Figure 8-1 shows the control arm. It is made of six millimetre thick high-strength low-alloyed steel S500MC. The control arm consists of a flange and a web welded together in a T-joint configuration and two sockets for assembly purposes. Hence, the component is comparable to a bent T-joint.

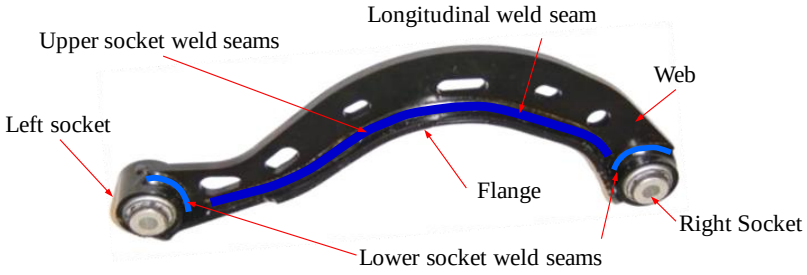

Figure 8-1 S500MC transverse control arm.

8.1 Numerical and Experimental Configuration

8.1.1 Thermomechanical Data

In common with the steels DP600 and S355, the thermomechanical material behaviour has been characterized. Uniaxial tests have been performed for several temperatures between room temperature and 800 °C. For this purpose, rods with a thickness of 4 mm were cut out of the samples.

Figure 8-2 shows the results and the numerical fit. At room temperature and up to 200 °C, a plateau has been found in the initial plastic domain where no hardening sets in. However, this effect cannot be modelled explicitely with the present material model. It has been found that the material behaviour remains almost constant up to a temperature of 400 °C. Above this temperature, softening sets-in and the steel looses all strength up to 800 °C.

Figure 8-3 (left) shows the result of a cylic test at room temperature. Unfortunately on compression, the sample does eventually buckle. Hence, it has not been possible to push the sample back to the initial state of zero strain. However, it has again been found that the material exhibits early yielding for a change of the loading direction; *i.e.*, kinematic

hardening. Also here the fraction of the kinematic hardening is approximately 50 % as for the DP600 and the S355.

Additionally, a Gleeble test has been performed on a S500MC specimen. Here, the sample was heated up to 900 °C and cooled down without external loads; *i.e.*, the sample was free to expand and contract. After the thermal treatment, a tensile test was performed at room temperature. In **Figure 8-3 (right)**, the results of this test are compared to the room temperature test for the S500MC base material. It has been found that the tested sample is weaker than the base material. In particular, the initial yield stress is 500 MPa, but the material exhibits a steep drop to 400 MPa in the early plastic domain. This initial drop might be explained by bake hardening during the thermo-mechanical treatment in the production of MC steel grades. The dislocations are locked by carbon atoms segregating in the regions around dislocations where the stresses are compressive. However, this effect cannot be considered in the simulations with the present model.

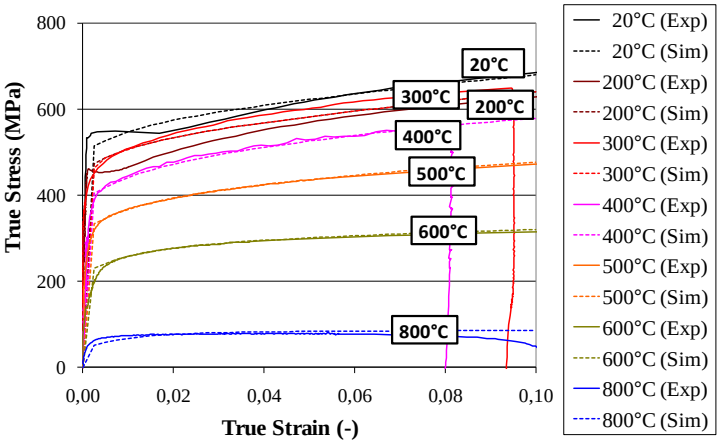

Figure 8-2 Temperature dependent tensile tests of the S500MC and fit.

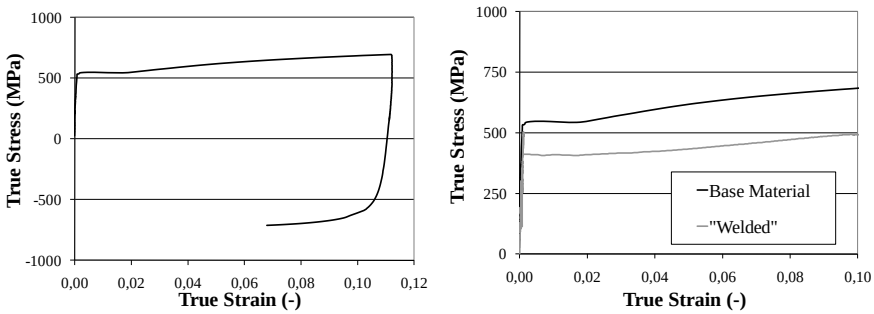

Figure 8-3 Left: Cyclic test at room temperature for the S500MC. Right: Comparison of tensile tests at room temperature for a weld simulated sample.

8.1.2 Numerical and Experimental Configuration

In order to perform welding experiments, the equipment has been modified, see **Figure 8-4**. Here, the clamping system for the other two case studies is not used and the mounting table is replaced. The new mounting table consists of a rail shaped frame, a base plate, two pins, a slide and a carriage bolt connected to the slide and the frame. The slide is moved by tightening the carriage bolt. The transverse control arm can be fixed by the two pins. The welding conditions are shown in **Table 8-1**.

Figure 8-5 shows the FE model and the applied mechanical boundary conditions. The model consists of 2270 elements and 4114 nodes. Only half of the workpiece has been modelled in order to take the symmetry plane into account. The total computation time for this model is approximately one hour using one CPU on a state-of-the-art workstation.

The clamping has been modelled at the sockets in accordance with the experimental conditions. Here, gapcyl elements were applied as bolts, see [ABAQUS]. Two elements are marked green in the figure. The gapcyl elements do not possess any stiffness as long as no contact occurs due to closing of the gap. If contact is established they react as very stiff springs and transfer the compression loads in the contact direction. The centre of the left pin has been modelled as fixed in all three spatial directions with no gap. The centre of the right pin is fixed in the directions of the x- and the y-axis, allowing a movement in the z-direction corresponding to the experimental arrangement. In order to fix the control arm at the right pin, a spring is modelled which represents the carriage bolt.



Figure 8-4 Modification of the experimental setup to weld the S500MC transverse control arm.

Table 8-1 Welding conditions for the S500MC control arm.

Material	**S500MC**
Configuration	T-Joint
Metal Transfer	Short Circuit / Dip
Material Thickness	6 mm
Shielding Gas	Ar + 2% CO_2
Gas Flow	10-15 l min^{-1}
Welding Speed	10 mm s^{-1}
Voltage	25 V (x2)
Current	230 A (x2)
Power	5500 W (x2)
Energy / Length	550 J mm^{-1} (x2)
Filler Material	SG2 (DIN)
Filler Thickness	1.2 mm
Feeding Rate	7 m min^{-1}

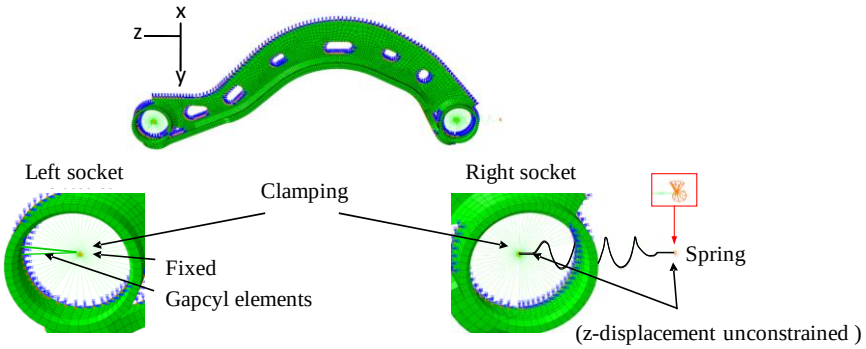

Figure 8-5 FE model and the applied mechanical boundary conditions.

8.1.3 Validation

Temperature Profile

The calibration of the temperature field has been done using experimentally measured annealing colours, see **Figure 8-6**. These annealing colours occur when the steel is heated above defined temperatures, corresponding to maximum temperature isotherms during welding. Depending on the maximum temperature, these colours are yellow, blue and grey and correspond to temperatures above 200 °C, 300 °C and 500 °C, respectively; see also the legend in the figure.

Here, a good agreement has been found between experiments and simulations. In order to fit these colours, the emissivity coefficient ε_r has been set to 0.5. The contact heat transfer coefficient h_c was found to be 50 $Wm^{-2}K^{-1}$, as for the 6 mm S355 T-joint.

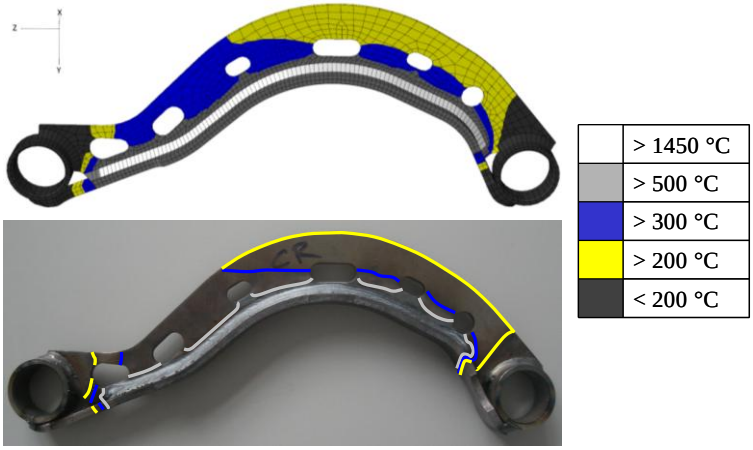

Figure 8-6 Experimental and numerical maximum temperatures (based on annealing colours).

Welding Distortion

Figure 8-7 shows the measured residual effective welding distortion for the control arm for two points. The transient qualitative tendency of the prediction agrees very well with the experiments. The distortion is dominated by a bending of the T-Joint. This leads to a shrinkage of the socket distance Δx by 1.8 ± 0.1 mm and an upward distortion Δy of 1.5 ± 0.1 mm. The predicted values are $\Delta x = 2.1$ mm and $\Delta y = 1.6$ mm which are about 17 % higher than the measured values.

Similar to the 6 mm S355 T-joint, it was found that deviations in the geometry of the workpieces due to production tolerances affect the distortion significantly if not considered. The deviation of the parts prior to welding is about ± 0.3 mm which is about three times larger than the measurement error of the welding distortion. Hence, it is recommended to always measure the predeformation in order to identify the real distortion deviations due to the welding process.

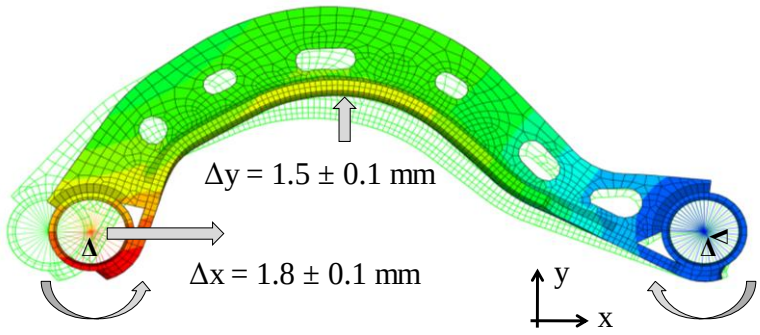

Figure 8-7 Measured residual welding distortion for the S500MC control arm without clamping. The geometry is obtained from the simulations.

Figure 8-8 shows the measured and simulated transient distortion of the socket distance Δx. The simulations predict the transient tendencies very well. It is very interesting to see that the extension of the socket distance during welding is about 3.5 mm ± 0.1 mm and significantly larger than the final shrinkage of 1.8 mm ± 0.1 mm after welding. Hence, it appears to be very important to consider the heating phase for the simulation of welding distortion of complex assemblies.

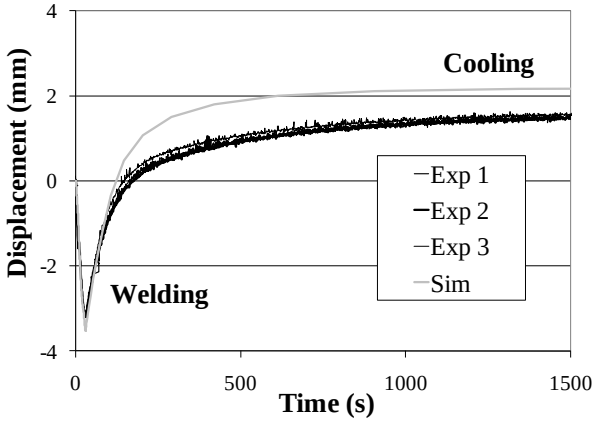

Figure 8-8 Measured and simulated transient welding distortion of the socket distance for the S500MC control arm without clamping.

8.2 Predictions

8.2.1 Optimisation of Clamping Conditions

From the overlap and T-joint case studies, it was found that the clamping conditions have a significant effect on the residual welding distortion. For the control arm, simulations have been performed for hot release and cold release conditions with various predeformation amplitudes, corresponding to a transient mechanical straightening.

Figure 8-9 shows the predicted welding distortion after cooling, the initial clamping force prior to welding, which is the same for both release conditions, and the clamping force at clamp release. The predeformation is applied at the carriage bolt; *i.e.*, at the spring element in the simulations. For lower predeformation amplitudes, the workpiece is deformed elastically, which can be seen by a linear dependency of the initial clamping forces on the predeformation. For predeformations above two millimetres, the workpiece starts to deform plastically.

For both clamping conditions, the welding distortion can be compensated by an optimized predeformation. The required predeformation is about 2.5 mm for the cold release condition and 4 mm for the hot release condition. These findings are similar to previous results that the distortion can be compensated more easily by longer clamping times. It can also be seen that clamping without predeformation increases the residual

welding distortion. Here, the material is forced to compress plastically during welding; *i.e.*, the expansion upon heating is restricted. This increases the shrinkage forces during cooling and hence, leads to a larger shrinkage.

For the hot release condition and predeformations lower than 3.5 mm, the clamping forces are compressive upon clamp release. This can be expected due to the expansion of the workpiece of about 3.5 mm due to welding. For the cold release condition, the clamping forces at release are in the order of 15-20 kN. Hence, although the welding distortion might be compensated by predeformation, high forces are required to do so.

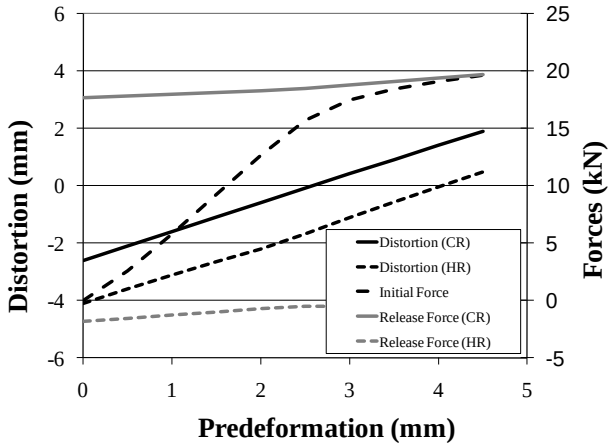

Figure 8-9 Shrinkage of the socket distance, initial clamping force prior to welding and clamping force at clamp release for the cold release (CR) and hot release (HR) condition.

8.2.2 Geometrical Predeformation

The application of high clamping forces in order to compensate welding distortion is generally undesirable due to wearing and the robustness of the process. Additionally, long clamping times; *i.e.*, half an hour, are impractical in automated industries. Here, the potential of a geometrical predeformation of the workpiece is investigated.

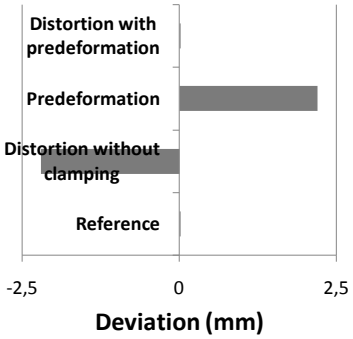

Figure 8-10 Deviation of the socket distance compared to the reference geometry.

Figure 8-10 shows the predicted socket distances obtained with and without geometrical predeformation. In the case of welding without clamping the distance is shrinking. The predicted welding distortion has been applied inversely as a geometrical predeformation to the control arm. Using the FE package ABAQUS, such a geometrical variations can be achieved using the option *imperfection. Using this extended sample, it has been found that the welding distortion can be eliminated completely.

Here, the reason for the applicability of an inverse geometrical predeformation might be due to the relatively small distortion amplitude compared to the dimensions of the workpiece; *i.e.*, 2 mm compared to 350 mm. For such small deformations, the behaviour can be assumed to be linear; *i.e.*, the influence of the geometrical predeformation on the welding distortion might be neglected. However, such a predeformation can be applied for bending and angular distortion (see **subsection 6.2.4**), but not for unstable buckling deformations as found for the DP600 overlap joint.

8.2.3 Sensitivity Analysis

FE Mesh

It has been found (**section 5.3**) that the chosen FE mesh as well as the element formulation might have a significant influence on the predictions. Here, simulations are performed for the reference mesh, a refined mesh, linear finite elements, elements with reduced integration, and elements with incompatible modes.

The refined mesh is shown in **Figure 8-11**. Here, the section of the weld seam is modelled by six elements instead of one element for the reference mesh. The refined mesh consists of 9176 elements with 13475 nodes. The number of nodes is increased by a factor of three and hence, the computation time is approximately nine times longer.

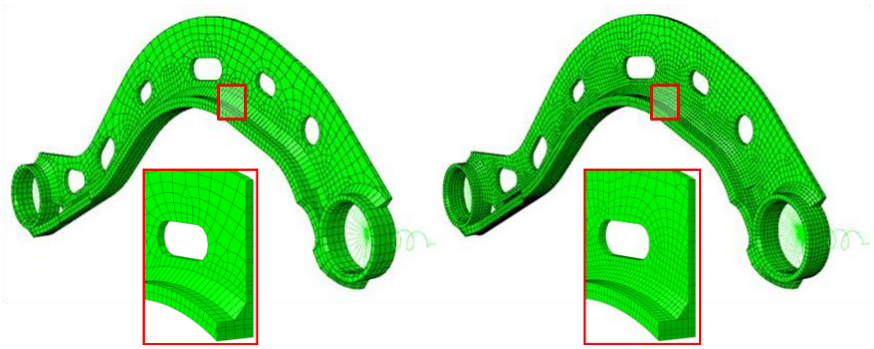

Figure 8-11 Comparison of the reference mesh and the refined mesh.

The welding distortion and the computation time have been evaluated for six combinations of mesh and element types, see **Figure 8-12**, where the coarse mesh refers to the reference mesh:

C(S) Coarse mesh - fully integrated elements

C(R) Coarse mesh - reduced integrated elements

C(I) Coarse mesh - elements with incompatible modes

R(S) Refined mesh – fully integrated elements

R(R) Refined mesh - reduced integrated elements

R(I) Refined mesh – elements with incompatible modes

There is a significant dependency of the results on the mesh; the mesh appears to be outside the converged range. With reference to the findings from **section 5.3**, case five and six would be expected to be closer to a converged state due to the finer mesh and the softer element types which reduce shear locking. Here, these two cases predict the same distortion and show a good agreement to experiments. However, this should be investigated further until a converged state has been obtained.

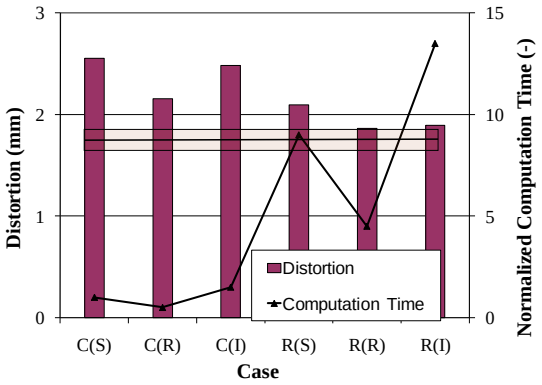

Figure 8-12 Predicted welding distortion and normalized computation time for all six mesh variations. The shaded box indicates the range of the experimental results.

Material Parameters

The results of sensitivity analysis performed for the control arm are shown in **Figure 8-13**. The following cases have been investigated:

1. Filler material activated from the beginning
2. 100 % isotropic hardening
3. 100 % kinematic hardening
4. No influence of martensite on the yield stress
5. No volume change during phase transformation
6. No strain-rate dependency at elevated temperatures

In general, the same results have been found as for the two case studies, see **section 5.4**. The activation of the filler material shows no significant influence on the predictions. The assumption of 100 % isotropic hardening overestimates welding distortion while the opposite is the case for 100 % kinematic hardening. Also the consideration of phase transformations influences the results by about 20 %. The predictions turned out to be very sensitive (25 %) to the strain-rate dependency of the material at elevated temperatures. This is of particular concern as the strain-rate dependency could not be measured for the S500MC but has been assumed to be the same as for the S355.

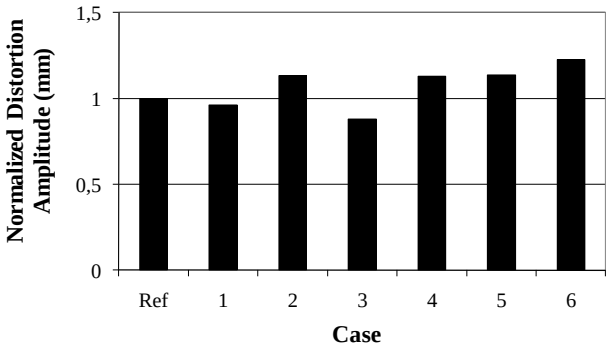

Figure 8-13 Results of the sensitivity analysis for the S500MC transverse control arm.

8.3 Concluding Remarks

The thermomechanical-metallurgical model was applied successfully to perform simulations and experimental validations of a 6mm thick S500MC transverse control arm. Tensile tests were performed for the S500MC in order to obtain reliable mechanical material data. Tensile tests were also performed for weld simulated samples. Here, a softening of the material in the early plastic domain was found which cannot be described with the present model.

The temperature profile has been validated by the maximum temperatures measured by the annealing colours occurring at elevated temperatures. It was found in both experiments and simulations that the control arm is subjected to bending due to welding, leading to shrinkage of the socket distance. Transient measurements of the distortion in an unclamped condition revealed that the socket separation is increased during welding. For the control arm, this expansion was found to be twice as large as the contraction after welding.

The shrinkage due to welding can be compensated by an optimisation of the clamping conditions, here by an adequate predeformation. However, high clamping forces and long clamping times are required. Also a geometrical predeformation of the workpiece has been assessed. It was found that a simple inverse predeformation is adequate to reduce welding distortion. Here, no additional clamping is required.

9 General Conclusions

In past decades, mitigation methods have been developed by many researchers in order to reduce welding distortion using different approaches. These include low-stress no distortion (LSND) techniques, welding with additional cooling, pre-deformation of the workpiece to be welded, transient or post-weld thermal tensioning, or using optimized welding sequences.

One parameter that affects the distortion, which is not explicitly considered in most studies, is the influence of the clamping system. This is an important aspect since clamps are almost always present during the welding process in order to hold the work-piece components in place. Unlike most of the mitigation techniques, making use of the clamps for in-line distortion control has the potential advantage that no further energy consuming technique has to be introduced into the process.

In the present work, the influence of the clamping system on the material behaviour during welding was investigated using a combined numerical and experimental approach. The simulations and experiments were performed for 1 mm thick DP600 overlap joints, 6 mm thick S355 T-joints and 6 mm thick S500MC control arms. A thermo-mechanical-metallurgical model was developed and welding simulations were performed for various clamping conditions and validated by experiments. This combination of modelling and experimental work has provided valuable insight into the process of welding in clamped conditions. Conclusions from these studies are summarised below.

Material Behaviour during Welding

- **Clamping Conditions** – For all investigated case studies, longer clamping of the workpiece, most preferably until cooling to room temperature, closer clamping to the weld seam, and late clamping reduces both residual distortion and residual stresses after unclamping. Longer and closer clamping leads to larger restraints at the weld seam and in the adjacent heat affected zone during cooling, this in turn increases plastic deformation. The remaining elastic strains, which cause distortion after unclamping, are reduced. Delayed clamping permits an increase of the workpiece expansion during heating, leading to increased restraints and plastic deformation upon subsequent cooling.
- **Hardening Behaviour** - The temperature-dependent material properties, phase transformations and mixed kinematic-isotropic hardening exhibit the largest influence on the predicted distortion. In particular, hardening is often represented in the literature by single kinematic or isotropic models. By means of cyclic tensile / compression and bending tests it has been shown in the present work that all three steels under consideration exhibit about 50% isotropic and 50% kinematic hardening. Using single isotropic or kinematic hardening models respectively overmatches or undermatches the residual distortion amplitude. It is therefore desirable to include a mixed hardening model in numerical simulations in order to obtain realistic distortion predictions.

- **Filler Material –** The material behaviour of the fillet was assumed to be the same as the workpiece material. In a sensitivity study, however, it was found that a better agreement to experiments is achieved if the yield stress and the tensile strength of the filler material are applied. Further research is required to develop an adequate characterisation of the filler material behaviour.
- **Residual Stress Distribution** – The longitudinal residual stress distribution can be understood using a simple bar model, which results in a typical distribution with a tensile zone at the seam and a compression zone in the adjacent parent material. Taking thickness variations of the overlap joints into account as well as superposed bending stresses due to the buckling distortion, good agreement between experiments and transient simulations can be achieved. The residual stress distribution in an overlap joint is dependent upon the asymmetric geometry of the workpiece.
- **Tensile Strength –** In transverse tensile tests performed on the overlap joints, cracking of the workpiece occurred in the heat-affected-zone. In the simulations the critical plastic strains are also attained in the HAZ region. However, the same results were obtained in the simulations if no material changes due to welding were considered; *i.e.*, the overlap joint geometry is assumed to be milled from one piece. Here, cracking in this case is not due to the altered material behaviour due to welding, but due to the asymmetric geometry leading to a local stress concentration.
- **Welding Sequences** – Welding in sequences has a significant effect on the residual material state after welding. Compared to welding in one step, the two additional effects that must be taken into account are preheating, which leads to more homogeneous temperature distribution and reheating, which causes stress relaxation. Both effects are present at the intermediate points between individual steps and reduce residual distortion. It is shown that the dominant effect on final distortion is reheating, which if optimized, causes higher plastic deformation and hence, lower residual distortion and stresses.

Modelling of Welding

- **Clamping Model** - Three contact models were compared; contact elements, spring elements and a newly developed 0D FricSpring element. Applying contact and FricSpring elements leads to good results while the latter reduces the complexity of the clamp model significantly. If friction is important for a correct process representation, for instance if the parts are not tack welded, then the clamping system should not be represented by springs. This overestimates shearing of the components to be joined and also leads to numerical convergence difficulties.
- **Spatial Discretisation** - In general, it is mandatory in FEM to perform mesh convergence analysis to evaluate the predictive quality of the simulation. However, in welding simulations it is common to apply refined meshes at the weld seam in order to resolve the temperature and stress gradients and a rather coarse mesh towards the edges of the specimen. In particular for linear finite

elements, such meshes might possess a large artificial geometrical stiffness leading to erroneous predictions. It was found that the meshing can affect not only the distortion amplitude but also the distortion shape, resulting in prediction of an incorrect buckling mode, although the predicted residual stresses were comparable for all meshes. For all FE based numerical simulations it is advisable to perform mesh convergence analyses.

- **Modal Convergence Analysis** – Performing a mesh convergence analysis is a very time-consuming task considering that a typical computation can take of the order of days for welding simulations. It is shown that these analyses can be replaced by eigenfrequency convergence analyses. This corresponds to a convergence study of the required distortion energy to obtain a certain eigenmode. It takes much less computation time to perform a modal analysis; *i.e.*, in the order of minutes, this approach can therefore offer significant savings.

- **Simplified Models** - Based on mesh convergence analyses and material sensitivity studies, the computation time of the stress and distortion simulations can be reduced significantly without seriously degrading the predictions. In this work, the computation time was reduced from days to less than one hour. Some simplified models exhibited an unsteady behaviour in the distortion prediction for small parameter variations, hence for the purposes of automated optimisation, it is advisable to examine the robustness of these models in future research.

- **Heating during Welding** – In some simplified models; *i.e.*, shrinkage models, the heating of the workpiece is neglected. However, the expansion during heating might be significant. For the transverse control arm, the expansion was found to be twice as larger as the final contraction after cooling. Hence, heating of the workpiece should be taken into account, particularly for complex assemblies where simple shrinkage models that disregard the influence of heating are commonly applied. It remains to be determined whether these simple models can be adapted to take account of thermal expansion during heating.

10 Future Work

The recommendations for future work from this thesis include:

- For welding sequencing, it was found that reheating appears to be the dominant effect on the residual distortions. However, its correlation with the number of steps, the seam length and the geometry need to be investigated in detail.
- For a good simulation model, it is not only important to validate the model by experiments but also to verify its reliability. Some models might not be robust for small parameter variations. The reason for this behaviour should be investigated.
- The prediction of the transformation from austenite to other phases on cooling showed good agreement with experiments. However, to date there is no general and simple model available for the prediction of the austenitisation on heating in the heat affected zone. Phase field models have been employed to predict the austenite fraction, although this is a time-consuming task. Consideration should therefore be given to the development of a more appropriate approach.
- Applying the Goldak heat source model for simulations of gas metal arc welding exhibited some inaccuracies in the predicted temperatures between 1000 and 1500 °C. In particular, the flow of liquid metal cannot be described using this model.
- In most simulations, the filler material is assumed to be the base material. This is not true in most cases and it was found that this can affect the results to a large extent. Model sensitivity to the material properties of the consumable material should be examined in more detail.

Summary

The distortion of structures due to time-dependent and localized heating imposed during welding is one of the major concerns related to the application of fusion welding as a joining method in industry. In general, distortion is regarded as a critical issue in terms of performance, quality and productivity, and can be problematic because it is not often taken into account in the initial design.

Significant research has been performed in the last four decades on techniques to mitigate residual stresses and distortion after welding. However, most of these techniques introduce new process parameters, increase the production time and hence the cycle time, or are environmental unfriendly. Despite ongoing attention, the influence of clamping has not been well reported in the literature, although it is generally acknowledged that the influence of clamping is considerable, and clamping fixed arrangements for the reduction of distortion in specific applications have been reported. This is an important aspect since clamps are almost always present during welding in order to fix the work-pieces. Unlike most of the mitigation techniques, making use of clamps for in-line distortion control has the potential advantage that no further energy consuming technique need be introduced into the process.

In this work, the influence of clamping on the residual welding distortion was investigated by means of conceptual, analytical, and finite element models, and by experimental techniques, including temperature, residual stress and residual deformation measurements. The combination of modelling and experimental work has provided considerable insight into the modifications due to the clamping system.

A thermo-mechanical-metallurgical welding model was developed which includes temperature and strain rate dependent mechanical behaviour, isotropic and kinematic work hardening, and phase transformations in the fusion zone and the adjacent heat affected zone. Simulations were performed for three case studies; a 1mm thick DP600 overlap joint, a 6mm thick S355 T-joint and a 6mm thick S500MC transverse control arm. Using these work-pieces, the influence of clamping on welding distortion could be investigated for buckling distortion of the overlap joint, bending and angular distortion of the T-joint and bending distortion of the control arm. The material data for the model was obtained from the literature if available and from mechanical tests otherwise. Mechanical tests were performed at elevated temperatures, for low and high strain rates and for a combined tension and compression in order to distinguish between isotropic and kinematic hardening. In the case of the 1mm thick DP600 specimen, bending tests were performed since compression leads to early buckling of the sample.

In order to validate the welding simulation model, an experimental welding set-up was constructed for gas metal arc welding of the selected case studies. This equipment allows control of the clamping time, the clamp release time, the clamping force and weld sequencing. The case studies were welded for different clamping conditions using various welding sequences. Temperature measurements were conducted during and after welding for clamped and unclamped conditions in order to calibrate the heat input model and to determine the heat conductance due to the clamping system. Out-of-plane distortion measurements were performed using a surface scan with LVDT sensors which measure distortion with an error of only micrometers. The measurements were repeated for all conditions in order to give an estimation of the experimental standard deviation which must

be known in order to evaluate the model. Residual stress measurements were made in cooperation with BAM, using laboratory X-ray diffraction techniques.

Using the simulations and experiments, it was found that the clamping conditions can have a significant effect on the residual stress state after welding. The temperature distribution is modified due to additional cooling by the clamps, which causes faster cooling of the workpiece. This leads to different phase transformations in the fusion zone and the heat-affected zone compared to the case without clamping. Residual welding distortion was investigated for various clamping times, clamp release times, and clamping distances. Later clamping; *i.e.*, when the workpiece has assumed its maximum thermal expansion, longer clamping; *i.e.*, a later clamp release and closer clamping, proved to be efficient in order to reduce distortion. For all these parameters, distortion is reduced by an increase of the plastic deformation due to the thermal contraction. This leads to lower remaining elastic strains after unclamping compared to the unclamped case and hence, to reduced distortion.

For the 1mm DP600 overlap joint, which exhibited buckling distortion, the distortion amplitude is correlated to the residual stress amplitude. Using a simple bar model, it could be shown that later and longer clamping leads to reduced stresses due to the increased plastic deformation. In the transient 3D model, this tendency cannot be observed easily since the stresses are affected by the asymmetry of the overlap joint and superposed bending stresses. However, the measured stresses could be employed in order to validate the model whose predictions showed a good agreement with the measurements.

In order to model the clamping conditions, different approaches were applied. Using volumetric clamps with numerical contact models shows good agreement with experiments but requires some expertise in order to obtain stable simulations. The second approach was to apply spring elements as clamps. This defines the clamping stiffness easily and also avoids the need for numerical contact modelling. However, spring elements may lead to numerical oscillations if the stiffness is non-zero only for compression and set to zero for tension. Additionally, the missing friction normal to the spring may lead to large shearing of the work-pieces during welding. In order to overcome these problems and to reduce the degrees of freedom, a simple 0D spring element FricSpring was developed. This element allows a simple definition of the clamp stiffness and the clamping direction, leads to no forces in tension, and requires no additional degrees of freedom. Using the FricSpring element makes it possible to conduct a simple parameterized optimisation of the clamping conditions.

In addition to clamping conditions, the effect of welding in sequences on residual distortion was investigated. Two effects are present if a work-piece is welded in sequences; the work-piece is preheated and also reheated. The latter involves a stress relaxation phenomenon, which causes stress relief depending on the reheating temperature. It was found that the reheating effect dominates. A simple statistical model was developed in order to optimise reheating and to reduce welding distortion; this model shows promising results. However, the effect of the seam length, the number of sequences, or the material thickness is not included yet.

A correlation between experiments and simulations is very important to assess the robustness of the model. Literature often deals with the sensitivity of simulations but rarely with the experimental accuracy and repeatability. However, measurements can vary due to positioning errors for temperature measurements, or pre-deformation of the work-pieces. It was found that particularly the latter can have a significant influence on the measured residual distortion for low distortion amplitudes but is often neglected in the literature. For

the S355 T-joint and the S500MC the measured distortion amplitudes are in the order of some tenths of a millimetre and the pre-deformation was determined to be in the same order of magnitude. For one specific example, simulations were performed with pre-deformation included, which improved the agreement between simulations and experiments. Although this is a time-consuming task, it is recommended to always take pre-deformations into account for welding of thick plates with small distortion amplitudes.

Similar to variables leading to deviations in experiments, the sensitivities of simulations must be known in order to assess the quality of the predictions. It is recommended to perform sensitivity studies by varying parameters that have an effect on the results. It was found that the assumed strengths of the materials, the hardening model; *i.e.*, kinematic or isotropic or mixed, and phase transformations have a large influence on the results. Also it is recommended to use the material behaviour of the filler material instead of using the properties of the base material. The strongest influence on the results was found to be due to the FE meshing if a non-converged mesh is applied; the predicted buckling mode and amplitude were found to be dependent on the mesh due to the additional geometrical stiffness of the finite elements. Here, using a converged mesh, or a mesh which is close to the converged mesh, yielded the correct mode and amplitude. In particular, it was found that the distortion shape is more sensitive to the geometrical stiffness than the residual stresses. Hence, a mesh convergence study must be performed before the mesh is approved for distortion analyses. Performing a mesh convergence study is a very time-consuming task because the common computation time required to complete a simulation is in the order of days. Fortunately, it could be shown that the geometrical stiffness can also be minimized by an eigenmode convergence analysis, which can be performed in minutes.

Based on the sensitivity analyses undertaken, simplified models were developed. It was found that the required computation time of the welding simulation can be reduced significantly by successive model simplifications. The largest reduction can be achieved if the mesh is simplified in such a manner that the geometrical stiffness remains small and if reduced integrated elements are employed. Using this approach, the computational time could be reduced from two days to two to three hours. The simulation time is reduced if only isotropic hardening is applied since kinematic hardening requires some internal degrees of freedom. The computation time could be reduced below one hour using shell meshes. With these meshes it has not been possible to simulate the switch of the buckling direction for the overlap joint or angular distortion for the T-joint. However, for qualitative predictions where tendencies are of interest, this might still be sufficient.

Regarding the findings of this thesis, for an optimum reduction of the welding distortion, it was found that the clamp release time should be as long as possible, the clamp should be closed when the work-piece has assumed its maximum thermal extension, and the clamp should be positioned as close to the weld seam as possible. Additionally, preheating of the clamps could be applied in order to reduce the inhomogeneity of the temperature distribution. Welding in sequences also reduces distortion if the stress relaxation effect is maximized.

Tobias Schenk, May 2011

References

[Aa 2006] E. van der Aa, M. Hermans, I. Richardson - *Welding with a Trailing Heat Sink: How to optimise the Cooling Parameters* - Trends in Welding Research, Proceedings of the 7th International Conference, 2006, pp. 577-582

[Aa 2006a] E. van der Aa, M. Hermans, I. Richardson - *Conceptual model for stress and strain development during welding with trailing heat sink* - Science and Technology of Welding and Joining, 2006, Vol. **11**(4), pp. 488-495

[Aa 2007] E. van der Aa - *Local Cooling during Welding: Prediction and Control of Residual Stresses and Buckling Distortion* - PhD Thesis, TU Delft, 2007, ISBN: 9789077172292

[ABAQUS] ABAQUS User`s Manual, Version 6.8, Hibbit, Karlsson and Sorensen Inc., USA

[Abed 2008] E. Abed, S. P. Edwardson, K. R. Edwards, C. Carey, G. Dearden, K. G. Watkins - Effect of Post Forming Heat Treatments on Laser Formed Components - Proceedings of the IWOTE'08, 2008, Bremen, pp. 315-322

[Abid 2005] M. Abid, M. Siddique - *Numerical simulation of the effect of constraints on welding deformations and residual stresses in a pipe-flange joint* - Modelling Simul. Mater. Sci. Eng., 2005, Vol. **13**, pp. 919-933

[Alberg 2003] H. Alberg, D. Berglund - *Comparison of plastic, viscoplastic, and creep models when modelling welding and stress relief heat treatment* - Comput. Methods. Appl. Mech. Engrg., 2003, Vol. **192**, pp. 5189-5208

[Allmeier 2005] S. Allmeier - *Untersuchung von Schweißeigenspannungen an Aluminiumkonstruktionen* – PhD Thesis, TU München, 2005

[Altenkirch 2008] J. Altenkirch, A. Steuwer, M. Peel, D.G. Richards, P.J. Withers – *The effect of tensioning and sectioning on residual stresses in aluminium AA7749 friction stir welds* – Materials Science and Engineering, 2008, Vol. **488A**, pp. 16-24

[Anca 2004] A. Anca, A. Cardona, J.M. Risso - *3D-Thermo-Mechanical Modelling of Welding Processes* - Mecánica Computacional, 2004, Vol. **23**, pp. 2301-2318

[Andersen 2000] L. Fuglsang-Andersen - *Residual Stresses and Deformations in Steel Structures* - PhD Thesis, DTU, 2000, ISBN: 8789502469

[Andrews 1965] K.W. Andrews - *Empirical Formulae for the Calculation of Some Transformation Temperatures* - Journal of the Iron and Steel Institute, 1965, Vol. **103**(7)

[Argyris 1982] J.H. Argyris, J. Szimmat, K.J. Willam - *Computational Aspects of Welding Stress Analysis* - Comput. Methods Appl. Mech. Engrg. 1982, Vol. **33**, pp. 635-666

[Auger 2005] A. Auger, N. Hansen - *A Restart CMA Evolution Strategy With Increasing Population Size* - Proceedings of the IEEE Congress on Evolutionary Computation, 2005, pp. 1769–1776

[Avrami 1939] M. Avrami - *Kinetics of Phase Change I* - Journal of Chemical Physics, 1939, Vol. **7**, pp. 1103-1112

[Backhaus 1983] G. Backhaus – *Deformationsgesetze* - Akademie-Verlag, Berlin, 1983

[Beghini 2005] M. Beghini, L. Bertinit, D. Cantemir - *The effect of thermal properties on transient temperatures during welding of perforated plates* - Associazione Italiana per l'Analisi delle Sollecitazioni, XXXIV Convegno Nazionale, 2005

[Belytschko 2001] T. Belytschko, W. Liu, B. Moran - *Nonlinear Finite Elements for Continua and Structures* - John Wiley & Sons, 2001, ISBN: 0471987735

[Berglund 2001] D. Berglund - *Simulation of Welding and Stress Relief Heat Treating in the Development of Aerospace Components* - Licentiate Thesis, Lulea Tekniska Universitet, 2001

[Berkhout 1968] C.F. Berkhout, P.H. van Lent – Anwendung von Spitzentemperatur-Abkühlzeit (STAZ) Schaubildern – Schweißen und Schneiden, 1968, Vol. **20**(6), pp. 256-260

[Björesson 2001] L. Börjesson, L-E. Lindgren - *Simulation of multipass welding with simultaneous computation of material properties* - J. eng. mater. technol., 2001, Vol. **123**, pp. 106-111

[Bleck 2004] W. Bleck, A. Frehn, P. Larour, G. Steinbek - *Untersuchung zur Ermittlung der Dehnratenabhängigkeit von modernen Karosseriestählen* - Mat.-wiss. u. Werkstofftech., 2004, Vol. **35**(8), pp. 505-513

[Blondeau 1973] R. Blondeau, P. Maynier, J. Dollet - *Prévisions de la dureté et de la resistance des aciers au carbone et faiblement allies d'après leur structure et leur composition* - Revue de Métallurgie, 1973, Vol. **70**(12), 883-892

[Boldt 2004] T. Boldt - *Clamping systems for laser welding processes* - Ölhydraulik und Pneumatik, 2004, Vol. **48**(2), pp. 1-26

[Böllinghaus 2003] T. Böllinghaus, T. Kannengießer – Effect of filler material selection and shrinkage restraint on stress strain buildup in component welds – Proceedings of the 6th International Trends in Welding Research Conference, 2003, pp. 906-911

[Böllinghaus 2005] T. Böllinghaus, T. Kannengießer, M. Neuhaus – *Effects of the structural restraint intensity on the stress strain build up in butt joints* – Mathematical Modelling of Weld Phenomena 7, 2005, pp. 651-669, ISBN: 9783901351990

[Brickstad 1998] B. Brickstad, B.L. Josefson - *A parametric study of residual stresses in multi-pass butt-welded stainless steel pipes* - International Journal of pressure Vessels and Piping, 1998, Vol.**75**, pp. 11-25.

[Bronstein 1997] I.N. Bronstein, K. A. Semendjajew, G. Musiol, H. Mühlig – *Taschenbuch der Mathematik* – Verlag Harri Deutsch, 1997, ISBN: 3817120052

[Brown 1992] S. Brown, H. Song - *Finite Element Simulation of Welding Large Structures* - J. Eng. Ind., 1992, Vol. **114**, pp. 441-451

[Burnett 1979] J.A. Burnett, J. Padovan - *Residual Stress Fields in Heat-Treated Case-Hardened Cylinders* - Journal of Thermal Stresses, 1979, Vol. **2**, 251-263

[Camilleri 2008] A.D. Camilleri, T.G.F. Gray, D. Nash – *Mitigation of welding distortion and residual stresses via cryogenic CO2 cooling – a numerical investigation* – Proceedings of the the Conference on Computer Technology in Welding and Manufacturing, 2008, Cranfield, UK

[Canas 1996] J. Cañas, R. Picón, F. París, J.C. Martin - *A simplified numerical analysis of residual stresses in Aluminium welded plates* - Comp. Struct., 1996, Vol. **58**(1), pp. 55-69

[Cary 2005] H. Cary, S. Helzer - *Modern Welding Technology*" - Upper Saddle River, New Jersey: Pearson Education. 2005, ISBN 0131130293.

[Chaboche 1986] J.-L. Chaboche - *Time independent constitutive theories for cyclic plasticity* - International Journal of Plasticity, 1986, Vol. **2**(2), pp. 247-302

[Chaboche 1989] J.-L. Chaboche - *Constitutive Equations for cyclic plasticity and cyclic viscoplasticity* - International Journal of Plasticity, 1989, Vol. **5**, pp. 247-254

[Chaboche 1993a] J.-L. Chaboche - *Cyclic viscoplastic constitutive equations. I: A thermodynamically consistent formulation* - Journal of applied mechanics, 1993, Vol. **60**(4), pp. 813-821

[Chaboche 1993b] J.-L. Chaboche - *Cyclic viscoplastic constitutive equations. II: Stored energy - comparison between models and experiments* - Journal of applied mechanics, 1993, Vol. **60**(4), pp. 822-828

[Chen 1985] Q. Chen, O. Pawelski, R. Kaspar - *Contribution to the deformation characteristics of dual-phase steels* - Z. Metallkunde, 1985, pp. 348–352

[Conrardy 1997] C. Conrardy, R. Dull – Control of distortion in thin ship panels – Journal of Ship Production, 1997, Vol. **13**(2), pp. 85-92

[Conrardy 2006] C. Conrardy, T.D. Huang, D. Harwig, P. Dong, Lö. Kvidahl, N. Evans, A. Treaster – *Practial welding techniques to minimize distortion in lightweight ship structures* – Journal of Ship Production, 2006, Vol. **22**(4), pp. 239-247

[Corus 2009] Personal communications with Corus steel, Ijmuiden, 2009

[Dahl 1978] W. Dahl, H. Rees – Zur Korngrößenabhängigkeit der unteren Streckgrenze von Baustählen – Archiv für das Eisenhüttenwesen, 1978, Vol. **49**(1), pp. 25-29

[Damsbo 1998] M. Damsbo, P.T. Ruhoff - *An evolutionary algorithm for welding task sequence ordering* - Lecture Notes in Computer Science, 1998, Vol. **1476**, pp. 120-131, ISBN: 9783540649601

[Davies 1978] R.G. Davies - *Influence of Martensite Composition and Content on the Properties of Dual Phase Steels* - Metallurgical Transactions A, 1978, Vol. **9A**, pp. 671-679

[Davis 1994] M.H. Davis, M.J. Painter, M. Wahab - *A Comparison of Weld Pool Shapes Predicted form Models incorporation Conduction and Convection* - 42nd Annual Welding Conference, Melbourne, 1994, paper 27.

[Dean 2006] D. Dean, M. Hidekazu - *Prediction of welding residual stress in multi-pass butt-welded modified 9Cr–1Mo steel pipe considering phase transformation effects* - Computational Material Science, 2006, Vol. **37**, pp. 209-216

[Dennis 1987] J.R. Dennis, R.B. Schnabel - *Numerical Methods for Unconstrained Optimization and Nonlinear Equations* - Prentice-Hall Inc., 1987, ISBN: 0898713641

[DenUijl 2007] N.J. den Uijl – *Post Weld Heat Treatment of advanced High Strength Steel for automotive Joining* - Mathematical Modelling of Weld Phenomena 8, 2007, ISBN: 9783902465696

[Deo 2002] M.V. Deo, P. Michaleris – *Experimental Verification of Distortion Analysis of Welded Stiffeners* – Ship Production, 2002, Vol. **18**(4), pp. 216-225

[Deo 2003] M.V. Deo, P. Michaleris – *Elimination of Bowing Distortion in Welded Stiffeners* – Ship Production, 2003, Vol. **19**(2), pp. 76-83

[Deo 2003a] M.V. Deo, P. Michaleris – *Mitigation of welding induced buckling distortion using transient thermal tensioning* – Science and Technology of Joining and Welding, 2003, Vol. **8**(1), pp. 49-54

[Deo 2003b] M.V. Deo, P. Michaleris – *Prediction of buckling distortion of welded structures* – Science and Technology of Joining and Welding, 2003, Vol. **8**(1), pp. 55-61

[Dilthey 1994] U. Dilthey - *Schweisstechnische Fertigungsverfahren, Bd. 1 – Schweiss- und Schneidetechnologien* - VDI-Verlag, 1994, ISBN: 3184013103

[Dilthey 1995] U. Dilthey - *Schweisstechnische Fertigungsverfahren, Bd. 2 – Verhalten der Werkstoffe beim Schweißen* - VDI-Verlag, 1995, ISBN: 3184013995

[Doig 2009] M. Doig, M. Kraska, P. Wyrwich, L. Kessler, J. Gerlach, M.-S. Aydin - *Inverse parameter identification by out-of-plane bending tests* - Proceedings of the Forming Technology Forum, 2009, Zürich

[Dong 1998] P. Dong, J.K. Hong, P. Rogers – *Analysis of Residual Stresses in Al-Li Repair Welds and Mitigation Techniques* – Welding Journal, 1998, November, pp. 439-445

[Dull 2004] R.M. Dull, J. R. Dydn, J. J. Russell, J. Shanghvi – *Method of Reducing Distortion by Transient Thermal Tensioning* – United States Patent US 2004/0245231 A1., 2004

[Easterling 1992] K. Easterling - *Introduction to the physical metallurgy of welding* – 2nd Edition, Butterworth-Heinemann, 1992, ISBN: 0750603941

[Ekrami 2005] A. Ekrami - *High temperature mechanical properties of dual phase steels* - Materials Letters, 2005, Vol. **59**, pp. 2070-2074

[Engelhard 2000] G. Engelhard, L.M. Habip, D. Pellkofer, J. Schmidt, J. Weber – *Optimization of residual welding stresses in austenitic steel piping: prooftesting and numerical simulation of welding and postwelding processes* – Nuclear Engineering and Design, 2000, Vol. **198**, pp. 141-151

[ESI 2008] ESI Group, PAM-Talk, Issue 36, Fall 2008, www.esi-group.com

[EWM] EWM, http://www.ewm.com, 2010

[Fanous 2005] I.F.Z. Fanous - *Introduction of the Element Interaction Technique for Welding Analysis and Simulation* - Journal of Pressure Vessel Technology, 2005, Vol. **127**, pp. 487-494

[Fassani 2003] R.N.S. Fassani, O. V. Trevisan - *Analytical Modeling of Multipass Welding Process with Distributed Heat Source* - J. Braz. Soc. Mech. Sci. & Eng., 2003, Vol. **15**(3), pp. 302-305

[Fergueson 1967] W.G. Fergueson, A. Kumar, J. E. Dorn - *Dislocation Damping in Aluminium at High Strain Rates* - Journal of Applied Physics, 1967, Vol. **38**(4), pp. 1863 et sqq.

[Ferro 2006] P. Ferro, H. Porzner, A. Tiziani, F. Bonollo - *The influence of phase transformations on residual stresses induced by the welding process – 3D and 2D numerical models* - Modelling Simul. Mater. Sci. Eng., 2006, Vol. **14**, pp. 117-136

[Flanagan 1981] D.P. Flanagan, T. Belytschko - *A Uniform Strain Hexahedron and Quadrilateral with Orthogonal Hourglass Control* - Num. Meth. Eng., 1981, Vol. **17**, pp. 679–706

[Fossum 1997] F. Fossum - *Parameter Estimation for an Internal Variable Model* - Journal of Engineering Materials and Technology, 1997, Vol. **119**, pp. 337 et sqq.

[Free 1989] J.A. Free, R. F. D. P. Goff - *Predicting residual stresses in multi-pass weldments with the finite element method* - Comp. Struct., 1989, Vol. **32**(2), pp. 365-378

[Friedman 1975] E. Friedman - *Thermomechanical Analysis of the Welding Process Using the Finite Element Method* - J. Press. Ves. Technol., 1975, Vol. **97**(3), pp. 206-213

[Fronius] Fronius, http://www.fronius.com, 2010

[Fukuda 1990] S. Fukuda, K. Yoshikawa - *Determination of welding sequence: a neural net approach* - Engineering Analysis with Boundary Elements, 1990, Vol. **7**(2), pp. 78-82

[Gery 2005] D. Gery, H. Long, P. Maropoulos - *Effect of welding speed, energy input and heat source distribution on temperature variations in butt joint welding* - Journal of Materials Processing Technology, 2005, Vol. **167**, pp. 393-401

[Giedt 1989] W.H. Giedt, L.N. Tallerico, P.W. Fuerschibach – *GTA Welding Efficiency – Calorimetric and Temperature Field Measurements* – Welding Journal, 1989, Vol. 68(1), pp. 28-31

[Goldak 1984] J. Goldak - *A finite element model for welding heat sources* - Metallurgical Transactions, 1984, Vol. **15B**, pp. 299-305

[Goodwin 1987] G.M. Goodwin – *Development of a New Hot-Cracking Test – The Sigmajig* – Welding Journal, 1987, Vol. **66**(1), pp. 33-38

[Gorzkulla 2010] T. Gorzkulla - *Prediction of welding distortion based on numerical simulation and its mitigation by optimization of the clamping conditions using the example of a transverse control arm* - Master Thesis, Beuth-Hochschule Berlin, 2010

[Gottstein 1998] G. Gottstein - *Physikalische Grundlagen der Materialkunde* - Springer Verlag, 1998, ISBN: 3540626700

[Grong 1997] Ø. Grong - *Metallurgical Modelling of Welding*- 2nd Edition, University Press, Cambridge, 1997, ISBN: 1861250363

[Gross 2006] D. Gross, T. Selig - *Bruchmechanik – mit einer Einführung in die Mikromechanik* - 3. Auflage, Springer, Berlin, 2006, ISBN: 354042203X

[Guan 1987] Q. Guan, D.L. Guo - *Method and Apparatus for Low Stress No-Distortion welding of thin-walled structural elements* - Chinese Patent, No. 8700959.5, 1987

[Guan 1994] Q. Guan, C. Zhang, D. Guo - *Dynamic control of welding distortion by moving spot heat sink* - Welding in the World, 1994, Vol.**33**(4), pp. 308-312

[Guan 1999] Q. Guan - *A survey of development in welding stress and distortion controlling in aerospace manufacturing engineering in China* - Welding in the World, 1999, Vol. **43**(1), pp. 64-74

[Guo 2005] S.Q. Guo, W. L. Xu, H. Yuan, W.H. Gu, X.T. Tian – *Numerical Simulation of Distortion Control by Static Thermal Tensioning in Welding of Thin Aluminum Alloys* – Materials Science Forum, 2005, pp. 3263-3266

[Hackmair 2003] C. Hackmair - *Messung und numerische Simulation der Schweißverzüge an Aluminium-Fahrwerkskomponenten* – PhD Thesis, University of Technology München, 2003

[Hänsch 2006] H.J. Hänsch, J.J. Krebs – *Eigenspannungen und Formänderungen in Schweißkonstruktionen* – DVS-Verlag, 2006, ISBN: 9783871551833

[Hansen 2010] N. Hansen - *The CMA Evolution Strategy: A Tutorial* – 2010, http://www.lri.fr/~hansen/cmatutorial.pdf

[Hardesty 2007] J.B. Hardesty, D. E. Nelson – Weld filler material that reduces residual stress and distortion – United States Patent, US 7,217,905 B2, 2008

[Hermans 1997] M.J.M. Hermans - *A Study of Short Circuiting Arc Welding* - PhD Thesis, TU Delft, 1997, ISBN: 9040714304

[Hibbit 1973] H.D. Hibbit, P. V. Marcal - *A Numerical Thermo-Mechanical Model for the Welding and subsequent Loading of a fabricated Structure* - Comp. Struct., 1973, Vol. **3**, pp. 1145-1174

[Higham 2000] N.J. Higham - *Evaluating Padé Approximants of the Matrix Logarithm* - Matrix Analysis and Applications, 2000, Vol. **22**(4), pp. 1126-1135

[Hill 1948] R. Hill - *A theory of the yielding and plastic flow of anisotropic materials* - Proc. R. Soc. London, 1948, Vol. **A193**, pp. 281 et sqq.

[Ho 1972] D. Ho - *The influence of imperfections on systems with coincident buckling loads* –International Journal of Non-Linear Mechanics, 1972, Vol. **7**(3), pp. 311-321

[Hoger 1984] A. Hoger, D. E. Carlson - *Determination of the stretch and rotation in the polar decomposition of the deformation gradient* - Quarterly of Applied Mathematics, 1984, April, pp. 113-117

[Hong 2004] S.-G. Hong, S.-B. Lee - *The tensile and low-cycle fatigue behaviour of cold worked 316L stainless steel: influence of dynamic strain aging* - International Journal of Fatigue, 2004, Vol. **26**, pp. 899-910

[Hu 2006] J.-F. Hu, J.-G. Yang, H.-Y. Fang, G.-M. Li, Y. Zhang - *Numerical simulation on temperature and stress fields of welding with weaving* - Science and Technology of Welding and joining, 2006, Vol. **11**(3), pp. 358-365

[Huang 1997] C.C. Huang, Y.C. Pan, T.H. Chuang - *Effects of Post-Weld Heat Treatments on the Residual Stress and Mechanical Properties of Electron Beam Welded SAE 4130 Steel Plates* - Materials Engineering and Performance, 1997, Volume **6**(1), pp. 61-68

[Huang 2004] T.D. Huang, P. Dong, L.A. DeCan, D.D. Harwig, R. Kumar - *Fabrication and engineering technology for lightweight ship structures, part 1: distortion and residual stresses in panel fabrication* - J. Ship Prod., 2004, Vol. **20**, pp. 43-59

[Hughes 1987] T. Hughes - *The Finite Element Method* - Dover Publications, 1987, ISBN: 0486411818

[Hull 1967] F.C. Hull – *Effect of Delta Ferrite on the Hot Cracking of Stainless Steel* – Welding Journal, Vol. **46**(9), pp. 399-409

[Igel 2006] C. Igel, T. Suttorp, N. Hansen - *A Computational Efficient Covariance Matrix Update and a (1+1)-CMA for Evolution Strategies* - Proceedings of the Genetic and Evolutionary Computation Conference (GECCO). 2006, pp. 453–460

[IIW 1971] International Institute of Welding - *Guide to the Welding and Weldability of C-Mn Steels and C-Mn Microalloyed Steels* - Publications Document II S/IIW-382-71, 1971

[Jonassen 1946] F. Jonassen, J.L. Meriam, E. P. Degarmo - *Effect of certain block and other special welding procedures on residual welding stresses* – Welding Journal, 1946, Vol. **25**(9), pp. 492–496

[Josefson 1983] B.L. Josefson - *Stresses redistribution during annealing of a multi-pass welded pipe* - Pressure Vessels Technology, 1983, Vol. **105**, pp. 165–170

[Josserand 2007] E. Josserand, J.-F. Jullien, D. Nellas, F. Boituout, D. Deloison - *Numerical Simulation of Welding-Induces Distortions taking into account Industrial Clamping Conditions* - 2007, Mathematical Modelling of Weld Phenomena, pp. 1073-1092, ISBN: 9783902465696

[Jung 2003] G.H. Jung – *Plasticity-based distortion analysis for fillet welded thin plate T-joints* - PhD Thesis, Ohio State University, 2003

[Jung 2004] G.H. Jung, C.L. Tsai - *Fundamental Studies on the Effect of Distortion Control Plans on Angular Distortion in Fillet Welded T-Joints* - Welding Journal, 2004, Vol. **83**(7), 213-223

[Kadivar 2000] M.H. Kadivar, K. Jafarpur, H.G. Baradaran - *Optimization welding sequence with genetic algorithm* - Comp. Mech., 2000, Vol. **26**, pp. 514-519

[Kang 1996] Y. Kang, Y. Shun, X. Wang - *A study on friction characteristics of coated and non-coated steel sheets in sheet forming* - Proceedings of the NUMISHEET'96, 1996, pp. 61-64

[Kannengießer 2001] T. Kannengießer, T. Böllinghaus, W. Florian, H. Herold – *Effect of weld metal strength and welding conditions on reaction forces and stress distribution of restrained components* – Welding in the World, 2001, Vol. **45**(1/2), pp. 18-26

[Kim 2002] K. Kim, D. Kim, B. O. Nnaji - *Robot arc welding task sequencing using genetic algorithms* - IIE Transactions, 2002, Vol. **34**(10), pp. 865-880

[Kim 2008] H.-G. Kim, S.-B. Shin, D.-S. Kim – *A Study on the Angular Distortion Control for the Multi-Pass Butt Weldment of STS 316LN* – Materials Science Forum, 2008, Vol. **580-582**, pp. 431-434

[Koistinen 1959] D. Koistinen, E. Marburger - *A general equation describing the extent of the austenite-Martensite transformation in pure iron-carbon alloys and plain carbon steels* - Acta Metallurgica, 1959, Vol. **7**, pp. 59-60

[Koschnick 2004] F. Koschnick - *Geometrische Locking-Effekte bei Finiten Elementen und ein allgemeines Konzept zu ihrer Vermeidung* - PhD Thesis, TU München, 2004

[Kraska 2004] European Patent No. EP 1 577 659, 2004

[Kurdjumov 1975] G.V. Kurdjumov, A.G. Khachaturyan – *Nature of Axial Ratio of the Martensite Lattice and Mechanism of Diffusionless $\alpha \rightarrow \gamma$ Transformation* – Acta Metallurgica, 1975, Vol. **23**(7), pp. 1077-1088

[Läpple 2006] V. Läpple – *Wärmebehandlung des Stahls* – 9th Edition, Verlag Europa-Lehrmittel, 2006, ISBN: 3808513098

[LeBlond 1984] J. Leblond, J. Devaux - *Mathematical Modelling of Transformation Plasticity in Steels I: Case of Ideal-Plastic Phases* - International Journal of Plasticity, 1989, Vol. **5**, 551-572

[Legatt 1986] R.H. Legatt - *Residual stresses and distortion in multipass butt welded joints in type 316 stainless steel* - Residual Stresses Sci Technol, 1986, Vol. **2**, pp. 997–1004

[Lenz 2001] B. Lenz – *Finite Elemente-Modellierung des Laserstrahlschweißens für den Einsatz in der Fertigungsplanung* – PhD Thesis, TU München, 2001

[LePera 1979] F.S. LePera - *Improved etching technique for the determination of percent martensite in high-strength dual-phase steels* – Metallography, 1979, Vol. **12**, pp. 263–268

[Li 2004] J. Li, Q. Guan, Y.W. Shi, D.L. Guo - *Stress and distortion mitigation technique for welding titanium alloy thin sheet* - Science and Technology of Welding and Joining, 2004, Vol. **9**(5), pp. 451 et sqq.

[Liedl 2002] U. Liedl, S. Traint, E.A. Werner - *An unexpected feature of the stress-strain diagram of dual-phase steels* - Computational Materials Science, 2002, Vol. **25**, pp. 122-128

[Lin 1995] Y.C. Lin, C.P. Chou – *A new technique for reducing the residual stress induced by welding in type 304 stainless steel* – Materials Processing Technology, 1995, Vol. **48**, pp. 693-698

[Lin 2005] Y.-M. Lin, C. Eichele, F.G. Shi - *Effect of welding sequence on welding-induced-alignmentdistortion in packaging of butterfly laser diode modules: Simulation and experiment* – Journal of Lightwave Technology, 2005, Vol. **23**(2), pp. 615-623.

[Lincoln 2000] James F. Lincoln Arc Welding Foundation - *The Procedure Handbook of Arc Welding* – 14th Edition, ASIN: B000FBCQ4M

[Lindgren 1997] L.-E. Lindgren, H.-A. Häggblad, J.M.J. McDill, A.S. Oddy - *Automatic remeshing for three-dimensional simulation of welding* - Comp. Methods Appl. Mech. Engrg., 1997, Vol. **147**, pp. 401-409

[Lindgren 2001] L.-E. Lindgren - *Finite Element modeling and simulation of welding: Part I* - Journal of Thermal Stresses, 2001, Vol. **24**, pp. 141-192

[Lindgren 2001a] L.-E. Lindgren - Finite Element modeling and simulation of welding: Part II - Journal of Thermal Stresses, 2001, Vol. **24**, pp. 195-231

[Lindgren 2002] L.-E. Lindgren – *Modelling for residual stresses and deformations due to welding – Knowing what isn't necessary to know* - Mathematical Modelling of Weld Phenomena 6, 2002, ISBN: 1902653564

[Little 1998] G.H. Little, A.G. Kamtekar - *The effect of thermal properties and weld efficiency on transient temperatures during welding* - Comp. Struct., 1998, Vol. **68**, pp. 157-165

[Liu 2009] C. Liu, J.X. Zhang – *Numerical simulation of transient welding angular distortion with external restraints* – Science and Technology of Welding and Joining, 2009, Vol. **14**(1), pp. 26-31

[Ma 1995] N. Ma, Y. Ueda, H. Murakawa, H. Maeda - *FEM Analysis of 3D Welding Residual Stresses and Angular Distortion in T-type Fillet Welds* - JWRI, 1995, Vol. **24**(2), pp. 115-122

[Mahnken 1994] R. Mahnken, E. Stein - *The identification of parameters for visco-plastic models via finite-element methods and gradient methods* - Modelling Simul. Mater. Sci. Eng., 1994, Vol. **2**, pp. 597-616

[Malisius 1977] R. Malisius – Schrumpfungen, Spannungen und Risse beim Schweißen – 4th Edition, Verlag für Schweißtechnik, 1977,

[Mandal 2004] N. R. Mandal - *Welding and Distortion Control* - Narosa Publishing House, 2004, ISBN: 1842651773

[Mase 1969] G. Mase - *Continuum Mechanics* - 1. Edition, McGraw-Hill, 1969, ISBN: 070406634

[Masubuchi 1980] K. Masubuchi - *Analysis of Welded Structures* - Pergamon Press Ltd., 1980, ISBN: 0080227147

[Matuszak 2000] A. Matuszak - *Determination of the frictional properties of coated steel sheets* - Journal of Materials Processing Technology, 2000, Vol. **106**, pp. 107-111

[McDowell 1992] D.L. McDowell - *A nonlinear kinematic hardening theory for cyclic thermoplasticity and thermoviscoplasticity* - International Journal of Plasticity, 1992, Vol. **8**, pp. 695-728

[Michaleris 1997] P. Michaleris, X. Sun - *Finite Element Analysis of Thermal Tensioning Techniques Mitigating Weld Buckling Distortion* - Welding Journal, 1997, Vol. **76**(11), pp. 451-457

[Michaleris 1999] P. Michaleris, J. Dantzig, D. Tortelli – *Minimization of Welding Residual Stress and Distortion in Large Structures* – Welding Journal, 1999, Vol. **78**(11), pp. 361-366

[Michaeleris 2006] P. Michaleris, L. Zhang, S.R. Bhide, P. Marugabandhu - *Evaluation of 2D, 3D and Applied Plastic Strain Methods for Predicting Welding Distortion and Residual Stress* - Science and Technology of Joining and Welding, 2006, Vol. **11**(6), pp. 707-717

[Mikami 2009] Y. Mikami, Y. Morikage, M. Mochizuki, M. Toyoda – *Angular distortion of filler welded T -joints using low transformation temperature welding wire* – Science and Technology of Welding and Joining, 2009, Vol. 14(2) pp. 97-105

[Mochizuki 2000] M. Mochizuki, M. Hayashi, T. Hattori - *Residual Stress Distribution Depending on Welding sequenze in Multi-Pass Welded Joints With X-Shaped Groove* - Journal of Pressare Vessel Technology, 2000, Vol.**122**, pp. 27-32

[Moon 2002] M.W. Moon, J.W. Chung, K.R. Lee, R. Wang, A. G. Evans - *An experimental study of the influence of imperfections on the buckling of compressed thin films* - Acta Materialia, 2002, Vol. **50**(5), pp. 1219-1227

[Moyer 1975] J.M. Moyer, G.S. Ansell - *The Volume Expansion accompanying the Martensite Transformation in Iron-Carbon Alloys* - Metallurgical Transactions, 1975, Vol. **6A**, pp. 1785-1791

[Mukherjee 2009] K. Mukherjee – *Grain Refinement in Dual Phase Steels* – PhD Thesis, University of British Columbia, 2009

[Murthy 1996] Y.V.L.N. Murthy, G. Venkata Rao, P. Krishna Iyer - *Numerical Simulation of Welding and Quenching Processes using transient Thermal and Thermo-Elastoplastic Formulations* - Comp. Struct., 1996, Vol. **60**(1), pp. 131-154

[Murugaiyan 2006] A. Murugaiyan, A. Saha Podder, A. Pandit, S. handra, D. Bhattacharjee, R. K. Ray - *Phase Transformations in Two C-Mn-Si-Cr Dual Phase Steels* - ISIJ International, 2006, Vol. **46**(10), pp. 1489-1494

[Nagy 2008] T. Nagy, S. Williams, P. Colegrove, C. Ikeagu, I. Fafiolu - *Distortion Mitigation in Welded Ship Panels* – Proceedings of the IWOTE'08, 2008, Bremen, pp. 265-275

[Nelder 1965] J.A. Nelder, R. Mead - *A simplex method for function minimization* - Computer Journal, 1965, Vol. **7**, pp 308–313

[Neumann 1978] A. Neumann, K.-D. Röbenack – *Verformungen und Spannungen beim Schweißen* – DVS-Verlag, 1978, ISBN: 3871550817

[Newport 1999] Newport News Shipbuilding and Dry Dock Co. USA - *Internally mounted pipe clamping device [for preventing distortion during welding]* - US Patent application 5 875 955, 1999

[Norrish 1992] J. Norrish - *Advanced Welding Processes* - Institute of Physics Publishing, 1992, ISBN: 0852743262

[Ohnimus 1996] S. Ohnimus - *Theorie und Numerik dimensions- und modelladaptiver Finite-Elemente-Methoden von Flächentragwerken* - PhD Thesis, University of Hannover, 1996

[Paley 1975] Z. Paley, P.D. Hibbert - *A new finite element model for welding heat sources* - Welding Journal Research Supplement, 1975, Vol. **54**, pp. 385-392

[Pan 1992] H.H. Pan, G.J. Weng - *Thermal stress and volume change during a cooling process involving phase transformation* - Journal of Thermal Stresses, 1992, Vol. **15**(1), pp. 1-12

[Pavelic 1969] V. Pavelic - *Experimental and Computed Temperature Histories in Gas Tungsten Arc Welding of Thin Plates* - Welding Journal, 1969, Vol. **48**, pp. 295-305

[Peil 2004] U. Peil, M. Wichers - *Schweißen unter Betriebsbeanspruchung – Werkstoffkennwerte für einen S355 J2G3 unter Temperaturen bis 1200°C* - Stahlbau, 2004, Vol. **73**(6), pp. 400-416

[Pietzsch 2000] R. Pietzsch - *Simulation und Minimierung des Verzuges von Stahlprofilen beider Abkühlung* - PhD Thesis, University of Magdeburg, 2000

[Pietzsch 2005] R. Pietzsch, M. Brzoza, Y. Kaymak, E. Specht, A. Bertram - *Minimizing the Distortion of Steel Profiles by Controlled Cooling* - Steel Research Int., 2005, Vol. **76**(5), pp. 399-407

[Pilipenko 2001] A. Pilipenko - *Computer simulation of residual stress and distortion of thick plates in multi-electrode submerged arc welding – Their mitigation techniques* - PhD Thesis, NTNU Trondheim, 2001

[Pittner 2004] A. Pittner, D. Weiß, J. Ji, P. Seyffarth - *Vorhersage der Nahtgeometrie beim Laser-MSG-Hybridschweißen durch verknüpfte mathematische und empirische Modelle* - Innovationsforum Hybridtechnologien, Halle, 2004, Beitrag der SLV M-V

[Pittner 2008] A. Pittner, D. Weiss, C. Schwenk, M. Rethmeier – *A new methodology for the fast temperature field generation for welding simulation* – Proceedings of the the Conference on Computer Technology in Welding and Manufacturing, 2008, Cranfield, UK

[Poorhaydari 2005] K. Poorhaydari, B.M. Patchett, D.G. Ivey - *Estimation of Cooling Rate in the Welding of Plates with Intermediate Thickness* - Welding Journal, 2005, Vol. **84**(10), pp. 149-155

[Porter 1992] D.A. Porter, K.E. Easterling - *Phase Transformations in Metals and Alloys* – 2nd Edition, Chapman Hall, 1992, ISBN: 0412450305

[Porzner 2005] H. Porzner - *Possibilities of Numerical Simulation for Evaluation and Optimisation of Welded Designs* - Mathematical Modelling of Weld Phenomena 5, Seggau, 2001

[Prager 1949] W. Prager - *Recent Developments in the Mathematical Theory of Plasticity* - J. Appl. Phys., 1949, Vol. **20**, pp. 235 et sqq.

[Prasad 1997] N.S. Prasad, M. Srinivasan – *Effect of boundary restraint and welding sequence on residual stresses in weldments* – Journal for the Joining of Materials, 1997, Vol. **9**(1), pp. 37-42

[Press 2001] W. Press, S. Teukolsky, W. Vettering, B. Flannery - *Numerical Recipes in C++* - Cambridge University Press, 2002, ISBN: 0521750334

[Price 2007] D.A. Price, S.W. Williams, A. Wescott, C.J.C. Harrison, A. Rezai, A. Steuwer, M. Peel, P. Staron, M. Kocak – *Distortion control in welding by mechanical straightening* – Science and Technology of Joining and Welding, 2007, Vol. **12**(7), pp. 620-633

[Provost 1981] W. Provost - *Effects of a stress relief heat treatment on the toughness of pressure vessel quality steels—Influence of the plate thickness* - Pressure Vessels and Piping, 1981, Vol. **10**(2), pp. 93-118

[Qiao 1996] G. Qiao et al. – *Progress and trends in distortion controlling for welded shell structure in aerospace manufacturing* – Proceedings of the 6th international symposium, 1996, JWS, Nagoya

[Radaj 1992] D. Radaj - *Heat Effects of Welding* - Springer, 1992, ISBN: 0387548203

[Radaj 1999] D. Radaj - *Schweißprozeßsimulation – Grundlagen und Anwendungen* - DVS-Verlag, 1999, ISBN: 3871551880

[Radaj 2002] D. Radaj - *Eigenspannungen und Verzug beim Schweißen – Rechen- und Meßverfahren* - DVS-Verlag, 2002, ISBN: 387155945

[Rammerstorfer 1981] F.G. Rammerstorfer, D.F. Fischer, W. Mitter - *On Thermo-Elastic-Plastic Analysis of Heat-Treatment Processes including Creep and Phase Changes* - Comp. Struct., 1981, Vol. **13**, pp. 771-779

[Rappe 1974] H.A. Rappe - *Betrachtungen zu Schweißeigenspannungen* - Schweißen und Schneiden, 1974, Vol. **26**(2), pp. 45-50

[Richards 2008] D.G. Richards, P.B. Prangnell, S.W. Williams, P.J. Withers – *Global mechanical tensioning for the management of residual stresses in welds* – Materials Science and Engineering, 2008, Vol. **489A**, pp. 351-362

[Richter 1971] F. Richter - *Die wichtigsten physikalischen Eigenschaften von 52 Eisenwerkstoffen* - 1973, Stahleisen Sonderberichte, Heft 8, Germany

[Roeren 2005] S. Roeren, A. Trautmann, M.F. Zaeh - *Modelling of Transient Clamping Conditions during Laser Beam Welding* - Proceedings of the Third International WLT-Conference on Lasers in Manufacturing, 2005, pp. 95-100

[Roeren 2006] S. Roeren, C. Schwenk, M. Rethmeier - *Different approaches to model clamping conditions within a weld simulation* - Proceedings of the 8th Conference on Mathematical Modelling of Weld Phenomena, 2006

[Rosenthal 1941] D. Rosenthal - *Mathematical theory of heat distribution during welding and cutting* - Welding Journal, 1941, Vol. **20**(5), pp. 220 - 234.

[Rykalin 1952] N. Rykalin - *Die Wärmegrundlagen des Schweißvorganges* - Verlag Technik, Berlin, 1952

[Sagalevich 1974] V.M. Sagalevich – *Methods for removal of welding distortions and stresses* - Moscow, Mashinostroenye, 1974

[Sakino 2003] K. Sakino - *Strain rate dependency of dynamic flow stress of iron in wide strain rate range* - Journal de Physique IV, 2003, Vol. **110**(1), pp.93-98

[Salzgitter] Salzgitter AG, www.salzgitter-flachstahl.de, 2010

[Savran 2009] V. Savran – *Austenite Formation in C-Mn Steels* – PhD Thesis, TU Delft, 2009

[Schenk 2006] T. Schenk - *Deformation Behaviour of Tungsten and Crack Propagation in Thin Tungsten Wires* - Master Thesis, Fraunhofer IWM Freiburg, 2006

[Schenk 2009a] T. Schenk, I.M. Richardson, M. Kraska, S. Ohnimus - *A study on the influence of clamping on welding distortion* - Computational Materials Science, 2009, Vol. **45**, pp. 999–1005

[Schenk 2009b] T. Schenk, I.M.Richardson, M. Kraska, S. Ohnimus - *The Influence of Clamping on the Distortion of Welded S355 T-Joints* - Science and Technology of Joining and Welding, 2009, Vol. **14**(4), pp.669-675

[Schneider 2009] C. Schneider - *Experimentelle und numerische Untersuchung zum Einfluss von Schweißverfahren und Schweißparameter auf die Kalibrierung eines Simulationsmodells für den Schweißverzug* - Master Thesis, Hochschule Aachen, 2009

[Schumann 1991] H. Schumann - *Metallographie* - Verlag für Grundstoffindustrie, 1991, ISBN: 3342004312

[Schwenk 2005] C. Schwenk, M. Rethmeier, K. Dilger, V. Michailov - *Schweißsimulation im Fahrzeugbau - Möglichkeiten, Grenzen und Herausforderungen* - DVS Report, 2005, Nr. 237, pp. 353 et sqq.

[Schwenk 2007] C. Schwenk - *FE-Simulation des Schweißverzugs laserstrahlgeschweißter dünner Bleche* - PhD Thesis, TU Berlin, 2007, ISBN: 9783981165555

[Schwenk 2007a] C. Schwenk, M. Rethmeier, K. Dilger – *Analysis of the transient deformation behaviour and numerical optimisation of an electron beam welded gearwheel* - Mathematical Modelling of Weld Phenomena 8, 2007, ISBN: 9783902465696

[Seifert 2003] T. Seifert - *Identification of Material Parameters Using Instrumented Indentation Test Data* - Master Thesis, COMMAS, University of Stuttgart, 2003

[Seifert 2007] T. Seifert, T. Schenk - *Efficient modular algorithms in modelling finite deformations; objective integration, parameter identification and sub-stepping techniques* - Comput. Meth. Appl. Mec., 2007, Vol. **196**(17-20), pp. 2269-2283

[Seyffarth 1992] P. Seyffarth, B. Meyer, A. Scharff - *Großer Atlas Schweiß-ZTU-Schaubilder* - DVS-Verlag, 1992, ISBN: 3871551279

[Shim 1992] Y. Shim, Z. Fng, D. Kim, J. Jaeger, J.C.Papritan, C.L. Tsai - *Determination of Residual Stresses in Thick-Section Weldments* - Welding Journal, 1992, Vol. **71**(9), pp. 305 - 312

[Siddique 2006] M. Siddique, M. Abid – *Finite element simulation of mechanical stress relieving in welded pipe-flange joint* – Process Mechanical Engineering, Vol. **220**, pp. 17-30

[Simo 1990] J.C. Simo, M. S. Rifai - *A Class of Assumed Strain Methods and the Method of Incompatible Modes* - Num. Meth. Eng., 1990, Vol. **29**, pp. 1595–1638

[Simo 1998] J. Simo, T. Hughes - *Computational Inelasticity* - Springer, 1998, ISBN: 0387975209

[Song 2004] J. Song, J.Y. Shanghvi, P. Michaleris – *Sensitivity analysis and optimization of thermo-elasto-plastic processes with applications to welding side heater design* – Computer Methods in Applied Mechanics and Engineering, 2004, Vol. **193**, pp. 4541-4566

[Sorensen 1999] M. Birk-Sorensen - *Simulation of Welding Distortions in Ship Sections* - PhD Thesis, Technical University of Denmark, 1999

[Staubach 2006] M. Staubach, R. Müller, S. Jüttner - *Messung und Minimierung schweißtechnisch bedingter Verzüge an Profil-T-Stoßverbindungen* - Schweißen und Schneiden, 2006, Vol. **58**(10), pp. 520-523

[Steven 1956] W. Steven, A.G. Haynes - *The Temperature of Formation of Martensite and Bainite in Low-Alloy Steels* - Journal of Iron and Steel Institute, 1956, Vol. **183**, pp. 349-359

[Suresh 1997] S. Suresh, V.P. Raghupathy, P.K. Nair, R. Vasudevan – *Analysis of longitudinal distortion in welding – Part 1: A critical review of existing theories* – Joining of Materials, 1997, Vol. **9**(1), pp. 21-30

[Taljat 1998] B. Taljat, B. Radhakrishnan, Z. Zacharia - *Numerical Analysis of GTA welding process with emphasis on post-solidification phase transformation effects on residual stresses* - Mater. Sci. Eng., 1998, Vol. **A246**, pp. 45-54

[Taylor 1976] R.L. Taylor, P.J. Berensford, E.L. Wilson - *Non-conforming element for stress analysis* - Num. Meth. Eng., 1976, Vol. **10**, pp. 1211-1219

[Tekriwal 1988] P. Tekriwal, J. Mazumder – *Finite Element Analysis of Three-Dimensional Transient Heat Transfer in GMA Welding* - Welding Journal, 1988, Vol.**67**(5), pp. 150-156

[Teng 1998] T.-L. Teng, C.C. Lin – *Effect of welding conditions on residual stresses due to butt welds* – Pressure Vessels and Piping, 1998, Vol. **75**, pp. 857-864

[Teng 2001] T.-L. Teng, C.-P. Fung, P.-H. Chang, W.-C. Yang – *Analysis of residual stresses and distortions in T-Joint fillet welds* – Pressure Vessels and Piping, 2001, Vol. **78**, pp. 523-538

[Teng 2003] T.-L. Teng, P.-H. Chang, W.-C. Tseng - *Effect of welding sequences on residual stresses* - Computers and Structures, 2003, Vol. **81**(5), pp. 273-286

[Thiessen 2006] R.G. Thiessen - *Physically-Based Modelling of Material Response to Welding* - PhD Thesis, TU Delft, 2006, ISBN: 9789077171247

[Thiessen 2006a] R.G. Thiessen, I.M. Richardson - *A Strategy for Modeling Microstructure in Macroscopic Simulations of Welded Material* - Metallurgical and Materials Transactions, 2006, Vol. **37B**, pp. 293-299

[Thyssen 1999] Thyssen-Krupp Steel - *High-strength steel for lightweight auto body manufacture* – Report, 1999

[Tikhomirov 2003] D. Tikhomirov – *Welding simulation of a transverse control arm* – Proceedings of the EuroPAM, 2003, Mainz, Germany

[Tikhomirov 2005] D. Tikhomirov, B. Rietman, K. Kose, M. Makkink - *Computing of welding distortion: comparison of different industrially applicable methods* - Advanced Materials Research, 2005, Vol. **6-8**, pp.195-202

[Tikhomirov 2007] D. Tikhomirov, C. Schwenk, T. Franz – *Methoden der Schweißverzugssimulation für die Anwendung in der Automobilindustrie* – Schweißen und Schneiden, 2007, Vol. **59**(12), pp. 678-680

[Timoshenko 1961] S. Timoshenko - *Theory of Elastic Stability* - 2nd Edition, McGraw-Hill, 1961, ISBN: 0070647496

[Tsai 1995] C.L. Tsai, W.T. Cheng, T. Lee – *Modelling Strategy for Control of Welding-Induced Distortion* – Modelling of Casting, Welding and Advanced Solidification Processes VII, 1995, pp. 335-345

[Tsai 1999] C.L. Tsai, S.C. Park, W.T. Cheng - *Welding Distortion of a Thin-Plate Panel Structure* - The Welding Journal, 1999, Vol. **78**(5), pp. 157-165

[Velthuis 1998] S.G.E. Velthuis, J.H. Root, J. Sietsma, M. T. RekveldtS. Van der Zwaag - *The ferrite and austenite lattice parameters of Fe-Co and Fe-Cu binary alloys as a function of temperature* - Acta Materialia, 1998, Vol. **46**(15), pp. 5223-5228

[Verhaeghe 1999] G. Verhaeghe - *Predictive Formulae for Weld Distortion: A Critical Review* - Woodhead Publishing Ltd, 1999, ISBN: 1855734443

[Wahab 1998] M.A. Wahab, M.J. Painter, M.H. Davies - *The prediction of the temperature distribution and weld pool geometry in the gas metal arc welding process* – Materials Processing Technology, 1998, Vol. **77**, pp. 233-239

[Wahab 2006] M.A. Wahab, M.S. Alam, M.J. PAiner, P.E. Stafford – *Experimental and Numerical Simulation of Restraining Forces in Gas Metal Arc Welded Joints* – Welding Journal, 2006, Vol. **85**(2), pp. 35-43

[Wang 2001] Y. Wang, Q. Shi, H.L. Tsai - *Modeling of the Effects of Surface-Active Elements on Flow Patterns and Weld Penetration* - Metallurgical and Materials Transactions, 2001, Vol. **32B**, pp. 145-162

[Watanabe 1955] M. Watanabe, K. Satoh, K. Kimura, R. Hoshi – *Effect of Welding Methods and Sequences on the Residual Stress Distribution of Welded Joints* – Japan Welding Society, 1955, Vol. **24**(4), pp. 146-153

[Watanabe 1961] M. Watanabe, K. Satoh - *Effect of welding conditions on the shrinkage distortion in welded structures* – Welding Journal, 1961, August, pp. 377-384

[Weber 1988] G. Weber - *Computational Procedures for a New Class of Finite Deformation Elastic-Plastic Constitutive Equations* - PhD Thesis, Massachusetts Institute of Technology, 1988

[Wei 2005] Y. Wei, Z. Dong, R. Liu, Z. Dong, Y. Pan – *Numerical simulation and prediction of weld solidification cracking* - Mathematical Modelling of Weld Phenomena 7, 2005, pp. 651-669, ISBN: 9783901351990

[Wilkening 1993] W.W. Wilkening, J.L. Snow - *Analysis of Welding-Induced Residual Stresses With the Adina System* - Comput. Struct., 1993, Vol. **47**(4/5), pp. 767-786

[Williams 2008] S. Williams, S. Morgan, A. Wescott, M. Poad, S. Wen - *Stress Engineering – Control of Residual Stresses and Distortion in Welding* – Proceedings of the IWOTE'08, 2008, Bremen

[Wilsen 2001] E. Wilson, S. Medina - *Application of Koistinen and Marburger`s athermal equation for volume fraction of Martensite to diffusional transformations obtained on continuous cooling of 0.13%C high strength low alloy steel* - Materials Science and Technology, 2000, Vol. **16**, pp. 630-633

[Wyrwich 2009] P. Wyrwich - *Validierung eines neuen Verfahrens zur Bestimmung kinematischer Verfestigungsparameter für Stahlwerkstoffe* - Master Thesis, TU Berlin, 2009

[Xie 2002] L.S. Xie, C. Hsieh - *Clamping and welding sequence optimization for minimizing cycle time and assembly deformation* - Materials & Product Technology, 2002, Vol.**17**(5-6), pp. 389-399

[Xu 2007] J. Xu, W. Li – *The Nonlinear Time-Varying Response of Dynamic Thermal Tensioning for Welding-Induced Distortion Control* – Manufacturing Science and Engineering, 2007, Vol. **129**, pp. 333-341

[Xu 2007a] J. Xu, W. Li – *A finite element analysis of welding-induced distortion control for large box beam structures* – Engineering Manufacture, 2007, Vol. **221B**, pp. 289-301

[Yang 1999] Z. Yang, T. Debroy - *Modeling Macro- and Microstructures of Gas-Metal-Arc-Welded HSLA-100 Steel* - Metallurgical and Materials Transactions, 1999, Vol. **30B**, pp. 483-493

[Yang 2000] Y. Yang, P. Dong, J. Zhang, X. Tian - *A Hot-Cracking Mitigation Technique for Welding High-Strength Aluminium Alloy* - Welding Journal, 2000, Vol. **79**(1), pp. 9-17

[Zacharia 1994] T. Zacharia – *Dynamic Stresses in Weld Metal Hot Cracking* – Welding Journal, 1994, July, pp. 164-172

[Zang 2007] S. Zang, J. Liang, C. Guo - A constitutive model for spring-back prediction in which the change of Young's modulus with plastic deformation is considered - International Journal of Machine Tools and Manufacture, Vol. 2007, Vol. **47**(11), pp. 1791-1797

[Zhang 2007] L.J. Zhang, J.X. Zhang, H. Serizawa, H. Murakawa – *Parametric studies of welding distortion in fillet welded structure based on FEA using iterative substructure method* – Science and Technology of Joining and Welding, 2007, Vol. **12**(8), pp. 703-707

[Zhu 2002] X.K. Zhu, Y.J. Chao - *Effects of temperature-dependent material properties on welding simulation* - Comp. Struct., 2002, Vol. **80**, pp. 967-976

[Zhu 2003] X.K. Zhu, Y.J. Chao – *Numerical simulation of transient temperature and residual stresses in friction stir welding of 304L stainless steel* – Materials Processing Technolog, 2004, Vol. **146**, pp. 263-272

[Zienkiewicz 1987] O.C. Zienkiewicz, J.Z. Zhu - *A simple error estimator and adaptive procedure for practical engineering analysis* - Num. Meth. Eng., 1987, **Vol.** 24, pp. 337-357

Acknowledgements

This work was done within the framework of the research program of the *Materials Innovation Institute* M2i (www.m2i.nl), project MC8.06256. The project was executed at *Innovationsgesellschaft für fortgeschrittene Produktionssysteme in der Fahrzeugindustrie mbH* INPRO (www.inpro.de), Berlin, Germany, and at Technical University of Delft, Delft, The Netherlands.

The research was supervised by my promoter Prof. Dr. Ian Richardson (JMB, TU Delft) and Dr.-Ing. Martin Kraska (INPRO). I would like to express sincere gratitude to both of them for their guidance, encouraging and enthusiastic support. They were always involved in my research and I am very grateful for the motivation and advices.

I would like to thank all members of the M2i head office for their help, understanding and organisation support. In particular, I would like to thank Monika Hoekstra, Bert van Haastrecht, Jonathan Hofman, Oscar Ruigrok and Monica Reulink for resolving all administrative challenges.

It would have been an extremely difficult task to perform this research without the excellent working relations and friendly atmosphere at the JMB group at TU Delft and at INPRO. Frankly, I almost have to thank all my colleagues and friends at TU Delft as well as INPRO for their friendship, discussions, support, and the great working atmosphere. At JMB, TU Delft, I particularly would like to thank Ian Richardson, Marcel Hermans, Yu Pan, Murugayian Amirthalingam, Jurrian Slingerland, and Frans Bosman. At INPRO, my thanks go especially to Martin Kraska, Maria Doig, Dmitrij Tikhomirov and also to Bert Rietman, Martin Petzoldt, Christian Weiß, Martin Nitsche, Stephan Ohnimus, and Jochen Weiher. Working together with all of you was always a great pleasure.

This thesis would not have been possible without the support of the industrial partners in my project. I would like to thank Joep Broekhuijsen and Bernd-Jan Bekkers from *Damen Schelde Naval Shipbuilding*, Nick den Uijl from *Corus*, and Claudia Brandes and Björn Heibei from *Volkswagen Braunschweig*. Your support, the hundreds of kilos of materials and samples as well as all discussions regarding the meaning and the relevance of the results of my thesis are greatly appreciated.

Also outside JMB, TU Delft, and INPRO, I met a lot of new friends during my research, in particular Raymond Machunze, Ivan Lazic, Michael Wank and Sonia da Silva de Vieira at Delft, Peter Wyrwich, Christopher Schwenk and Andreas Pittner from BAM, Berlin, Jens Sakkietibutra from BIAS, Bremen, as well as Carmen Schäfer and Ulrich Prahl from RWTH Aachen. I would like to thank all of you for your friendship, discussions and also often for challenging the reason why we are all doing our research and what the outcome might be. In particular the latter question was mostly answered having a beer after a long working day. I hope we will still have fun remembering these days when we are old and bald.

Last but not least, many thanks go to my family, mother, father, sister and nieces and all my old friends from Freiburg and Berlin for believing in me, being proud of me and for the continuous encouragement. Finally, I of course want and have to thank my girlfriend Anja for her understanding and patience and the indispensable support I received from her during my research career and especially during the last difficult months of writing the manuscript.

List of Publications

- T. Schenk – *Deformation Behaviour of Tungsten and Crack Propagation in thin Tungsten Wires* – Master Thesis, 2006, Fraunhofer IWM, Freiburg
- T. Schenk, H. Brehm, T. Seifert - *A simple analogous model for the determination of cyclic plasticity parameters of thin wires to model wire drawing* - Journal of Engineering Materials and Technology, 2007, Vol. **129**(3), pp. 488-495
- T. Seifert, T. Schenk - *Efficient modular algorithms in modelling finite deformations; objective integration, parameter identification and sub-stepping techniques* - Computer Methods in Applied Mechanics and Engineering, 2007, Vol. **196**(17-20), pp. 2269-2283
- T. Schenk, I.M. Richardson, G. Eßer, M. Kraska, S. Ohnimus - *Welding Distortion of DP600 Overlap Joints and Influence of Clamping and Phase Transformation* - 2nd International Workshop on Thermal Forming and Welding Distortion, 2008, BIAS, Bremen, pp. 83-96
- T. Schenk, I.M. Richardson, M. Kraska, S. Ohnimus - *A Sensitivity Analysis for Modelling of Buckling Distortion of DP600 Overlap Joints* – Conference on Computers in Welding Technology 2008, TWI, Cranfield, UK
- T. Schenk, D. Tikhomirov, M. Kraska, I. M. Richardson - *Modelling clamping conditions for welding simulations of 1mm thick DP600 overlap joints* – 9th International Seminar on Numerical Analysis of Weldability, 2009, Seggau, Austria, pp. 675-698, ISBN 9783851251272
- T. Schenk, D. Tikhomirov, M. Kraska, I. M. Richardson - *Simplified Models for Welding Simulations with controlled Accuracy* - 9th International Seminar on Numerical Analysis of Weldability, 2009, Seggau, Austria, pp. 523-550, ISBN 9783851251272
- T. Schenk, I.M.Richardson, G. Eßer, M. Kraska - *Influence of the Hardening Model on the Predicted Welding Distortion of DP600 Lap Joints* - International Conference on Processing & Manufacturing of Advanced Materials, Berlin, Germany, August 25-29, 2009. Advanced Materials Research, Vol. **638-642**(2010), pp. 3710-3715
- T. Schenk – *Modelling Welding Distortion and the Influence of Clamping* - Presentation at the M2i Conference, Materials to Innovate Industry and Society, December 2009, Noordwijkerhout, NL
- T. Schenk, I.M.Richardson, M.Kraska, S. Ohnimus - *A non-isothermal thermomechanical-metallurgical model and its application to welding simulations* - Science and Technology of Joining and Welding, 2009, Vol. **14**(2), pp.152-160

- T. Schenk, I.M.Richardson, M. Kraska, S. Ohnimus - *The Influence of Clamping on the Distortion of Welded S355 T-Joints* - Science and Technology of Joining and Welding, 2009, Vol. **14**(4), pp. 669-675
- T. Schenk, I.M. Richardson, M. Kraska, S. Ohnimus - *A study on the influence of clamping on welding distortion* - Computational Materials Science, 2009, Vol. **45**, pp. 999–1005
- T. Schenk, I.M.Richardson, M. Kraska, S. Ohnimus - *Modelling buckling distortion of DP600 overlap joints due to gas metal arc welding and the influence of the mesh density* - Computational Materials Science, 2009, Vol. **46**, pp. 977-986
- T. Schenk, M. Kraska, S. Ohnimus, G. Eßer, I.M.Richardson - *The Influence of Welding Sequences on Distortion* – Science and Technology of Joining and Welding, 2010, Submitted for publication
- T. Schenk, C. Schwenk - *Material Response of GMA welded 1mm thick DP600 Overlap Joints – Science and Technol*ogy of Joining and Welding, Vol. **15**(7), pp. 567-574, 2010
- *T. Schenk, M. Doig, G. Eßer, I. Richardson - The Influence of the Clamping Distance on 6mm GMA welded S355 T-Joints* – Science and Technology of Joining and Welding, Vol. **15**(7), pp. 575-582, 2010
- T. Schenk, M. Kraska, I.M. Richardson - *Material Data for Welding Simulations of Steels* – IIW Intermediate Meeting SC-Auto, IIW-Doc. No. SC-Auto-35-10, April 2010, Berlin, Germany
- T. Schenk - *Modeling the Influence of Fixtures and Clamping on Distortion of Welded Structures* – Presentation at the ESI Welding Planner Shareholder User Group, January 2010, Berlin, Germany
- T. Schenk, M. Kraska, S. Ohnimus, I.M. Richardson - *A Study on the Influence of Welding Sequences on Distortion* - 3rd International Workshop on Thermal Forming and Welding Distortion, 2011, BIAS, Bremen, to be published

Curriculum Vitae



Name	Tobias Schenk
Academical degree	Diplom-Physiker
Date of birth	15.01.1980
Place of birth	Emmendingen, Germany

06.2010 – current	Simulation engineer at TRW Automotive, Alfdorf, Germany • Structural strength of seat belt components
08.2006 – 05.2010	Ph.D. researcher for the *Material innovation institute* (M2i), Delft, The Netherlands, at *Innovationsgesellschaft für fortgeschrittene Produktionssysteme in der Fahrzeugindustrie mbH* (INPRO), Berlin, Germany and Technical University of Delft, The Netherlands • Title: „Modelling Welding Distortion - The Influence of Clamping & Sequencing and Sensitivity Analyses" • At Delft 10.2006 – 11.2007 Remaining time at INPRO
10.2008 – 01.2010	Project Management (IHK) at Hamburger Akademie für Fernstudien (correspondence course)
10.2000 – 06.2006	Diploma degree in physics at Albert-Ludwigs-Universität Freiburg, Germany • Specialisations: Physics of polymers and solid state physics • Year abroad at „École Normale Supérieure", Lyon, France, 09-2003 – 04.2004 • Diploma thesis at Fraunhofer IWM, Freiburg, Title: „Deformation Behavior of Tungsten and Crack Propagation in thin Tungsten Wires"

06.2004 – 06.2006	Student at Fraunhofer Institut für Werkstoffmechanik IWM in Freiburg • Modelling of crack propagation during hot forming of wires • Prediction of thermomechanical fatigue (TMF) of exhaustion systems
09.1999 – 07.2000	Civlian servce at AWO Mobiler Sozialer Dienst, Denzlingen, Germany
09.1996 – 07.1999	Abitur at commercial high school Max-Weber, Freiburg, Germany
08.1990 – 07.1996	Realschule am Mauracher Berg, Denzlingen
08.1986 – 06.1990	Grundschule Brückleacker, Denzlingen